Jet formation and propagation in the nearby radio galaxy NGC 315

INAUGURAL-DISSERTATION

zur Erlangung des Doktorgrades der
Mathematisch-Naturwissenschaftlichen Fakultät der
Universität zu Köln

vorgelegt von

Luca Ricci
aus Torino, Italien

Köln, 2023

Berichterstatter: Prof. Dr. J. Anton Zensus
Prof. Dr. Andreas Eckart

Beginn Promotionsphase: 21.09.2020
Dissertation abgegeben: 13.08.2023
Disputation: 16.10.2023
Dissertation angenommen von der Mathematisch-Naturwissenschaftlichen Fakultät der Universität zu Köln: 16.10.2023

Erklärung

Hiermit versichere ich an Eides statt, dass ich die vorliegende Dissertation selbstständig und ohne die Benutzung anderer als der angegebenen Hilfsmittel und Literatur angefertigt habe. Alle Stellen, die wörtlich oder sinngemäß aus veröffentlichten und nicht veröffentlichten Werken dem Wortlaut oder dem Sinn nach entnommen wurden, sind als solche kenntlich gemacht. Ich versichere an Eides statt, dass diese Dissertation noch keiner anderen Fakultät oder Universität zur Prüfung vorgelegen hat; dass sie - abgesehen von unten angegebenen Teilpublikationen und eingebundenen Artikeln und Manuskripten - noch nicht veröffentlicht worden ist sowie, dass ich eine Veröffentlichung der Dissertation vor Abschluss der Promotion nicht ohne Genehmigung des Promotionsausschusses vornehmen werde. Die Bestimmungen dieser Ordnung sind mir bekannt. Darüber hinaus erkläre ich hiermit, dass ich die Ordnung zur Sicherung guter wissenschaftlicher Praxis und zum Umgang mit wissenschaftlichem Fehlverhalten der Universität zu Köln gelesen und sie bei der Durchführung der Dissertation zugrundeliegenden Arbeiten und der schriftlich verfassten Dissertation beachtet habe und verpflichte mich hiermit, die dort genannten Vorgaben bei allen wissenschaftlichen Tätigkeiten zu beachten und umzusetzen. Ich versichere, dass die eingereichte elektronische Fassung der eingereichten Druckfassung vollständig entspricht.

Köln, den 13.08.2023

Luca Ricci

Relevante zur Doktorarbeit Teilpublikationen [1]

Ricci, L.; Boccardi, B.; Nokhrina, E.; Perucho, M.; MacDonald, N.; Mattia, G.; Grandi, P.; Madika, E.; Krichbaum T. P.; Zensus J. A.: *Exploring the disk-jet connection in NGC 315*, 2022, A&A, 664, A166

Ricci, L.; Perucho, M.; López-Miralles J.; Martí J. M.; Boccardi, B.; *Magnetic and thermal acceleration in extragalactic jets: An application to NGC 315*, accepted for publication in A&A, 2023arXiv231206410R

Ricci, L.; Boccardi, B.; Röder, J.; Mattia, G.; Kadler, M.; Perucho, M.; Benke, P.; Bartolini V.; *Magnetic and spectral properties of the inner parsec scales jet in NGC 315*, draft manuscript

---

[1] Siehe Lebenslauf am Ende für eine umfassende Liste.

To my entire family and in particular to my grandfather
“Nino”, whose spirit inspired my life and he is
now among his beloved “*Gli invincibili*”.

To all the people who dropped their studies because they
got crushed by the sick seek of perfection
imposed by our society.

Abstract

Since their discovery many decades ago, relativistic jets have intrigued and fascinated astronomers. Besides being crucial elements in shaping the Universe as we observe it today, jets are unique laboratories to test and broaden our knowledge in many fields of physics, such as plasma physics and cosmology.

This thesis aims at investigating the relativistic jets launched from radio galaxies, a specific class of Active Galactic Nuclei (AGN), with the goal of understanding the jet formation and propagation phenomena, as well as the connection between accretion and ejection. Specifically, the work focuses on NGC 315, a giant radio galaxy whose vicinity and large mass of the central black hole offer a unique opportunity to address these subjects. The study combines two approaches: the analysis of Very Long Baseline Interferometry (VLBI) observations is accompanied by a theoretical study carried out by means of numerical simulations. These are performed using a relativistic magnetohydrodynamic (RMHD) code.

The thesis is composed of three introductory chapters followed by three results chapters. In Chapter 1, I introduce the fundamental physical and astronomical concepts concerning AGN, which are central throughout the thesis. In Chapter 2, I describe the basic elements of plasma physics and provide an overview of the state-of-the-art knowledge regarding the theory of jet formation and propagation together with the currently open questions. In Chapter 3, I explain the fundamental concepts concerning the VLBI technique, and how to perform the analysis of VLBI data. Finally, Chapters 4, 5, and 6 present the series of works on NGC 315, with Chapters 4 and 6 focusing on the observational studies and Chapter 5 describing the theoretical one.

From the analysis of a multi-frequency and multi-epoch VLBI data set, the extents of the jet collimation and acceleration regions in NGC 315 are suggested to coincide. Namely, the jet is observed to collimate within $\sim 0.6\,\mathrm{pc}$ from its apex, and to accelerate up to $v \sim 0.9\,c$ on the same scale. The co-spatiality of the two phenomena is in agreement with theoretical predictions for magnetically-driven outflows, in which the magnetic energy is progressively converted into kinetic energy of the bulk flow. Remarkably, a very steep spectral index down to $\alpha \sim -2$ ($S_\nu \propto \nu^\alpha$) is observed in the same region, in agreement with the findings for the jet in M 87. The spectral properties in the jet acceleration and collimation region are still poorly studied, and the possible physical processes leading to the steep spectrum, such as magnetic reconnection and cooling due to synchrotron losses, are discussed.

Different and independent approaches considering the jet brightness temperature and turnover frequency along the jet indicate that the magnetic field strength

increases (quasi-)linearly from parsec scales up to the jet apex. Such a behavior, together with measured strengths of $\sim 0.1\,\mathrm{G}$ on parsec scales, implies magnetic fields of $10^2 - 10^3\,\mathrm{G}$ in the nuclear region. The combination of the observational constraints, especially on the jet magnetization, together with theoretical models suggests that the jet in NGC 315 is launched by a maximally spinning black hole surrounded by a Magnetically Arrested Disk.

The synergy between the observational results and the RMHD simulations further suggests that thermal acceleration, in addition to magnetic acceleration, plays a relevant role in increasing the jet speed on sub-parsec and parsec scales. In conclusion, the simulations hint at the necessity of winds launched from the accretion disk to favor the propagation of relativistic jets by delaying the growth of instabilities and by shielding the internal spine from the influence of the ambient medium.

Zusammenfassung

Seit ihrer Entdeckung vor vielen Jahrzehnten haben relativistische Jets Astronomen fasziniert und begeistert. Neben ihrer entscheidenden Rolle bei der Entwicklung des Universums, wie wir es heute beobachten, bieten Jets einzigartige Möglichkeiten unser Wissen in vielen physikalischen Bereichen zu testen und zu erweitern, wie beispielsweise in der Plasmaphysik und Kosmologie.

Diese Dissertation zielt darauf ab, die relativistischen Jets zu untersuchen, die in Radiogalaxien beobachtet werden, eine spezielle Art von aktiven galaktischen Kernen (AGN), mit dem Ziel, die Entstehung und Ausbreitung von Jets zu verstehen, ebenso wie die Verbindung zwischen Akkretion und emittierter Strahlung. Konkret konzentriert sich die Arbeit auf NGC 315, eine riesige Radiogalaxie, deren Nähe sowie hohe Masse des zentralen Schwarzen Lochs eine einzigartige Gelegenheit bietet, diese Themen anzugehen. Die Studie vereint zwei Ansätze: Die Analyse von Beobachtungen mittels Interferometrie mit sehr langen Basislinien (VLBI) wird durch eine theoretische Studie ergänzt, die mithilfe von numerischen Simulationen durchgeführt wird. Diese werden unter Verwendung eines relativistischen magnetohydrodynamischen (RMHD) Codes durchgeführt.

Die Dissertation besteht aus drei einführenden Kapiteln, gefolgt von drei Ergebniskapiteln. Im Kapitel 1 führe ich die grundlegenden physikalischen und astronomischen Konzepte bezüglich AGN ein, die im Verlauf der Arbeit eine zentrale Rolle spielen. Im Kapitel 2 beschreibe ich die grundlegenden Elemente der Plasmaphysik und gebe einen Überblick über den aktuellen Wissensstand in Bezug auf die Theorie der Entstehung und Ausbreitung von Jets sowie die derzeit offenen Fragen. Im Kapitel 3 erkläre ich die grundlegenden Konzepte der VLBI-Technik und wie die Analyse von VLBI-Daten durchgeführt wird. Schließlich präsentieren die Kapitel 4, 5 und 6 die Reihe von Arbeiten zu NGC 315, wobei die Kapitel 4 und 6 den Beobachtungsstudien gewidmet sind und Kapitel 5 die theoretische Sichtweise beschreibt.

Aus der Analyse eines VLBI-Datensatzes in mehreren Frequenzen und Epochen wird vorgeschlagen, dass die Ausbreitungs- und Kollimationsbereiche des Jets in NGC 315 zusammenfallen. Der Jet wird beobachtet, sich innerhalb von $\sim 0,6,\mathrm{pc}$ von seinem Scheitelpunkt zu verengen und sich auf derselben Skala auf Geschwindigkeiten von bis zu $v \sim 0,9\,c$ zu beschleunigen. Die räumliche Übereinstimmung der beiden Phänomene stimmt mit theoretischen Vorhersagen für magnetisch angetriebene emittierte Strahlung überein, bei denen die magnetische Energie allmählich in kinetische Energie in beobachtbaren vorangehenden Strömung des Jets umgewandelt wird. Bemerkenswerterweise wird in derselben Region ein sehr steiler spektraler Index von etwa $\alpha \sim -2$ ($S_\nu \propto \nu^\alpha$) beobachtet,

was mit den Ergebnissen für den Jet in der Radiogalaxie M 87 übereinstimmt. Die spektralen Eigenschaften in der Beschleunigungs- und Kollimationsregion in Jets sind noch unzureichend erforscht, und die möglichen physikalischen Prozesse, die zu dem stark steigenden und abfallenden Spektrum führen, wie magnetische Verbindungen und Energieverlusten aufgrund von Synchrotronstrahlung, werden diskutiert.

Unterschiedliche und unabhängige Ansätze, die die Helligkeitstemperatur des Jets und die Frequenz des Wechsels zwischen der steigenden und abfallenden Kurve definiert werden entlang des Jets berücksichtigt und deuten darauf hin, dass die Stärke des Magnetfelds (quasi-)linear von Skalen mehrere Parsec entfernt bis zum Ankerpunkt des Jets zunimmt. Ein solches Verhalten, zusammen mit gemessenen Stärken von $\sim 0,1\,\mathrm{G}$ auf diesen Parsec-Skalen, impliziert Magnetfelder mit einer Stärke von $10^2 - 10^3, \mathrm{G}$ im Kernbereich. Die Kombination der beobachteten Einschränkungen, insbesondere in Bezug auf die Magnetstärke des Jets, zusammen mit theoretischen Modellen legt nahe, dass der Jet in NGC 315 von einem maximal rotierenden Schwarzen Loch hervorgeht, das von einer stark magnetischen Scheibe aus Staub und Gas umgeben ist.

Die Synergie zwischen den beobachteten Ergebnissen und den RMHD-Simulationen legt weiterhin nahe, dass thermische Beschleunigung neben der magnetischen Beschleunigung eine relevante Rolle spielt, um die Geschwindigkeit des Jets auf auf kleinen bis hin zu großen Skalen zu erhöhen. Zusammenfassend deuten die Simulationen darauf hin, dass es notwendig ist, von der Akkretionsscheibe gestartete (magnetische) Strömungen zu haben, um die Ausbreitung relativistischer Jets zu unterstützen, indem das Wachstum von Turbulenzen verzögert und die interne Struktur vor dem Einfluss des Umgebungsmediums geschützt wird.

Contents

List of Figures

1 Introduction

"Man must rise above the Earth to the top of the atmosphere and beyond for only thus will he fully understand the world in which he lives."

Socrates, Philosopher

Since the dawn of humanity, we have always been fascinated by the magnificence of the Cosmos and we have never stopped asking ourselves where those wonderful clouds and small lights may come from. It is a long journey until modern times. A long journey through all the civilizations which have trod the Earth, constellated by myth, amazing stories of Gods playing with the celestial bodies, along with astonishingly precise calculations of the motion of the stars obtained with nothing but the patient observations and genius of the ancient. The turning point in this story is represented by Galileo Galilei, who in the 17th Century pointed his telescope to the sky opening a new era in humankind. Fast traveling until modern times, thanks to the incredible technologies available to us, many details of the mysterious gears of the Universe have been discovered, while many more are still there, waiting to be unveiled. Currently, we are able to fathom the Universe from the very weak radio waves up to the most energetic γ-rays, covering the entire electromagnetic spectrum. Such capability allows us to investigate the astronomical sources from different points of view, providing an unprecedented source of information to tackle the physics behind them.

In this thesis I focus on the weakest part of the electromagnetic spectrum, the radio band. Through radio observations, my goal is to investigate the nature of the most luminous persistent sources in the entire Universe, the Active Galactic Nuclei (AGN), and the relativistic jets they produce. The first chapter [2] is divided as follows: in Sect. 1.1, I briefly describe the advantages of studying the Cosmos with the radio waves together with a brief history of the radio observations; in Sect. 1.2, I delineate the main properties of the Active Galactic Nuclei along with their current classification and observational signatures; in Sect. 1.3, I describe what relativistic jets are.

1.1 Radio astronomy

"The data give for the coordinates of the region from which the disturbance comes, a right ascension of 18 hours and declination of -10 deg."

Karl G. Jansky, Scientist

---

[2] This chapter is partially based on the textbooks Burke & Graham-Smith (2014) and Ferrari (2011)

With these very words, a new branch of science was born: Radio Astronomy. In 1932 Carl Janksy, with his self-built directional antenna designed to receive at a frequency of 20.5 MHz, while scanning the sky looking for noise in the radio communication, detected an unknown emission with a steady period of 24 hours. Roughly a year later he realized that such a signal was being detected with an interval that coincides with the sidereal day, i.e., the time needed by the Earth to complete a full rotation, implying that the signal had to be associated with something far beyond our planet. He noticed that a weak emission was spread throughout the sky but the stronger signal he was detecting was focused on one specific location in the Sagittarius constellation. He associated this emission with the interstellar medium. In the following years, Jansky struggled to convince the astronomical community of his discoveries, also due to the critical political situation the world was going through at the time accompanied by the Great Depression. Nonetheless, in 1940 the work of Jansky was picked up by Grote Reber, who, with a self-built parabolic reflector placed in his backyard, confirmed the presence of the emission detected a few years before with observations at 160 MHz. A few years later, he produced a detailed map of the Galactic radiation finding two different maxima later associated with the radio galaxy Cygnus A and with the supernova remnant Cassiopeia A (see Fig. 1.1).

The Second World War led to an incredible enhancement in radio technology with countless antennas that rose all over the world for military use. However, after the war ended the existing capabilities were used for a more noble cause, being pointed towards the sky. It would not be an exaggeration to call such a period one of the golden times in radio astronomy, with radio observatories growing throughout the surface of Earth and with new and important discoveries happening yearly. Thanks to radio observations, the first radio galaxies, along with the quasars and the interstellar medium were detected for the first time.

A turning point in radio astronomy happened in 1967 when scientists from the US and Canada started the experiments which later would have led to the birth of the so-called Very Long Baseline Interferometry (VLBI) technique. The VLBI technique is based on the physical principles of interferometry and it allows to merge data acquired from different antennas and consider them as if they were obtained by a single antenna with size of the maximum distance between two observatories in the array. In this way, the resolution of such observations (which depends on the inverse of the size of the observing instrument, as shown in Sect. 3.2.1) vastly overwhelms the one obtained through single-dish observations. In Sect. 3 I provide a comprehensive explanation of the functioning of a single-dish antenna along with the details on the VLBI technique and how to extrapolate physical information from it.

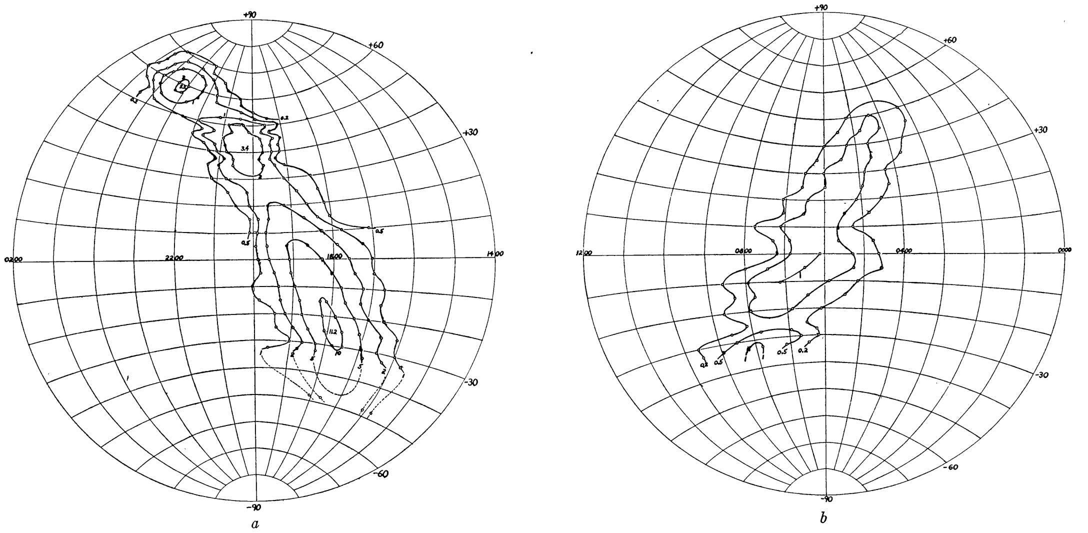

Figure 1.1: First map of the radio sky, obtained at 160 MHz (Reber 1944). The two emission peaks were later associated with Cygnus A and Cassiopeia A.

1.1.1 The radio window

The radio band covers frequencies from about 10 MHz up to 300 GHz. Observing the sky in such a window offers numerous advantages. The radio sky is extremely rich due to the possibility of observing low energetic phenomena or very distant objects.

A crucial advantage of the radio window is the possibility of performing observations from the ground. Indeed, as shown in Fig. 1.2, the atmosphere of our planet is opaque to most of the electromagnetic spectrum. The opacity of the atmosphere derives from the Ozone layer: molecules of oxygen and nitrogen are able to ionize the incoming ultraviolet, X-, and γ-rays radiation creating such an ionized layer. This region, called the ionosphere, is found around 100 km above the level of the sea and is able to absorb or reflect the majority of the incoming electromagnetic waves. However, there are two specific windows in the electromagnetic spectrum in which the opacity of the atmosphere drops to zero or nearly zero. The first one is between 3000 and 7000 Å and occupies the optical part of the spectrum, while the second is in the window roughly from 1 mm up to 20 m, i.e., within the radio band. The second window is a gold mine for radio astronomers. Here, no photons are missed during the traveling of the signal through the ionosphere giving the possibility to build radio telescopes on the surface of Earth. The advantage of ground observations is enormous. While generally maintaining the cost of production for such telescopes lower with respect to the space telescopes, it avoids the logistic problem of having to launch them into space: this gives the chance to fix any possible problem and to update them following the evolution of the technology of the radio receivers. Moreover, ground telescopes have fewer

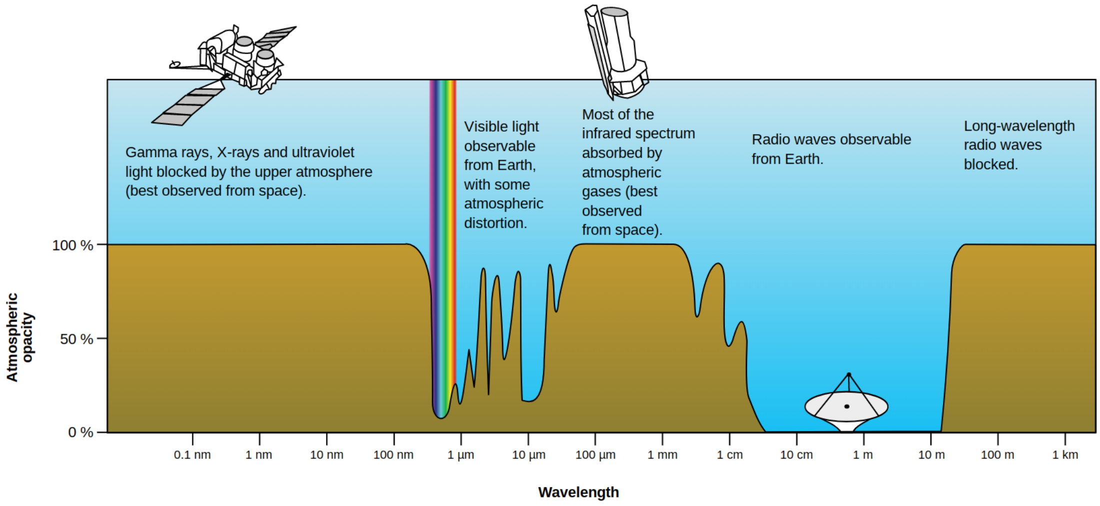

Figure 1.2: Atmospheric opacity as a function of the wavelength. Note the zero atmospheric opacity in a large part of the radio band. Public domain image.

constraints on the dimension of the collective area, i.e., the area which detects and records the incoming photons, allowing them to reach remarkable sizes. A compelling example is the 100-m diameter radio telescope Effelsberg located in Germany. However, I note that observations at a few mm are affected by some degree of atmospheric opacity due to water vapor. This is why the most recent radio observatories that are able to observe at mm wavelengths or lower, are positioned in very high altitude, dry sites like the Atacama Large Millimeter Array (ALMA) built in the Atacama Desert in Chile.

The radio window is sub-divided into several bands; the ones relevant to the work presented in this thesis are: L band (1 - 2 GHz), S band (2 -4 GHz), C band (4-8 GHz), X band (8 - 12 GHz), K_u band (12 - 18 GHz), K band (18 - 27 GHz), K_a band (27 - 40 GHz), V band (40 - 75 GHz), and W band (75 - 110 GHz).

1.2 Active Galactic Nuclei

[3] Active Galactic Nuclei (AGN) are among the most spectacular objects in our Universe and, since their discovery in the nearly half of the 20th Century (the first detections were in 1943, Seyfert 1943), they have been at the center of the debate of the astronomical community. The term “Active Galactic Nucleus” was first introduced by Viktor Ambartsumian in the 1950s, while the mechanism behind their energy production, i.e., the accretion of gas onto a supermassive object that resides at the center of the galaxy, was first proposed by Edwin Salpeter and Yakov Zeldovich (Lynden-Bell 1969; Salpeter 1964; Zel’dovich & Novikov 1964). They understood that, with their luminosities higher than 1000 times

---

[3] This chapter is mostly based on the review by Padovani et al. (2017).

the one of normal galaxies, the emission of the AGN had to come from non-stellar mechanisms. The active galaxies have luminosities up to $L \sim 10^{48}\,\mathrm{erg\,s^{-1}}$ (Padovani et al. 2017) with their emission being produced by both thermal and non-thermal processes. The dominant mechanism varies between the different AGN categories. AGN emit throughout the electromagnetic spectrum, from radio wavelengths up to γ-rays, and have been recently associated with neutrino events, making them suitable candidates for performing multimessenger studies. The first AGN-neutrino connection was established with the event on the 22nd of September 2017, when a high-energy neutrino was detected by the IceCube observatory and later associated with the blazar TXS 0506+056 (IceCube Collaboration et al. 2018). Since then, such correlation has been extensively explored, with the most recent results giving positive outcomes in associating neutrino production with the blazars (Plavin et al. 2020). For the description of blazars, see Sect. 1.2.2.

From statistical studies, AGN account for $\sim 10\%$ of the galaxy population, and it is currently believed that almost all galaxies go through an active phase, at some point during their evolution. The most spectacular consequence of such activity, present in only a minority of AGN, is the production of powerful collimated and magnetized plasma outflows that can reach highly relativistic velocities and that can propagate up to distances of hundreds of kpc (see Blandford et al. 2019, and references therein).

Due to their complex nature, AGN are excellent laboratories to study many different physical aspects, such as plasma physics. Moreover, thanks to their high luminosities, they can be detected at high redshifts providing crucial constraints on cosmological and galaxy evolution models.

In Sect. 1.2.1 I describe the different elements that compose an AGN and their interplay, in Sect. 1.2.2 I describe the unified scheme, a model which attempts to enclose different radio sources into one model, and in Sect. 1.2.3 I show the typical spectra of AGN.

1.2.1 The anatomy of AGN

The energy produced by the AGN arises from the gravitational energy released during the accretion process, i.e., material from the accretion disk falling into the central object. The energy output resulting from the accretion is expressed as

$$L_{\mathrm{bol}} = \eta_d \dot{M} c^2 \tag{1.1}$$

in which L_{bol} is the bolometric luminosity, i.e. luminosity across the entire electromagnetic spectrum, η_d is the efficiency of such process, $\dot{M}$ is the mass accretion

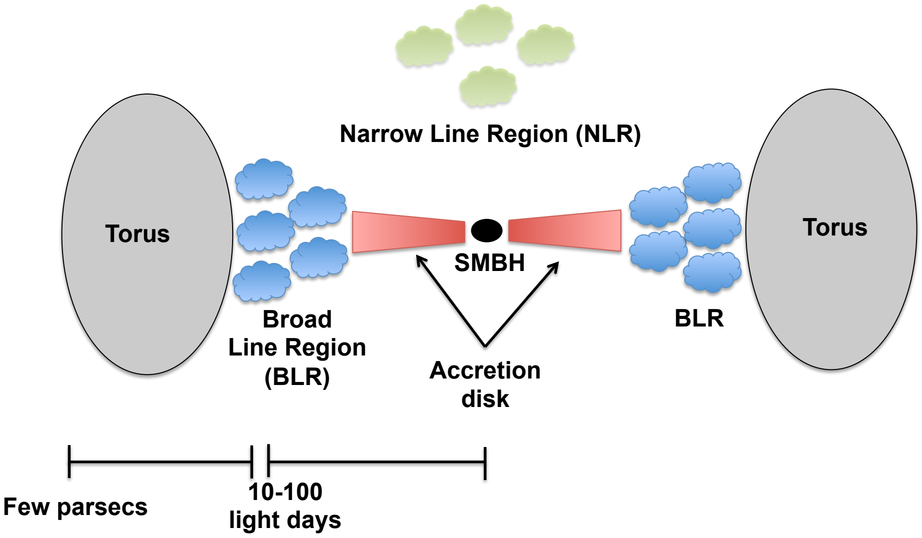

Figure 1.3: A simplified representation of an AGN with the five main elements highlighted. The different components in the image are not on scale. Credits: `https://www.isdc.unige.ch/~ricci/Website/Active_Galactic_Nuclei.html`.

rate, and c is the speed of light.

The mass accretion rate cannot be arbitrarily high. The upper limit, known as the **Eddington limit**, derives from the Eddington luminosity. The latter is achieved when, during the accretion process, there is a balance between the inward gravitational force and the outward force of radiation. By assuming a fully ionized accreting gas, the luminosity value can be extracted as:

$$L_{\mathrm{Edd}} = \frac{4\pi G M m_p c}{\sigma_{\mathrm{T}}} = 1.26 \times 10^{38} \left(\frac{M}{M_\odot}\right) \mathrm{erg\,s^{-1}} \tag{1.2}$$

in which G is the gravitation constant, M the mass of central object, m_p the proton mass, σ_{T} the cross section of the Thomson scattering, and $M_\odot = 1.98 \times 10^{33}$ g is the mass of the Sun. By combining Eqs. 1.1 and 1.2, the upper limit on the mass accretion rate reads as

$$\dot{M} = 2.52 \times 10^{-9} \eta_d^{-1} \left(\frac{M}{M_\odot}\right) \mathrm{M}_\odot \, yr^{-1} \, . \tag{1.3}$$

Therefore, in the first approximation, since $\dot{M} \propto M$ the energy produced by the AGN is proportional to the mass of the central massive object. For completeness, I highlight that recent studies are pointing out that Super-Eddington accretion

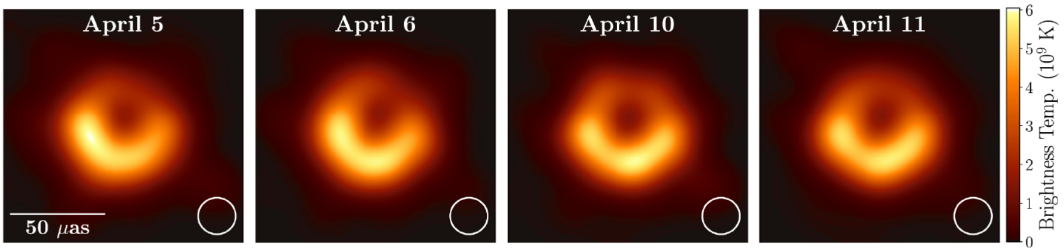

Figure 1.4: Average images of M87 for each of the four observing days (Event Horizon Telescope Collaboration et al. 2019a).

regimes may exist under specific conditions (e.g., Mayer 2019), meaning that the mentioned limit can be in theory exceeded for brief periods of time.

An AGN can be divided into five parts: the central object, likely associated to a supermassive black hole (SMBH), the accretion disk, the narrow line region, the broad line region, and the torus. While the first three are fundamental elements, the torus, and the broad line region are not present in every AGN (e.g., Chiaberge et al. 1999; Whysong & Antonucci 2004). A summarizing sketch is shown in Fig. 1.3.

- **Central supermassive black hole**

We know that a large mass resides at the center of active galaxies. Whether this mass is in the form of a supermassive black hole is still subject of discussion. However, the recent observations of the center of the radio galaxy M 87 (Fig 1.4, Event Horizon Telescope Collaboration et al. 2019a,b,c,d,e,f) and Sgr A* (Event Horizon Telescope Collaboration et al. 2022a,b,c,d,e,f) are strongly supporting this scenario.

Black holes are singularities of space-time in which the gravitational force is so strong that not even light is able to escape from it. In a non-spinning black hole, its size is linked to the event horizon, i.e., the sphere whose radius is determined by the furthest distance from the gravitational center from which the photons cannot escape the gravity of the singularity. The radius, called **Schwarzschild radius** in honor of Karl Schwarzschild, who, in 1916 resolved the Einstein equations for a sphere theorizing for the first time the black holes, is computed as

$$\mathrm{R_s} = \frac{2GM}{c^2}\,. \tag{1.4}$$

The black holes sizes vary from $\sim 30\,\mathrm{km}$ for the smallest stable ones (order of few solar masses), up to $\sim 10^{10}\,\mathrm{km}$ for the biggest ones.

Depending on their rotation and electric charge, there are different possible black hole configurations:

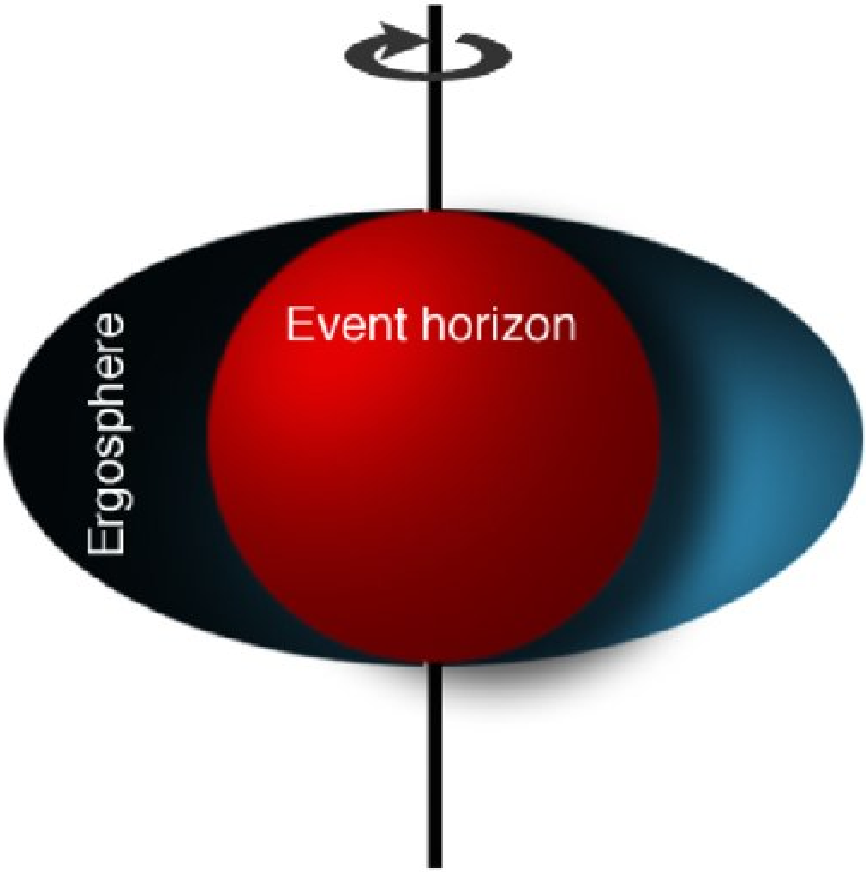

Figure 1.5: Event horizon and geometry of the ergosphere in a Kerr black hole. Credits: MesserWolandVectorization: Perhelion, CC BY-SA 3.0, via Wikimedia Commons.

- **Schwarzschild black hole**: non-rotating object with no electric charge;
- **Kerr black hole**: rotating object with no electric charge;
- **Reissner-Nordström black hole**: non-rotating object with electric charge;
- **Kerr-Newman black hole**: the most general solution, with both rotation and electric charge.

The total angular momentum J_a of the black hole can be parametrized via the dimensionless spin

$$s = \frac{cJ_a}{GM^2} \tag{1.5}$$

a parameter that varies from 0 to 1 for a non-spinning and maximally spinning black hole, respectively. When rotating, the spherical symmetry of the black hole is not maintained and an ergosphere is formed. The ergosphere arises because, in general relativity, the mass of a rotating object forces the surrounding space-time to move with it, creating a region in which it is impossible to maintain a stationary position. The size of the ergosphere is expected to be the same as the event horizon at the two poles, and bigger along the equatorial plane (see Fig. 1.5). The relevant consequence for AGN is the possibility for a particle within the ergosphere to extract rotational energy from it and escape with enhanced energy, slowing down the black hole rotation. When strong magnetic fields enter the equation, this may lead to the formation of relativistic jets via the Blandford-Znajek process (Blandford & Znajek 1977). The theory behind the formation of relativistic jets is discussed in Sect. 2.2.

The supermassive black holes at the center of active galaxies have masses spanning from $\sim 10^5\,M_\odot$ to $\sim 10^9\,M_\odot$, with the most massive ones showing extreme values of $\sim 10^{10}\,M_\odot$ (e.g., Wang et al. 2015; Wu et al. 2015). Historically, black holes were thought to be formed only by the collapse of stars. When a neutron star reaches the Tolman–Oppenheimer–Volkoff limit (e.g., Kalogera & Baym 1996), the radiation pressure generated by the degenerate neutrons is not able to bear the gravitational force anymore, and a black hole forms. The final black hole mass typically ranges from $\sim 5\,M_\odot$ up to tens of solar masses (among the most massive stellar black holes observed there is Cygnus X-1 with a mass of $21\,M_\odot$, Miller-Jones et al. 2021). A question arises naturally. With such low-mass seeds, how is it possible to form the mentioned supermassive black holes? While the answer is not yet clear, several hypotheses have been advanced.

The most accredited ones see the massive black holes being formed through two main channels: black hole merging and accretion. The former has been directly observed with the first detection of gravitational waves (Abbott et al. 2016). The merging process results in a final black hole whose mass is the sum of the two initial masses minus a small fraction, which is released as energy. In the accretion channel, the seed black holes grow their masses by accretion of the surrounding gas or stars they encounter. However, none of these channels are able to explain how the most massive, ancient black holes are formed. Examples are SDSS J0100+2802 with a mass of $M = 1.2 \times 10^{10}\,M_\odot$ (Wu et al. 2015) and J0306+1853 with $M = 1.1 \times 10^{10}\,M_\odot$ at redshift of $z = 6.326$ and $z = 5.363$, respectively (Wang et al. 2015; Wu et al. 2015). To explain their formation through stellar collapse or merging and following accretion, seeds with masses of $\sim 10^9\,M_\odot$ at $z = 20$ are needed (see, e.g., Sbarrato et al. 2021). This scenario is unrealistic. Indeed, not even accretion at the Eddington rate from Population III stars could lead to such massive objects. In the current cosmological models, their existence could only be explained by the hypothetical class of primordial black holes (Zel'dovich & Novikov 1967). Primordial black holes are expected to be formed immediately after the Big Bang when the Universe was experiencing extreme conditions and extremely dense conglomerates of particles led to the formation of needed seeds (Clesse & García-Bellido 2015; Liu & Bromm 2022;

Yuan et al. 2023). While this formation channel looks promising and would explain the formation of the SMBH, there are currently no observational proofs of the existence of primordial black holes.

Possible alternatives to black holes in the center of the galaxies consider the existence of exotic objects, such as gravastars or wormholes (Lobanov 2017). Such theories would require magnetic fields higher than $\sim 10^4\,\mathrm{G}$ threading the central region of AGN, magnetic strengths that black holes would not be able to sustain. Currently, the Mapping Magnetic Fields with INterferometry Down to Event hoRizon Scales (M2FINDERS) project [4] is working towards the crucial step of inferring the magnetization level in the central region of AGN.

- **Accretion disk**

Surrounding the central black hole lays the accretion disk. This structure assumes the characteristic disk configuration due to its rotation around the central object. It is composed of a highly ionized plasma (Fendt & Čemeljić 2002) in which the particles (mostly electrons and protons) are losing angular momentum and moving toward the central region. The accretion disks can, in a first approximation, be described following the thin disk model proposed by Shakura & Sunyaev (1973). The viscosity determines the disk shape since it plays the crucial role of dissipating the angular momentum of the particles, which otherwise would have been conserved, and the overall rotational energy of the disk.

The viscosity is enhanced by the presence of the magnetic field. The latter is deformed by the differential rotation of the disk, leading to the formation of magnetorotational instabilities, which give rise to turbulences, which in turn increase the magnetic field and generate viscosity (Balbus & Hawley 1991). The viscosity in magnetized disks has been further explored by Murphy et al. (2010), among others. Along with viscosity, the presence of the magnetic fields in disks may lead to two other phenomena: the formation of resistivity (Casse & Keppens 2002) and dynamo effects (Mattia & Fendt 2022), which would later contribute to the formation of jets (Blandford & Payne 1982; Blandford & Znajek 1977).

Overall, the structure of the accretion disks can be parametrized by the ratio δ between the disk and the Eddington luminosity.

- $\delta < 0.01$: the very low accretion rate implies that the density is too low for radiative cooling to be effective. Consequently, the disk becomes thicker and thicker due to the pressure of the ions, creating a so-called **ion torus**;
- $0.01 < \delta < 0.1$: this corresponds to the **thin disk** structure proposed by Shakura & Sunyaev (1973), with an efficient radiative cooling and bright disk;

---

[4] `https://www.mpifr-bonn.mpg.de/m2finders`

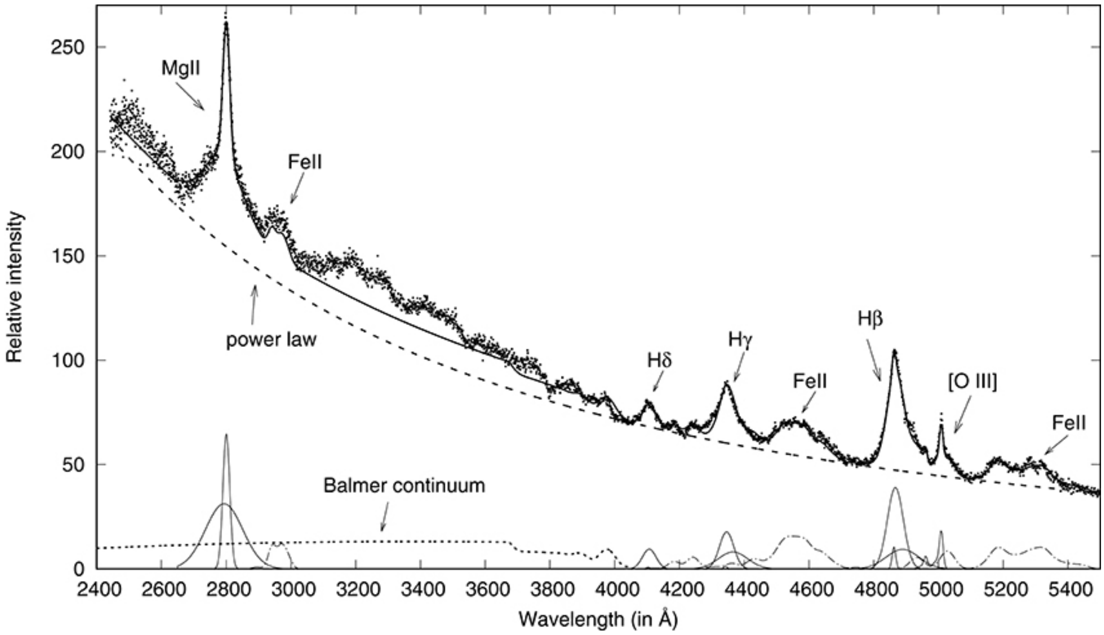

Figure 1.6: Example of an emission line pattern. The observations are for the object SDSS J014942.50+001501.7. Credits: Kovačević-Dojčinović et al. (2017).

- $\delta \to 1$: due to the high accretion rate, the disk is hot, and the radiative pressure dominates the system. The latter is able to win the gravitational force, expanding and leading to the formation of a thick disk.

The most accredited studies (e.g., Esin et al. 1997) are suggesting how the different disk configurations may exist at the same time: an inner hot and inefficient disk known as **Advection-Dominated Accretion Flow** (ADAF) with an outer cold and thin structure. Above the inner ADAF, there is a **hot corona** which is a continuation of the ADAF itself. The ADAF and the corona are associated with X-ray emission from the central region of AGN (Elvis et al. 1994; Keek & Ballantyne 2016; Nandra & Pounds 1994).

The accretion disk emits thermal radiation. Calculations of its temperature are possible, although it is not uniform throughout the disk. In the framework of thin, stationary disks in which the flux of inward matter is the same as the outward one, the temperature is computed as

$$T_{\mathrm{disk}} = \left(\frac{c^2 L_{\mathrm{Edd}}}{\eta_d 8\pi\sigma G^2 M^2} \right)^{1/4} \mathrm{K} \tag{1.6}$$

in which σ is the Stefan-Boltzmann constant. Typical temperatures of disks surrounding SMBH are $T_{\mathrm{disk}} \sim 10^4 - 10^6\,\mathrm{K}$.

- **The broad- and narrow-line regions**

Optical lines of elements like H, Ne, C, N, and O, among others, are detected when observing AGN. The lines arise from the recombination of particles in clouds which are constantly ionized by the intense radiation coming from the central engine. The main characteristic of both regions is the broadening of the lines, a consequence of the turbulent motion and rotation of the involved clouds. An example of the observed emission lines is shown in Fig. 1.6. Two classes of lines are distinguished in the observations: broad and narrow. Broad lines originate in the **broad-line region** (BLR), with the exceptional broadening implying velocities of the clouds up to several thousands of km s^{-1} (Peterson 2006). For the narrow lines, originating in the **narrow-line region** (NLR), velocities of hundreds of km s^{-1} are inferred from the line width.

The BLR, as seen from Fig. 1.3, is located in the immediate proximity of the accretion disk, and with an estimated average radius of $\sim 10^{14}\,\mathrm{m}$ it lays within the torus. Its typical density is $10^{10}\,\mathrm{cm}^{-3}$ and since the clouds are exposed to radiation coming from the accretion, high temperatures of the order of $T \sim 10^4\,\mathrm{K}$ are expected. The BLR is a structure typical of the high luminosity AGN, and in many of the low luminosity.

The NLR instead has characteristic densities of $10^4\,\mathrm{cm}^{-3}$ and lays well above the central region reaching distances up to kiloparsec scales if considering the extended NLR (see Groves 2007, and references therein). Due to such a large extension, the NLR is not affected by the obscuration due to the torus (when present). The [OIII]λ5007 is among the strongest lines observed.

- **Torus**

Surrounding the central region resides molecular clouds commonly referred to as the torus. Its existence was firstly deduced from the exceeding infrared photons produced by AGN. Indeed, the torus is associated with the region that absorbs the optical, ultraviolet, and X-ray radiation, produced by the accretion disk and/or by the hot corona, and re-emits it at infrared wavelengths. While the first models described this structure as an optically thick ring surrounding the central structure with radii in the order of parsecs, a torus indeed, recent studies are proving how this simplified assumption does not account for the latest observational results (see Hönig 2019, and references therein). Thanks to observations performed with the Very Large Telescope Interferometer (VLTI), high enough angular resolution has been achieved to resolve the torus in nearby AGN, suggesting a two-component structure: an equatorial, thin disk and a structure that extends in the polar direction (see Burtscher et al. 2013, and references therein). The latter likely is formed by a dusty wind that reconnects the torus with the edges of the NLR. As for the BLR, the torus is missing in many of the low luminosity AGN (e.g., Chiaberge et al. 1999).

1.2.2 The unified scheme for AGN

The existence of the complex structure described in the previous section can explain the properties observed in the different AGN. The AGN were historically divided into two main classes based on their radio luminosity (Kellermann et al. 1989): **radio-loud** and **radio-quiet**. The radio-loud accounts for the sources whose radio flux density is at least ten times higher than the optical counterpart and are generally able to produce powerful and collimated outflows (see Sect. 1.3 for an insight on the relativistic jets). Their emission is dominated by non-thermal processes, such as synchrotron emission and inverse Compton scattering (see Sect. 1.3.1), which happen within the relativistic jets. The radio-quiet objects, on the contrary, have their radio-to-optical flux density ratio spanning from 0.1 to 1, and typically do not produce jets or the outflows formed have: i) insufficient power to pierce through the launching region and propagate; ii) high powers but are unable to collimate. Their emission signature is dominated by the thermal processes which take place in the accretion disk region. Whether there are intrinsic differences in the central region of radio-loud and radio-quiet objects (see, e.g., Wilson & Colbert 1995), such as the different spin of the black holes (Narayan et al. 2021), is currently a matter of discussion.

The radio-loud/radio-quiet classification was used in the astronomical community for many years. However, this nomenclature is slowly being abandoned in favor of shifting towards the definition of **jetted** and **non-jetted** AGN. This was first proposed by Padovani (2016). The reason relies on the necessity to underline that the main difference between the two distinct classes of AGN is not their radio luminosity but the presence or lack of extended relativistic jets, which are now known to account for the main observational differences between them.

Due to the presence of the extended outflows, the jetted AGN have been considered for a long time to be part of a completely different source category. Nonetheless, at the end of the 20th Century (Antonucci 1993; Urry & Padovani 1995) proposed that the different AGN are none other than similar objects observed at different angles with respect to the line of sight. This led to the development of the **unified AGN scheme**, which is summarized in Fig. 1.7 and I describe in the following.

- **Seyfert galaxies**: the first AGN to be discovered, they have very luminous nuclei with typical values of $L \sim 10^{43} - 10^{45}\,\mathrm{erg\,s^{-1}}$ (see Ferrari 2011, and references therein). They are non-jetted, low-redshift AGN in which their host galaxies, almost exclusively spirals, are easily detected across different wavelengths. Occasionally, Seyferts show strong X-ray emission but their main characteristic is the presence of strong broad emission lines. Depend-

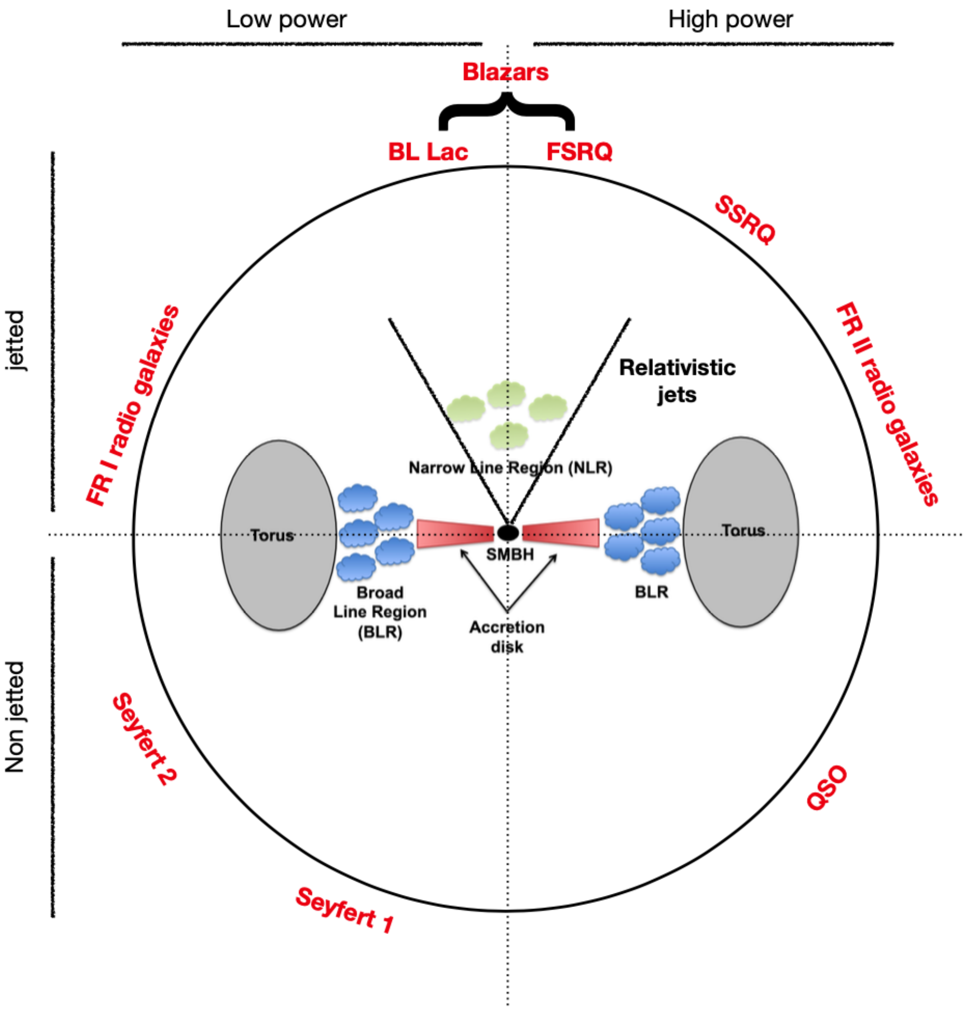

Figure 1.7: Cartoon representing the AGN unification scheme, based on the division between the jetted/non-jetted and low/high electromagnetic power dichotomies. The sphere represents the different viewing angles, with the north-south poles indicating a face-on source and the east-west poles an edge-on source. Re-adapted from: `https://www.isdc.unige.ch/~ricci/Website/Active_Galactic_Nuclei.html`.

ing on the broadening of the latter, the Seyfert galaxies are mainly divided into type 1 and type 2.

- **Type 1**: they show both narrow- and broad-emission lines. The broadening of the latter suggests them to be formed in clouds with velocities $\sim 10^3\,\mathrm{km\,s^{-1}}$, i.e., the broad-line region. Consequently, Seyferts 1 are AGN seen at viewing angles small enough to allow us to observe the broad-line region directly.
- **Type 2**: they only show narrow-emission lines with typical velocities of $\sim 10^2\,\mathrm{km\,s^{-1}}$, suggesting that the BLR is either hidden behind the optically thick torus or is not present. These galaxies, therefore, are

  generally observed from the side and only the NLR is visible.

  - **other types**: there are intermediate classes of Seyfert galaxies, in which along with the narrow-line emission some and typically weak broad-lines are observed. An example is Type 1.9 in which the only broad component observed is the Hα line. A further class of Seyfert objects is the **Low-Ionisation Narrow-Line Emission Radio galaxies** (LINER) in which the emission lines from strongly ionized atoms are weaker relative to the ones produced by weakly ionized or neutral atoms.

- **Radio galaxies**: they are jetted AGN seen at large angles with respect to the line of sight. In radio galaxies, the extended outflows are aligned close to the plane of the sky, making them excellent targets to explore the nature of the relativistic jets (see Sect. 1.3). Their host galaxies are elliptical. Depending on the physical properties considered, radio galaxies can be further divided into different sub-classes. On one hand, when taking into account their nuclear properties, they can be distinguished into:

  - **Low-Excitation Radio Galaxies** (LERGs): their optical and X-ray emission are mainly associated with the mechanisms happening in the jets and they do not show strong narrow or broad lines. Their characteristic accretion mechanism is expected to be hot and radiatively inefficient.
  - **High-Excitation Radio Galaxies** (HERGs): they can qualitatively be thought of as Seyfert 2 galaxies with jets, showing clear indications of strong narrow-line emission. Their accretion mechanism is expected to be cold and efficient.

  In detail, the two classes are distinguished considering the spectroscopic property of the [OIII] emission line which is produced in the NLR. In LERGs, the latter can be up to ~ 10 times fainter compared to the line intensity in HERGs having the same radio luminosity (Scipione et al. 2011). Such difference is usually attributed to the different nature of the accretion mechanisms.

  On the other hand, when considering the radio morphology of the emitted jets, the sub-classes are (Fanaroff & Riley 1974):

  - **Fanaroff-Riley I**: center-brightened, low-power radio galaxies with weak radio lobes. The vast majority of FR I radio galaxies are observed to be LERGs (Heckman & Best 2014).

  - **Fanaroff-Riley II**: edge-brightened, high-power radio galaxies with radio lobes showing strong hotspots, i.e., bright radio regions likely associated with sites of particle re-acceleration. FR II jets can be produced by both LERGs and HERGs (Heckman & Best 2014).

- **Quasars**: also defined as **Quasi-Stellar Objects** (QSO) are non-jetted sources detected at high redshift and their host galaxies are not visible. Their high distance, together with our possibility to detect them, implies high intrinsic luminosities, higher than their Seyfert counterpart. Quasars have optical and X-ray continuum emission and show both narrow and broad emission lines.

- **Blazars**: AGN seen face-on and dominated by the non-thermal emission from the jets. Due to their viewing angles close to zero, their appearance is dominated by relativistic effects. Characterized by the emission of the parsec scales jet, this class of AGN shows strong emission variability across the entire spectrum. Blazars dominate the radio sky at γ-ray energies and have been recently associated with neutrino production events (as mentioned earlier in Sect. 1.2). Depending on the equivalent width in their optical spectra, blazars are further divided into two sub-classes:
  - **BL Lacertae** (BL Lac): identified by their weak lines (which reflect weak nuclei), are among the less powerful blazars.
  - **Flat-Spectrum Radio Quasars** (FSRQs): the more powerful blazars, characterized by strong lines. Thanks to their high luminosity, the most powerful ones can be detected at high redshifts, i.e., $z > 6$ (Belladitta et al. 2020).

Radio galaxies and blazars are expected to be intrinsically the same objects, with the only difference being the viewing angle. Specifically, FR I radio galaxies are associated with the BL Lacs, while FR II radio galaxies are associated with the FSRQs. When the viewing angle is around 10°, i.e., in the transition range between FR II radio galaxies and FSRQs, lies the class of the **Steep-Spectrum Radio Quasars** (SSRQ): in which the detected extended jet structure leads to a steepening of the spectrum.

1.2.3 The spectra of AGN

Along with the characteristic emission lines aforementioned, the AGN span a vast range of wavelengths in the continuum from radio up to γ-rays. Their spectrum is modeled as a sum of the contribution of the different observed fundamental parts.

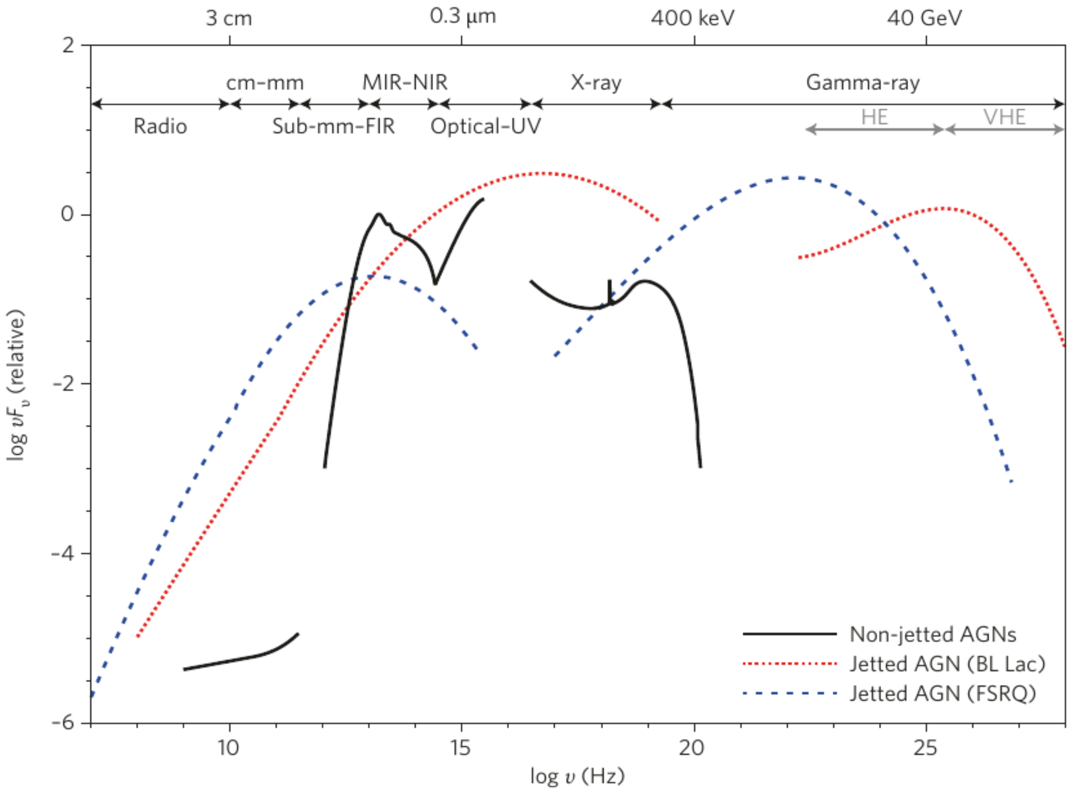

Figure 1.8: SED examples for the three main different types of AGN: non-jetted, low power jetted (BL Lac like), and high power jetted (FSRQ like) (Padovani et al. 2017).

Fig. 1.8 shows the Spectral Energy Distribution (SED) of the three main different classes of AGN: the non-jetted, the low-power jetted, and the high-power jetted.

In the radio window, the emission is dominated by the relativistic jet structure which emits non-thermally following the classic synchrotron spectrum (see Sect. 1.3.1). Naturally, in this band, the jetted AGN are much brighter than the non-jetted ones. In the nearby infrared window, the emission comes from a thermal source, specifically from the torus. When the AGN is seen from the side, the radiation that is supposed to arrive from the accretion disk region is absorbed by the optically thick torus, which later re-emits it in the infrared band. Instead, when the inclination of the AGN allows for a direct view of the accretion disk, optical emission is observed. In the optical wavelengths, relativistic jets are observed as well and the number of their detections increased in the last decade thanks to the observations carried out with the Hubble Space Telescope. In the optical-ultraviolet part of the spectrum, a rise in the SED may be observed, the so-called **Big Blue Bump**. The latter is produced by the optically thick, thermal radiation coming from the accretion disk, and, when observed, is a sign of efficient accretion. In the soft X-rays, and specifically in the range 0.3 - 6.0 keV, the photons are produced by the hot corona via Compton scattering of the optical/ultra-violet photons produced in the central accretion disk. Few astronomical objects are expected to be able to emit above these energies, towards the γ-rays regime. As shown in Fig. 1.8, such high energies are not detected from non-jetted AGN. Indeed, with their characteristic thermal emission, they may not be able to produce γ-rays. Other reasons for the non-detection may account for the sensitivity limit of our instruments or for the absorption of the photons along their path to us. The hard X-rays and γ-rays regime is populated by jetted AGN, specifically by blazars and a few nearby radio galaxies. How photons in AGN can reach such high energies is still a matter of discussion, and currently, two different families of models have been proposed: the leptonic (Maraschi et al. 1992) and hadronic (Böttcher et al. 2013) ones. In the former, the γ-rays are produced by the electrons flowing in the jet and interacting with either their own synchrotron emission, i.e., synchrotron self-Compton, or with an external photon field, i.e., external inverse Compton. In the latter, the protons are responsible for the observed γ-rays through synchrotron emission or photo-meson interaction.

1.3 Relativistic jets

The most powerful manifestation of AGN activity is the magnetized, relativistic outflows launched by the central region. In jetted AGN, the relativistic jets can reach distances up to hundreds and even thousands of kpc, largely exceeding the size of their host galaxies. In this thesis, the focus is on exploring the physical properties of such phenomena in a specific jetted AGN class: the radio galaxies. Among the most visually magnificent sources, there are Centaurus A and Cygnus A, shown in Fig. 1.9 upper and lower panel, respectively. Note the collimated jets that propagate on kiloparsec scales and that later expand, creating the radio lobes. Studying relativistic jets is of great importance in the current astronomical landscape. While being perfect laboratories to explore the physics of highly magnetized relativistic plasma, they play a relevant role in shaping the Universe as it is observable today.

The energy released by the outflows can deeply affect the host galaxy in a self-regulating process called **AGN feedback** (see Morganti 2017, and references therein). According to it, the AGN outflows can severely impact the star formation in galaxies, either by supporting it (positive AGN feedback) or by preventing it (negative AGN feedback). Two modes are currently explored to explain this phenomenon: the **quasar mode**, which belongs to the AGN with high nuclear luminosity, and the **jet mode**, which is connected with the low nuclear luminosity ones. In the quasar mode, the radiation released from the accretion disk, and by a small fraction also by the jets, expel the gas that could nourish star

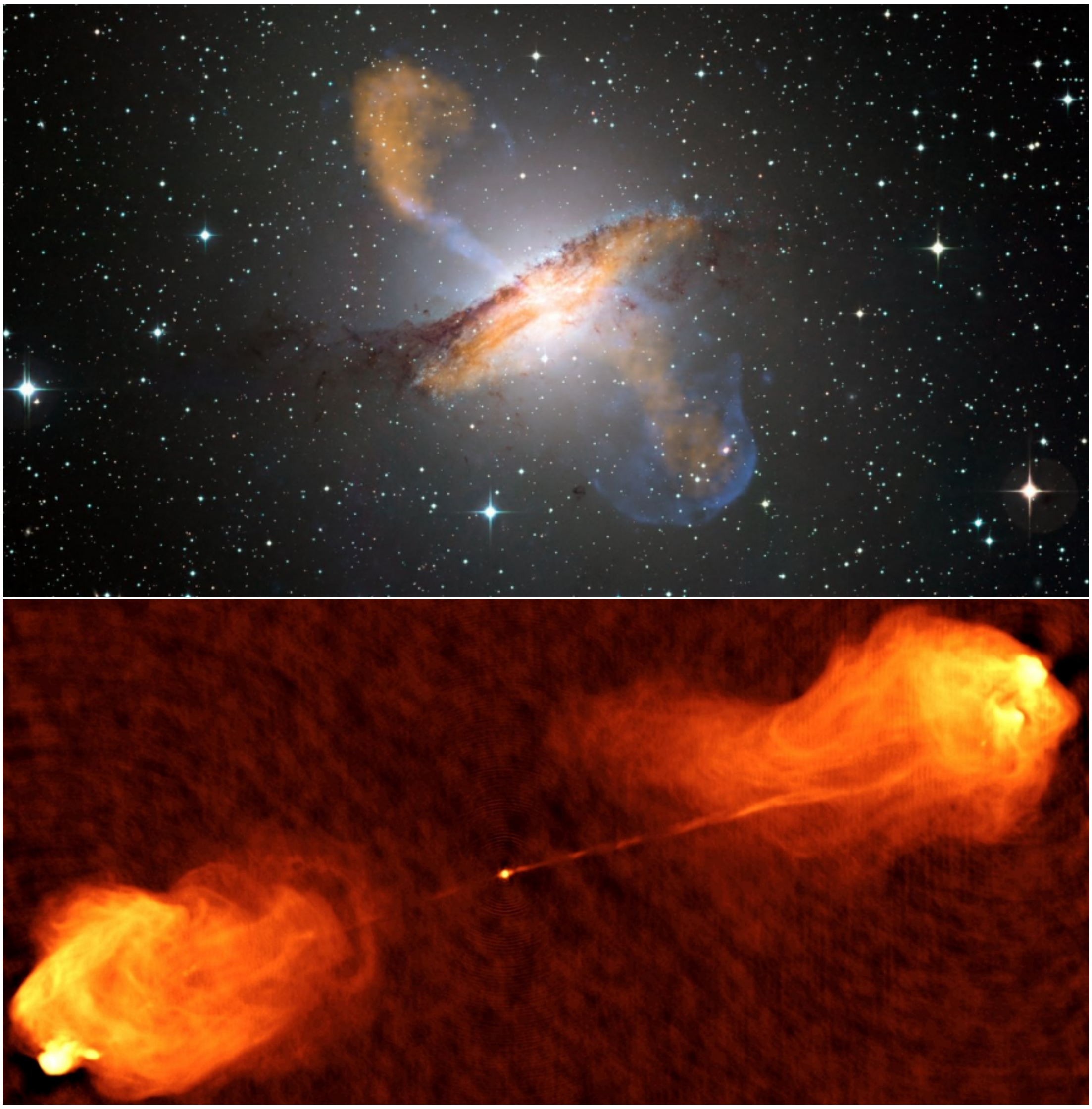

Figure 1.9: Upper panel: multi-wavelengths image of Centaurus A. Credits: `https://www.eso.org`. Lower panel: radio image of Cygnus A. Credits: NRAO/AU.

formations outside of the galaxy. In the jet mode, the ejected plasma prevents the cooling of the surrounding gas. In the majority of AGN, the two different mechanisms can operate at the same time, and distinguishing between them is rather difficult. One of the main consequences suggested by the AGN feedback, and especially the quasar mode, is its ability to regulate the co-evolution of the black hole with its host galaxy, explaining for instance the relation between the black hole mass and the velocity dispersion in the galaxy bulge (Merritt 1999).

1.3.1 The radiative mechanisms

The vast majority of the photons emitted from relativistic jets are produced in non-thermal processes. A process is defined as “non-thermal” when the emission does not depend on the temperature of the source. In this context, it is custom to define the **brightness temperature** of the emitting source. This temperature corresponds to the one that a putative black body, in thermal equilibrium with its surroundings, would need to reproduce the intensity of the detected signal. The brightness temperature is then not a physical temperature and can reach very high values (up to 10^{26} K in the case of pulsars). The formula for the brightness temperature derives from the Planck law for a black body and reads as

$$T_b^{-1} = \frac{k}{h\nu} \ln \left[1 + \frac{e^{\frac{h\nu}{KT}} - 1}{\epsilon_m} \right] , \tag{1.7}$$

where k is the Boltzmann constant, h is the Planck constant, ϵ_m is the emissivity, T is the temperature of the putative black hole, and ν is the frequency. The brightness temperature is largely used to characterize the radio emission from AGN and is an indicator of the physical conditions of the particles emitting the detected photons.

The two main radiative mechanisms from jets are the synchrotron and the inverse Compton radiations, and are described as follows.

- **Synchrotron radiation**

Synchrotron radiation occurs in the presence of relativistic charged particles surrounded by magnetic fields. Due to the Lorentz force, the particle undergoes an acceleration perpendicular to the direction of motion, consequently emitting electromagnetic radiation in the direction of the unperturbed propagation. The characteristic frequency of the synchrotron emission is

$$\nu_{\text{syn}} = \frac{\gamma^2 \text{B} e}{2\pi m c} \tag{1.8}$$

in which $\gamma = 1/\sqrt{1 - (v/c)^2}$ is the Lorentz factor of the particle, B the magnetic field strength, m the mass of the electron, and e its electric charge.

Since in jets the particles are moving at speeds close to the speed of light, special relativistic effects have to be taken into account. To understand the observational signature of such phenomenon, i.e., the signal received in the observer frame, it is necessary to apply the Lorentz transformations starting from the comoving frame, i.e., the reference system in which the particle is at rest. The crucial quantity is the aberration angle ψ, defined as the ratio of the parallel velocity component of the particle over the perpendicular one. After mathematical considerations, such an angle can be approximated as

$$\psi \sim \gamma^{-1} . \tag{1.9}$$

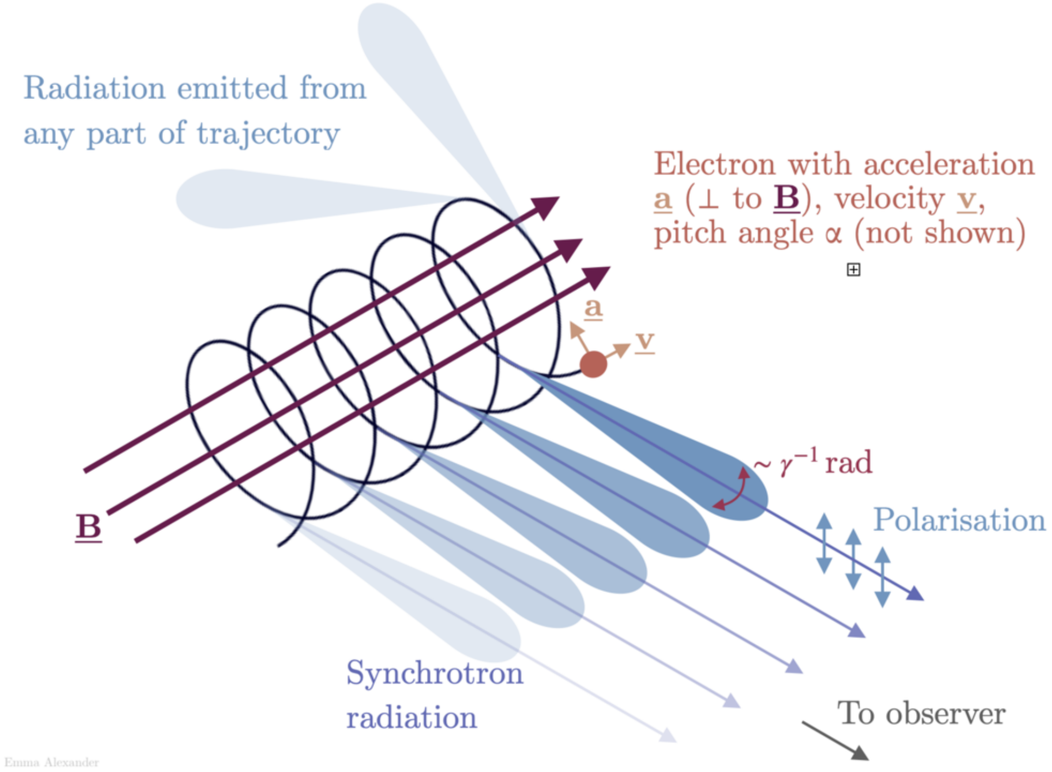

Figure 1.10: Sketch of the synchrotron radiation process. Credits: Emma Alexander (`https://emmaalexander.github.io/resources.html`), CC BY 4.0 via Wikimedia Commons.

This proportionality expresses the so-called **relativistic beaming** effect, shown in Fig. 1.10. Due to this effect, the faster the particle, the smaller the beaming cone, implying a more directional distribution of the signal and so an amplified signal for a face-on observer.

The emission power spectrum for a single particle follows the law (assuming isotropy in the emission):

$$S_{\mathrm{syn}} = \frac{4}{3}\sigma_{\mathrm{T}} c \beta^2 \gamma^2 U_{\mathrm{B}} \tag{1.10}$$

in which σ_{T} is the Thompson cross-section, $\beta = v/c$, and U_{B} is the magnetic density. Its shape is shown in Fig. 1.11 in the top right frame. The emission from a population of particles can be computed as a sum of such spectra, assuming a certain energy distribution of the particles. These are assumed to follow a power-law distribution:

$$n(\gamma)d\gamma = n_0 \gamma^{-p_{\mathrm{inj}}} d\gamma \tag{1.11}$$

with n_0 the number of particles and p_{inj} their injection index.

Convolving the power spectrum for single particles (Eq. 1.10) with their dis-

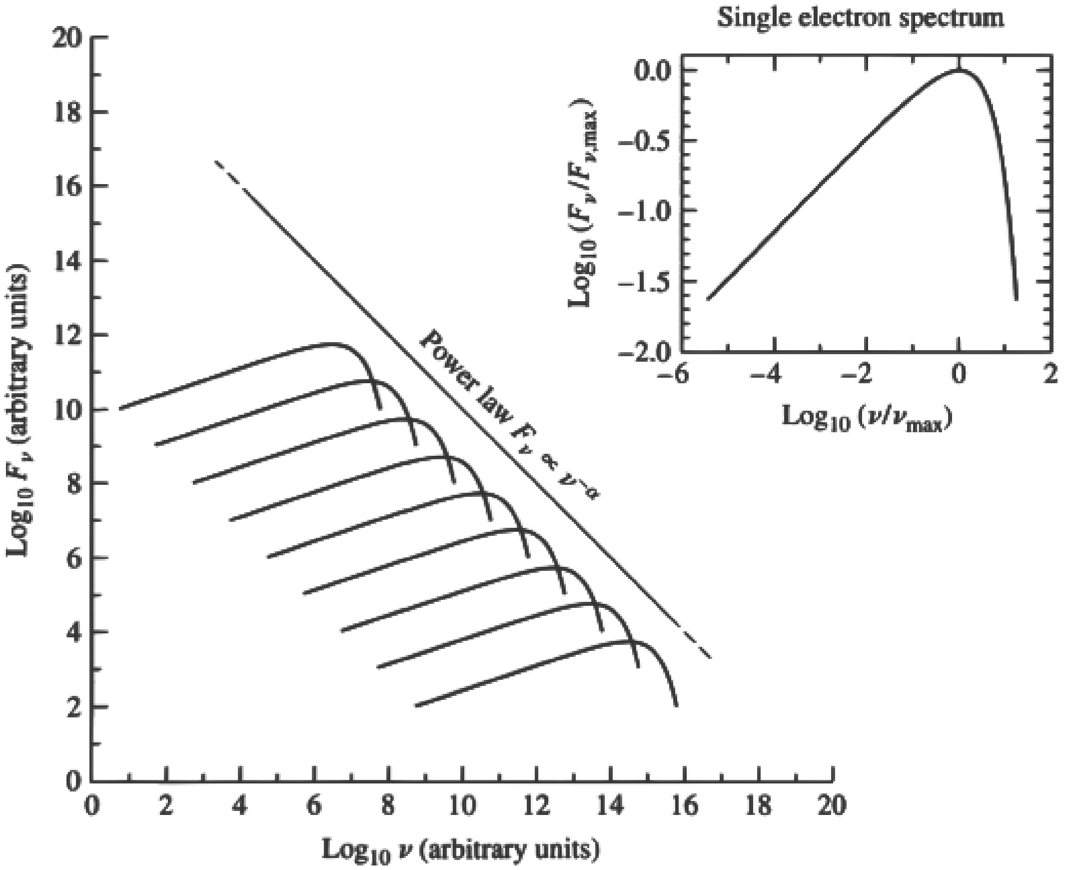

Figure 1.11: Single electron spectrum from synchrotron radiation in the top right frame, together with the total spectrum given by the sum of the individual spectra (Carroll & Ostlie 2017).

tribution (Eq. 1.11) leads to a power-law function of the form (see Fig. 1.11)

$$S(\nu) = \frac{2}{3} c \sigma_{\mathrm{T}} n_0 \frac{U_{\mathrm{B}}}{\nu_{\mathrm{L}}} \left(\frac{\nu}{\nu_{\mathrm{L}}} \right)^{-\frac{p_{\mathrm{inj}}-1}{2}} \tag{1.12}$$

with ν_{L} being the Larmor frequency, i.e., the precession of the magnetic moment of a proton around an external magnetic field. The power-law exponent, referred as **spectral index**, is typically written as $\alpha = -(p_{\mathrm{inj}} - 1)/2$. Eq. 1.12 is obtained assuming an isotropic distribution of the pitch angles, i.e., the angle between the direction of motion of the particle and of the magnetic field.

The resultant synchrotron emission can be either **optically thin** or **optically thick**. In the former, the photons emitted from the synchrotron process are able to travel freely through the surrounding medium and, when detected, show a power law distribution with index α. In the second case, when the produced photons do not have enough high energies, they can be re-absorbed, scattering over the electrons present in the medium. This phenomenon is called "synchrotron self-absorption" and leads to the formation of optically thick regions.

The overall theoretical synchrotron spectrum is shown in Fig. 1.12. In the optically thick region, for a plasma with a homogeneous synchrotron spectrum, it follows the power law $S(\nu) \propto \nu^{5/2}$ (see, e.g., Lobanov 1998), while in the optically thin regime the spectrum assumes the mentioned form $S(\nu) \propto \nu^{\alpha}$. The frequency at which the synchrotron emission switches from one regime to the other is called **turnover frequency** (ν_{br}, see Fig. 1.12) and strongly depends on the density and magnetic field of the particle population. As a consequence, when inferred, the turnover frequency can provide important information on the magnetization of the jets (see Sect. 1.3.2 for the theory behind it and Chapter 6 for its application).

In the AGN environment, the most plausible scenario for the particles to gain velocity is through the so-called **Fermi acceleration** mechanisms. Referred also as diffusive shock acceleration, in such mechanisms a particle accelerates when repeatedly reflected in shocks, gaining velocity after every reflection. There are two Fermi acceleration mechanisms, first and second order, with the first one being the important one in the case of AGN. In the **first order Fermi acceleration** model, the particles are accelerated by continuously moving upstream and downstream shock waves, gaining energy after every crossing. This process greatly enhances the velocity of the particles, with the spectrum following $S(\epsilon_p) \propto \epsilon_p^{-p_{\mathrm{inj}}}$ (ϵ_p is the energy of the particles). The typical power-law index for the Fermi mechanism is $p_{\mathrm{inj}} \geq 2$. Consequently, following Eq. 1.12, the characteristic observational signatures of the synchrotron emission is a power-law spectrum with a spectral index $\alpha \leq -0.5$.

A further observational signature of synchrotron emission is **polarization**. Polarization is a characteristic of transverse waves, such as light, which describes the geometrical orientation of the electric field component. It can be linear, circular, or elliptical. When linear, the electric field oscillates in a plane along the direction of propagation. When circular, the electric field has two linear components with the same amplitude that oscillate in two planes perpendicular to each other. In case the amplitudes in the two planes differ, the polarization is said to the elliptical. The photons emitted through synchrotron radiation in jets are expected to be intrinsically highly polarized, showing high degrees of linear polarization. Whether such emission can show circular polarization, while expected, is currently a matter of investigation (Kramer et al., in prep.).

- **Inverse Compton**

The inverse Compton radiation is produced when a low-energy photon scatters against a high-energy relativistic electron, gaining energy. The mathematical approach to describe this phenomenon is similar to the one used for synchrotron

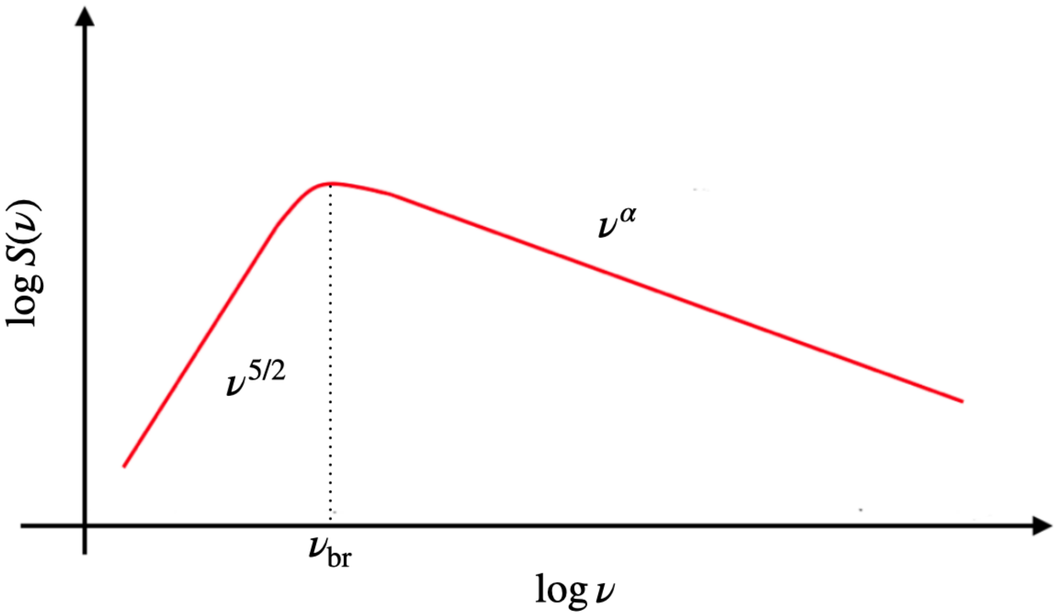

Figure 1.12: Synchrotron spectrum. In the optically thick regime, the self-absorbed one, the power law index is typically ~ 2.5, while in the optically thin it evolves as ν^{α}, where α is observed in the majority of jets to lay around ~ -0.7.

radiation, leading to a single electron spectrum of the form

$$S_{\rm IC} = \frac{4}{3}\sigma_{\rm T} c \beta^2 \gamma^2 U_{\rm rad} \,. \tag{1.13}$$

The equation is equivalent to the synchrotron case, with the only difference represented by the last term $U_{\rm rad}$, which, in this case, describes the energy density of the photon field. The power law index of the inverse Compton spectrum for an electron population follows the same dependence as the synchrotron one, i.e., $\alpha = -(p_{\rm inj} - 1)/2$ with $p_{\rm inj}$ being the power law index of the electron distribution. The inverse Compton process is relevant in the high-energy part of the spectrum (see Sect. 1.2.3) and accounts for the production of hard X-ray and γ-ray radiation.

When the photon energy density in a certain region of the jet is higher than the magnetic field density, the Compton losses become far more important than the synchrotron losses. This phenomenon is called **Compton catastrophe** and is expected to occur when the brightness temperature associated with the synchrotron emitting region is $\sim 10^{12}$ K. The rapid inverse Compton cooling leads to a dramatic decrease in the temperature below the mentioned limit (Kellermann & Pauliny-Toth 1969). Nonetheless, sources with jet components $T_b > 10^{12}$ K have been observed, questioning how such phenomenon occurs in relativistic jets (see, e.g., Tsang & Kirk 2007, and references therein).

1.3.2 The sub-parsec and parsec jets

In this section, I highlight the sub-parsec and parsec scales observational properties of relativistic jets which are central to this thesis.

- **The VLBI core and core-shift effect**

Starting from the very base, jets show a bright, optically thick feature: the **VLBI core** (Blandford & Königl 1979). The size of such region at each given frequency, i.e., the surface with optical depth $\tau_\nu = 1$, depends on the numerical density and magnetic field of the underline electron population. Moreover, as mentioned in the previous section, since the less energetic photons are the more likely to be re-absorbed, the position of the surface $\tau_\nu = 1$ varies as a function of the frequency: the smaller the observing frequency, the furthest the position of the surface, the larger the size of the core. This situation is visualized in Fig. 1.13, in which the displacement of the transition surface while changing frequency is shown. Therefore, the VLBI core can be seen as a layered sphere in which each consecutive layer is characterized by a certain turnover frequency. When the latter, together with the respective flux density ($S_{\rm br}$), is known, the underlying magnetic field can be estimated as (Pacholczyk 1970)

$$B \propto S_{\rm br}^{-2} \nu_{\rm br}^{5} \, . \tag{1.14}$$

For an application of this procedure, see Chapter 6.

The described relation between the frequency and the core position is known as the **core-shift effect**, and needs to be considered when analyzing multi-frequency VLBI data sets. Indeed, in order to be compared, maps at different frequencies have to be aligned with respect to a common reference point. This is ideally the hypothetical position of the jet origin, i.e., the central black hole. Several methods have been developed for the alignment of images (e.g., O'Sullivan & Gabuzda 2009), among them: i) 2-D cross-correlation of optically thin regions in the jet; ii) cross-identification of optically thin **Gaussian component** (see Sect. 3.3.3) along the jet. Throughout the thesis, I followed the first approach.

Because of the face-on orientation of blazars, their emission is dominated by the superposition of multiple synchrotron self-absorbed features. As a consequence, the total spectrum of blazars is flatter with respect to the higher-viewing-angle AGN counterpart, i.e., the steep spectrum radio quasars, and the radio galaxies.

- **The projection effects and the superluminal motion**

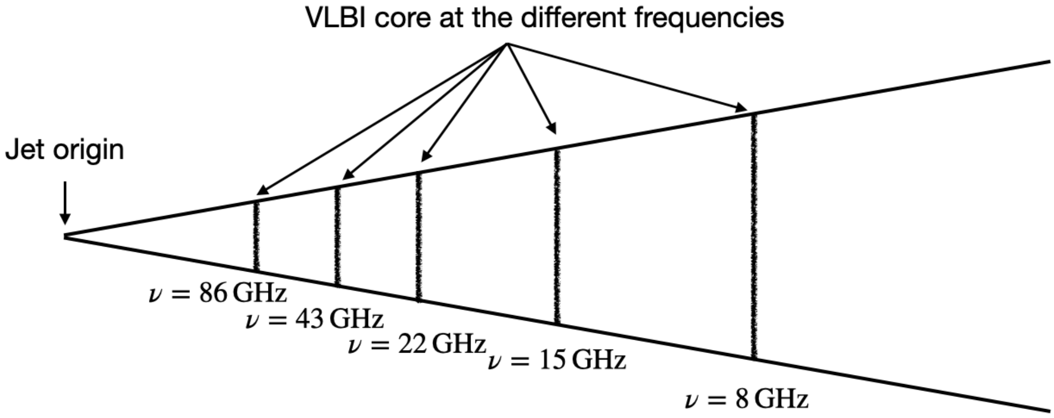

Figure 1.13: Representation of the core-shift effect. The lower the frequency, the further from the jet origin the transition surface ($\tau_\nu = 1$) between optically thick and optically thin emission. Template of the design from Kovalev et al. (2008).

Projection effects strongly influence the appearance of the majority of jets we observe. They arise from seeing a 3-dimensional object in a 2-dimensional plane. As shown in Fig. 1.14 left panel, the real extent of the jet is the segment AC while the observed one is CB. To infer the real distance, it is necessary to build the right triangle ABC and to use trigonometry to relate AC and BC. To do that, the knowledge of the viewing angle θ is needed to determine AC from BC as

$$\mathrm{AC} = \frac{\mathrm{BC}}{\sin(\theta)} \,. \tag{1.15}$$

Because of their larger viewing angles, implying $\sin(\theta) \to 1$, the difference between the apparent distance (CB) and the de-projected one (AC) is relatively small when observing radio galaxies. As a consequence, through VLBI observations, in radio galaxies we have generally the possibility to resolve the jet on smaller scales with respect to the small-viewing-angle counterparts.

Since the jets are propagating at velocities close to the speed of light, one of the main consequences of the different viewing angles is the boosting and de-boosting of the incoming radiation due to the relativistic Doppler effect, i.e., the change in the luminosity of the detected photons due to relative motion between the emitting source and the observer. The Doppler factor is defined as

$$\delta \;=\; [\Gamma(1-\beta\cos(\theta))]^{-1} \tag{1.16}$$

in which Γ is the Lorentz factor of the bulk emission. The emitted (S_e) and received (S_r) flux densities are related as

$$S_\mathrm{r} = S_\mathrm{e}\delta^{(3-\alpha)} \tag{1.17}$$

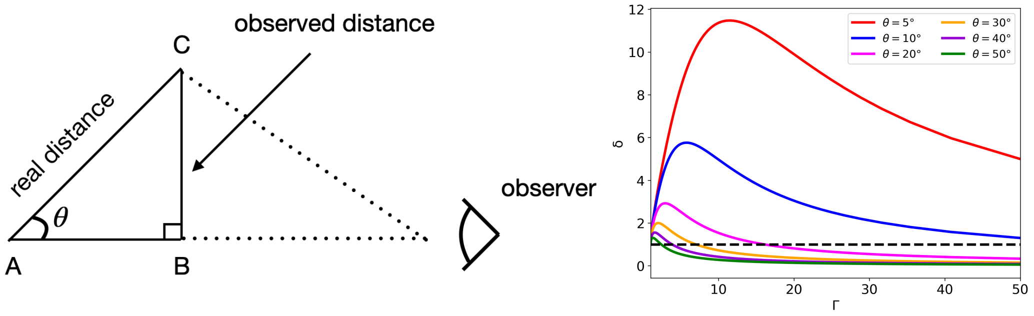

Figure 1.14: Left panel: explanatory sketch for the projection effect. Right panel: Doppler factor as a function of Lorentz factor for different viewing angles.

where α is the spectral index as defined in Sect. 1.3.1. The relation between Doppler factor and Γ for different viewing angles is shown in Fig. 1.14, right panel. Specifically, the larger the viewing angle, the lower the velocity threshold for the emitted radiation to be de-boosted.

The relativistic Doppler effect leads to numerous and important consequences: among the others, a crucial one for this thesis is the asymmetry between the jet and the counter-jet. Relativistic jets from AGN are launched as a pair of outflows in perpendicular and opposite directions with similar intrinsic properties. However, due to selection effects, most of the sources we observe show one-sided jets as a consequence of their orientation approaching our line of sight. The counter-jet is detected in a minority of cases, mostly in nearby radio galaxies (such as NGC 315). When this is the case, its detection can be used to constrain fundamental jet properties, such as the intrinsic speed, which can be estimated based on the jet to counter-jet intensity ratio (R) (Urry & Padovani 1995) as

$$\beta = \frac{1}{\cos(\theta)} \frac{R^{1/p} - 1}{R^{1/p} + 1} \tag{1.18}$$

in which $p = (2 - \alpha)$. The calculation of the jet bulk speed with Eq. 1.18 relies on the hypothesis of symmetry between the two jets, with their differences in brightness arising only from the Doppler effect. It should be noted that, for certain orientations, asymmetries between the approaching and receding sides could arise in radio galaxies also as a consequence of the opacity introduced by a circumnuclear torus, Therefore, the use of Eq. 1.18 for the speed estimate should only be made in cases where obscuration from the torus is negligible. The jet to counter-jet method is applied in Chapter 4.

Along their lengths, jets are usually showing faster than light motion, i.e., **superluminal motion**. This effect was predicted by Rees (1966) and has been observed for the first time in the blazar 3C 273 (Gubbay et al. 1969). The apparent discrepancy with the fundamental axiom of general relativity can be explained by accounting for projection effects. Let us assume a jet that moves at a certain velocity from point A to point B and assume that both regions emit a photon at two different times. From geometrical considerations involving the different path lengths traveled by the two photons and the viewing angle (θ), the intrinsic jet speed β is extracted from the apparent, measured speed β_{app} as

$$\beta = \frac{\beta_{\mathrm{app}}}{\sin\theta + \beta_{\mathrm{app}}\cos\theta} \, . \tag{1.19}$$

Therefore, the smaller the viewing angle, the more impacting this effect on the observed jets. In blazars, superluminal motions up to $\sim 50\,c$ have been observed (Lister et al. 2009).

- **The recollimation shocks**

A further observational signature of jets on sub-parsec, parsec scales are the **recollimation shocks**: high luminosity regions associated with strong magnetic fields and particle re-acceleration. Their formation is a direct consequence of the evolution and propagation of (magneto-)hydrodynamical waves within the jet, which are enhanced at the interface that separates the jet from the external medium (see, e.g., Martí et al. 2018; Mizuno et al. 2015). Recollimation shocks can be both stationary or moving downstream of the jet dragged by the underlying motion of the bulk flow (Lister et al. 2016).

- **The stratified structure**

The jets are not expected to be uniform beams, but both observational and theoretical results are strongly suggesting a transversely **stratified structure**, with a central spine surrounded by an outer layer (see, e.g., Boccardi et al. 2017, and references therein). An overview of the theories behind its formation is given in Sect. 2.2.

When enough angular resolution is achieved (see Chapter 3), it is possible to resolve such a structure. The latter is typically associated with the **limb-brightening**: the jet spine is far less luminous than the surrounding layers. While the origin of limb-brightening has not been settled yet, some hypotheses have been proposed. The most accredited one involves the interplay between the stratified jet structure and the Doppler effect: the spine, expected to be faster, undergoes a Doppler de-boosting (see Fig. 1.14), resulting in a lower flux density with respect to the slower external layers. Alternatively, the emissivity of the spine is intrinsically lower with respect to the sheath. This scenario could explain limb-brightening in blazars. Other models involve different launching mechanisms or morphology of the magnetic fields threading the jets as a trigger of the limb-brightening (see, e.g., Kramer & MacDonald 2021). An astonishing example of limb-brightening is recent observations of the jet in Centaurus A from 1 mm observations (Janssen et al. 2021).

2 The theory of jet formation and propagation

In this section, I describe the currently known theories for jet formation and propagation (Sect. 2.2) with emphasis on the open questions that are addressed in this thesis. The framework behind such theories is the physics of the plasma, for which I give an introduction in Sect. 2.1 [5].

2.1 Elements of plasma physics

Plasma is a state of matter characterized by the presence of a relevant fraction of unbound, i.e., free to move, electrons and ions. This condition happens due to the temperature of the system being high enough to overcome the attraction exerted by the strong nuclear force. The study of plasma physics faced a rapid increase in interest and development during the ’70s and ’80s of the past Century, starting from the experiments of Hannes Alfvén on the ionosphere. Nowadays, this research field plays a prominent role in the current scientific landscape due to its application both at the industry level and for astrophysical studies. Indeed, while on Earth this state of matter is quite rare, throughout the Universe it is found in more than 99% of the known matter.

To determine the **ionization level** of a certain system, i.e., the fraction of free charged particles, the **Saha equation** is used. The latter is extrapolated by assuming an ensemble of particles with certain energy E_m and temperature T, and whose numerical density is expressed as

$$n_m = g_m \mathrm{e}^{-E_m/(kT)} \,. \tag{2.1}$$

Here, g_m is the number of possible states at the energy E_m. The Saha equation reads as

$$\frac{1-\chi}{\chi} = 4.14 \times 10^{-16} n_{\mathrm{tot}} T^{-3/2} \mathrm{e}^{1.58\times10^3/T} \,, \tag{2.2}$$

where χ is the ionization level and n_{tot} the total number of particles in the system. The equation implies that the higher temperatures of the system, the higher the ionization level.

Along with it, a certain system to be defined as plasma needs to fulfill the condition of **quasineutrality**, i.e., the positive-negative charges have to balance, leading to a neutral gas. Such a condition can be achieved since in the surroundings of a positive charge there is a lack of ions due to the repulsive force. On the contrary, due to the attractive force, there is an overpopulation of negative charges. Consequently, the potential of each positive charge quickly falls to zero,

---

[5] This Section is based on the book Chiuderi & Velli (2012) and the PLUTO User’s guide `http://plutocode.ph.unito.it/userguide.pdf`.

shielding them on long distances. The extension of this region is called **Debye length**.

To build a formalism for plasma physics, the starting point is the famous Maxwell equations, which describe the behavior of the magnetic and electric fields. The Maxwell equations are:

$$\nabla \times \mathbf{E} = -\frac{1}{c}\frac{\partial \mathbf{B}}{\partial t}\,; \tag{2.3}$$

$$\nabla \times \mathbf{B} = \frac{1}{c}\frac{\partial \mathbf{E}}{\partial t} + \frac{4\pi}{c}\mathbf{J}\,; \tag{2.4}$$

$$\nabla \cdot \mathbf{E} = 4\pi q\,; \tag{2.5}$$

$$\nabla \cdot \mathbf{B} = 0\,. \tag{2.6}$$

Here, **E** is the electric field, **B** is the magnetic field, q is the density of electric charges, **J** is the current density, and t is the time. In plasma theory, it is common to work in 6-dimensional space, i.e. **the phase space**, defined by the three spatial coordinates $(\mathrm{x}_x, \mathrm{x}_y, \mathrm{x}_z)$ and the three velocity coordinates $(\mathrm{v}_x, \mathrm{v}_y, \mathrm{v}_z)$.

The description of the velocity and the position in the ordinary space of every single particle is impossible, and anyway not meaningful. Therefore, the plasma theory is built around the **distribution function** $f(\mathbf{x}, \mathbf{v}, t)\,\mathrm{dx}\,\mathrm{dv}$, which represents the number of particles with a certain position and velocity at a fixed moment in time. In this formalism, the average number of particles within a certain space $\mathrm{x} + \mathrm{dx}$ and velocity $\mathrm{v} + \mathrm{dv}$ is given by

$$\mathrm{d}N = f(\mathbf{x}, \mathbf{v}, t)\,\mathrm{dx}\,\mathrm{dv}\,, \tag{2.7}$$

and, to describe the temporal evolution of a certain quantity ε, the **continuity equations** is used

$$\frac{\partial \varepsilon}{\partial t} + \nabla \cdot (\varepsilon \mathbf{v}) = 0\,. \tag{2.8}$$

Solving the distribution function and its temporal evolution is extremely challenging. A complete knowledge of $f(\mathbf{x}, \mathbf{v}, t)$ would imply knowing the exact number of particles having a certain position and velocity at every instant. A set of information that is too broad to be handled with ease. While this can be doable under specific and simplified conditions, such a high level of detail is not needed when describing the astrophysical plasma subject of this thesis. Indeed, knowing the average physical quantities of interest is sufficient.

To do that, step one is to define the average number of particles having any velocity within the space $\mathrm{x} + \mathrm{dx}$. This operation is done by integrating the distribution function over the three velocity components

$$n(\mathbf{x},t) = \int f(\mathbf{x},\mathbf{v},t) d\mathbf{v}\,. \tag{2.9}$$

The obtained function is used as a normalization factor in the averaging process. Consequently, the average generic quantity of the particles in a certain system is defined as

$$\varepsilon(\mathbf{x},t) = \frac{1}{n(\mathbf{x},t)} \int \varepsilon f(\mathbf{x},\mathbf{v},t)\, \mathbf{dv}\,. \tag{2.10}$$

The equations mentioned here are the foundations upon which the different plasma theories are built. There are different approaches to describe these systems, which depend on the initial conditions assumed:

- **Neutral gas**: all particles are considered to have the same mass and the net charge is zero. The system is described with one distribution function.
- **Two fluids plasma**: when the ionization level is $\chi = 1$ there are two particle distributions, one for the ions and one for the electrons.
- **One fluid plasma**: the system is described as a single fake fluid that summarizes the properties of the two particle populations.

Nonetheless, the ensemble of equations used to describe these theories is still too broad to be solved easily. To overcome this tangled forest, the concept of **regime** is introduced: not the entire spectrum of solutions is of interest, but only the specific range that is helpful to describe the desired scenario. The fundamental regime used to describe the relativistic jets physics is the **(relativistic) magnetohydrodynamic** one (R)MHD, described in the next section.

2.1.1 The magnetohydrodynamic regime

The MHD regime is defined so that the ratio of the length scale over the temporal scale of variations of the physical parameters is similar to the typical velocity of electromagnetic phenomena. In this theory, crucial is the concept of **characteristic velocity of the plasma**, which describes the propagation velocity of the waves evolving within the system. The relevant waves for this thesis are discussed in Sect. 2.1.3.

The MHD regime is further divided into two sub-classes, depending on whether the relativistic effects have to be taken into account: the non-relativistic and the relativistic one.

- **Non-relativistic MHD**

In non-relativistic MHD, the characteristic velocity of plasma and of the electromagnetic phenomena is way smaller than the speed of light, so the relativistic effects can be totally neglected. The MHD equations are usually described with the following system of conservation laws:

$$\frac{\partial \rho}{\partial t} + \nabla \cdot (\rho \mathbf{v}) = 0\,; \tag{2.11}$$

$$\frac{\partial \mathbf{m}}{\partial t} + \nabla \cdot \left[\mathbf{m}\mathbf{v} - \mathbf{B}\mathbf{B} + \mathrm{I}\left(p + \frac{\mathbf{B}^2}{2} \right) \right]^T = -\rho \nabla \Phi + \rho \mathbf{g}\,; \tag{2.12}$$

$$\frac{\partial \mathbf{B}}{\partial t} + \nabla \times (c\mathbf{E}) = 0\,, \tag{2.13}$$

$$\frac{\partial \left(E_t + \rho \Phi \right)}{\partial t} + \nabla \cdot \left[\left(\frac{\rho \mathbf{v}^2}{2} + \rho e + p + \rho \Phi \right) \mathbf{v} + c\mathbf{E} \times \mathbf{B} \right] = \mathbf{m} \cdot \mathbf{g}\,. \tag{2.14}$$

Here: I is the unity matrix, ρ is the mass density, $\mathbf{m} = \rho \mathbf{v}$ is the momentum density, p is the thermal pressure, e is the internal energy, and E_t is the total energy density. The exponent T indicates the transpose of the matrix defined by the elements in the squared brackets. The right terms include the contribution of gravity, namely from the gravitational potential Φ and the acceleration vector $\mathbf{g}$.

The electric field in Eq. 2.13 can be expressed as:

$$c\mathbf{E} = -\mathbf{v} \times \mathbf{B} + \frac{\eta}{c} \cdot \mathbf{J_r} \tag{2.15}$$

in which $\mathbf{J_r} = c\nabla \times \mathbf{B}$ and η is the resistivity tensor. The first term of Eq. 2.15 is the convective term, while the second one is the resistive term. According to the interplay between them, the MHD theory is further divided into two sub-regimes: the **ideal MHD regime** and the **resistive MHD regime**. The former one is valid when the convective term dominates the system, while the second one is in the opposite case. The separation between the two is dictated by the **Reynolds magnetic number**, i.e., the ratio between the diffusive term over the resistive one.

Ideal MHD: in this regime, the Reynolds number is way higher than one, and the resistivity in the plasma can be neglected. Here, Eq. 2.15 becomes

$$c\mathbf{E} = -\mathbf{v} \times \mathbf{B}\,. \tag{2.16}$$

This assumption leads to the **Alfvén theorem**, which asserts that the magnetic field and the bulk matter are frozen and forced to move together. The main consequence of such a theorem is that when $\eta = 0$ the magnetic field lines will not change their structure being coupled to the matter, which implies a fixed magnetic field topology. The ideal MHD is valid when the electric conductivity σ (which is the inverse of the resistivity) is very high or when the spatial scales considered are very large. This regime finds application in many astrophysical plasma, such as the one explored in Chapter 5.

Resistive MHD: when σ is low or the considered scales are small, the Reynolds number is lower than one, and the resistive term cannot be neglected. In the resistive MHD the electric field equation (Eq. 2.15) becomes

$$c\mathbf{E} = \frac{\eta}{c} \cdot \mathbf{J_r} \,, \tag{2.17}$$

while the magnetic field is described as:

$$\frac{\partial B}{\partial t} = \eta \nabla^2 \mathbf{B} \,. \tag{2.18}$$

The solutions for this equation can be found by applying a Fourier analysis and has the form

$$B(\mathbf{x}, t) = \int \mathrm{e}^{-\eta k^2 t} \mathbf{B}(\mathbf{k}) \mathrm{e}^{i\mathbf{k} \cdot \mathbf{x}} \, \mathrm{d}\mathbf{k} \,. \tag{2.19}$$

As a consequence, the resistivity dissipates the magnetic field causing its decrease over time and its conversion into kinetic and/or thermal energy. This results in the acceleration of the bulk flow due to the action of the generated electric field. This effect is known as **Joule effect**. While the majority of the astrophysical plasma can be described in terms of the ideal MHD, the resistivity plays an important role on small scales and has to be considered when studying in detail the magnetic field behavior both in the accretion disk and in the launched relativistic jets (see, e.g., Mattia & Fendt 2020).

- **Relativistic MHD**

The relativistic magnetohydrodynamic regime applies when the velocity of the particles or the characteristics velocities of the sound (which increases with T) or Alfvèn waves (proportional to B, the Alfvèn waves are defined in Sect. 2.1.3) are close to the speed of light. The last two conditions imply that a relativistic regime can also be achieved with a small velocity of the fluid but with high temperatures or high magnetic field strengths. Generally, when neglecting the relativistic effects generated by the rotation of the black hole (out of the scope of this thesis), the geometry space in which this theory is developed is the Minkowski space, defined by the metric tensor

$$\mathbf{g}^{\mu\nu} = \mathrm{diag}(+1, -1, -1, -1) \,. \tag{2.20}$$

To obtain the final set of equations, it is necessary to combine the Maxwell equations together with the description of the evolution of the matter, which is derived from the conservation of the stress-energy momentum tensor and the continuity equations, respectively:

$$\partial_\mu \mathbf{T}^{\mu\nu} = \partial\mu \left(\mathbf{T}^{\mu\nu}_{\text{fluid}} + \mathbf{T}^{\mu\nu}_{\text{EM}}\right) = 0\,, \tag{2.21}$$

$$\partial_\mu(\rho u^\mu) = 0\,. \tag{2.22}$$

Here, $\mathbf{T}^{\mu\nu}_{\text{EM}}$ and $\mathbf{T}^{\mu\nu}_{\text{fluid}}$ are the energy-momentum tensor for the field and the matter, respectively, and u is the four-dimension velocity vector. Defining the total energy as E_{tot}, the relativistic enthalpy as ω_t, the Lorentz factor as Γ, the laboratory density as D, and the gravity acceleration term as $\mathbf{f}_g$, the final set of equations (in the ideal, special relativistic regime) is given by

$$\frac{\partial D}{\partial t} + \nabla \cdot (D\mathbf{v})^T = 0\,; \tag{2.23}$$

$$\frac{\partial \mathbf{m}}{\partial t} + \nabla \cdot \left(\omega_t \Gamma^2 \mathbf{v}\mathbf{v} - \mathbf{b}\mathbf{b} + \mathrm{I} p_{\text{tot}}\right)^T = \mathbf{f}_g\,; \tag{2.24}$$

$$\frac{\partial E_{\text{tot}}}{\partial t} + \nabla \cdot (\mathbf{m})^T = \mathbf{v} \cdot \mathbf{f}_g\,; \tag{2.25}$$

$$\frac{\partial \mathbf{B}}{\partial t} + \nabla \cdot (\mathbf{v}\mathbf{B} - \mathbf{B}\mathbf{v})^T = 0\,. \tag{2.26}$$

In here, $\mathbf{b}$ and p_{tot} are respectively $\mathbf{b} = \mathbf{B}/\Gamma + \Gamma(\mathbf{v}\cdot\mathbf{B})\mathbf{v}$ and $p_{\text{tot}} = \mathbf{p} + \left[\mathbf{B}^2/\Gamma^2 + (\mathbf{v}\cdot\mathbf{B})^2\right]/2$. The RMHD regime is vastly used to study the jet formation and propagation mechanisms due to the relativistic nature of the freshly injected outflows. In this thesis, the RMHD equations are solved numerically and used to explore the behavior of relativistic jets on sub-parsec and parsec scales. The work is presented in Chapter 5.

2.1.2 Instabilities

A crucial aspect of plasma physics is represented by the instabilities. A certain plasma is in equilibrium when the resultant of all the forces acting on the system is zero. However, considering the very turbulent environment in which the jets develop, it is very difficult, if not impossible, to achieve such a condition, leading to the formation of the mentioned instabilities. In the following, the instabilities and consequent waves (see next sections) are described, for simplicity, in the context of the MHD regime. Nonetheless, the information and properties reported are valid in the RMHD regime as well.

To develop the formalism used to describe the instabilities, the starting points are the equations for a non-relativistic plasma (from Eq. 2.11 to Eq. 2.14) written in the ideal MHD regime. A small perturbation ξ is introduced in the system following

$$h = h_0 + \xi h_1 \tag{2.27}$$

where h_0 is the non-perturbed quantity and h_1 is the perturbed one. By solving the mentioned equations for h_1 with different initial conditions and forces acting on the system, the relations that characterize the different instabilities are found. In the following, I give a brief introduction of the most important ones for the AGN environment.

- **Rayleigh-Taylor instability**

The Rayleigh-Taylor instability develops between two unmagnetized fluids immersed in a gravitational field. For the instability to arise, the two fluids must have two different densities with the heavier standing above the lighter. In the surface of contact, assumed to be linear at the beginning, as the system evolves in time waves begin to appear with portions of the lighter medium making their way into the denser one. One of the most astonishing examples of Rayleigh-Taylor instability is represented by the Crab Nebula (see Fig. 2.15, in which the filaments caused by the instability are clearly visible). This instability is expected to be visible in the lobe region of radio galaxies, where the magnetic fields are expected to be relatively small.

- **Kelvin-Helmholtz instability**

For the Kelvin-Helmholtz instability to arise, a medium with a stratified velocity whose gradient is normal to its direction of propagation is necessary. The instability leads to the formation of wiggles between two consecutive layers of the stratified structure (as seen in Fig. 2.16, which shows the formation of the Kelvin-Helmholtz instability in the clouds of Saturn). In an unmagnetized plasma, the instability is relatively easy to trigger, since small velocity gradients are sufficient. On the contrary, the presence of a poloidal magnetic field helps the stability of the system, making the formation of the wiggles more difficult. Indeed, the deformation of the topology of the perpendicular magnetic field lines creates magnetic tension, which compresses and stabilizes the plasma. Instead, the toroidal magnetic field component has no influence on this instability since the magnetic field lines do not create any tension, being parallel to the deformation.

When the velocity gradient is parallel to the direction of the gravitational force, the KH instability is the dynamic generalization of the Rayleigh-Taylor instability. The Kelvin-Helmholtz instability can occur in the relativistic jets,

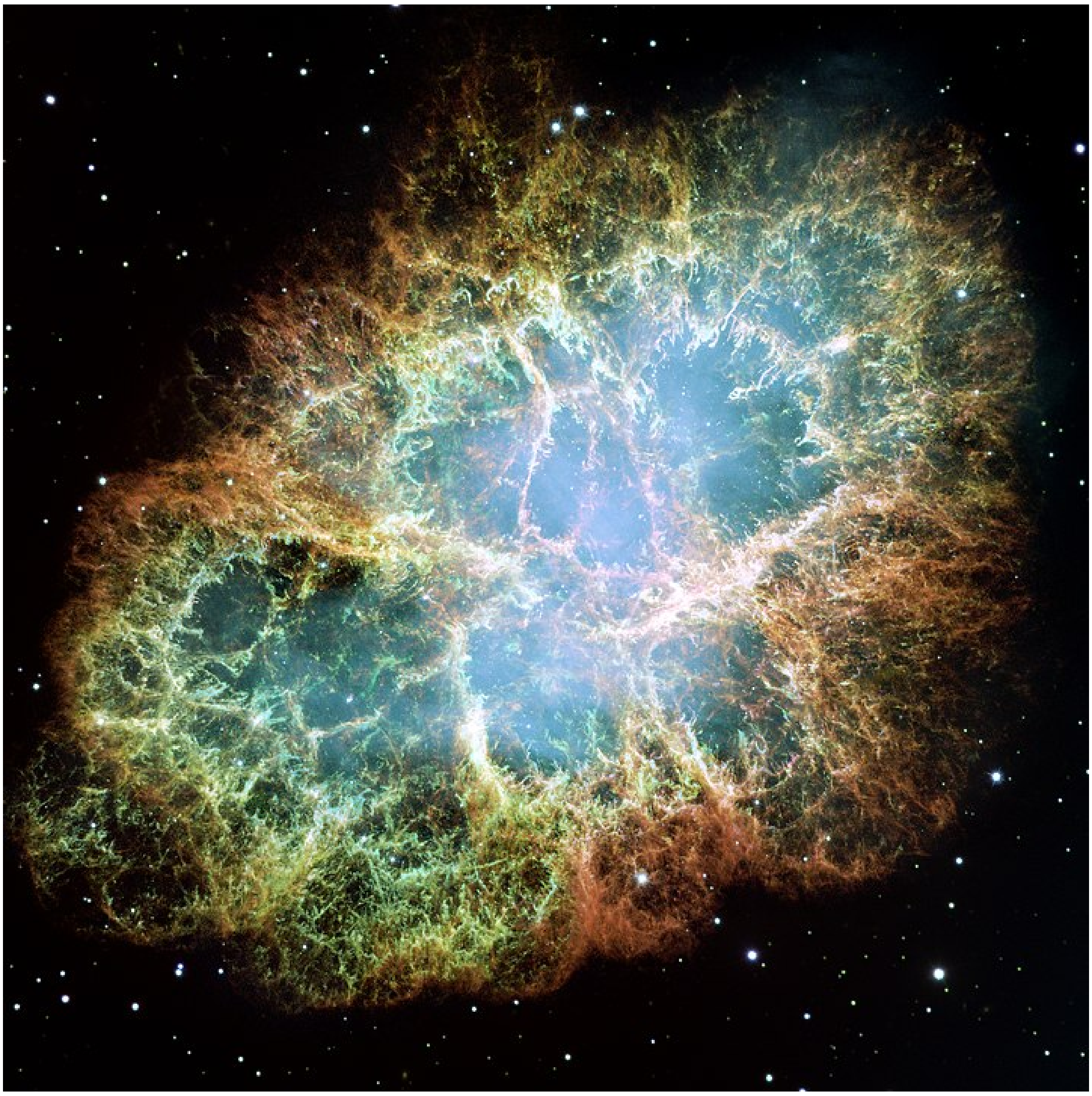

Figure 2.15: The supernova remnant called Crab Nebula. The Rayleigh-Taylor instability effects are clearly visible. Credits: NASA, ESA, J. Hester and A. Loll (Arizona State University) - HubbleSite: gallery, release., Public Domain, `https://commons.wikimedia.org/w/index.php?curid=516106`.

across the different stratified layers, or at the contact surface with the external medium. The second scenario is observed in the work presented in Chapter 5.

- **Plasma column instability**

The framework to derive solutions for the plasma column instability requires the force of gravity to be null or negligible and the plasma to be in a cylindrical geometry, meaning that its length is infinitely bigger than its radius. In the plasma column instability, both components of the magnetic fields are acting, and the configuration of the system arises from their interplay with the pressure profile. There are two different plasma column instability modes: i) the “sausage instability”, in which the plasma shows consecutive expansions and compressions,

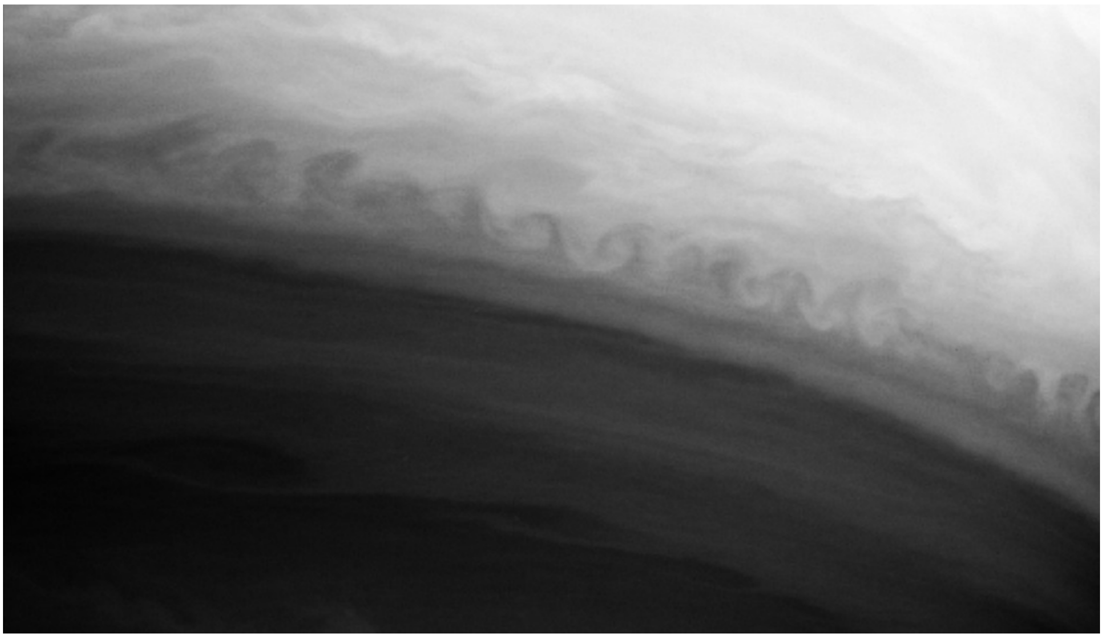

Figure 2.16: Kelvin-Helmholtz instabilities seen in the atmosphere of Saturn. Credits: NASA - `http://photojournal.jpl.nasa.gov/catalog/PIA06502en.wiki` originally uploaded by User:The Singing Badger there., Public Domain, `https://commons.wikimedia.org/w/index.php?curid=577763`.

ii) the "kink instability", where the entire plasma column oscillates in the normal direction with respect to the direction of propagation. The plasma column instability is an outcome of the effects of the toroidal magnetic field, while the poloidal component helps the stability of the system. The plasma column instabilities can be detected along the relativistic jets.

- **Magnetorotational instability**

The magnetorotational instability takes place in accretion disk-like structures and contributes to the loss of the angular momentum of the accreting material. As already mentioned in Sect. 1.2.1, when a disk has a Keplerian rotational motion, the distortion of the magnetic field lines leads to the formation of instabilities from which viscosity is generated. The latter dissipates the angular momentum, dragging the particles toward the central region. The magnetorotational instability is expected to happen even in the presence of very weak magnetic fields and, due to its action, is deeply involved in the jet formation process.

2.1.3 Waves

Once one of the aforementioned instabilities is formed, how does it propagate throughout the medium? The answer is: through the action of the waves. Their propagation velocity and direction is called **phase velocity** and is defined as

$\mathbf{v}_f = \omega/K$, in which ω is the angular frequency and K the angular wavenumber. The phase velocity, describing the evolution of a single wave, is not associated with any physical variation or energy transportation in the system. To account for such variations, a wave packet has to be considered. The propagation of the wave packet is called **group velocity** and describes the behavior of the overall shape of the wave amplitudes. The group velocity reads as $\mathbf{v}_g = \partial\omega/\partial K$.

In the ideal MHD formalism, two types of waves are of interest for this thesis: the **Alfvén waves** and the **magnetosonic waves**. In the former, the information on the thermal pressure (transported by the sound speed c_s) is negligible. In the latter, it plays an important role.

- **Alfvén waves**

The Alfvénic waves are further divided into the two categories of incompressible and compressible, depending respectively on their ability or inability to generate variations in the density of the medium.

In the incompressible case, i.e., the one in which the density of the medium does not vary, the phase and group velocities are respectively

$$\mathbf{v}_f = \pm c_a \cos(\kappa)\, \mathbf{e}_K \ \text{ and } \ \mathbf{v}_g = \pm c_a\, \mathbf{e}_b \tag{2.28}$$

where c_a is the Alfvén velocity $c_a^2 = B/(4\pi\rho)$, κ is the wave propagation angle, and $\mathbf{e}_K$ and $\mathbf{e}_b$ are the unit vectors of the wave vector [6] and the magnetic field. Equations 2.28 imply that the Alfvén waves propagate by carrying the magnetic perturbations in the normal direction with respect to the one of the magnetic field. On the contrary, the energy propagation moves in the same direction. The Alfvénic waves are generated by the magnetic tension and they may lead to important variations in the velocity and magnetic field of the plasma in which they develop.

In the compressible scenario, the waves propagate isotropically and their phase and group velocities coincide

$$\mathbf{v}_f = \mathbf{v}_g = \pm c_a\, \mathbf{e}_K\,. \tag{2.29}$$

When they propagate along the normal direction with respect to the magnetic field, they are indistinguishable from the incompressible scenario.

- **Magnetosonic waves**

---

[6] The wave vector is a vector whose module is the wave number K and its direction is the one of the wave propagation.

In magnetosonic waves, the effect of the thermal pressure is not negligible. Their dispersion relation, i.e., the relation that connects the wave number to the wave frequency ω, is:

$$\left(\frac{\omega}{K}\right)^2 = 0.5\left[(c_s^2 + c_a^2) \pm \sqrt{c_s^4 + c_a^4 - 2c_s^2c_a^2\cos(2\kappa)}\right] . \tag{2.30}$$

When using the plus sign in the parenthesis, the equation describes the fast magnetosonic waves. On the contrary, when using the minus sign, it describes the slow magnetosonic waves. In the former case, when the wave direction is parallel to the magnetic field, the wave velocity is c_s when $c_s > c_a$ or c_a when $c_s < c_a$. In the latter case, it is true the opposite. The magnetosonic waves are driven by the thermal pressure along with the pressure and tension generated by the magnetic fields.

2.2 Jet formation and propagation

The spatial, and temporal, evolution of relativistic jets can be roughly divided into four different phases, as shown in Fig. 2.17. In the sketch, the spatial scales are given in units of parsecs as well as Schwarzschild radii. The latter is the fundamental scale unit for describing the launching and propagation of relativistic jets. Within the first $\sim 10^2\,\mathrm{R_s}$, lays the **launching region** in which the jets are injected from the central region of the AGN. Here, the dynamical properties of the plasma are expected to be dominated by the strong magnetic fields extracted for the surroundings of the SMBH (Sect. 2.2.1). What follows is the **acceleration and collimation region**, in which the jets accelerate up to relativistic velocities, with peaks up to $\Gamma \sim 50$ in the most powerful ones, and collimate. In the collimation region, the jet presents a quasi-parabolic geometry, i.e, its radius grows with the distance as $\mathrm{z}^{\sim 0.5}$, while a transition to a conical geometry ($\mathrm{z}^{\sim 1}$) is observed at the end of this region (Sect. 2.2.2). In the large-scale structure (up to $\sim 10^9 - 10^{10}\,\mathrm{R_s}$), the jets evolve in the so-called **kinetic-flux dominated region** creating structures up to hundreds of kiloparsec scales before ending in the **dissipation region**. This thesis focuses on the first two regions.

2.2.1 The disk-jet connection

Among the astronomical community, there is broad consensus towards the relativistic jets being launched by the central region of AGN in a strongly magnetized environment in which the rotation of a Kerr black hole plays a direct role. However, several crucial aspects of the **disk-jet connection** have yet to be answered.

The launched plasma can be powered either by subtracting rotational energy

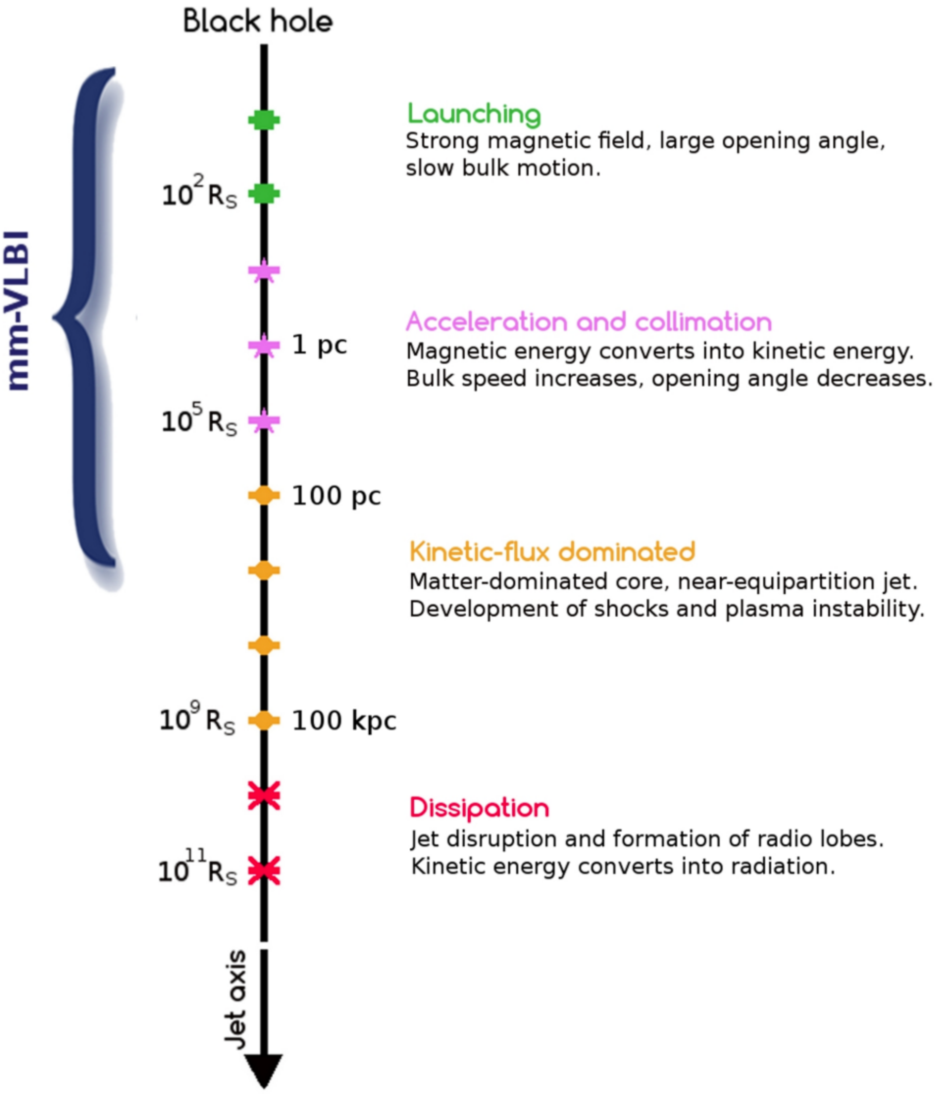

Figure 2.17: Sketch representing the four different stages of jet evolution (Boccardi et al. 2017).

from the central black hole (BZ, Blandford & Znajek 1977) or by extracting the energy stockpiled in the accretion disk (BP, Blandford & Payne 1982). Whether the outflows are fueled by either one of the two components, or both, is still a matter of discussion. The current paradigm points toward the BZ mechanism being able to produce high-energy jets, while the BP mechanism is typically associated with weaker outflows. Current studies are suggesting how both launching mechanisms can co-exist. In this scenario, the BZ might be associated with the most internal jet spine and the BP may be linked with the slower external winds that envelope the jet, leading to the aforementioned stratified jet structure (e.g., Hardee et al. 2007). Hints on the launching mechanisms can be inferred by extrapolating the jet width profile down to the jet base, now possible thanks to the enhanced VLBI capabilities. A remarkable example is the observations of Cygnus

A (Boccardi et al. 2016), in which the large jet width at its nozzle suggests an outflow launched way further than the black hole ergosphere, i.e., in the accretion disk via the BP mechanism.

Accounting for the nature of the accretion disks, theoretical models and observational studies are pointing towards a scenario in which the cold and radiatively efficient accretion flows (see Sect. 1.2.1) power the most energetic AGN jets such as the FSRQs (Ballantyne & Fabian 2005; Baum et al. 1995; Grandi et al. 2006; Grandi & Palumbo 2004; Hardcastle et al. 2007; Sambruna et al. 1999), whereas the hot and radiatively inefficient ones produce weaker jets, such as the BL Lacs (Allen et al. 2006; Balmaverde et al. 2006; Baum et al. 1995; Chiaberge et al. 2000; Hardcastle et al. 2007; Yuan & Narayan 2014). Focusing on the hot accretion flows, relevant to the source studied in this thesis (NGC 315), the current research is focused on understanding which mechanisms allow such inefficient disks to efficiently produce extended relativistic jets.

The most favored models aimed at describing the jet launching from hot disks are the **Standard and Normal Evolution** (SANE) and **Magnetically Arrested Disk** (MAD). The SANE model, as the name suggests, represents the classical scenario for the accretion mechanism from a weakly magnetized accretion disk in which the particles lose angular momentum due to the magnetorotational instability (Balbus & Hawley 1991; Narayan et al. 2012). On the contrary, in the MAD model, the accretion disks are naturally permeated by strong magnetic fields. When, due to the turbulent nature and motion of the components of the disk, enough poloidal magnetic field is gathered so that the magnetic force is able to counter-balance the gravitational one, the inflow of the particles stops, and a magnetosphere forms (see Fig. 2.18). Within such a structure, the flow is disrupted into blobs which later stream towards the central black hole (Bisnovatyi-Kogan & Ruzmaikin 1974, 1976; Narayan et al. 2003). The plasma accreted through a MAD, is channeled in the surroundings of a fast-rotating black hole, leading to the formation of the powerful relativistic jets, as shown in Narayan et al. (2021). The same authors showed that in the case of slowly rotating black holes, relativistic jets can still be launched but with lower efficiencies.

Overall, whichever process leads the charged particles to lose angular momentum, the particles are forced to follow the magnetic field lines bent towards the poles by the rotation of the black hole.

While theoretical studies are suggesting that the MAD model can describe efficient jet launching from highly magnetized accretion disks (Narayan et al. 2021; Zamaninasab et al. 2014), the observational evidence supporting it is currently limited. The observational properties needed to explore the presence of a MAD, such as the magnetic field strength and polarization in the inner parsec scale re-

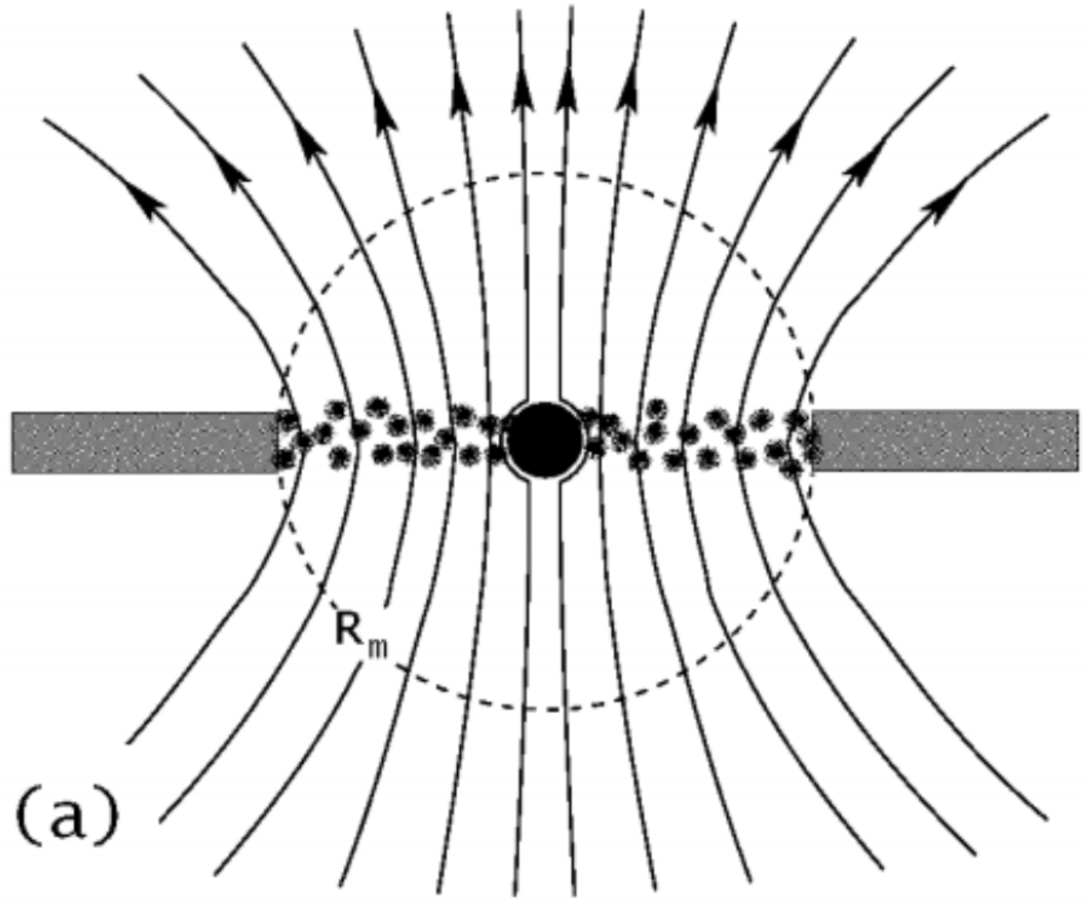

Figure 2.18: Representation of a MAD. The poloidal magnetic field saturates the accretion disk forming the magnetosphere, causing the particles to fall towards the central black hole. The lines are the magnetic field lines (Narayan et al. 2003).

gion (see, e.g., Yuan et al. 2022), have made it challenging to test such a scenario for a large number of sources. Examples of galaxies in which the MAD is suggested are M 87 (Event Horizon Telescope Collaboration et al. 2019a,b,c,d,e,f) and Sgr A* (Event Horizon Telescope Collaboration et al. 2022a,b,c,d,e,f). Therefore, exploring nearby sources is crucial to providing the observational counterpart of such studies, due to the possibility to achieve enough angular resolution to resolve the inner jet region. Thanks to its vicinity and large black hole mass, and consequently the remarkable angular resolution one can achieve with interferometric observations, NGC 315 offers a unique opportunity to investigate the presence of a MAD and its disk-jet connection in general. This work is presented in Chapter 4.

2.2.2 The acceleration and collimation region

Once launched, relativistic jets evolve into the external medium as Poynting-flux dominated outflows, i.e., outflows in which the magnetic fields dominate

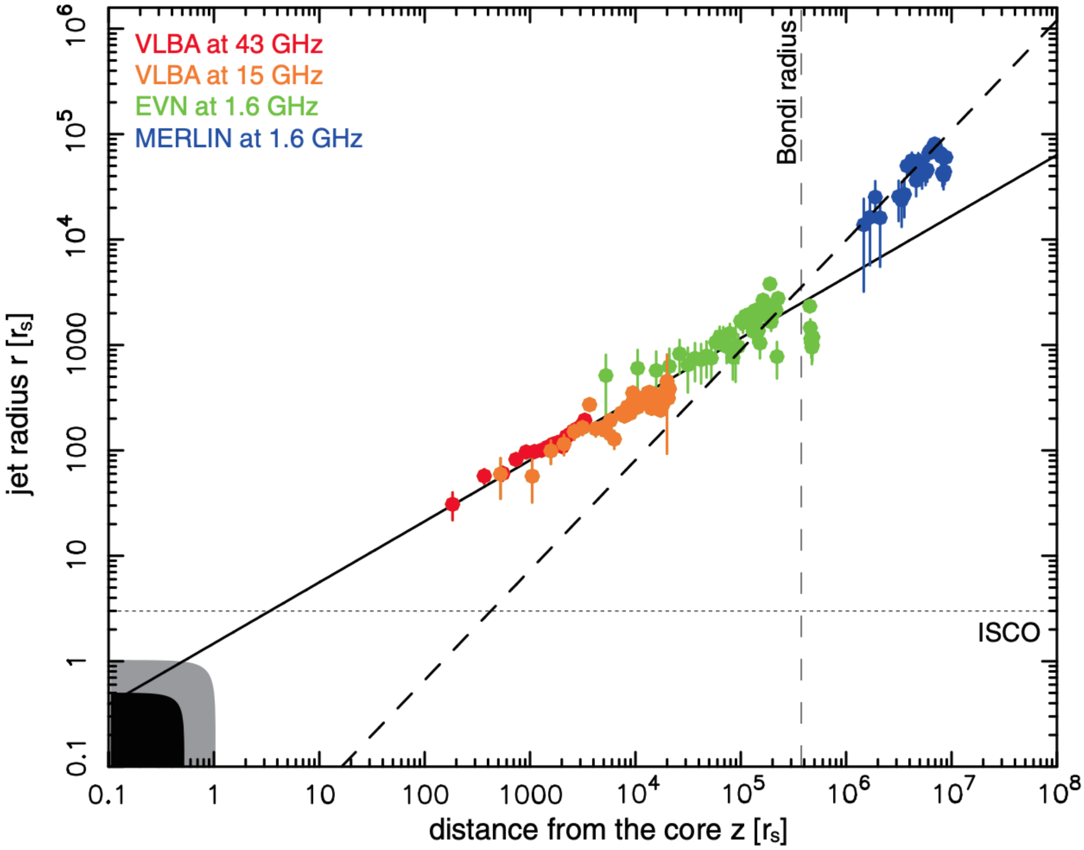

Figure 2.19: Jet width as a function of the distance from the core for M 87 based on the use of a multi-frequency VLBI data set. The transition from a parabolic to a conical geometry is observed around $\sim 5 \times 10^5\,\mathrm{R_s}$ (Asada & Nakamura 2012).

the dynamics of the jets. Downstream the launching region, relativistic outflows manage to remain collimated for long distances with typical opening angles of the order of a few degrees. Exploring the collimation process is of great importance in understanding the establishment of such extended structures. This phenomenon can be observed thanks to the high-resolution observations achieved by means of the VLBI technique (see Sect. 3), which allows nearby sources to be explored on scales down to $10^2 - 10^7\,\mathrm{R_s}$ from the jet injection point, i.e., along the region in which the jets are expected to collimate (Boccardi et al. 2021; Kovalev et al. 2020).

A jet collimates until its opening angle decreases with the distance, while the geometrical transition to a conical shape, i.e., to a constant opening angle, implies the end of the collimation process. The first observation of such phenomenon was performed by Asada & Nakamura (2012) for M 87. The authors, as shown in Fig. 2.19, observed a change in the jet width profile on scales of $\sim 10^5\,\mathrm{R_s}$, in the proximity of the Bondi radius. The latter delimitates the region in which the particles infall speed transits from subsonic to supersonic and has roughly the same order of magnitude as the gravitational sphere of influence of the black hole. Following the M 87 study, in the last ten years, the geometrical transition was discovered in many other sources, both in single object studies (e.g., for NGC 315, Boccardi et al. 2021; Park et al. 2021) and in sample studies (Burd et al. 2022; Kovalev et al. 2020), finally probing the existence of the parabolic region. Indeed, its existence was long expected from a theoretical point of view but never observed due to insufficient angular resolution of previous VLBI arrays.

In the physical process behind the establishment of the parabolic region, and consequent collimation, both jet internal and external factors play a relevant role. Kovalev et al. (2020) following the work from Pushkarev et al. (2017) on the MOJAVE sample [7], found that several AGN collimate in correspondence with the Bondi radius. Under the assumption of an external medium dominated on small scales by the Bondi accretion, this may suggest that variations of the external conditions can trigger the change in the jet geometry. Recently, however, several cases of AGN jets whose shape transition takes place way before the Bondi radius have been presented. Examples are the aforementioned NGC 315 and NGC 1052 (Nakahara et al. 2020). These new results suggest how the correspondence between the transition region and the Bondi radius is not valid in general. Further studies (e.g., Beskin & Nokhrina 2006) propose that the jet shape transition is expected to reflect internal changes in the bulk flow, which would transit from a magnetically dominated state to an equipartition state between the plasma kinetic and magnetic energy. Other scenarios consider the action of the thick accretion disk when present (Boccardi et al. 2021). Indeed, thick disks are expected to have extensions around $10^2 - 10^3\,\mathrm{R_s}$, and, when jets are collimating on the same distances, the geometrical change may be induced by a change in the external conditions. Moreover, mostly for high-luminosity AGN, the BP-launched winds may favor the collimation of the most internal spine (Boccardi et al. 2021). In conclusion, as shown, while many theories have been developed to address jet collimation, an overall picture is still missing. Moreover, since jets may present both Blandford & Znajek (1977) and Blandford & Payne (1982) outflows, it is currently under debate whether they may undergo two different collimation processes, one for the central spine and one for the winds.

The properties of the acceleration and collimation region are deeply intersected. This is a consequence of the nature of the magnetic acceleration which was shown by Komissarov et al. (2007) among the others, to be a viable way to accelerate the jet. Magnetic acceleration is only effective when the outflow is collimating, while it becomes ineffective during a conical expansion. As a result,

---

[7] The MOJAVE (Monitoring Of Jets in Active galactic nuclei with VLBA Experiments) is a monitoring program aimed at investigating the brightness and polarization variations in the jets from active galaxies in the northern sky. Website: `https://www.cv.nrao.edu/MOJAVE/index.html`.

when only magnetic acceleration is involved, the extent of the acceleration and collimation regions are expected to coincide. In recent years theoretical and simulation studies on jet acceleration have mostly focused on the magnetic component of the acceleration, largely ignoring the thermal acceleration by assuming a small internal flux compared to the overall jet energy flux at injection. Authors such as Vlahakis & Königl (2003a,b, 2004) pointed to thermal acceleration being relevant only on compact scales, at the very jet base, with the magnetic one taking over on sub-parsec, parsec scales. The magnetic acceleration is driven by the differential collimation mechanism (Komissarov et al. 2007). The toroidal magnetic field due to the action of the hoop stress generated by the magnetic tension, favors both the collimation of the jet and the conversion of magnetic energy into kinetic energy, accelerating thus the outflow. On the other side, the thermal acceleration is driven by the Bernoulli mechanism. Whether relaxing the assumption of small initial internal flux and considering relativistic hot jets (Perucho et al. 2017) would lead to a more extended thermal acceleration is currently a matter of discussion. This scenario was suggested, for example, by López-Miralles et al. (2022) for the case of jets from high-mass X-ray binaries. This topic is addressed in Chapter 5.

3 Very Long Baseline Interferometry

Aperture synthesis, when introduced in the second half of the past century, completely changed the way radio astronomy is done (Ryle & Hewish 1960). Thanks to it and its application, the Very Long Baseline Interferometry technique, it is possible to achieve angular resolution orders of magnitude higher than the ones achieved with single telescope observations. In this Section, I describe the fundamental physics behind the technique along with how radio astronomers are able to constrain physical information on astronomical sources from VLBI observations. In Sect. 3.1 I describe the nature of the radio signal, in Sect. 3.2 the VLBI technique, in Sect. 3.3 how the data are reduced and imaged.

3.1 The radio signal

When observing the sky, a radio telescope detects the electromagnetic field of the incoming radiation and is exposed to the entire **surface brightness** of the portion of the sky toward which it is pointed. The surface brightness is the flux density per unit of solid angle, whereas the **flux density** is the energy per unit time per unit area per unit frequency. Therefore, the surface brightness reads as:

$$dI_\nu = (dE_r/d\Omega)\, dA\, d\nu\, dt\,, \tag{3.1}$$

in which E_r is the energy of the radiation, Ω is the observed solid angle, and A is the surface area. Since the flux densities of astronomical sources are extremely low, it is common in the astronomical community to employ the unit of measurement called the **Jansky**, named after Karl Jansky. The Jansky is defined as:

$$1\,\mathrm{Jy} = 10^{-26}\,\mathrm{Wm^{-2}Hz^{-1}}\,. \tag{3.2}$$

The continuum radio emission is characterized by: i) the total intensity, ii) the fractional degree of polarization, iii) the shape of the polarization ellipse. To easily describe these properties, George Gabriel Stokes in 1851 (Stokes 1851) introduced what will be later called the **Stokes parameters**:

$$I = I\,, \tag{3.3}$$

$$Q = I\, p_e \cos(2\psi)\cos(2\chi)\,, \tag{3.4}$$

$$U = I\, p_e \sin(2\psi)\cos(2\chi)\,, \tag{3.5}$$

$$V = I\, p_e \sin(2\chi)\,. \tag{3.6}$$

Here, I is the total intensity, p_e is the degree of polarization which spans from

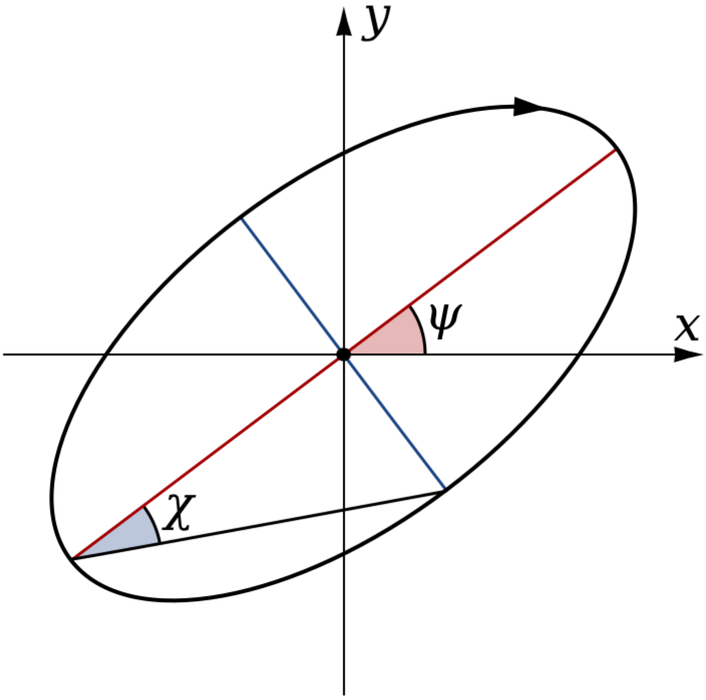

Figure 3.20: Representation of the polarization ellipse with highlighted the parameters ψ and χ. Credits: Wikipedia, public domain.

0 to 1, while ψ and χ are the parameters defining the polarization ellipse (see Fig. 3.20). The latter is the surface defined by the electric vector at a fixed point in space and can be used to describe any polarization state. In the two special cases, i.e., linear and circular polarization, the ratio of the major over the minor axis is infinite and one, respectively.

In this formalism, the first Stokes parameter I represents the total intensity, Q and U measure the degree of linear polarization at 0°/90° and -45°/45° respectively, and V quantifies the circular polarization. For monochromatic coherent radiation, the relation between the Stokes parameters reads $I^2 = Q^2 + U^2 + V^2$. However, since the detected radiation is non-coherent the Stokes parameters are average values. In this case, the relation between them is $I^2 \geq Q^2 + U^2 + V^2$. When equal, the sum of Q,U, and V defines the total polarization intensity I_p. Consequently, the fraction of total polarization of the incoming radiation can be determined as I_p/I. When $Q = U = V = 0$, the radiation is entirely unpolarized.

3.2 The VLBI technique

The concept of interferometric observations of celestial objects was first proposed by Martin Ryle and Anton L. Rogers in 1946. The VLBI technique later rose in the 1960s and quickly started to play a central role in radio astronomy observations. VLBI is based on the **aperture synthesis** technique, in which the radio

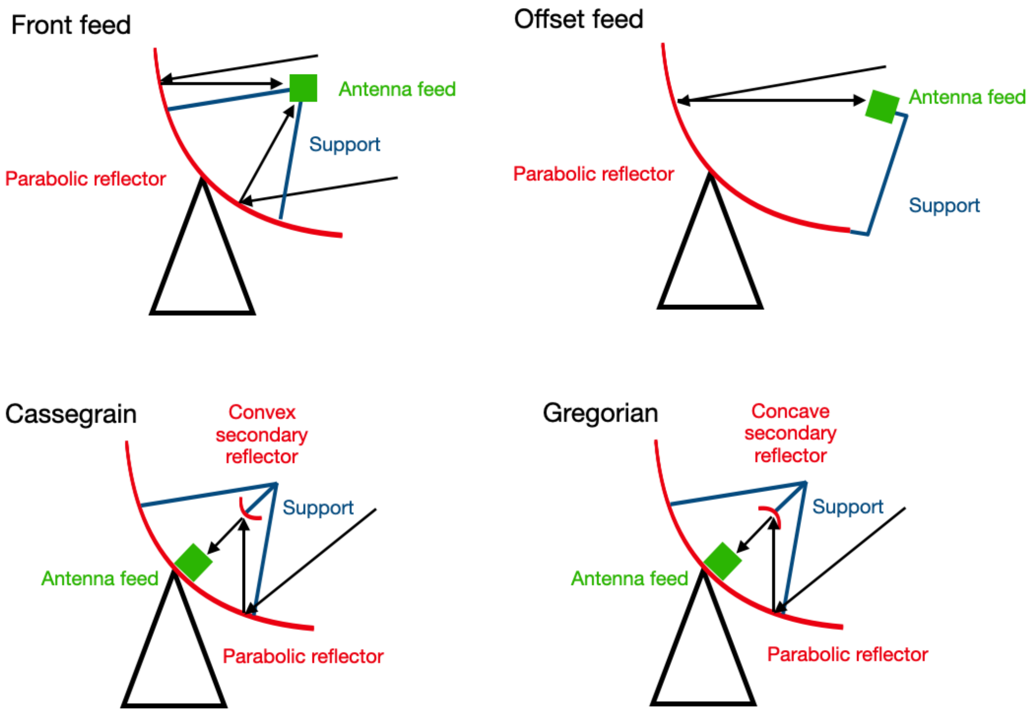

Figure 3.21: Schemes of the different configurations for parabolic antennas. The red elements are the reflectors, the blue ones are the support, and the green ones are the antenna feed. In a receiving system, the path of the incoming photons is highlighted by the black arrows. Readapted from: Chetvorno, Public domain, via Wikimedia Commons.

signal is recorded from different radio telescopes, precisely timed, and later used to produce the high-resolution radio images.

In the following, I describe the main properties of single-dish telescopes used for radio-astronomical observations (Sect. 3.2.1) together with the theory behind the aperture synthesis technique (Sect. 3.2.2). In Sect. 3.2.3 I briefly describe the VLBI arrays relevant for this thesis.

3.2.1 The single-dish antenna

An antenna is a device composed of conductive material that can act as a transmitter or receiver. When receiving, the radio waves reaching the antenna induce an electric current within it. In the following, I focus on describing the receiving, paraboloid-type antennas, such as Effelsberg, which are among the most employed in radio astronomy arrays when observing at sub-meter wavelengths. Effelsberg is a 100-m dish antenna located in Bad Münstereifel, Germany, and operated by the Max Planck Institute for Radio Astronomy. It was inaugurated on August 1st, 1972 and, for almost 30 years, it has been the largest steerable radio telescope in the world.

The parabolic dish is the first contact point for the incoming signal. Its goal is to collect as much flux as possible from the pointed position in the sky and redirect it to the focal point of the antenna. The total power received can be expressed as:

$$P = A_{\text{eff}} S_\nu \Delta\nu \tag{3.7}$$

in which A_{eff} is the effective collecting area of the antenna, i.e., the geometrical area $\pi(D/2)^2$ multiplied by the aperture efficiency (D is the antenna diameter), S_ν is the flux density received, and $\Delta\nu$ is the bandwidth of the receiver. The aperture efficiency is a function of the wavelength of the incoming radiation and always assumes values lower than one as a consequence of the imperfections in the reflecting dish and of the obstruction caused by the support (blue elements, Fig. 3.21).

There are different possible configurations for a parabolic antenna, depending on the position of the feed and the shape of the secondary mirror. When employed as a receiver, the **antenna feed** is the element that supplies the alternating currents, generated by the incoming radiation, to the receiving system. The possible configurations for parabolic antennas are (see Fig. 3.21): i) front feed; ii) offset feed; iii) Cassegrain; iv) Gregorian. In general, the vast majority of prime focus-fed systems use the front feed. However, due to the complexity of the front-end system, in radio astronomy Cassegrain or Gregorian configurations are preferred. Indeed, in such configurations, the antenna feed is positioned behind, or on, the parabolic dish and is not placed in front of the reflector.

In Cassegrain or Gregorian configurations, the signal, after being focused by the primary mirror, is redirected to the secondary reflector, highlighted by the small red structure in Fig. 3.21. The secondary reflector is positioned over the center of the primary dish. In the Cassegrain system, the secondary reflector consists of a hyperboloid with the concavity directed in the same direction as the primary one. On the contrary, in the Gregorian system, the reflector is an elliptical-shaped secondary mirror with an opposite direction of concavity. The latter is the system used in Effelsberg. The signal is consequently redirected to the antenna feed. Here, the radiation travels through the **feed horn**, a crucial component to reduce the amount of power lost in the passage between the antenna and the waveguide due to impedance.

In the Cassegrain or Gregorian systems, the receivers can be positioned both in the primary focus, i.e., where the secondary reflector is, or in the secondary focus. For example, in Effelsberg some receivers, such as 18 cm and 3 mm, are positioned in the primary focus. There are different types of receivers. Vastly used is the **heterodyne receiver**. In these systems, the signal is amplified by a Low Noise Amplifier, which, for noise minimization, is a device maintained at cryogenic temperatures. In the later stage, the signal is down-converted. This step is necessary since the observing frequencies are too high to be sampled properly. Additionally, lower frequencies imply lower signal losses, being the latter proportional to the square of the frequency. To be down-converted, the signal is mixed with a single tone given by a Local Oscillator. The operation is performed by a mixer. The output of this process is the "Intermediate Frequency". A second type of receiver, used for sub-mm observations, is the **bolometric receiver**. Within it the incoming radiation generates heat, increasing the material temperature and consequently changing the total power.

After passing the receiver, the signal proceeds further to the backend for processing and detection and is later redirected to a digitizer. The digitization is performed with an analog-to-digital converter.

A crucial parameter characterizing the performance of an antenna is the **radiation or beam pattern**, which describes the angular dependence of the response of the antenna. The beam pattern is expressed as the power received from a point source as a function of the angular distance from the antenna axis. A typical radiation pattern is shown in Fig. 3.22 and arises from overlapping incoherent phases at the focus due to Fraunhofer diffraction. The principal component of the beam pattern is represented by the main lobe. In contrast, the side and back lobes are undesired maxima of the antenna response, and the goal is to have them as small as possible. **The angular resolution** of a certain antenna, arises from the beam pattern. The angular resolution is approximated by the first null of the beam

$$\theta_b \sim 1.22\frac{\lambda}{D} \tag{3.8}$$

in which λ is the wavelength of the incoming signal.

When the antenna points to a certain area, it records its temperature distribution. The latter is far from isotropic due to the mentioned response of the antenna and to the surface brightness distribution of the sky I_ν. Their convolution, called **antenna temperature**, is the quantity measured by the receiver, which at a given frequency assumes the form

$$T_\mathrm{A} = \frac{A_\mathrm{eff}}{2k}\int_{4\pi} I_\nu(\phi,\vartheta)P_\mathrm{n}(\phi,\vartheta)d\Omega\,, \tag{3.9}$$

where $P_\mathrm{n}(\phi,\vartheta)$ is the normalized beam pattern distribution in polar coordinates ϕ and ϑ, and Ω is the solid angle observed by the antenna.

The output signal, associated with a temperature as well, is referred to as **system temperature** (T_sys), which is the sum of T_A and other sources of noise.

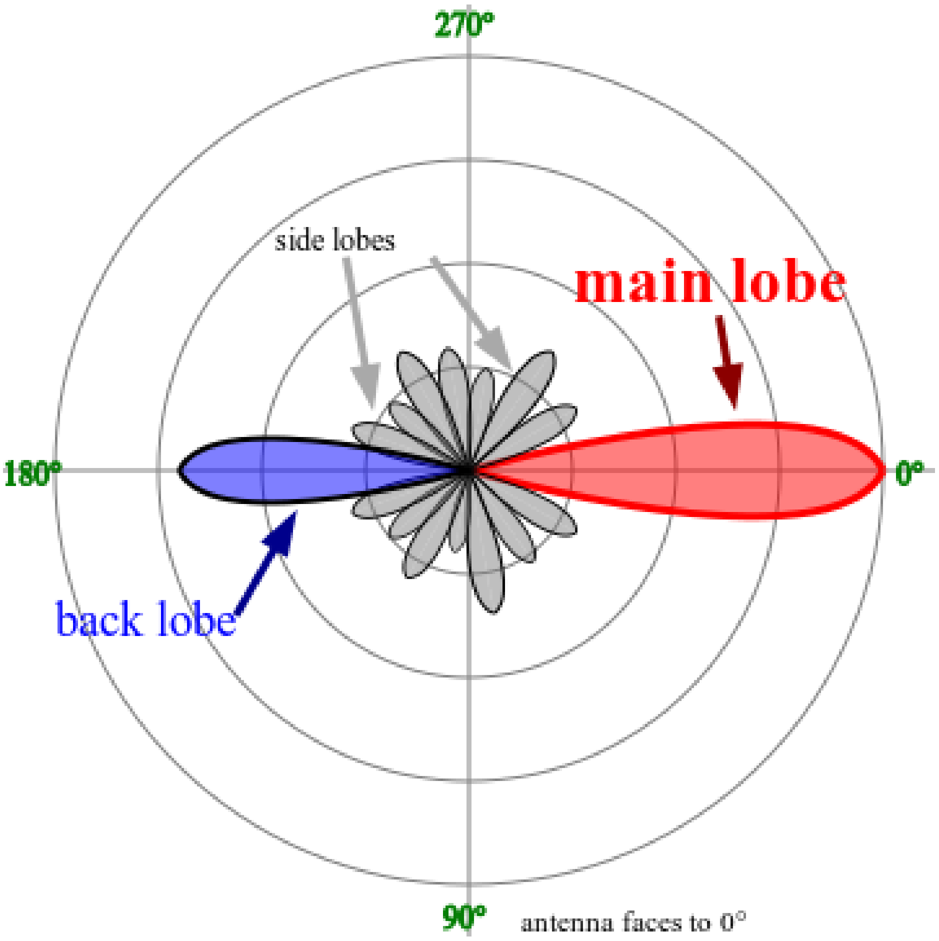

Figure 3.22: Representation of the beam pattern. The red area is the main lobe, the blue one the back lobe, and the grey ones the side lobes. Credits by Timothy Truckle - Own work, CC BY-SA 4.0, `https://commons.wikimedia.org/w/index.php?curid=4245213`.

Among them, the most relevant are the atmosphere temperature T_{atm} and the equivalent temperature from the receiver T_{rec}. The latter is typically the dominant source of noise and is usually much larger than T_{A}. The ratio between T_{A} and T_{sys} is called signal-to-noise ratio (S/N). Increasing the S/N as much as possible requires averaging over an increasing number of samples since the signal from the source is correlated while the noise is not. This is expressed by the **radiometer equation**

$$S/N = \frac{T_{\mathrm{A}}}{T_{\mathrm{sys}}}\sqrt{\tau\,\Delta\nu}\,. \tag{3.10}$$

It is important to underline that the bandwidth $\Delta\nu$ limits the number of samples n, as a consequence of the **Nyquist sampling theorem**: if the samples are considered over time intervals $\Delta\tau$ shorter than the inverse of the bandwidth ($1/\Delta\nu^{-1}$), they are not independent. As a consequence, increasing the number of samples requires either increasing the on-source time τ or the bandwidth, i.e., $n = \tau\,\Delta\nu$. Equation 3.10 is obtained by assuming a Gaussian error, i.e., $\propto \sqrt{n}$.

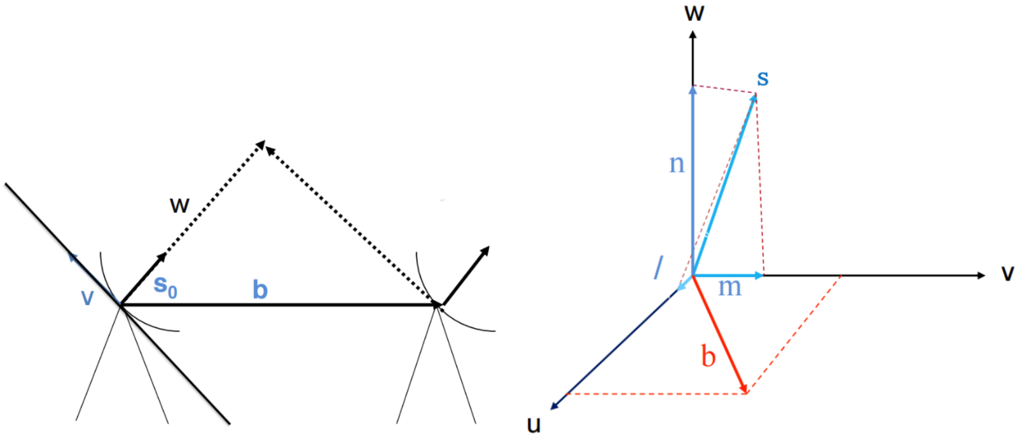

Figure 3.23: Scheme of the direction cosine (l,m,n) and the u,v,w coordinate systems. Credits: IMPRS Blackboard Lectures 2014, Hans-Rainer Kloeckner.

The flux density (in Jansky) is related to the antenna temperature (in Kelvin) as

$$S_\nu = \frac{2k}{A_{\text{eff}}} T_{\text{A}} \, . \tag{3.11}$$

The conversion factor is known as **antenna gain** (g) and its calculation requires a precise determination of the aperture efficiency.

3.2.2 Aperture synthesis

The quest to increase the angular resolution pushed the community in the 20th Century towards the construction of progressively larger dishes leading to the creation of authentic giants, such as the aforementioned Effelsberg and the Green Bank Telescope (whose size is 100 m by 110 m). However, this approach quickly encountered physical, economic, and engineering problems, preventing further increases in the antenna size and so in the angular resolution. The VLBI technique has been developed to overcome this issue. When observing a certain source at a certain time, the different antennas connected in VLBI mode act as one single telescope whose diameter is the maximum distance between the antennas in the array. The revolution of such an approach can be proved with a quick example. Assuming to observe a certain region of the sky with Effelsberg, the resolution of the observation is $\theta_b \sim 1.22\lambda/(\sim 100\,\text{m})$. When observing in VLBI mode the same region of the sky with Effelsberg and the Green Bank Telescope (as an example), the final resolution is expected to be $\theta_b \sim 1.22\lambda/(\sim 6 \times 10^6\,\text{m})$, more than four orders of magnitude higher!

To describe how aperture synthesis works, it is easier to start by considering a two-element array. Before that, two important concepts need to be defined: i) the **baseline** and ii) the **uv-plane**. The first is the projected distance between

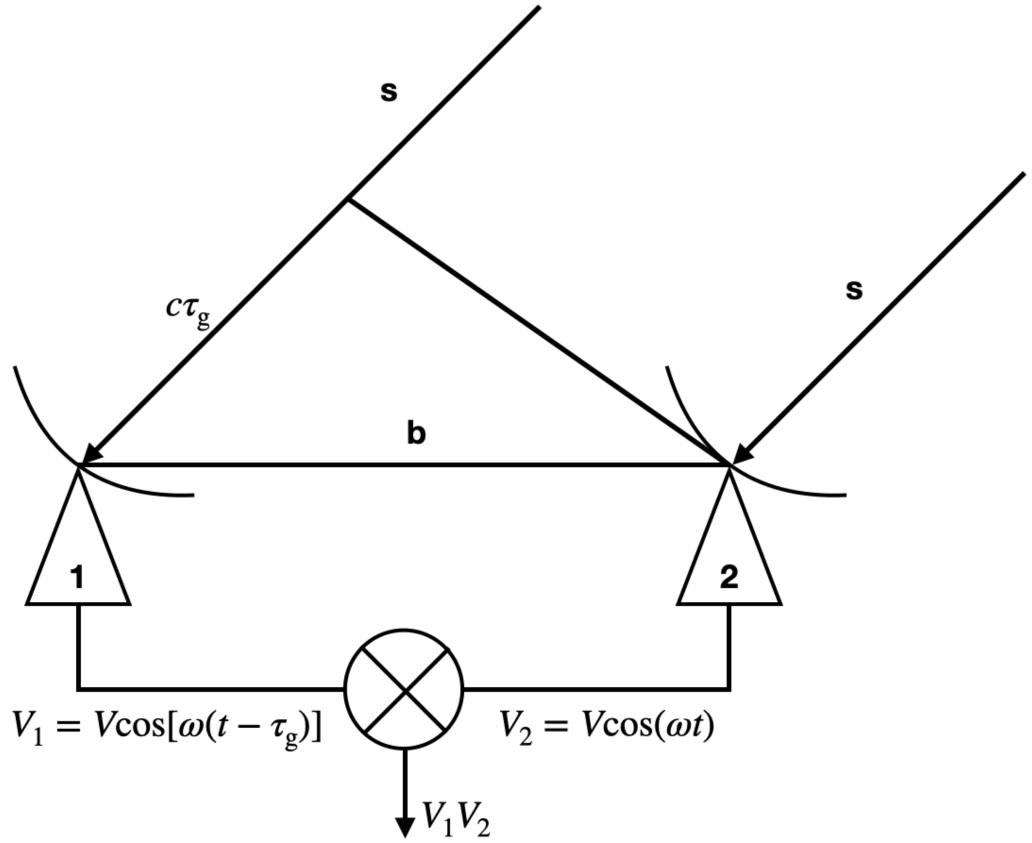

Figure 3.24: Two-elements array. **b** is the separation length between the two antennas, i.e., the baseline, while τ_g is the time delay. The unit-vector **s** marks the direction of the observed region of the sky.

two antennas, expressed in wavelength units. The number of baselines depends on the number of antennas (N) and increases as $N(N+1)/2$. The uv-plane is defined by considering the 3D-space created by the direction cosines (l,m,n): w points towards the observed region in the sky, while u and v identify the plane perpendicular to it with u pointing towards the east and v towards the north celestial pole (see Fig. 3.23). The coordinates in the uv-plane are expressed in units of wavelengths.

The scheme of the two-element interferometry is shown in Fig. 3.24. The furthest antenna (number 1 in the figure) detects the signal with a delay $\tau_\mathrm{g} = \mathbf{b}\cdot\mathbf{s}/c$, with **b** the baseline length and **s** the unit vector along the source direction. The voltage measured by the two antennas is respectively:

$$V_1 = V\cos\left[\omega(t-\tau_\mathrm{g})\right] \, , \tag{3.12}$$

$$V_2 = V\cos\left(\omega t\right) \, , \tag{3.13}$$

with V the maximum amplitude and $\omega = 2\pi\nu$, where ν is the frequency of the incoming wave. As a consequence of the delay τ_{g}, the signals must be corrected for the time-variable phase shift to be later coherently combined. The correlation of the signals is performed by the **correlator**. In the first steps, the signals are first multiplied and then averaged. After the multiplication of the voltages V_1 and V_2, the output signal has the form

$$V_1 V_2 = \left(\frac{V^2}{2}\right)\left[\cos(2\omega t - \omega\tau_{\mathrm{g}}) + \cos(\omega\tau_{\mathrm{g}})\right]. \tag{3.14}$$

When averaging for a sufficiently large time, i.e., of the order of seconds, the term $\cos(2\omega t - \omega\tau_{\mathrm{g}})$ becomes negligible, and the operation of averaging yields to:

$$< V_1 V_2 >= \left(\frac{V^2}{2}\right)\cos(\omega\tau_{\mathrm{g}}) = \left(\frac{V^2}{2}\right)\cos\left(2\pi\frac{\mathbf{b}\cdot\mathbf{s}}{\lambda}\right). \tag{3.15}$$

As a consequence of these first steps performed by the correlator, the output signal is described by a cosine function. However, Eq. 3.15 is not sufficient to properly describe the source function. Indeed its output is null for the odd values of the distribution, being the cosine an even function. To overcome this problem, it is necessary to derive a sine function by applying a phase shift of 90° to one of the two signals. After the same multiplication and averaging steps, the output signal is:

$$< V_1 V_2 >= \left(\frac{V^2}{2}\right)\sin(\omega\tau_{\mathrm{g}}). \tag{3.16}$$

The final step is to combine the signals and form the **complex visibility** according to the function:

$$\mathcal{V} = Re - iIm = Ae^{-i\Phi} \tag{3.17}$$

where the real part Re is the cosine function, the imaginary part Im is the sine function, $A = \sqrt{Re^2 + Im^2}$ is the **visibility amplitude**, and $\Phi = \tan^{-1}(Im/Re)$ is the **visibility phase**. The signal produced during the correlation is related to the brightness of the source $I_\nu(\mathrm{s})$ through a Fourier transform integration in the form

$$\mathcal{V}(\mathbf{b}) = \int\int I_\nu(\mathbf{s}) e^{-2\pi i\nu\mathbf{b}\cdot\mathbf{s}/c}\, d\Omega\,. \tag{3.18}$$

By translating such an equation in the uv-plane, the **visibility function** acquires the most-known form:

$$\mathcal{V}(u,v,w) = \int\int \frac{I_\nu(l,m)}{\sqrt{1-l^2-m^2}} e^{-2\pi(ul+vm+wn)}\, dl\, dm\,. \tag{3.19}$$

Following the visibility equation, to obtain a more reliable reconstruction of

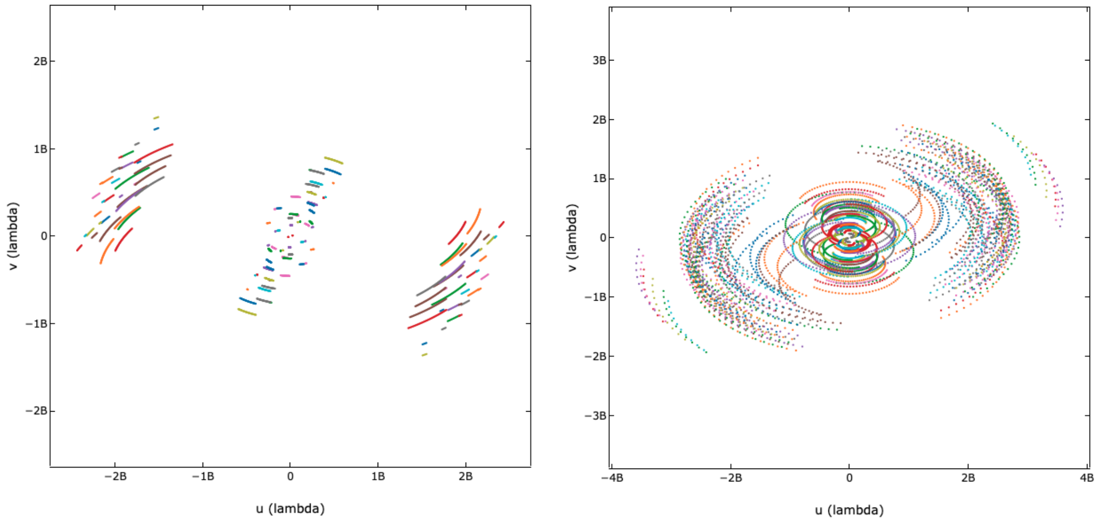

Figure 3.25: uv-coverage for observations of NGC 315 with the GMVA. Left panel: 1 hour-long observation. Right panel: 12 hours-long observations. The plots are produced using the online tool: `https://planobs.jive.eu/`.

the source brightness, more interferometry elements are needed, i.e., it is necessary to fill the uv-plane to increase the **uv-coverage**. Along with adding as many as possible antennas to the array, one can also take advantage of the rotation of the Earth to increase the number of points in the uv-plane. An example is given in Fig. 3.25. The left panel represents the uv-coverage for 1-hour-long observations of NGC 315 with the global mm-VLBI array (GMVA, see next section), while the right panel is for 12 hours-long observations. The more points in the uv-plane, the more accurate the description of the sky brightness distribution (and so of the source) during the calibration and imaging process (see Sect. 3.3).

When observing a region of the sky with the aperture synthesis technique, the array is sensitive along the baseline direction, since the fringe pattern is oriented perpendicular to it. Moreover, since the spacing between the fringes is $\propto b^{-1}$, the longer baselines will be sensitive to the small-scale structures, while the shorter baselines will be to the large-scale structures. Naturally, for the best possible description of the source, both long and short baselines in all possible directions are desired.

The sensitivity of a VLBI array depends on many factors. Among them, the bandwidth, and thus the recording rate, of the receiving system is of great importance, especially due to its high impact/cost ratio. The bandwidth-sensitivity relation is a direct consequence of the theoretical thermal noise of a VLBI image varying as $1/\sqrt{\Delta\nu}$. Other factors impact the sensitivity, such as: i) the sensitivity of each single antenna; ii) the number of observatories participating in the experiment; iii) the on-source integration time. Therefore, the sensitivity also improves by increasing the number of antennas participating in the VLBI observations, with a preference for telescopes with a large collecting area. Nonetheless, also smaller antennas are of great importance. Indeed, they help fill up as much as possible the uv-plane while maintaining the production cost relatively low. To maximize the sensitivity during an experiment, up-to-date receiver, and ideal weather conditions are further desired.

The receivers installed in the antennas are not monochromatic, but have a finite bandwidth (up to hundreds of MHz). However, the theoretical foundations of synthesis imaging are valid only for monochromatic radiation. This causes the so-called **bandwidth smearing**, i.e., an attenuation of the fringes and the introduction of distortions in the final image. The smearing effects become more relevant with increasing baseline length and larger bandwidth. Nonetheless, wide bandwidth systems are preferred to increase the signal-to-noise ratio of the observations, as mentioned. To mitigate this problem, the bandwidth is divided into a high number of channels which are later averaged.

3.2.3 VLBI arrays

Several radio telescope arrays across the globe are currently operating. In this section, I describe the three arrays used in this thesis, together with the currently most-famous one, the **Event Horizon Telescope** (EHT). The three arrays are i) The **Very Long Baseline Array** (VLBA); ii) the **European VLBI Network** (EVN); iii) The **Global mm-VLBI Array** (GMVA).

- The VLBA is entirely based in the United States and is formed by ten antennas: St. Croix, Hancock, North Liberty, Fort Davis, Los Alamos, Pie Town, Kitt Peak, Owens Valley, Brewster, and Mauna Kea. They are all 25-m parabolic dishes with the operational center (along with the correlator) based in Socorro, New Mexico. The VLBA can observe in a wavelength range that spans from 3 mm up to 90 cm, and its longest baseline is 8611 km (Mauna Kea - St. Croix). The peculiarity of the VLBA is that the antennas were conceived and built all equal, with the same frequency standards and at ideal locations to work as VLBI elements.

- The EVN is the most sensitive array in the world and counts antennas mostly based in Europe, with some additions in China and South Africa. The antenna composing this array are (the reported names are the ones that are commonly used in the community): Effelsberg, Westerbork, Sardinia, Lovell, Cambridge, Mark II, Medicina, Onsala, Ventspils, Noto, Toruń, Metsähovi, Sheshan, Nanshan, Yebes, Wettzell, Robledo de Chavela, Har-

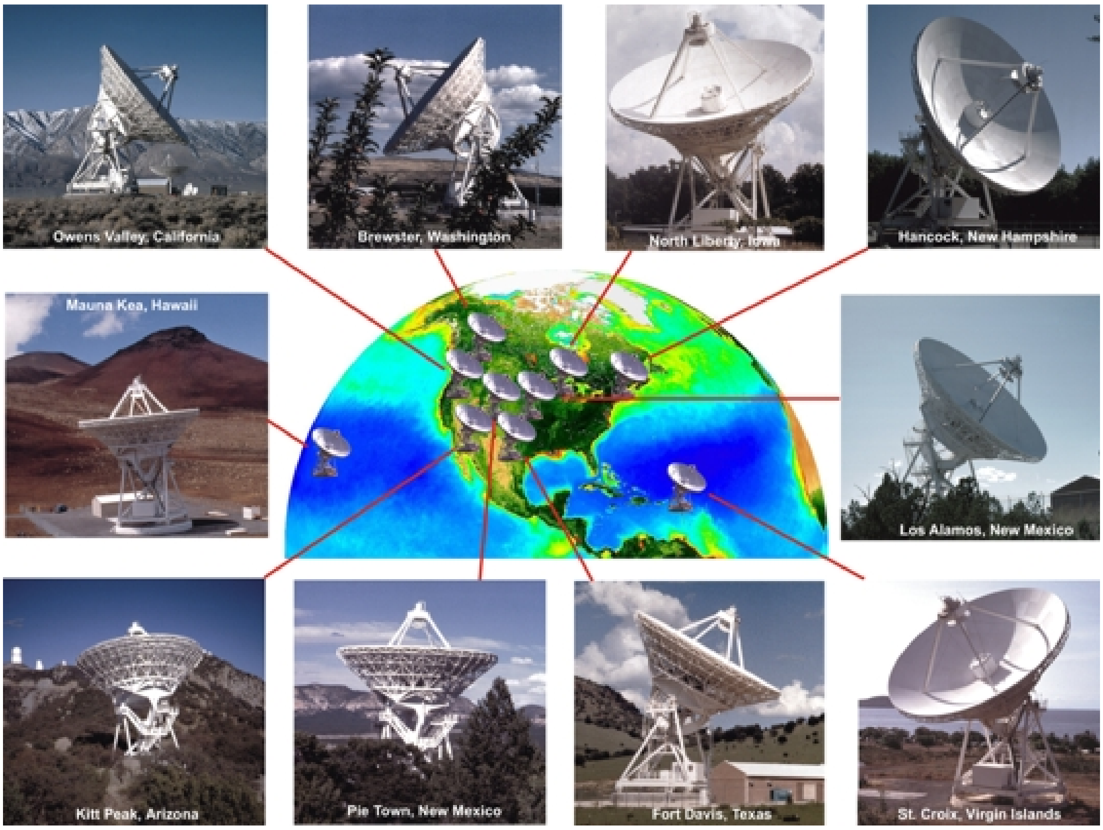

Figure 3.26: Distribution of the radio telescopes being part of the VLBA. Credits: Image courtesy of NRAO/AUI and Earth image courtesy of the SeaWiFS Project NASA/GSFC and ORBIMAGE

tebeesthoek. The operational center is based in the Netherlands, at the Joint Institute for VLBI ERIC.

- The GMVA is a worldwide array that operates at 3 mm. The array is composed by a certain number of fixed antennas plus some that participate depending on the different projects. The antenna involved are: the VLBA (excluding Hancock and St. Croix, which are not equipped with a 3 mm receiver) plus the Green Bank Telescope, Effelsberg, Onsala, Pico Veleta, NOEMA, Metsähovi, Yebes, the Greenland Telescope, the Korean VLBI Network (KVN, which consists of three antennas: Ku, Kt, and Ky), the Large Millimeter Telescope, and ALMA. The correlation is performed at the Max Planck Institute for Radio Astronomy in Bonn, Germany.

Worth mentioning is ALMA, a connected-elements interferometer composed of 66 radio telescopes that operate in the Atacama Desert, in Chile. ALMA can participate in the observations in the so-called "phased" mode, in which the array operates as a single antenna, increasing the sensitivity of the VLBI array by an order of magnitude (Matthews et al. 2018). An instrument that works similarly and has a relevant historical importance is the **Very Large Array** (VLA). Built in the 1970s it has served the community for decades leading to highly important scientific discoveries and that will be in the future upgraded, leading to the birth of the Next Generation VLA.

Remarkable is the **RadioAstron** program, a space-antenna that led to the biggest radio interferometer experiments to date. In July 2011, a 10-m radio telescope was launched in an elliptical orbit that spanned from ~10000 km up to ~338000 km. The experiment was operational until January 2019 and provided radio images with a unique resolution, thanks to the extremely long baseline.

In conclusion, the EHT is currently the most-known array due to the observations of the black hole shadows lying at the center of M 87 (Event Horizon Telescope Collaboration et al. 2019a,b,c,d,e,f) and our own Milky Way (Event Horizon Telescope Collaboration et al. 2022a,b,c,d,e,f). The EHT can perform observations at wavelength of 1 mm, and it is composed of: the Submillimeter Telescope, The Atacama Pathfinder Experiment, IRAM, James Clerk Maxwell Telescope, LMT, Submillimeter Array, ALMA, South Pole Telescope, the Greenland Telescope, NOEMA, and KP. In the near future, more antennas and more frequencies will be available in the Next Generation EHT project.

3.3 The data reduction

In this section, I describe the necessary steps to convert the recorded astronomical signal into radio images used to do science. The data reduction process consists of two main steps: the **calibration step** (Sect. 3.3.1), in which the amplitude and phases of the visibilities are corrected after identifying different sources of errors and the amplitude are converted into physical units, and the **imaging/self-calibration step** (Sect. 3.3.2) in which the astronomical images are produced from the calibrated data.

The logic of the data calibration is to extrapolate and correct for the corruption terms that arise during the measurements due to atmospheric and instrumentation effects together with positional inaccuracies. The desired, real visibilities $\mathcal{V}_{\rm real}$ for two antennas i and j are connected to the observed ones $\mathcal{V}_{\rm obs}$ as

$$\mathcal{V}^{i,j}_{\rm obs}(t) = \mathcal{V}^{i,j}_{\rm real}(t) g^i(t) g^{j*}(t) \; + \epsilon^{i,j}. \tag{3.20}$$

Here, g^i and g^j are complex gains of station i and the conjugate complex gains of station j, respectively, while $\epsilon^{i,j}$ is the thermal noise. The complex gains can be expressed as $g = ae^{i\phi}$, where a is the amplitude and ϕ is the phase. The goal of the calibration process is to calculate the complex gains for each individual station.

Before proceeding with the calibration procedure, the data need to be inspected. The data used in this thesis were calibrated using the program **Astronomical Image Processing System** (AIPS) (Greisen 1990). Before handling the raw data, checking the observer logs from the single antennas that participated in the observations and the correlator team is a good habit. Such documents contain important information on the data quality and whether certain antennas or scans have been flagged or need to be handled carefully during calibration. Once the data are loaded into AIPS, two tasks are used to extract the basic information from them: PRTAN, which provides the list of antennas that participated in the observations, and LISTR, which prints out information on the scans and the frequency setup of the experiment. To inspect the quality of the uncalibrated data, the task POSSM is used since it allows plotting the phases and amplitudes as a function of frequency, also for specific time ranges, baselines, or sources.

3.3.1 The calibration steps

The calibration procedure is mostly divided into two main branches: the **phase calibration** and the **amplitude calibration**. Together with the desired scientific target, when scheduling the observations, it is necessary to plan a sufficient amount of time on sources that will be essential to properly calibrate the data. Crucial in a VLBI experiment is to observe **fringe finder calibrators**: ideally point-like sources bright enough (order of Jansky) to be used for correlation and, often, for the correction of instrumental phases (explained below). Alongside it, the observer must point to **bandpass calibrators**, which are expected to have the same properties as the fringe finder calibrators. In many VLBI experiments, the fringe finder and bandpass calibrators coincide. Moreover, if opacity corrections are required, it is a good habit to observe a bright source often enough to track the evolution of the system temperatures with the elevation.

Finally, when performing phase referencing experiments (which are necessary when the scientific target is too faint for self-calibration in the fringe fitting, see next section for its description), it is necessary to observe **phase reference calibrators.** The calibrators need to be observed frequently and must be as close as possible to the target, in order to transfer the proper information of the atmospheric effects.

- **Phase calibration**

In the phase calibration process, the residual delay and delay rates corrections are computed and later applied to the data for them to be coherently integrated into the frequency and time space. The residual delays arise from the differences between the modeled arrival time of the signals at the different stations and the measured one. Such delays are caused by a combination of instrumental and atmospheric effects. The delay rates describe the time variations of the residuals, i.e., their time derivative.

The phase calibration is performed through the **fringe fitting** technique. The fringe fitting is based on identifying the fringes, i.e., **fringe search**, in the delay-delay rate plane. Historically, the fringe search procedure was baseline-based (Moran 1976). However, this method has the downside that is not able to account for baselines in which there is no detection. In the following years, more refined algorithms have been developed. The global fringe fitting technique developed by Cotton (1995); Diamond (1995), aims at finding the fringes with an antenna-based approach. Its main advantage is its ability to increase the detection of weak sources. In detail, the algorithm computes a first guess of the residuals for each antenna using each respective baseline connected with the reference antenna, chosen by the user. In the following stage, the solutions are refined through the least-squared method using all the remaining baselines. To increase the number of detections, the algorithm can utilize the exhaustive fringe search: if no fringes are found for a particular antenna with respect to the reference antenna, the solutions are searched for using other elements of the array. To increase the chances for detection, the larger, and more sensitive, antennas are preferred choices as reference and for the exhaustive fringe search.

In AIPS, the fringe fitting operation is performed using the task FRING in two different steps. In the first one, the fringe fitting is done using an appropriate single scan on a bright calibrator. Such a scan needs to have a high S/N ratio, especially for the reference antenna chosen, and all the antennas (in each sub-band) must have participated in it. When this is not possible, for example when the array is formed by antennas placed on opposite sides of the globe, this procedure must be performed with more intermediate steps, progressively connecting the various observatories. The reference antenna should be chosen to be as close as possible to the center of the array. The “manual” fringe fitting aims at correcting instrumental phases and delays and its result is the removal of the phase jumps between different frequency sub-bands. The second step consists of the global fringe fitting, in which the entire experiment is considered. The results of the fringe finding technique are shown in Fig. 3.27, in which example observations of BL Lac are shown. In the left panel, the uncalibrated data, as provided by the correlator, are shown, while in the right panel, the data have undergone the entire calibration process. In the right panel, after the phase calibration, the phases (upper plots) mostly follow a straight line with a weak dispersion having been corrected for the residual delays and rates.

- **Amplitude calibration**

In the amplitude calibration process, the final result is the conversion from arbitrary correlator units to Jansky. At frequencies above 15 GHz, an opacity correction also needs to be performed. In this step, the crucial quantity is the **System Equivalent Flux Density** (SEFD) that is connected to the system temperature T_{sys} via the antenna gain introduced in Sect. 3.2.1:

$$\mathrm{SEFD} = \frac{2kT_{\mathrm{sys}}}{\mathrm{A_{eff}}} \, . \tag{3.21}$$

The conversion factor in Jansky for a correlated signal between two antennas i and j is:

$$S^{i,j} = \zeta\xi \frac{\sqrt{\mathrm{SEFD}^i \mathrm{SEFD}^j}}{2\Delta\nu\Delta\tau} \, \mathrm{Jy} \tag{3.22}$$

in which ζ is a multiplication factor and ξ quantifies the data loss during the digital sampling. The amplitude calibration is performed with the task APCAL. The task converts the T_{sys} values recorded for each antenna into Jansky, by dividing for the antenna gains which are described by the gain curves. At a given frequency, the gain curve describes the variation of the effective area A_{eff} as a function of elevation.

At high frequencies, the atmosphere can strongly attenuate the signal. The attenuation is regulated by the factor $e^{-\tau_{\mathrm{atm}}}$, in which τ_{atm} is the atmospheric opacity. The latter is a function of the source elevation since it is proportional to the zenith opacity and the airmass, which is a function of the zenith angle. The opacity corrections can be taken into account while performing the amplitude calibration with APCAL.

Naturally, to perform the amplitude calibration, information on the antenna temperature, gain curves, and weather (when the opacity corrections are applied), are necessary. These information are stored in AIPS when uploading the data in the tables TY, GC, and WX, respectively. However, this may not be the case for some arrays, e.g., the GMVA. In such a situation, one needs to collect the required information and load them into AIPS. On one hand, to upload the antenna temperature and gain curves information, the task ANTAB is used which generates/uploads the needed TY and GC tables. On the other hand, the weather information can be stored in a text file loaded in AIPS when performing the amplitude calibration with APCAL.

Operatively, the calibration in AIPS is done by following some additional steps. At first, on the uncalibrated data the tasks TECOR and CLCOR are applied. The first is a phase calibration that applies corrections for the ionospheric delays and is relevant at low frequencies ($\lesssim 8\,\mathrm{GHz}$). The latter applies the parallactic angle corrections. At a later stage, it is advisable to perform a

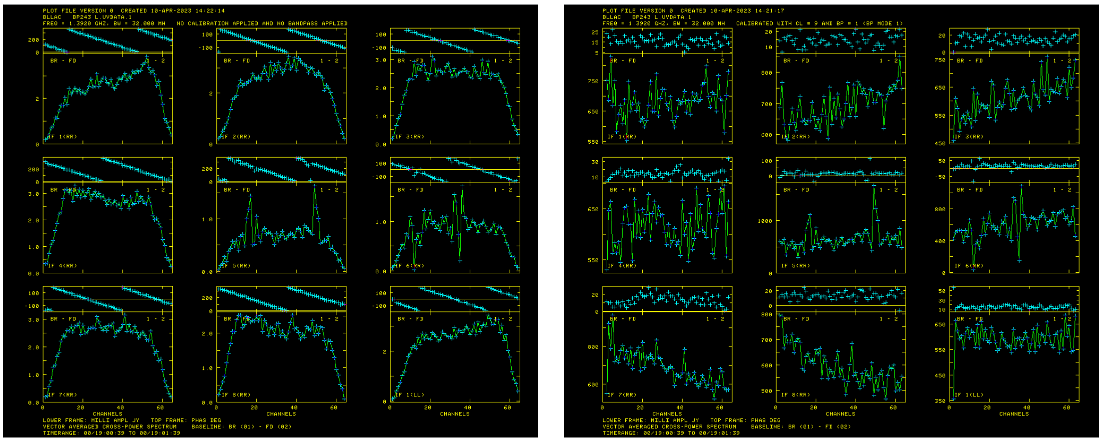

Figure 3.27: Phase and amplitude plots for a BL Lac data set at 1 GHz as seen in AIPS. Left panel: uncalibrated data. Right panel: calibrated data.

bandpass calibration through the task BPASS, which corrects the amplitudes for the errors introduced by the instrument response of the electronic system across each sub-band. The most relevant effect of such a response can be seen in the most outer channels within each sub-band, in which the signal is typically strongly attenuated (see Fig. 3.27, left panel). After the bandpass and amplitude calibration, the amplitudes of the calibrated data (Fig. 3.27, right panel) are now relatively constant within each sub-band and are expressed in units of Jansky.

3.3.2 The imaging and self-calibration step

The imaging process is the final step of the path that leads the emitted radiation from a certain source to be converted into a radio image. Throughout the thesis, the imaging process has been performed using the software **difmap** (Shepherd et al. 1994). The fundamental idea behind the imaging process is to apply an Inverse Fourier transform to the visibilities and represent them in the image plane. Due to the sparse uv-coverage (see Fig. 3.25), in the imaging process it is necessary to use algorithms aimed at interpolating the information contained in the empty regions. This further underlines how crucial is to have a uv-plane as filled as possible.

The imaging software transforms the visibilities through a Fast Fourier Transform algorithm after the data have been regularly spaced in a grid. Through this process a **dirty image** is produced, i.e., an image convolved with the **dirty beam**. The latter, defining the response of the interferometer, is the Fourier transform of the uv-plane. To recover the real sky brightness distribution it is necessary to run de-convolution cycles using algorithms aimed at subtracting the contamination from the dirty beam. The most-known and widely used algorithm for the imaging of VLBI data is **CLEAN** (Högbom 1974). Through several de-convolution cycles, CLEAN subtracts the map emission peak convolved with the dirty beam and adds **clean delta components**; it then displays a new residual image in which the fainter emission is visible, being the previous peak subtracted. Fig. 3.28 left panel shows the dirty image of 1 GHz observations of NGC 315. To aid the algorithm in properly modeling the source and not the spurious emission, it is advisable in the dirty image to delimit through windows the regions in which emission is observed. An example of this process is shown in Fig. 3.28. Here, the peak seen in the left panel is windowed (the clean window is visible in the right panel) and, after a cleaning cycle, the weaker emission in the residual image becomes visible, as seen in the right panel. CLEAN is an iterative process that repeats until all the emission has been modeled with clean components, generating a **clean model**. To produce the final clean image, the clean model is convolved with the clean beam, whose full-width half maximum (FWHM) is obtained from fitting the main lobe of the dirty beam.

Deeply intersected with the imaging process is self-calibration. During the self-calibration, the algorithm uses at each step the model of the visibilities to improve them. The main requirement for self-calibration is to have a sufficient S/N of the observed target. Performing such a step is crucial to highly enhance the quality of the map. Indeed, due to the sparse uv-coverage, when Inverse Fourier transforming the visibilities, the errors on the amplitudes and phases from each element of the interferometer are sparse across the image plane.

The self-calibration reduces this effect, thanks to the use of the **closure relations** (Wilkinson 1989). When enough antennas participate in the observations (three for the phases and four for the amplitudes), the closure relations allow us to get rid of the antenna-based errors. Concerning the phases, by considering the set of antenna gains from three antennas (i, j, k), the equations between each pair of antennas follow:

$$\phi_{i,j} = \Phi_{i,j} + C_i - C_j \,, \tag{3.23}$$

$$\phi_{j,k} = \Phi_{j,k} + C_j - C_k \,, \tag{3.24}$$

$$\phi_{k,i} = \Phi_{k,i} + C_k - C_i \,. \tag{3.25}$$

Here, ϕ are the observed visibility phases, and Φ are the real phases without the corruption terms C. The phase closure relation is obtained by linearly adding the three terms:

$$\phi_{i,j,k} = \phi_{i,j} + \phi_{j,k} + \phi_{k,i} \,. \tag{3.26}$$

Consequently, $\phi_{i,j,k}$ is independent from phase shifts at each individual station. By calculating all the closure relations with respect to an antenna chosen as reference, for which the phase offset is considered to be null, the number of phase

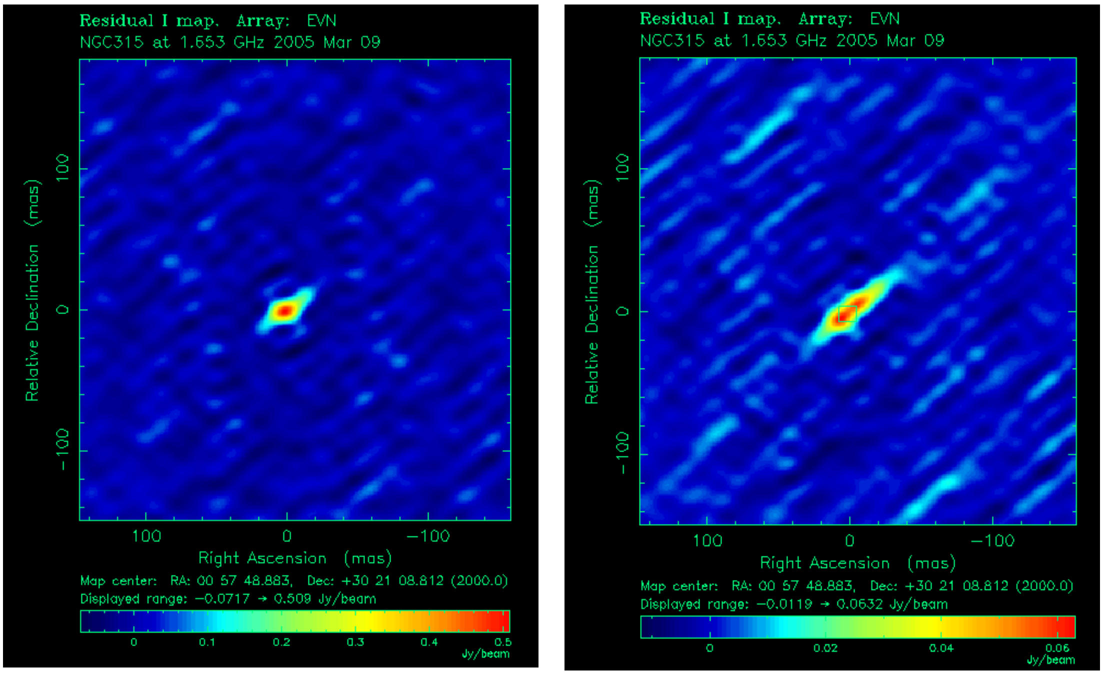

Figure 3.28: Residual image of NGC 315 from observations at 1 GHz. Left panel: dirty image obtained by Inverse Fourier Transform of the calibrated visibilities. Right panel: residual image after the subtraction of the first peak. The first clean window is visible in the center.

closure relations is the number of antennas minus one. The closure relation for the amplitudes is slightly different due to the multiplicative nature of the corruption amplitudes. In this case, the set of equations considering four stations, in which A are the observed visibility amplitudes, a are the real amplitudes, and C the corruption terms, is

$$A_{i,j} = a_{i,j} \times C_i C_j \,, \tag{3.27}$$

$$A_{j,k} = a_{j,k} \times C_j C_k \,, \tag{3.28}$$

$$A_{k,w} = a_{k,w} \times C_k C_w \,, \tag{3.29}$$

$$A_{w,i} = a_{w,i} \times C_w C_i \,, \tag{3.30}$$

and the amplitude closure relation is

$$A_{i,j,k,w} = \frac{a_{i,j} a_{k,w}}{a_{i,k} a_{j,w}} \,. \tag{3.31}$$

As the number of closure relations increases, i.e., it increases the number of antennas in the array, the self-calibration procedure leads to progressively better results. Operationally, using the current model for the visibilities at each step, the algorithm computes the corruption terms for each antenna by using a least square minimization algorithm that must be consistent with the closure quantities.

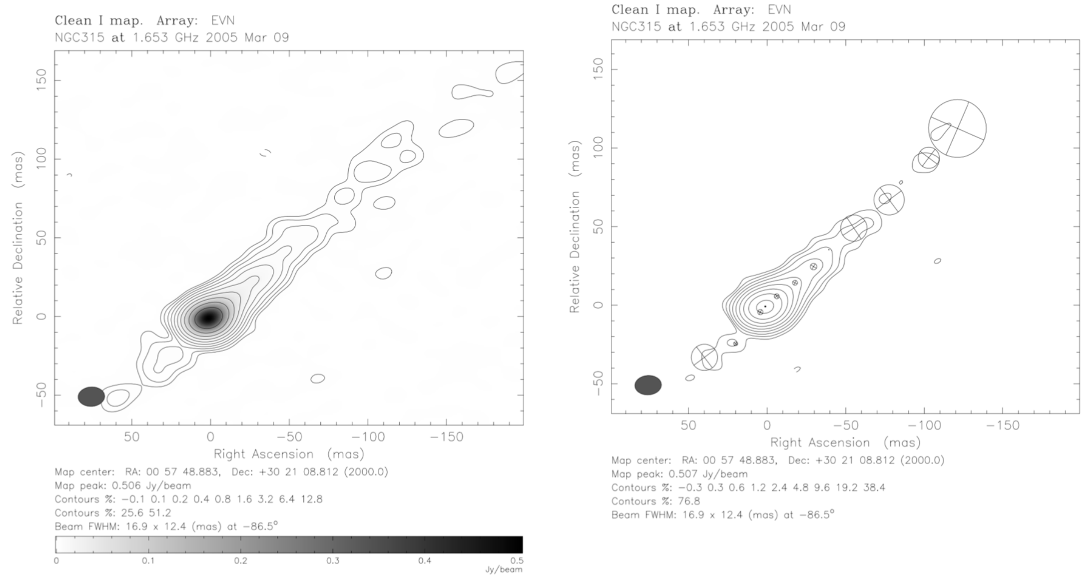

Figure 3.29: Observations of NGC 315 at 1 GHz performed the 09-03-2005 with the EVN array. Left panel: map produced using CLEAN. Right panel: map reconstructed by modeling the visibilities using Gaussian components.

In the imaging process, after the new clean windows have been established for each de-convolution cycle, a number of cleaning steps are run together with the same number of phase self-calibration runs. Instead, amplitude self-calibration is performed when the visibilities are properly modeled. This step is performed several times during the imaging process with progressively smaller solution intervals.

3.3.3 AGN seen with VLBI and modelfitting

The final products of the data reduction process are radio maps ready to be used to perform science. An example of how a VLBI image of an AGN looks is given in Fig. 3.29, in which I show a 1 GHz observation of NGC 315. In the image, it is possible to recognize the brightest spot associated with the VLBI core emission (described in Sect. 1.3.2) and the two-sided jet. The jet pointing towards the northeast, the most elongated one, is proceeding toward us, so its flux density is enhanced due to the relativistic Doppler effect. The other side of the outflow, i.e., the counter-jet, is receding with respect to our position, and its flux density is reduced due to the de-boosting effect.

A further way to reconstruct the radio emission in the image plane is by modeling the self-calibrated visibilities with discrete Gaussian components. This analysis is typically performed in difmap through the task **modelfit**. To fit the visibilities, the task performs Levenberg-Marquardt non-linear least squared minimization on self-calibrated data. Fig. 3.29 right panel shows the same image but reconstructed with the Gaussian components.

While the quality of the final image produced with this method is lower with respect to the clean image, since it is an even more simplified modeling of a continuum emission, the modelfit analysis is helpful for different reasons, among them: i) model, identify and explore the physical properties of steady shock components or newly emitted blob of plasma; ii) compute the brightness temperature of the core and jet components, to have insights on the physical properties of the emitting plasma; iii) compute the core-shift between pair of frequencies (see Sect. 1.3.2).

4 Exploring the disk-jet connection in NGC 315

This paper is the first in the series of works exploring the sub-parsec and parsec scale properties of the jet in NGC 315. In this first chapter, we[8] address the topic of the disk-jet connection, discussed in Sect. 2.2.1. In detail, we aim at exploring whether the properties of the acceleration and collimation region are consistent with the expectations for a jet launched by an accretion disk that has reached the MAD state. To do that, we consider the multi-frequency and multi-epoch VLBI data set published by Boccardi et al. (2021). The final images are studied employing a pixel-based analysis that allows extrapolating information on the spectral index, the jet opening angle, and the jet bulk speed. The latter parameter is estimated based on the jet to counter-jet ratio (Sect. 1.3.2) calculated at varying distances from the jet apex.

We suggest the bulk of the acceleration to occur on sub-parsec scales, with the jet accelerating from $\beta \sim 0.05$ to $\beta \sim 0.9$ within one parsec. Noticeably, the acceleration scale coincides with the extent of the parabolic region proposed by Boccardi et al. (2021). From the co-spatiality of the two phenomena, we propose that the bulk of the jet acceleration is magnetically-driven, i.e., the magnetic energy is converted into kinetic energy of the flow.

Under the assumption of a jet in which the equipartition state (between the magnetic and kinetic energies) is reached at the end of the parabolic expansion, the properties of the acceleration and collimation region can be linked via theoretical models to the nature of the accretion disk. In detail, we extrapolate the spin of the central black hole and the magnetization of the accretion disk, as well as the magnetization of the jet from its base down to parsec scales. The magnetic field strength is estimated based on the measured core shift by using a novel approach that considers for the first time the parabolic jet shape, as opposed to the standard methods assuming a conical geometry. Altogether, our observational results suggest that the accretion disk in NGC 315 has reached a MAD state.

In this paper, I performed the totality of the analysis of the radio images through the development of the Python code described in Sect. 2 in the paper. The calibrated and imaged data were provided by B. Boccardi, who supported me in writing the text. E. Nokhrina highly contributed to the development of the mathematical models used in Sections 4.3 and 4.4. Moreover, she contributed to the writing of the same sections alongside Appendix A. The rest of the co-authors contributed to enriching the discussion.

The papers accepted in A&A after April 2022 are published under a CC-BY

---

[8] When describing the work on the different papers and manuscripts, I will use “we” instead of “I” to acknowledge the contribution of the co-authors.

4.0 license. Therefore, the first author retains the copyright and no permission is needed to reproduce the material.

A&A 664, A166 (2022)
https://doi.org/10.1051/0004-6361/202243958

Astronomy & Astrophysics

Exploring the disk-jet connection in NGC 315

L. Ricci[1], B. Boccardi[1], E. Nokhrina[2], M. Perucho[3,4], N. MacDonald[1], G. Mattia[5], P. Grandi[6], E. Madika[1],
T. P. Krichbaum[1], and J. A. Zensus[1]

[1] Max-Planck-Institut für Radioastronomie, Auf dem Hügel 69, 53121 Bonn, Germany
e-mail: `lricci@mpifr-bonn.mpg.de`
[2] Moscow Institute of Physics and Technology, Dolgoprudny, Institutsky per., 9, Moscow region 141700, Russia
[3] Departament d'Astronomia i Astrofísica, Universitat de València, C/ Dr. Moliner, 50, 46100 Burjassot, València, Spain
[4] Observatori Astronómic, Universitat de València, C/ Catedrátic José Beltrán 2, 46980 Paterna, València, Spain
[5] Max Planck Institute für Astronomie, Kßnigstuhl 17, 69117 Heidelberg, Germany
[6] INAF – Osservatorio di Astrofisica e Scienza dello Spazio di Bologna, Via Gobetti 101, 40129 Bologna, Italy

Received 5 May 2022 / Accepted 22 June 2022

ABSTRACT

Aims. Hot accretion flows are thought to be able to power the relativistic jets observed in active galactic nuclei. They can be presented as standard and normal evolution (SANE) disks or magnetically arrested disks (MAD) – two states that imply profound differences in the physical properties of the disks themselves and the outflows they produce.

Methods. We used a multifrequency and multiepoch data set to study the giant radio galaxy NGC 315, with the goal of exploring the properties of its accretion disk and sub-parsec jet. We analyzed the source maps with a pixel-based analysis and we used theoretical models to link the observational properties of the jet to the physical state of the accretion disk.

Results. We propose that the bulk flow in NGC 315 accelerates on sub-pc scales, concurrently with the parabolic expansion. We show that this fast acceleration can be theoretically reconciled with a magnetically driven acceleration. Along the acceleration and collimation zone, we observe an unexpected spectral behavior, with very steep spectral index values $\alpha \sim -1.5$ ($S_\nu \propto \nu^\alpha$) between 22 GHz and 43 GHz. Based on the properties of this region, we predict the black hole of NGC 315 to be rotating fast and the magnetic flux threading the accretion disk to be in excellent agreement with that expected in the case of a MAD. Using a new formalism based on the core shift effect, we modeled the magnetic field downstream a quasi-parabolic accelerating jet and we reconstructed it up to the event horizon radius. In the MAD scenario, we compared it with the expected magnetic saturation strengths in the disk, finding a good agreement.

Key words. galaxies: active – galaxies: jets – instrumentation: high angular resolution – galaxies: individual: NGC 315

1. Introduction

The disk-jet connection is one of the most compelling and studied topics concerning the physics of active galactic nuclei (AGN), with the efforts of the community being focused on unveiling the nature of the accretion disks that are capable of launching different categories of jets. Hot accretion flows are able to produce the powerful relativistic jets we observe in AGN. They may present themselves in two different flavors, namely as standard and normal evolution (SANE, Narayan et al. 2012) disks or magnetically arrested disks (MAD, Bisnovatyi-Kogan & Ruzmaikin 1974, 1976; Narayan et al. 2003). In the first case, the magnetic field is not dynamically important and it only generates effective viscosity, facilitating accretion through the outward transport of the angular momentum. In the MAD scenario, in contrast, the disk is naturally permeated by strong magnetic fields which are carried by the inflowing matter. This leads the magnetic field to gradually accumulate in the vicinity of the central black hole. Once a certain threshold is reached, the magnetic field becomes dynamically important and its strength is high enough to balance the gravitational force of the accreting gas, blocking its inflow and creating a magnetosphere. In the magnetosphere, the torque exerted by the rotation of the central black hole alters the magnetic field lines, which bend toward the directions perpendicular to the disk plane. Since the gas within the accretion disk is in a plasma state, the charged particles are forced to follow the magnetic field lines and the jets are launched (Blandford & Znajek 1977). The two disk states differ in terms of their magnetic field distribution and strength, both in the disk and in the resultant jets.

The most direct way to distinguish between the SANE and MAD state is by observing the polarization and Faraday rotation of the central core and the inner jet region (Yuan et al. 2022, and references therein). When the polarization is not seen or is very weak, which is the case for most radio galaxies, we need to rely on alternative methods based on the indirect estimation of the magnetic activity in the disk. This is possible since the physical properties of the accretion disk are closely related to some observational properties of the jets on very long baseline interferometry (VLBI) scales, such as the extent of the collimation and acceleration region. In particular, the jets are initially dominated by the magnetic energy extracted from the accretion disk and propagate as a pure Poynting flux. While expanding within the external medium, they collimate, showing a parabolic shape on scales of $10^3-10^7\,R_S$[1] (Kovalev et al. 2020; Boccardi et al. 2021), and accelerate up to relativistic velocities. The acceleration and collimation processes are expected to be cospatial in the case of a magnetically driven cold outflow

---

[1] R_S is the Schwarzschild radius defined as $R_S = 2GM_{BH}/c^2$ where M_{BH} is the mass of the black hole.

(Komissarov et al. 2007; Tchekhovskoy et al. 2008; Lyubarsky 2009). The jets are accelerated mainly through the conversion of the initial magnetic energy into kinetic energy of the bulk flow and radiation and this process is believed to continue until equipartition between the particle energy and the magnetic field is reached (Komissarov et al. 2009). Therefore, by examining the properties of the acceleration and collimation in a jet, it is possible to reconstruct, by means of theoretical models, the magnetic field that permeates the accretion disk and to explore the physical state of the disk itself.

The properties of such magnetic fields are highly debated. Estimates based on the assumption of a conical jet in equipartition (Lobanov 1998; Hirotani 2005) result in magnetic field strengths of hundreds of mG at 1 pc from the core (e.g., O'Sullivan & Gabuzda 2009), which implies strengths of $\sim 10^3 - 10^4$ G in the surroundings of the black hole, assuming a toroidal-dominated magnetic field evolution ($B \propto \mathtt{z}^{-1}$, where $\mathtt{z}$ denotes the distance from the black hole along the jet). However, rotation measure studies have provided evidence of helical fields along the acceleration region (Hovatta 2017, and references therein), suggesting that the poloidal field component ($B \propto \mathtt{z}^{-2}$ in a conical jet) cannot be neglected when extrapolating the magnetic field strength. The steeper evolution implies higher field strengths in the core region. Magnetic fields stronger than $\sim 10^4$ G are not sustainable by black holes and may point to the existence of exotic objects in the core of the galaxies, such as gravastars or wormholes (Lobanov 2017).

In this paper, we explore the nearby ($z = 0.0165$, Trager et al. 2000) giant radio galaxy NGC 315 through VLBI observations. NGC 315 extends in total up to ∼1 Mpc and shows a Fanaroff–Riley (Fanaroff & Riley 1974) I morphology (e.g., Laing et al. 2006). In NGC 315, the acceleration and collimation region is observed on VLBI scales (Boccardi et al. 2021; Park et al. 2021), making it a perfect target to investigate the disk-jet connection.

This paper is organized as follows. In Sect. 2, we describe the data set and the methods used for the analysis. In Sect. 3, we present our observational results. In Sect. 4, we apply different theoretical models to interpret our results and in Sect. 5, we present our conclusions.

We assume a ΛCDM cosmology with $H_0 = 71$ h km^{-1} Mpc^{-1}, $\Omega_M = 0.27$, $\Omega_\Lambda = 0.73$ (Komatsu et al. 2009). At the redshift of NGC 315, the luminosity distance is $D_L = 70.6$ Mpc and 1 mas corresponds to 0.331 pc.

2. Data set and image analysis

In this article, we consider the multifrequency and multiepoch VLBI data set presented by Boccardi et al. (2021, hereafter B21), which consists of eighteen observations in the frequency range between 1 GHz–86 GHz. In particular, since we are interested in utilising the symmetry properties of the approaching and receding jets to derive fundamental jet parameters, we focus on those epochs where both the jet and the counter-jet have been detected. The main properties of the maps are summarized in Table 1. Together with the B21 observations, we analyzed one image from 2019 at 15 GHz from the MOJAVE program (Lister et al. 2018), where a small counter-jet has been detected. The images used in our analysis are shown in Appendix C. In addition, we analyzed stacked images at 5 GHz and 15 GHz. The 5 GHz stacked image was created by considering four different observations in the period 1994–1996 (see Table 1, B21), while the 15 GHz stacked image was obtained from the MOJAVE archive, and was previously analyzed by Pushkarev et al. (2017), Kovalev et al. (2020). The 5 GHz stacked image with the overlaid jet ridgeline is shown in Fig. 1.

Table 1. Characteristics of the CLEAN maps considered in this article.

Freq. [GHz]	Date	Beam [mas × mas, deg]	Array
1.6	2005-03-09	16.90 × 12.40, −87	EVN
5.0	1994-11-15	2.48 × 1.29, −5	VLBA
5.0	1995-10-28	2.21 × 1.34, −3	VLBA
5.0	1996-05-10	3.65 × 2.56, −18	VLBA$^{(*)}$, Y
5.0	1996-10-07	2.31 × 1.35, −5	VLBA, Y
15.4	2019-08-23	0.82 × 0.42, −5	VLBA
22.3	2007-12-02	0.94 × 0.25, −22	VLBA$^{(**)}$, Y, GB, EF
22.3	2018-11-24	0.59 × 0.27, −11	VLBA, Y, EF
43.2	2008-02-03	0.27 × 0.14, −20	VLBA$^{(*)}$, Y, GB, EF
43.2	2018-11-24	0.30 × 0.16, −13	VLBA, Y, EF

Notes. Column (1): Frequency; Col. (2): Date of observation; Col. (3): Beam FWHM and position angle; Col. (4): Array: VLBA – Very Long Baseline Array: $^{(*)}$no data from Mauna Kea, $^{(**)}$no data from Saint Croix; Y – Very Large Array; EVN – European VLBI network; EF – Effelsberg; GB – Green Bank.

In our analysis, we assume that the approaching jet is oriented at an angle $\theta = 38°$ with respect to the line of sight, following the results of the 5 GHz Very Large Array (VLA) study presented by Canvin et al. (2005), and within the range of 30°–40° derived by Giovannini et al. (2001), based on VLBI data. While noticing that a larger angle of the order of 50° has been derived in the works of Laing & Bridle (2014) and Park et al. (2021), we provide a further constraint (detailed in Sect. 3.2) in support of our selection of $\theta = 38°$.

With respect to B21, a more recent estimate of the black hole mass in NGC 315 is assumed in this work. Through CO observations performed with the Atacama Large Millimeter/submillimeter Array (ALMA), the black hole mass was estimated to be $M_{\rm BH} = (2.08 \pm 0.01)^{+0.32}_{-0.14} \times 10^9 M_\odot$ (Boizelle et al. 2021). Under this assumption, and for $\theta = 38°$, one projected milliarcsecond correponds to 2701 $R_{\rm S}$ de-projected.

The opacity shifts necessary to properly align maps at different frequencies are assumed from B21 (Table 4), who performed 2D cross-correlation analyzes between different pairs of frequencies. All distances are expressed with respect to the 43 GHz core, assumed to coincide with the actual position of the black hole. This assumption is supported by previous observational results, showing that the mm-core in radio galaxies lies very close ($<100\, R_{\rm S}$) to the true position of the central black hole (e.g., Hada et al. 2011; Baczko et al. 2022).

We analyzed the CLEAN maps through a pixel-based analysis using a Python code. This requires, as input, maps aligned along the y axis restored with a circular beam. It divides both the jet and the counter-jet in one-pixel width slices oriented perpendicularly to the jet direction. The intensity profiles in the slices are subsequently fitted with a single 1D Gaussian profile by means of the Levenberg-Marquardt algorithm (`LevMarLSQFitter` in `Astropy`). Pixels with value lower than $3\sigma_{\rm rms}$ are discarded, to avoid the contamination from the background noise at the edges of the jet. The code stops its iteration when the most luminous pixel in the slice has a brightness lower than $10\sigma_{\rm rms}$. Finally, the fitted Gaussian profiles are integrated to obtain the flux density in each slice. The integrated fluxes, together with the full width at half maximum (FWHM) of the Gaussian profiles, are stored and used to compute the jet to

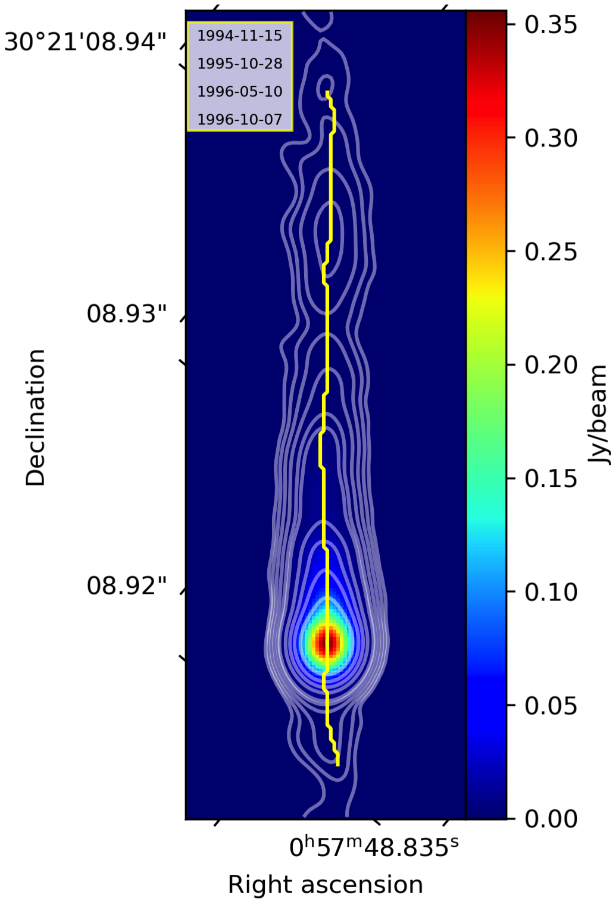

Fig. 1. 5 GHz stacked VLBI image obtained using the four observations reported in figure. The contour levels are set at [0.001, 0.002, 0.004, 0.008, 0.012, 0.034, 0.068, 0.126, 0.254] × the peak brightness of 0.356 Jy/beam. The jet ridgeline is highlighted by the yellow line, and is found to be remarkably straight.

counter-jet ratio (Sect. 3.2) and the jet opening angle as a function of distance from the core (Sect. 3.3). We point out that in our analysis, we discard the pixels within a beam size region centered in the image core due to the inability to distinguish between nuclear and jet emission.

3. Results

3.1. Spectral index

We used our 22 GHz and 43 GHz images to investigate the spectral index ($S_\nu \propto \nu^\alpha$) from sub-parsec to parsec scales. We considered our simultaneous observations from 2018, as well as the 2007–2008 observations (see Table 1), which are separated by 63 days. In the latter case the analysis is aimed at a consistency check for the 2018 data set, taking into account that in a low-power radio galaxy such as NGC 315, we would not expect strong variability over such a relatively short period. Indeed, in radio galaxies, the flux variability is softened by a reduced relativistic beaming due to the large viewing angles. Moreover, even small flux density variations statistically occur on timescales of one to two years (Hovatta et al. 2007). The paired maps were produced by limiting the uv-range to the same interval and were convolved with the same equivalent circular beam. Moreover, the core shift between the two frequencies was applied as explained in Sect. 2. The uncertainties are computed by propagating the errors on the flux calibration, set to 5% for the 22 GHz map and to 10% for the 43 GHz map, together with the rms noise (for the image noise values, we refer to B21, Table 1). Pixels with value lower than $10\sigma_{\rm rms}$ were masked.

In the case of the 2018 data set, the analysis was performed twice, first by considering the maps obtaining using the full HSA array and the second after reproducing the images using only the VLBA. This second approach was aimed at minimizing the uncertainties possibly introduced in the amplitude calibration by the two non-VLBA antennas (Effelsberg and the phased-VLA). We obtained comparable results in the two cases, with slightly steeper values determined when the full array was considered. In Fig. 2 (left panel), we show the spectral map from the 2018 VLBA data. The contours describe the 43 GHz continuum emission. The core structure is marked by the red patch which identifies the optically thick region, with inverted spectral index values up to $\alpha \sim 0.7$. The average spectral index evolution along one-pixel slices is presented in Fig. 2 (right panel) for both epochs, showing a remarkable agreement. In the optically thin region the spectral index drops down to steep values of $\sim\!-1.5$ using the VLBA-only data. Slightly steeper values down to $\alpha \sim -1.75$ are observed using the full-HSA data as well as based on the 2007–2008 epochs. The steep index region extends up to ~1 pc, a distance comparable to the extent of the jet parabolic region proposed by B21. Beyond this region, the spectrum become flatter and reaches typical values of $\alpha \sim -0.75$. Synchrotron losses reflecting the presence of strong magnetic fields may explain the steep spectrum we observe upstream of the shape transition distance. We note that, in general, the spectral properties in the jet acceleration and collimation region are unknown, as they have not yet been investigated in observational studies. A detailed analysis considering a broader multifrequency data set will be necessary in the case of NGC 315, as well as of other sources that can be examined on similar scales.

3.2. Jet speed profile

We constrain the intrinsic jet speed by considering the jet to counter-jet intensity ratio, R. Under the assumption of intrinsic symmetry the jet and counter-jet, the observed flux density differences are only due to the Doppler boosting of the incoming jet and de-boosting of the receding one. We compute the flux density ratio between slices which are equidistant with respect to the 43 GHz core position. The intrinsic jet speed β may be expressed as:

$$\beta = \frac{1}{\cos(\theta)} \frac{R^{1/p} - 1}{R^{1/p} + 1}, \tag{1}$$

where $p = (2 - \alpha)$ and α is the spectral index (Urry & Padovani 1995). To compute Eq. (1), we assume, in the case of the 22 GHz and 43 GHz data, the spectral index values (in Sect. 3.1) for the VLBA-only maps, while at the lower frequencies we adopt average values following the results of Park et al. (2021). Namely, we set $\alpha = -0.80 \pm 0.20$ for the 5 and 15 GHz data and $\alpha = -0.60 \pm 0.30$ for the 1 GHz data. The assumption of an average value for the index does not affect our conclusions due to the small oscillations of the spectral index around the assumed values.

The uncertainties on β are computed by propagating the error on the spectral index and the error on the intensity ratio. The uncertainties on the intensity are computed taking into account both systematic errors and uncertainties associated with the method. The systematic errors, including errors on the calibration and imaging of the data, are assumed to introduce a fixed

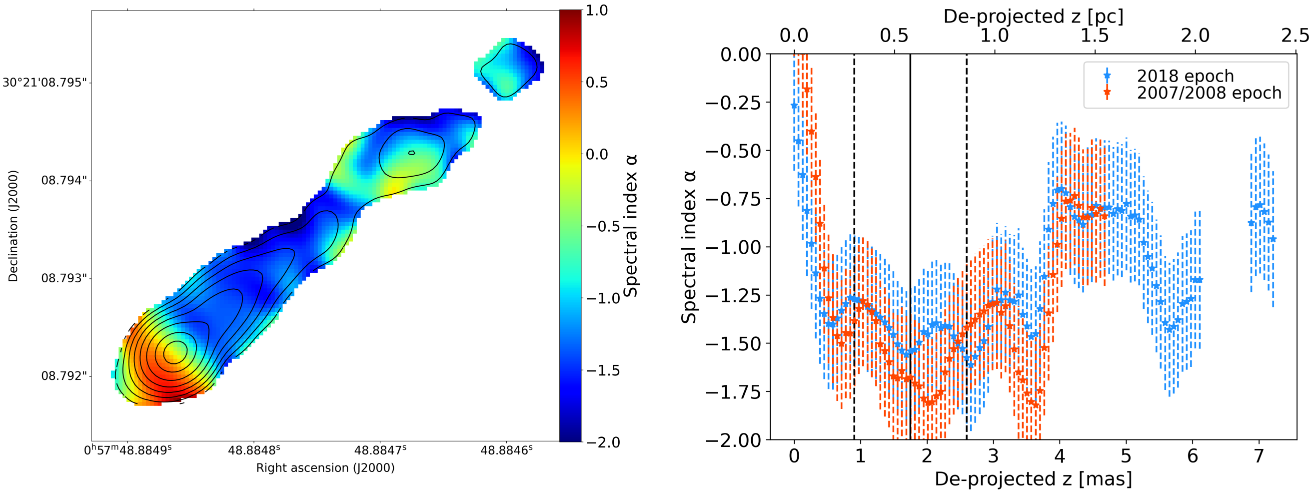

Fig. 2. Spectral index analysis between the frequencies 22 GHz and 43 GHz. *Left panel*: spectral index map, the contours outline the 43 GHz continuum emission. *Right panel*: average spectral index along one-pixel slices as a function of distance from the core for two different epochs. The two profiles are in agreement within the errors. The black vertical lines demarcate the jet shape transition distance with its uncertainty. Within the collimation region, the spectral index rapidly decreases down to values of $\alpha \sim -1.5$, while it rises to typical values of $\alpha \sim -0.75$ beyond the shape transition distance.

error on the final intrinsic ratio equal to 10% of its value. The uncertainties associated with the slicing method are predominantly related to the position angle of each slice and to quantify them, we vary the position angle within the range of ±3°, with an interval of 1°. Then we compute the standard deviation in each slice for each angle and sum them in quadrature. Pushkarev et al. (2017) used a similar method spanning a range of ±15°, but since the direction of NGC 315 is well-defined (as seen from the ridgeline in Fig. 1), we span an interval of 6° in total, as with a shift of 3° the jet is clearly misaligned. The β profile for each analyzed map is shown in Fig. 3. The lack of data points around 1 and 4 pc results from the inner pixels discarded in the 1 GHz and 5 GHz maps, following the procedure detailed in Sect. 2.

We observe a very fast accelerating jet on sub-parsec scales, where terminal intrinsic velocities of $\beta \sim 0.9$ are reached already around ~0.6 pc. Such fast acceleration is inferred in all the maps that sample the parabolic region and is discussed in Sect. 4.3. The acceleration observed in the 22 GHz–43 GHz maps from 2018 is steeper than the one observed at the same frequencies in 2007–2008. This may indicate that the gradient is time-variable, due to variable physical conditions at the jet base. Moreover, we notice how the 22 GHz – 2007 map is slightly misaligned with respect to the 43 GHz – 2008 map. This is not surprising, since the parsec-scale core location can vary with time, even drastically during flares, due to the varying opacity at the jet base (Plavin et al. 2019).

On the scales sampled by the multiepoch observations at 5 GHz, we observed no acceleration, but, instead, a small deceleration between one and two parsecs. The velocity inferred from four different epochs at 5 GHz varies between $\beta \sim 0.8$–0.95. The 1 GHz data indicate a deceleration on scales of ~10 pc, down to $\beta \sim 0.4$, and a similar behavior has been reported for the 1 GHz data points by Park et al. (2021). However, it is unclear whether we are observing a true deceleration of the bulk flow. Indeed, intrinsic velocities of ~0.9c are measured on kiloparsec scales as well, suggesting that the terminal speed reached by the jet on sub-parsec scales is maintained up to large distances, with the deceleration actually found to occur at distances between 8 and 18 kpc, where the speed decreases to $\beta \sim 0.4$ (Canvin et al. 2005; Laing et al. 2006). One possibility for reconciling these results is that the VLBI jet is not uniform but stratified. The 1 GHz emission may be produced in a wider sheath at the jet edges, where the bulk speed might be lower, while the higher frequency emission may be produced by more compact regions closer to the jet axis. This interpretation may be supported by the observation of a frequency-dependent opening angle, which we discuss in the next section.

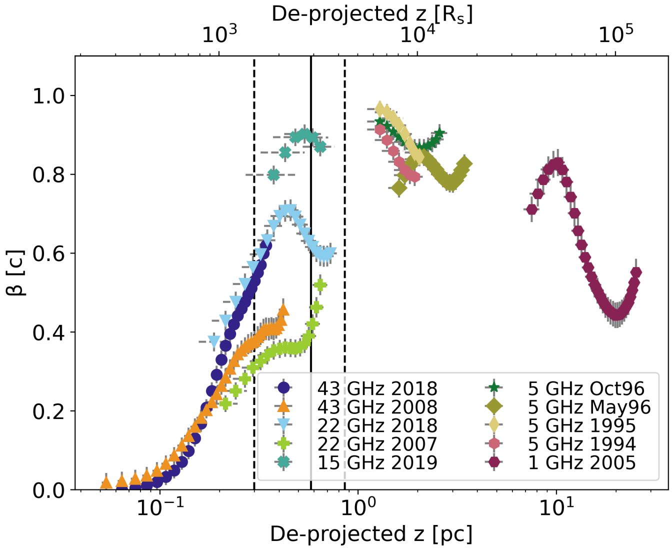

Fig. 3. Jet intrinsic speed profile based on the analysis of the jet to counter-jet intensity ratio. The solid black vertical line indicates the transition distance of $z = 0.58 \pm 0.28$ pc (accordingly to B21) with the uncertainties enclosed by the dashed black lines. The bulk of the jet accelerates on sub-parsec scales, concurrently with the parabolic jet expansion. The highest velocity of $\beta = 0.95 \pm 0.03$ is reached around 1 pc.

The jet break distance, that is where the transition from parabolic to conical profile occurs, of $z_{\rm br} = 0.58 \pm 0.28$ pc (B21), is emphasized by the black vertical lines in Fig. 3. From a visual inspection of the speed profile, the acceleration takes place within the jet parabolic region, while approximately

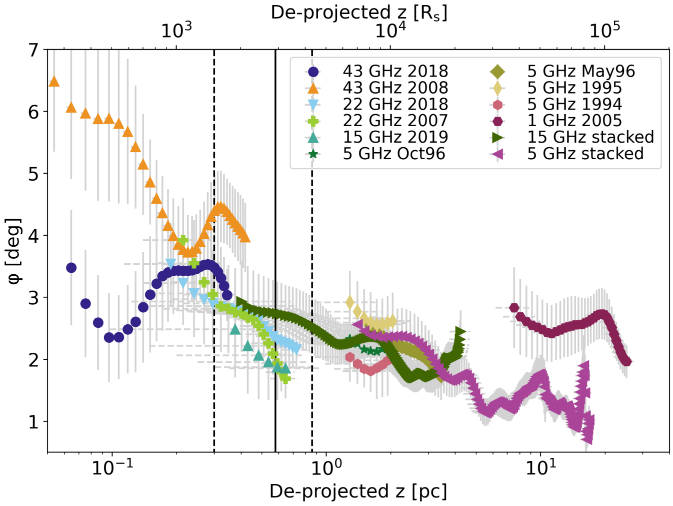

Fig. 4. Intrinsic half opening angle in the frequency range between 1 GHz–43 GHz. The angle varies between ∼1° and ∼6°. A decrease is observed within one parsec, while an approximately constant value of 2°−3° is determined downstream. We note that the discrepancy between the results at 1 GHz and 5 GHz, which may indicate that the jet cross-section is not fully detected at 5 GHz beyond 4 pc.

constant speeds are observed at the start of the conical jet expansion. This is expected when the acceleration is mainly driven by the conversion of Poynting flux into kinetic energy of the bulk flow (Komissarov 2012).

Using Eq. (1) with $\beta = 1$ and the maximum ratios R observed, we can set an upper limit to the viewing angle. We use the highest ratios detected at 5 GHz and 15 GHz, since they are the maps from which we infer the highest velocities. The highest ratios at 5 GHz, starting from the newest map, are $R_1 = 194 \pm 22$, $R_2 = 89 \pm 11$, $R_3 = 267 \pm 32$, and $R_4 = 161 \pm 20$, while at 15 GHz is $R_5 = 145 \pm 22$. From them, we find an average maximum viewing angle of $\theta_{\rm max} = 44 \pm 4°$, in agreement with our assumption of $\theta = 38°$.

3.3. Jet opening angle

In this section, we investigate the intrinsic jet opening angle profile using the observations reported in Fig. 3, as well as the stacked images at 5 GHz and 15 GHz.

To study the opening angle $\phi_{\rm app}$ we need to first obtain the deconvolved transverse jet width, computed as $w = (w_{\rm m}^2 - \theta_b^2)^{1/2}$, where $w_{\rm m}$ is the width of the fitted Gaussian profile and θ_b is the full width at half maximum of the equivalent circular beam, defined as $\theta_b = \sqrt{\theta_{\rm min} \cdot \theta_{\rm max}}$ with $\theta_{\rm min}$ and $\theta_{\rm max}$ being the minor and major beam axis, respectively. The uncertainties on the width are computed as described in Sect. 3.2 for the intensity ratio.

Finally, from our knowledge of both the jet width and the jet viewing angle, we compute the apparent jet opening angle as:

$$\phi_{\rm app} = 2\arctan(0.5w/\mathsf{z})\,, \tag{2}$$

where z is the projected distance from the core along the jet, as well as the intrinsic half opening angle ϕ as

$$\phi = \arctan[\tan(\phi_{\rm app}/2)\sin\theta]\,. \tag{3}$$

The intrinsic half opening angle profiles are illustrated in Fig. 4. For the single-epoch maps, we plotted the points up to the same jet extension as in Fig. 3, while for the stacked images we show the full jet. The uncertainties are computed by propagating the errors obtained on the intrinsic jet width. The intrinsic half angle is on average $\phi \sim 2°{-}3°$ and spans a range between ∼1° and ∼6°, in agreement with the typical values for radio galaxies (Pushkarev et al. 2017). While results for most frequencies and distances agree quite well with each other, we notice large discrepancies on sub-parsec scales between the two 43 GHz epochs and at a distance larger than ∼5 deprojected pc, where the 5 GHz jet appears narrower than at 1 GHz. The sub-parsec scales discrepancy may arise due to an intrinsic jet variability across the epochs, combined with the inability to recover the full jet cross-section in the 43 GHz 2018 epoch, where the inner part of the jet is indeed less bright than the 2008 epoch (see Fig. C.5). The narrowed jet at 5 GHz may indicate that, even in the stacked image, part of the jet at its edges is too faint to be imaged, so we are not able to recover the full jet cross-section. This of course would also have an impact on the determination of the global jet shape, which was found to be not perfectly conical (power law index of ∼0.84 ± 0.04) on those scales in B21. These results suggest that the jet may, in fact, be perfectly conical, but part of its emission may be lost in the noise at 5 GHz. Moreover, a frequency-dependent opening angle may be consistent with the discrepancy in the speeds discussed in Sect. 3.2 and may explain the apparent deceleration observed at 1 GHz.

3.4. Γϕ profile

The product $\Gamma\phi$, where $\Gamma = 1/\sqrt{1-\beta^2}$ is the bulk Lorentz factor, is of a great interest, since it carries information on the causal connection between the edges and the symmetry axis of the flow, with $\Gamma\phi \lesssim 1$ meaning that the jet is causally connected (Clausen-Brown et al. 2013).

In magnetically accelerating relativistic outflows, the bulk acceleration requires the jets to be causally connected, with $\Gamma\phi \sim 1$, while a product higher than one can be observed if the dissipation of thermal energy contributes to the jet acceleration (e.g., Komissarov et al. 2009). Moreover, the product is connected to physical aspects of the accretion disk. In particular, $\Gamma\phi$ is related to the dimensionless magnetic flux $\phi_{\rm BH}$, which is an important indicator of the magnetic activity in the core. When $\phi_{\rm BH}$ is of the order of few units, a SANE disk is expected, while when it is of the order of tens and especially when it reaches the saturation level ∼50, we expect the disk to achieve a MAD state (Tchekhovskoy et al. 2011; Narayan et al. 2012). The dimensionless flux is defined as:

$$\phi_{\rm BH} = \Phi/(\sqrt{\dot{M}c}\,r_{\rm g}), \tag{4}$$

in which Φ is the total magnetic flux in the jet, $\dot{M}$ is the accretion rate, c is the speed of light, $r_{\rm g} = GM_{\rm BH}/c^2$ is the gravitational radius, and in the surroundings of the central black hole the quantity $\Gamma\phi$ is related to $\phi_{\rm BH}$ via $\phi_{\rm BH} = (52 \pm 5)\Gamma\phi$ (Zamaninasab et al. 2014).

Here, we compute the $\Gamma\phi$ profile using our information on the jet speed (Sect. 3.2) and on the half opening angle (Sect. 3.3). The uncertainties are computed by propagating the respective errors. The resulting profile is shown in Fig. 5. We find a fairly constant product, varying between ∼0.04 and ∼0.2 with an average value of ∼0.07, consistent with the median products found in large samples, $\Gamma\phi = 0.13{-}0.17$ (Jorstad et al. 2005; Pushkarev et al. 2009, 2017). Similar values are observed in M87, specifically $\Gamma\phi \sim 0.046$ at 0.3 pc and $\Gamma\phi \sim 0.044$ at 4 pc Nokhrina et al. (2019). Hints of a decreasing trend downstream

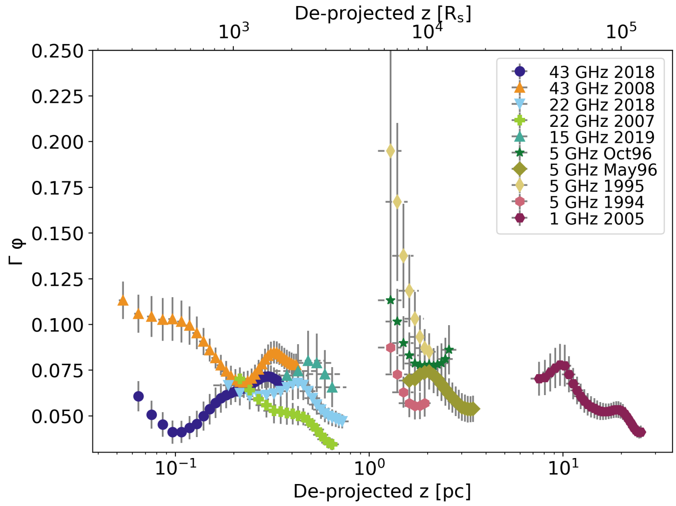

Fig. 5. $\Gamma\phi$ product as a function of distance. The profile is fairly constant, with hints of a decreasing trend downstream the jet on scales smaller than 0.1 pc and 0.2 pc seen from the 43 GHz 2018 and 43 GHz 2008 data points, respectively. The average product is $\Gamma\phi \sim 0.07$.

the jet are given on scales smaller than 0.1 pc and 0.2 pc by the 43 GHz 2018 and 43 GHz 2008 data points, respectively. These observational findings deviate from the theoretical expectation that $\Gamma\phi \sim 1$ in a purely magnetically driven accelerated jet (e.g., Komissarov et al. 2009). In the discussion (Sect. 4), we indirectly infer a value of $\Gamma\phi$ in the disk region by means of our estimate of the dimensionless magnetic flux. The implications on the evolution of the product are discussed in Sect. 4.2.

4. Discussion

In the following, we apply theoretical models to our observational data to explore the nature of the accretion disk and of the outflow in NGC 315. In particular, we aim at modeling the jet acceleration seen in Fig. 3, the magnetic field down to the jet base, and at investigating whether the properties of the VLBI jet are consistent with the expectations for a jet powered by the rotational energy of a black hole fed by an accretion flow in MAD state. Such a test will be performed starting from two independent observables: the location of the jet shape transition and the mass accretion rate. To define the main properties of the accretion flow, we make use of optical and X-ray observational constraints.

4.1. Spin and magnetic flux inferred from the shape transition distance

First, we use the information on the jet shape transition distance to estimate two fundamental parameters of the nuclear region, the black hole spin, and the total magnetic flux threading the accretion disk. The former is used to evaluate the jet power (see Sect. 4.6), while the latter is compared with the expected flux in case of a MAD. To do that, we apply the model proposed by Nokhrina et al. (2019, 2020). The model assumes equilibrium between the ambient medium and the jet edges, with the former being balanced only by the jet thermal pressure at the boundary. An electric current is assumed to be mainly locked within the bulk jet volume and only a residual fraction of it is left in the outer jet boundary. Following Beskin et al. (2017), for a non-relativistic boundary flow, the conservation of the total pressure allows us to connect the pressure balance at the jet boundary with the electric current inside the jet. The boundary pressure is expressed as function of the jet width. Kovalev et al. (2020) showed that when the jet energy regime switches from magnetically dominated to equipartition, that is, when the Poynting flux is equal to the kinetic energy of the bulk, this coincides with a transition between two power laws in the jet boundary pressure profile due to different behaviors of the electric current in the two regimes. Therefore, when the acceleration of the bulk flow saturates the residual electric current, which diminished due to the transformation of the Poynting flux, the current impacts the pressure at the jet boundary, leading to the occurrence of a break in the jet shape. By knowing the jet properties at the transition, this model enables us to obtain information on the central engine, given the observed transition distance and assuming that the external ambient pressure evolves with a single power law profile $P(z) \propto z^{-b}$. The spin is expressed via the dimensionless parameter $a_* = J/M_{\rm BH} \in [0, 1]$, where J is the angular momentum of the central black hole, as:

$$a_* = \frac{8\,(r_{\rm g}/R_{\rm L})}{1 + 16\,(r_{\rm g}/R_{\rm L})^2}, \tag{5}$$

where the light cylinder radius $R_{\rm L}$:

$$R_{\rm L} = \frac{r_{\rm br}}{d_*(\sigma_{\rm M})}. \tag{6}$$

Here, the light cylinder radius is the intrinsic length scale in MHD models and d_* is the non-dimensional jet radius that depends on the initial magnetization of the jet $\sigma_{\rm M}$, defined as the ratio between the Poynting flux to the plasma rest mass energy flux[2]. In a cold outflow the jet accelerates efficiently up to the equipartition regime, where approximately half of the initial electromagnetic energy is converted into kinetic energy of the particles (see Nokhrina et al. 2019, and references therein). Thus, $\sigma_{\rm M}$ is roughly twice the maximum observed Lorentz factor. From our analysis on the jet kinematics (see Sect. 3.2), we constrain a maximum Lorentz factor of $\Gamma \sim 3$–4. Therefore, a initial magnetization of the order of ~10 seems reasonable in our case. However, the Γ observed in our study is unlikely to be the true maximum reached by the jet. Indeed, if the jet has a spine-sheath structure, the large viewing angle of NGC 315 implies that the radio emission is mainly associated with the slower sheath, thus we may be unable to directly probe the central spine. Since NGC 315 is a low-excitation FRI radio galaxy, a realistic assumption for the speed of the spine can rely on VLBI studies of the blazar parent population, formed by BLLac objects. Their findings typically show $\Gamma_{\rm max} \sim 10$ (e.g., Hovatta et al. 2009), which leads us to consider $\sigma_{\rm M} \sim 20$ as a reasonable upper limit for our analysis. For the jet radius at the break, we assume $r_{\rm br} = 0.036 \pm 0.013$ pc following the results in B21. Then, for $\sigma_{\rm M} = 10$ and $\sigma_{\rm M} = 20$, Eq. (5) yield to black hole spins $a_* = 0.86^{+0.13}_{-0.14}$ and $a_* = 0.99^{-0.04}_{-0.08}$, respectively. The asymmetric errors arise due to the particular relation of the spin a_* with respect to the radius at the break $r_{\rm br}$, with the former first increasing and then decreasing with increasing radius. This model points toward a fast rotating black hole, which is necessary to efficiently launch powerful jets from a MAD accretion flow (e.g., Narayan et al. 2022).

The total magnetic flux in the jet is computed as (Nokhrina et al. 2019):

$$\Phi = 2\pi R_{\rm L}^2 \sigma_{\rm M} \left[\left(\frac{z_{\rm br}}{r_0} \right)^{-b} \frac{P_0}{p_*(\sigma_{\rm M})} \right]^{1/2} \text{G cm}^2, \tag{7}$$

---

[2] The values for d_* are taken from Nokhrina et al. (2019), Table 1.

where P_0 is the external pressure in the nuclear region within a sphere of radius r_0 and $p_*(\sigma_{\rm M})$ is the non-dimensional ambient pressure. The break distance of $z_{\rm br} = 0.58 \pm 0.28$ pc is inferred by B21, while the external pressure of $P_0 = 4.5 \times 10^{-10}$ dyn cm^{-2} at 1 arcsec from the core was determined by Worrall et al. (2007) based on X-ray *Chandra* data. We note that the radius within which the pressure measurement was extracted (~0.3 kpc) is larger than the estimated Bondi radius[3] (~0.15 kpc for a black hole mass of $M_{\rm BH} = 2.08 \times 10^9\,M_\odot$), but not by a great deal. The value of b may vary between 1.0 and 2.0 (see discussion in Sect. 3, Nokhrina et al. 2019). In the first case, we find $\Phi = (4.6 \pm 3.5) \times 10^{31}$ G cm^2, while in the second, $\Phi = (1.1 \pm 0.9) \times 10^{33}$ G cm^2. These two values set the upper and lower limit on the total magnetic flux accordingly to the variation of b. The magnetic flux depends weakly on the initial magnetization $\sigma_{\rm M}$.

We now compare the jet magnetic flux obtained via Eq. (7) with the expected one in the MAD scenario. The latter is computed as (Zamaninasab et al. 2014):

$$\Phi^{\rm exp} = 2.4 \times 10^{34} \left[\frac{M_{\rm BH}}{10^9 M_\odot}\right] \left[\frac{\dot{M}c^2}{3.15 \times 10^{47} {\rm erg\,s^{-1}}}\right]^{1/2} {\rm G\ cm^2}. \quad (8)$$

Following Heckman et al. (2004), we derive the mass accretion rate from the luminosity of the [O III] λ5007 emission line as $L_{\rm bol} = 3500\, L_{\rm O\ III}$, where $L_{\rm bol}$ is the bolometric luminosity and the bolometric correction has an uncertainty of 0.38 dex. Ho et al. (1993) derived a flux for the [O III] λ5007 line of 1.17×10^{-14} erg s^{-1} cm^{-2}, leading to $L_{\rm bol} = (2.44 \pm 0.93) \times 10^{43}$ erg s^{-1}. The result is in a good agreement with the bolometric luminosity of 1.9×10^{43} erg s^{-1}, obtained by Gu et al. (2007) by integrating the SED of the nucleus of NGC 315. The mass accretion rate $\dot{M} = L_{\rm bol}/(\eta_d c^2) = (2.7 \pm 1.1) \times 10^{23}$ g s^{-1} is obtained by assuming an efficiency $\eta_d = 0.1$ (e.g., Yu & Tremaine 2002)[4]. Throughout the paper, the asymmetric errors are treated conservatively by computing the maximum and minimum values of the quantity and by considering them, respectively, as the upper and lower limits of the uncertainty interval.

Equation (8) yields $\Phi^{\rm exp} = (1.4 \pm 0.3) \times 10^{33}$ G cm^2. The expected magnetic flux is consistent with Φ when $b \sim 2$ in the external pressure profile ($P(z) \propto z^{-b}$). Assuming $\eta_d = 0.4$, Eq. (8) would yield to $\Phi^{\rm exp} \sim 6 \times 10^{32}$ G cm^2, which is consistent with Φ when $b \sim 1.8$. For a highly magnetized accelerating jet confined by an ambient medium, a quadratic decrease of the external pressure indeed matches the observation of a jet with parabolic shape, since the jet radius is predicted to grow as $r \propto z^{b/4}$ (e.g., Komissarov et al. 2009). As in NGC 315, we observe $r \propto z^{0.45 \pm 0.15}$ in the acceleration region (B21), and the index of the external pressure is expected to be $b = 1.8 \pm 0.6$. The excellent agreement between Φ and $\Phi^{\rm exp}$ is a first hint of a jet launched by an established magnetically arrested disk in the nuclear region of NGC 315. Park et al. (2021) found a close to ten times more extended parabolic region in NGC 315. By using their jet properties at the break, we infer a slower rotation of the black hole with $a_* \sim 0.20$, while Φ and $\Phi^{\rm exp}$ are still in agreement.

4.2. Exploring the $\Gamma\Phi$ profile

In the framework of a Blandford-Znajek jet model and in the hypothesis of flux-freezing approximation (Blandford & Znajek 1977; Zamaninasab et al. 2014), we can derive the dimensionless magnetic flux threading the accretion disk via Eq. (4) based on our determination of the jet magnetic flux in physical units. Using Φ and $\dot{M}$ both with $\eta_d = 0.1$ and $\eta_d = 0.4$, we obtain a dimensionless magnetic flux threading the accretion disk $\phi_{\rm BH} = 40 \pm 33$, which is consistent with the saturation level of ~50 for a magnetically arrested disk. Unfortunately, the large error bar does not allow us to directly discriminate between SANE and MAD.

The saturation condition $\phi_{\rm BH} = (52 \pm 5)\Gamma\phi$ implies $\Gamma\phi = 0.76 \pm 0.64$ at the jet base. The large uncertainties prevent us from retrieving a solid constrain on this parameter. However, the estimated mean value suggests a $\Gamma\phi$ product likely close to one, in agreement with the prediction for the jet launching region (see Zamaninasab et al. 2014, and references therein), but that is a departure from what we observe on sub-parsec, parsec scales (see Fig. 5). If the product is actually close to 1 in the nuclear region, as expected in a cold accelerating outflow (see Sect. 3.4), then one of two scenarios may be invoked: $\Gamma\phi$ may start close to one and they rapidly decrease in the parabolic region (hints of a decreasing trend are given by the 43 GHz maps) down to ~0.1 at 0.1 pc. Alternatively, the prediction is only valid for the very central jet spine launched in the surroundings of the black hole ergosphere, while what we infer with our observations is determined by the behavior of the external sheath.

4.3. Jet acceleration gradient

The jet undergoes a rapid acceleration up to ~0.9 c on sub-parsec scales (see Sect. 3.2). In order to check whether the acceleration rate is consistent with the standard magneto-hydrodynamical (MHD) mechanism, we fit the speeds profile with a generic model. We work under the assumption of a parabolic jet shape $r = \lambda z^{\psi}$, with $\psi = 0.45$ accordingly to B21. The scaling parameter λ is computed from the knowledge of the jet radius at the transition distance $z_{\rm br} = 0.58$ pc, namely $r_{\rm br} = 0.036$ pc. To describe the observational data reported in Fig. 3, we adopted a hyperbolic tangent function of the type $\Gamma(x) = A + B\tanh(ax - b)$, which we constrained to follow the MHD approach for a magnetically accelerating jet. The function is used to describe the data in the Lorentz factor parameter space. The hyperbolic tangent function mimics both the Lorentz factor growth onset on a scale of a light cylinder radius $R_{\rm L}$ and an acceleration saturation close to its observed maximum value $\Gamma_{\rm max} \sim \sigma_{\rm M}/2$. Moreover, it is linear for the argument close to zero. We find the constants A and B by setting the function limits as 1 and $\Gamma_{\rm max}$. By ensuring that the growth rate (derivative over r) never exceeds $R_{\rm L}^{-1}$, as expected from MHD modeling (Beskin & Nokhrina 2006; Tchekhovskoy et al. 2009; Lyubarsky 2009; Nakamura et al. 2018), we constrain the parameter a. Finally, we set b so as to set $\Gamma \approx \Gamma_{\rm max}/2$ approximately at the distance $r \approx R_{\rm L}\Gamma_{\rm max}/2f$. Here, the parameter f is defined as the ratio between the radius at which the maximum Lorentz factor is reached and the total jet radius. For models assuming a constant angular velocity (Lyubarsky 2009) the maximum Lorentz factor is reached at the jet boundary ($\rho = 1$), while models with a slower sheath flow provide $f \sim 0.2$–0.7 (Komissarov et al. 2007; Beskin et al. 2017; Chatterjee et al. 2019). In our model, we use f as a free parameters. Thus we obtain:

$$\Gamma(z) = \frac{\Gamma_{\rm max}+1}{2} + \frac{\Gamma_{\rm max}-1}{2}\tanh\left(\frac{z}{R_{\rm L}}\frac{2}{\Gamma_{\rm max}-1} - \frac{\Gamma_{\rm max}}{f(\Gamma_{\rm max}-1)}\right), \quad (9)$$

where we associate the distance z with the Lorentz factor $\Gamma(fr)$. We plot Eq. (9) using a light cylinder radius of

---

[3] The Bondi radius is estimated following Russell et al. (2015).

[4] Assuming $\eta_d = 0.4$ (e.g., Zamaninasab et al. 2014) slightly changes the quantities computed in the discussion but leaves the main conclusions unaltered.

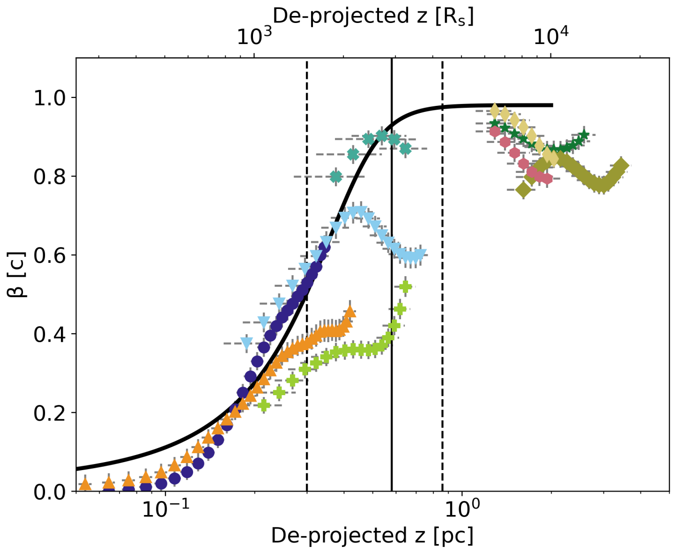

Fig. 6. Zoom onto the intrinsic speed profile in the distance range 0.1–5 pc. The black continuous line represents the modeled hyperbolic tangent function (Eq. (9)). For the label, we refer to Fig. 3.

$R_{\rm L} = 6.9\times10^{-4}$ pc, obtained when $\sigma_{\rm M} = 10$, which corresponds to $\Gamma_{\rm max} = 5.0$ (see Sect. 4.1). The value of f that minimize the $\chi^2_{\rm red}$ is $f = 0.216$ ($\chi^2_{\rm red} = 33.3$). The data-model comparison is done by using the 15 GHz and 22–43 GHz 2018 epochs data, since they are the ones that fully describe the acceleration region. While the high $\chi^2_{\rm red}$ implies the fitting to be not statistically acceptable, here our goal is not to find a function that strictly interpolate the data with their oscillations, but instead to reconcile the general trend of the fast-acceleration with a function that follows the current MHD theories. Figure 6 shows a zoom onto the β(z) plane together with the best fit. The hyperbolic tangent function properly describes the linear acceleration on sub-parsec scales, although a discrepancy is present around 0.01 pc, where the model overestimates the observed velocities. Overall, this formalism allows us to reconcile the observed fast acceleration with a magnetically driven one in the context of the MHD theory.

Given the co-spatiality of the acceleration and collimation region (see Sect. 3.2), in our modeling we considered the acceleration to be driven uniquely by the conversion of magnetic into kinetic energy. We note, however, that the jets may dissipate thermal energy as well to accelerate (Komissarov et al. 2009). Even if our observational data suggest that the jet in NGC 315 is magnetically dominated, the thermal acceleration may not be completely negligible and still play a role.

4.4. Core shift magnetic field for a conical jet and for a quasi-parabolic accelerating jet

The magnetic field strength is expected to vary with distance z from the black hole as $B(\mathrm{z}) = B_\xi(\mathrm{z}/\xi)^\tau$, where B_ξ is the magnetic field strength at ξ pc (see e.g., O'Sullivan & Gabuzda 2009). To compute the magnetic field strength at one parsec, following the works by Lobanov (1998) and Hirotani (2005), we define the core-position offset measure:

$$\Omega_{r\nu} = 4.85\times10^{-9}\frac{\Delta r_{\rm mas} D_{\rm L}}{(1+z)^2}\left(\frac{\nu_1^{1/k_r}\nu_2^{1/k_r}}{\nu_2^{1/k_r}-\nu_1^{1/k_r}}\right)\ \mathrm{pc\ GHz}, \qquad (10)$$

where $\Delta r_{\rm mas}$ is the core shift between ν_2 and ν_1 (in mas) and D_L is the luminosity distance (in pc). In the scenario of a conical jet with spectral index $\alpha = -0.5$ and in equipartition between the particle and magnetic field energy density, the magnetic field is expressed as:

$$B_1 = 0.025\left(\frac{\Omega^3_{r\nu}(1+z)^2}{\delta^2\phi\sin^2\theta}\right)^{1/4}\ \mathrm{G}, \qquad (11)$$

where $\delta = [\Gamma(1-\beta\cos\theta)]^{-1}$ is the Doppler factor. Under the same assumptions, we also expect the core shift coefficient to be $k_r = 1$ (Lobanov 1998). This value is slightly larger than the core shift index assumed in this work, $k_r = 0.84 \pm 0.06$ (see Sect. 2.1, B21). The latter is indeed obtained by fitting the core shift at all available frequencies (1–22 GHz), which sample both the parabolic and the conical jet region. If the jet break occurs at the distance where the jet switches from a magnetically dominated to an equipartition regime (Nokhrina et al. 2020), we should expect to obtain an index k_r close to unity if we fit the core shift only in the conical region. Thus, we fit the parabolic and conical regions separately. In the former, sampled by the frequency range (8–22) GHz, we determined an index of $k_r = 0.57 \pm 0.17$, while in the latter, sampled at 1, 5, and 8 GHz, we obtained $k_r = 0.93 \pm 0.01$ (see Fig. 7). The point at 8 GHz is used to connect the two regions, since it is the closest one to the jet break. After the break, we obtain an index slightly lower than the unity, in reasonable agreement with the equipartition hypothesis. The other two hypotheses are not fully matched. Indeed, $\alpha = -0.5$ is flatter with respect to the observed values (see Park et al. 2021) and the jet does not show a conical shape up to its apex. Nevertheless, we can use Eq. (11) to obtain an order-of-magnitude estimate of the magnetic field strength. The core-position offset $\Omega_{r\nu}$ is computed between $\nu_2 = 1.4$ GHz and $\nu_1 = 5.0$ GHz, since these frequencies sample the one-parsec region. The Doppler factor is estimated to be $\delta = 1.24 \pm 0.25$ with $\beta = 0.95 \pm 0.03$ (observed at one pc; see Fig. 3).

We assume an intrinsic half opening angle of $\phi = (2.5 \pm 1)^\circ$ (Fig. 4). Using Eq. (11), we find $B_1 = 0.13 \pm 0.02$ G. The magnetic field strength matches the values obtained by O'Sullivan & Gabuzda (2009) in their small samples of objects and it is fairly smaller than the median value $B_1 \sim 0.4$ G obtained for the BL Lac sources in the MOJAVE sample (Pushkarev et al. 2012).

In the following, we propose a new formalism to compute the magnetic field for a quasi-parabolic accelerating jet, which better describes the case of NGC 315. We calculate the expressions for a magnetic field at a generic distance from the jet base based on the assumption that the flow radius evolves as $r \sim \mathrm{z}^\psi$, with $\psi = 0.5$, corresponding to a strictly parabolic jet boundary. The details are reported in Appendix A. First, we assume the Doppler factor δ as a constant. By recalculating the position of the surface with optical depth equal to unity, the expression for $\Omega_{r\nu}$ is still Eq. (10) but with $k_r = \psi$, and the magnetic field is:

$$B_{\rm z} = 0.025\left(\frac{\Omega^{3\psi}_{r\nu}(1+z)^2}{\mathrm{z}^{3\psi}r_{\rm z}\delta^2\sin^{3\psi-1}\theta}\right)^{1/4}\ \mathrm{G}. \qquad (12)$$

Here, $r_{\rm z}$ in parsec is the jet radius at z parsec from the jet base. This expression transforms into Eq. (11) for $\mathrm{z} = 1$, $\psi = 1$ and noting that $\varphi \approx r_{\rm z}/\mathrm{z} = r_{\rm z}$ at one parsec.

For an accelerating flow, we assume a linear acceleration with the jet radius as $\Gamma = r/R_L$ and with the Doppler factor changing along the accelerating flow. We distinguish between three possible cases, depending on the interplay between the viewing angle θ and the Lorentz factor Γ in the expression for δ.

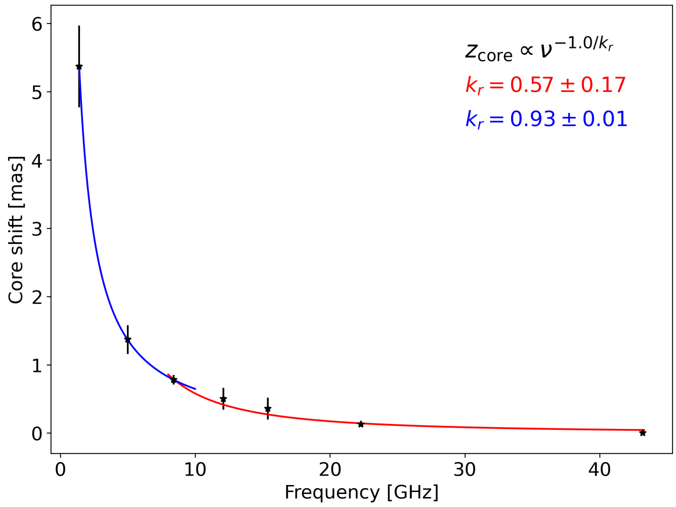

Fig. 7. Core positions as a function of frequency, assumed from B21. The data are fitted with two different power laws: one for the parabolic region (red curve) and one for the conical region (blue curve). In the former case, the best fit index is $k_r = 0.57 \pm 0.17$, while in the latter, it is $k_r = 0.93 \pm 0.01$. An index close to 1 is expected when assuming equipartition between the particles and magnetic field energy densities in the jet.

For case A: the viewing angle $\theta \sim \Gamma^{-1}$ is such that the Doppler factor is close to its peak, so we may set it as a constant. In this scenario, $k_r = 2\psi$ and the expression for the magnetic field becomes (see details in Appendix A):

$$B_z = 0.025\left(\frac{\Omega_{r\nu}^{6\psi}(1+z)^2}{\mathrm{z}^{6\psi} r_{\mathrm{z}} \delta^2 \sin^{6\psi-1}\theta}\right)^{1/4}\ \mathrm{G}, \tag{13}$$

with z and r_{z} in parsec.

For case B: for a smaller viewing angle $\theta \lesssim \Gamma^{-1}$, we may use the approximations $\beta \approx 1 - 1/(2\Gamma^2)$ and $\cos\theta \approx 1 - \theta^2/2$, and by neglecting the factor θ^2 we obtain $\delta \approx 2\Gamma$. The core shift coefficient becomes $k_r = 4\psi/3$, and the magnetic field is given by:

$$B_z = 0.018\left(\frac{\Omega_{r\nu}^{4\psi}(1+z)^2}{\mathrm{z}^{4\psi} r_{\mathrm{z}} \sin^{4\psi-1}\theta}\left(\frac{R_L}{r_{\mathrm{z}}}\right)^2\right)^{1/4}\ \mathrm{G}, \tag{14}$$

with the light cylinder radius R_L measured in parsec.

For case C: for a larger viewing angle $\theta \gtrsim \Gamma^{-1}$, we use the exact expression for a Doppler factor with variable Γ, but assuming $\beta = 1$, since the term $\beta\cos\theta$ in δ is not close to unity and the difference of velocity from speed of light is not important. In this case $k_r = 8\psi/3$, and the magnetic field is expressed as:

$$B_z = 0.025\left(\frac{\Omega_{r\nu}^{8\psi}(1+z)^2(1-\cos\theta)^2}{\mathrm{z}^{8\psi} r_{\mathrm{z}} \sin^{8\psi-1}\theta}\left(\frac{r_{\mathrm{z}}}{R_L}\right)^2\right)^{1/4}\ \mathrm{G}. \tag{15}$$

For NGC 315, the viewing angle is $\theta \sim 0.66$ rad and the inverse of the Lorentz factor evolves with a distance from $\Gamma^{-1} \sim 1$ at the jet base to $\Gamma^{-1} \sim 0.5$ at $\mathrm{z_{br}}$. Therefore, case A is the most adequate at the transition distance, while case B is true in the accelerating part of the jet. At $\mathrm{z} = \mathrm{z_{br}} = 0.58 \pm 0.28$ pc, we obtain $B_{\mathrm{z_{br}}} = 0.18 \pm 0.06$ G and $B_{\mathrm{z_{br}}} = 0.013 \pm 0.003$ G, respectively. As we expect a larger magnetic field value closer to the jet base, the estimate in the case A corresponds better to the value at $\mathrm{z} = 1$ pc than in the case B. However, we note that Eq. (14) contains a factor $(R_L/r_{\mathrm{z}})^2$ that follows from the ideal linear acceleration $\Gamma = r/R_L$. Slower accelerations or the maximum Lorentz factor reached closer to the jet axis will boost this magnetic field estimate (Beskin et al. 2017).

We note that the relation $k_r = 4\psi/3$, valid in case B, is in excellent agreement with the observations, with $\psi = 0.45$ and the measured k_r at high frequencies $k_r = 0.57 \pm 0.17$. Instead, the relation $k_r = 2\psi$, valid in case A, implies a k_r value beyond the observed interval.

4.5. Magnetic field: From the parsec jet up to the accretion disk

In this section, we explore the properties of the magnetic fields in the nuclear region in two different ways: 1) from the disk magnetic flux (Sect. 4.1) assuming a simplified geometry for the disk and 2) by extrapolating up to the jet base our field strengths estimation (Sect. 4.4). The results are compared with the expected field strength needed to saturate the disk and form a MAD, whose presence is suggested from the comparison of the magnetic fluxes (Sect. 4.1).

4.5.1. Saturation magnetic field

In the MAD state, the accretion disk is disrupted by the accumulated poloidal field within the extent of the magnetosphere (r_{m} in units of R_{S}), which corresponds to the jet launching radius. The magnetosphere radius, following Narayan et al. (2003), is defined as:

$$r_{\mathrm{m}} \sim 8.2 \times 10^3 (\epsilon \times 10^2)^{2/3} m_8^{-2} \dot{m}^{-2/3} \left(\frac{\Phi}{0.1\ \mathrm{pc^2\,G}}\right)^{4/3} R_{\mathrm{s}}, \tag{16}$$

where: ϵ defines the ratio between the radial velocity of the gas within the magnetosphere and its free-fall velocity and for which we assume an upper limit of 0.1 (Narayan et al. 2003), $m_8 = M_{\mathrm{BH}}/(10^8 M_\odot)$, $\dot{m} = \dot{M}/\dot{M}_{\mathrm{Edd}}$, and Φ is the magnetic flux in the central region, for which we adopt our Φ estimation with $b = 2$. We infer the upper limit of the magnetosphere radius as $r_{\mathrm{m}} = 1.1 \pm 1.0\,R_{\mathrm{S}}$. The error is computed by propagating the uncertainties on the magnetic flux and the accretion mass rate. We notice that in NGC 315, the event horizon radius varies between $r_{\mathrm{H}} \in [0.6, 0.8]\,R_{\mathrm{s}}$ when $a_* = 0.99$ and $a_* = 0.86$, respectively. Since a magnetosphere smaller than an event horizon would be unphysical, the lower limit on r_{m} is set by the lower limit on the event horizon radius. Therefore, the magnetosphere radius lays in the range ∼0.6–2.1 R_{S}, or ∼1.2–4.2 r_{g} when $\eta_d = 0.1$ and ∼0.6–5.3 R_{S}, or ∼1.2–10.6 r_{g} when $\eta_d = 0.4$. The derived range is relatively small with respect to estimates from simulations. For instance, Narayan et al. (2022) inferred magnetosphere radii on the order of several tens of r_{g}.

Next, we extrapolate the saturation magnetic field in the accretion disk based on the knowledge that a MAD forms when enough of the field is accumulated within it, so that the magnetic force F_{B} overcomes the gravitational force F_{G}. When $F_{\mathrm{B}} > F_{\mathrm{G}}$, the magnetic field is expelled from the disk until the condition $F_{\mathrm{B}} = F_{\mathrm{G}}$ is reached. Following Contopoulos et al. (2015), we express the forces as $F_{\mathrm{B}} = (B^2/8\pi)4\pi r^2 h/r$ and $F_{\mathrm{G}} = G M_{\mathrm{BH}} M_{\mathrm{disk}}/r^2$, in which h/r is the scale height of the accretion disk, $r = r_{\mathrm{m}}$ is the radius and M_{disk} is the disk mass in the region in which the MAD forms. Expressing the disk mass as $M_{\mathrm{disk}} = 4/3\rho\pi r^3 h/r$ and the density ρ from the mass continuity equation as $\rho = \dot{M}/(4\pi r^2\ v_r h/r)$ yields the following saturation magnetic field:

$$B_{\mathrm{MAD}} = \left(\frac{2}{3}\frac{GM_{\mathrm{BH}}\dot{M}}{r^3 v_r h/r}\right)^{1/2}, \tag{17}$$

in which v_r is the radial velocity of the infalling gas and is assumed to be close to the speed of light. We solve Eq. (17) by adopting the mass accretion rate derived from the [O III] line luminosity in Sect. 4.1. We set the scale height to 0.25 ± 0.10, accordingly to Narayan et al. (2022) (see Fig. 7, right lower panel in that article) and extrapolate a saturation magnetic field spanning the range $B_{\mathrm{MAD}} = 125{-}480\,\mathrm{G}$ at $r_{\mathrm{m}} = 0.6\,R_{\mathrm{S}}$ and $B_{\mathrm{MAD}} = 5{-}18\,\mathrm{G}$ at $r_{\mathrm{m}} = 5.3\,R_{\mathrm{S}}$.

4.5.2. Poloidal field from the magnetic flux Φ

In the accretion disk within the supposed magnetosphere, the strength of the poloidal magnetic field component B_P is related to the magnetic flux Φ in the flux freezing approximation. The poloidal strength is $B_P = \Phi/S$, where we assume a circular surface $S = \pi r^2$ with $r \in [0.6, 5.3]R_{\mathrm{S}}$. The field varies between $B_P = 4640{-}464\,\mathrm{G}$ and $B_P = 60{-}6\,\mathrm{G}$ at the lower and upper limit of the magnetosphere.

4.5.3. Extrapolation from the field strength in the jet

Finally, we extrapolate the magnetic field values inferred in Sect. 4.4 up to the jet base. To do so, we assume that the magnetic flux is conserved along the sub-parsec jet. Under this assumption, both the toroidal and poloidal components of the magnetic field in the parabolic region evolve as

$$B(\mathrm{z}) = B_0(\mathrm{z}_0/\mathrm{z})^{2\psi}. \tag{18}$$

The details are shown in Appendix B. Being $\psi = 0.45$ upstream of the transition distance, both the poloidal and toroidal magnetic field components evolve as $\sim\mathrm{z}^{-1}$, while in the conical region the poloidal component evolves as $\sim\mathrm{z}^{-2}$.

Our results are summarized in Fig. 8. From the first two methods, the magnetic field strength in the accretion disk is found to be in the range of $\sim 10{-}10^3\,\mathrm{G}$, based on the possible extent of the magnetosphere. On the other hand, the strengths at the jet base are up to tens of Gauss by extrapolating case B and up to $\sim 10^3\,\mathrm{G}$ by extrapolating case A and the conical case. A comparable range ($360\,\mathrm{G} < B < 6.9 \times 10^4\,\mathrm{G}$ at $1\,R_{\mathrm{S}}$ from the core) was derived by Baczko et al. (2016) for the radio galaxy NGC 1052.

From general relativistic magnetohydrodynamical (GRMHD) simulations, the magnetic energy ($\propto B^2$) in a Blandford-Znajek jet is expected to be one-two orders of magnitude stronger than the one in the disk (McKinney & Narayan 2007a,b). In this scenario, the conical and A cases are favored, leading to fields that are several orders of magnitude stronger than the strengths needed to form a magnetically arrested disk, especially at the largest magnetosphere radius.

4.6. Jet power: Expected versus observed

A final test of the models described above can be performed by comparing the expected jet power to the observed one. By knowing the accretion rate, the expected jet power can be computed as $P_{\mathrm{jet}} = \eta \dot{M} c^2$. By means of GRMHD simulations within the MAD scenario, Narayan et al. (2022) linked different black hole spins to the expected accretion efficiencies. From our determined spin range of $a_* = 0.72{-}0.99$, we expect $\eta \in [0.72, 1.50]$ in the prograde case (i.e., the black hole and the accretion disk rotating in the same direction) and $\eta \in [0.14, 0.42]$ in the retrograde case (i.e., the black hole and the accretion disk rotating in opposite directions). Using the [OIII] line estimation for the accretion rate $\dot{M}$ and $\eta_d = 0.1$, the jet power of NGC 315 is $P_{\mathrm{jet}} \sim 1{-}4 \times 10^{44}\,\mathrm{erg\,s^{-1}}$ in the prograde case and $P_{\mathrm{jet}} \sim 0.3{-}1{\times}10^{44}\,\mathrm{erg\,s^{-1}}$ in the retrograde case. In the case of $\eta_d = 0.4$, the jet power is expected to be $P_{\mathrm{jet}} \sim 4{-}9 \times 10^{43}\,\mathrm{erg\,s^{-1}}$ and $P_{\mathrm{jet}} \sim 0.9{-}3 \times 10^{43}\,\mathrm{erg\,s^{-1}}$, respectively.

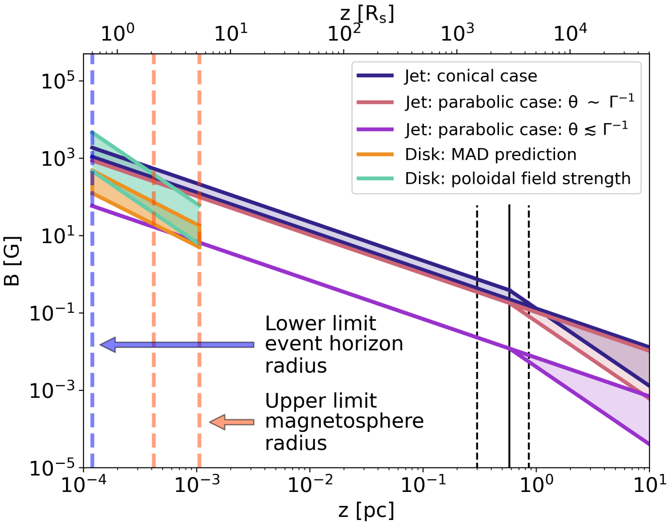

Fig. 8. Extrapolation of the magnetic field computed using Eq. (11) (blue lines), case A (red lines), and case B (purple lines) down to the event horizon radius $r_{\mathrm{H}} = 0.6\,R_{\mathrm{S}}$ (highlighted by the blue dashed line) assuming $B(\mathrm{z}) = B_0(\mathrm{z}/\mathrm{z}_0)^{2\psi}$. See the text for details on the different dependence. The orange dashed lines indicate the upper limit on the magnetosphere radius, namely $r_{\mathrm{m}} = 2.1\,R_{\mathrm{S}}$ with $\eta_d = 0.1$ and $r_{\mathrm{m}} = 5.3\,R_{\mathrm{S}}$ with $\eta_d = 0.4$. The orange box highlights the range of variation of the expected saturation magnetic field strength in the MAD scenario, while the light green box indicates the poloidal field strengths inferred based on the magnetic flux.

A further method to compute the total jet power is provided by Nokhrina et al. (2019) based on their model (see Sect. 4.1):

$$P_{\mathrm{jet}} = \frac{c}{8}\left(\frac{\Phi}{\pi R_{\mathrm{L}}}\right)^2. \tag{19}$$

By assuming $b = 1$ and $b = 2$ we obtain respectively the lower and upper limit for the jet power, $P_{\mathrm{jet}} \sim 2{\times}10^{41}\,\mathrm{erg\,s^{-1}}$ and $P_{\mathrm{jet}} \sim 1 \times 10^{44}\,\mathrm{erg\,s^{-1}}$. The comparison with the previous P_{jet} estimates favours an index for the external pressure $b \sim 2$, consistent with our findings in Sect. 4.1.

In the following, we compare these expected values with observational estimates of the jet power in NGC 315. We first work under the assumption of a Bondi accretion flow (Bondi 1952). Following Russell et al. (2015), we can derive the accretion rate, in convenient units, as:

$$\dot{M}_{\mathrm{B}} = 0.012\left(\frac{k_{\mathrm{B}}T}{\mathrm{keV}}\right)^{-3/2}\left(\frac{n_{\mathrm{e}}}{\mathrm{cm^{-3}}}\right)\left(\frac{M_{\mathrm{BH}}}{10^9\,\mathrm{M_\odot}}\right)^2 M_\odot\,\mathrm{yr^{-1}}, \tag{20}$$

in which n_{e} is the electron number density and $k_{\mathrm{B}}T$ is the temperature of the medium at the Bondi radius. In this equation, an adiabatic index of 5/3 is assumed. The parameters of the gas within the Bondi radius, $k_{\mathrm{B}}T = 0.44\,\mathrm{keV}$ and $n_{\mathrm{e}} = 2.8 \times 10^{-1}\,\mathrm{cm^{-3}}$, are extracted from X-ray *Chandra* data (Worrall et al. 2007). Equation 20 yields an accretion rate of $\dot{M}_{\rm B} = 3.1 \times 10^{24}\,{\rm g\,s^{-1}} = 5 \times 10^{-2}\,M_\odot\,{\rm yr^{-1}}$, around 100 times lower than the Eddington accretion rate $M_{\rm Edd} = 2.9 \times 10^{26}\,{\rm g\,s^{-1}}$. Nemmen & Tchekhovskoy (2015) and Allen et al. (2006), among others, observed that a relation exists between the Bondi accretion rate and the jet power. The latter can be directly inferred as $\log P_{\rm jet} = A \log (0.1 \dot{M}_{\rm B} c^2) + B$ in which the parameters are either $A = 1.05$ and $B = -3.51$ (Nemmen & Tchekhovskoy 2015) or $A = 1.29$ and $B = -0.84$ (Allen et al. 2006) meaning $P_{\rm jet} \sim 2 \times 10^{43}\,{\rm erg\,s^{-1}}$ and $P_{\rm jet} \sim 1 \times 10^{44}\,{\rm erg\,s^{-1}}$, respectively. A second method relies on the existence of an empirical relationship between the radio core luminosity and the jet power. Following the work of Heinz et al. (2007), Morganti et al. (2009), we assume the inferred $P_{\rm jet} = 1.4 \times 10^{44}\,{\rm erg\,s^{-1}}$. While the validity of such a relation may, in general, be affected by the core variability and Doppler boosting, we do not expect these effects to be strong in NGC 315, and the obtained value lies in the same range as the previous estimates.

This analysis shows a substantial agreement between the order-of-magnitude of the jet powers computed in the MAD scenario and from Eq. (19) and the observational estimates. Obtaining tighter constraints concerning, for instance, which type of spin configuration is the most likely is not possible based on the current data due to the large uncertainties and the degeneracy between the different parameters.

5. Conclusion

In this paper, we explore the disk-jet connection in the nearby radio galaxy NGC 315 using a multifrequency and multiepoch VLBI data set. We constrained the observational properties of the jet in the acceleration and collimation region and used them to retrieve information on the physics of the accretion disk and of the jet itself. Our results are summarized as follows.

- We used simultaneous 22 GHz and 43 GHz observations to study the evolution of the spectral index on VLBI scales. We inferred an unexpected spectral behavior, with very steep values ($\alpha \sim -1.5$) in a region whose extent is comparable with that of the collimation zone. These steep values may result from strong synchrotron losses at the highest frequencies, reflecting the presence of strong magnetic fields at the jet base.
- Using a pixel-based analysis, we derived the jet speed profile from the observed jet-to-counterjet ratio profile, under the assumption of intrinsic symmetry between the two jets. We inferred a fast-acceleration on sub-parsec scales, where the jet collimation is also taking place. The co-spatiality between the two phenomena suggests the jet to consist of a cold outflow in which the acceleration is mainly driven by the conversion of magnetic energy into kinetic energy of the bulk. Following this, we modeled the jet acceleration in the context of MHD theories.
- We found the half intrinsic opening angle to span the range between ~1° and ~6°, consistent with typical values observed in radio galaxies. The opening angle decreases on sub-parsec scales down to approximately constant values of ~2°−3°. Consequently, we examined the $\Gamma\phi$ product along the jet, finding a fairly constant profile that varies between 0.04 and 0.2, with $\Gamma\phi = 0.07$ as average. This value is consistent with the median product of $\Gamma\phi = 0.13{-}0.17$ from sample studies. At the jet base, we indirectly estimate the average $\Gamma\phi$ product to be likely close to the expectation of $\Gamma\phi \sim 1$ for magnetically accelerating jets. The discrepancy between the expected and the observed value may be explained if either the $\Gamma\phi$ product drops swiftly in the acceleration region, or if the condition $\Gamma\phi \sim 1$ is only valid in the very central jet spine, and the observed values mainly reflect the properties of the outer sheath.
- Under the assumption that an equipartition state is reached at the end of the acceleration and collimation region, within the framework of the model proposed by Nokhrina et al. (2019, 2020), we found the black hole of NGC 315 to be fast-rotating, with $a_* \gtrsim 0.72$. Moreover, based on the X-ray properties of the accretion flow, we constrained the total magnetic flux threading the accretion disk in to be in excellent agreement with the expected flux in case of a magnetically arrested disk. The two are estimated independently, with the former being extrapolated from the jet properties at the transition and the expected one based on the accretion rate and black hole mass. The average dimensionless magnetic flux $\phi_{\rm BH} \sim 40$ is in a good agreement with the saturation value of ~50, which is expected when the accretion disk reaches the magnetically arrested state.
- We estimated three different magnetic field values down to the jet base based on the core shift effect in the case of both a conical and a quasi-parabolic accelerating jet. The latter case required the development of a new formalism. In the case of $\theta \sim \Gamma^{-1}$, we found a magnetic field strength of $B \sim 0.18$ G at $z_{\rm br} = 0.58$ pc consistent with the one in the conical assumption, while if $\theta \lesssim \Gamma^{-1}$ the magnetic strength is lower, $B \sim 0.01$ G. Later, we extrapolated the field values down the event horizon radius assuming both a poloidal and toroidal field configuration. The extrapolated strengths are consistent with both the poloidal field values obtained from the magnetic disk flux and the needed saturation field strengths to form a MAD. This result offers evidence that the magnetic field in the accretion disk has reached high enough values to saturate, establishing a magnetically arrested state.

In conclusion, our analysis and modeling of the jet observational properties on VLBI scales are compatible with the expectations from an accretion disk that has reached a magnetically arrested state. Our results will be expanded in future papers by means of numerical simulations and new VLBI data sets, especially multiepoch 86 GHz GMVA observations.

Acknowledgements. We thank the referee, Richard A. Perley, for the insightful comments that helped improve the overall clarity of the manuscript. We would like to thank Maciek Wielgus, for his helpful comments. L.R., B.B., and E.M. acknowledge the financial support of a Otto Hahn research group from the Max Planck Society. E.E.N. was supported by the Russian Science Foundation (project 20-62-46021). M.P. acknowledges support by the Spanish Ministerio de Ciencia through grants PID2019-105510GB-C31 and PID2019-107427GB-C33, and from the Generalitat Valenciana through grant PROMETEU/2019/071. This research has made use of data from the MOJAVE database that is maintained by the MOJAVE team (Lister et al. 2018). The VLBA is a facility of the National Science Foundation under cooperative agreement by Associated Universities, Inc. The European VLBI Network is a joint facility of European, Chinese, South African and other radio astronomy institutes funded by their national research councils.

References

Allen, S. W., Dunn, R. J. H., Fabian, A. C., Taylor, G. B., & Reynolds, C. S. 2006, MNRAS, 372, 21
Baczko, A. K., Schulz, R., Kadler, M., et al. 2016, A&A, 593, A47
Baczko, A. K., Ros, E., Kadler, M., et al. 2022, A&A, 658, A119
Beskin, V. S., & Nokhrina, E. E. 2006, MNRAS, 367, 375
Beskin, V. S., Chernoglazov, A. V., Kiselev, A. M., & Nokhrina, E. E. 2017, MNRAS, 472, 3971
Bisnovatyi-Kogan, G. S., & Ruzmaikin, A. A. 1974, Ap&SS, 28, 45
Bisnovatyi-Kogan, G. S., & Ruzmaikin, A. A. 1976, Ap&SS, 42, 401
Blandford, R. D., & Königl, A. 1979, ApJ, 232, 34
Blandford, R. D., & Znajek, R. L. 1977, MNRAS, 179, 433

Boccardi, B., Perucho, M., Casadio, C., et al. 2021, A&A, 647, A67
Boizelle, B. D., Walsh, J. L., Barth, A. J., et al. 2021, ApJ, 908, 19
Bondi, H. 1952, MNRAS, 112, 195
Canvin, J. R., Laing, R. A., Bridle, A. H., & Cotton, W. D. 2005, MNRAS, 363, 1223
Chatterjee, K., Liska, M., Tchekhovskoy, A., & Markoff, S. B. 2019, MNRAS, 490, 2200
Clausen-Brown, E., Savolainen, T., Pushkarev, A. B., Kovalev, Y. Y., & Zensus, J. A. 2013, A&A, 558, A144
Contopoulos, I., Gabuzda, D., & Kylafis, N. 2015, in The Formation and Disruption of Black Hole Jets, (Switzerland: Springer International Publishing), Astrophysics and Space Science Library, 414
Fanaroff, B. L., & Riley, J. M. 1974, MNRAS, 167, 31P
Giovannini, G., Cotton, W. D., Feretti, L., Lara, L., & Venturi, T. 2001, ApJ, 552, 508
Gu, Q. S., Huang, J. S., Wilson, G., & Fazio, G. G. 2007, ApJ, 671, L105
Hada, K., Doi, A., Kino, M., et al. 2011, Nature, 477, 185
Heckman, T. M., Kauffmann, G., Brinchmann, J., et al. 2004, ApJ, 613, 109
Heinz, S., Merloni, A., & Schwab, J. 2007, ApJ, 658, L9
Hirotani, K. 2005, ApJ, 619, 73
Ho, L. C., Filippenko, A. V., & Sargent, W. L. W. 1993, ApJ, 417, 63
Hovatta, T. 2017, in New Frontiers in Black Hole Astrophysics, ed. A. Gomboc, 324, 149
Hovatta, T., Tornikoski, M., Lainela, M., et al. 2007, A&A, 469, 899
Hovatta, T., Valtaoja, E., Tornikoski, M., & Lähteenmäki, A. 2009, A&A, 494, 527
Jorstad, S. G., Marscher, A. P., Lister, M. L., et al. 2005, AJ, 130, 1418
Komatsu, E., Dunkley, J., Nolta, M. R., et al. 2009, ApJS, 180, 330
Komissarov, S. 2012, Central Engines: Acceleration, Collimation and Confinement of Jets (Berlin: Wiley), 81
Komissarov, S. S., Barkov, M. V., Vlahakis, N., & Königl, A. 2007, MNRAS, 380, 51
Komissarov, S. S., Vlahakis, N., Königl, A., & Barkov, M. V. 2009, MNRAS, 394, 1182
Kovalev, Y. Y., Pushkarev, A. B., Nokhrina, E. E., et al. 2020, MNRAS, 495, 3576
Laing, R. A., & Bridle, A. H. 2014, MNRAS, 437, 3405
Laing, R. A., Canvin, J. R., Cotton, W. D., & Bridle, A. H. 2006, MNRAS, 368, 48
Lister, M. L., Aller, M. F., Aller, H. D., et al. 2018, ApJS, 234, 12
Lobanov, A. P. 1998, A&A, 330, 79
Lobanov, A. 2017, Nat. Astron., 1, 0069
Lyubarsky, Y. 2009, ApJ, 698, 1570
McKinney, J. C., & Narayan, R. 2007a, MNRAS, 375, 513
McKinney, J. C., & Narayan, R. 2007b, MNRAS, 375, 531
Morganti, R., Peck, A. B., Oosterloo, T. A., et al. 2009, A&A, 505, 559
Nakamura, M., Asada, K., Hada, K., et al. 2018, ApJ, 868, 146
Narayan, R., Igumenshchev, I. V., & Abramowicz, M. A. 2003, PASJ, 55, L69
Narayan, R., SÄ dowski, A., Penna, R. F., & Kulkarni, A. K. 2012, MNRAS, 426, 3241
Narayan, R., Chael, A., Chatterjee, K., Ricarte, A., & Curd, B. 2022, MNRAS, 511, 3795
Nemmen, R. S., & Tchekhovskoy, A. 2015, MNRAS, 449, 316
Nokhrina, E. E., Beskin, V. S., Kovalev, Y. Y., & Zheltoukhov, A. A. 2015, MNRAS, 447, 2726
Nokhrina, E. E., Gurvits, L. I., Beskin, V. S., et al. 2019, MNRAS, 489, 1197
Nokhrina, E. E., Kovalev, Y. Y., & Pushkarev, A. B. 2020, MNRAS, 498, 2532
O'Sullivan, S. P., & Gabuzda, D. C. 2009, MNRAS, 400, 26
Park, J., Hada, K., Nakamura, M., et al. 2021, ApJ, 909, 76
Plavin, A. V., Kovalev, Y. Y., Pushkarev, A. B., & Lobanov, A. P. 2019, MNRAS, 485, 1822
Pushkarev, A. B., Kovalev, Y. Y., Lister, M. L., & Savolainen, T. 2009, A&A, 507, L33
Pushkarev, A. B., Hovatta, T., Kovalev, Y. Y., et al. 2012, A&A, 545, A113
Pushkarev, A. B., Kovalev, Y. Y., Lister, M. L., & Savolainen, T. 2017, MNRAS, 468, 4992
Russell, H. R., Fabian, A. C., McNamara, B. R., & Broderick, A. E. 2015, MNRAS, 451, 588
Tchekhovskoy, A., McKinney, J. C., & Narayan, R. 2008, MNRAS, 388, 551
Tchekhovskoy, A., McKinney, J., & Narayan, R. 2009, ApJ, 699, 1789
Tchekhovskoy, A., Narayan, R., & McKinney, J. C. 2011, MNRAS, 418, L79
Trager, S. C., Faber, S. M., Worthey, G., & González, J. J. 2000, AJ, 119, 1645
Urry, C. M., & Padovani, P. 1995, PASP, 107, 803
Worrall, D. M., Birkinshaw, M., Laing, R. A., Cotton, W. D., & Bridle, A. H. 2007, MNRAS, 380, 2
Yu, Q., & Tremaine, S. 2002, MNRAS, 335, 965
Yuan, F., Wang, H., & Yang, H. 2022, ApJ, 924, 124
Zamaninasab, M., Clausen-Brown, E., Savolainen, T., & Tchekhovskoy, A. 2014, Nature, 510, 126

Appendix A: Core shift in a quasi-parabolic flow

We suppose that the flow has a shape $r \sim \mathsf{z}^{\psi}$, with $\psi = 0.5$ corresponding to a strictly parabolic jet boundary. We start with Eq. 6 in Nokhrina et al. (2015):

$$\left(\nu\frac{1+z}{\delta}\right)^{2.5-\alpha} = c(\alpha)\frac{1+z}{\delta}\frac{2r}{\sin\theta}r_0^2\nu_0\left(\frac{e}{2\pi mc}\right)^{1.5-\alpha}k_eB^{1.5-\alpha}. \tag{A.1}$$

Here, we assume the following emitting particle energy distribution: $dn = k_e\gamma^{-1+2\alpha}d\gamma$, $\gamma \in [\gamma_{\rm min}; \gamma_{\rm max}]$, where r_0 is the electron classical radius, $\nu_0 = c/r_0$, the function $c(\alpha)$ is defined in Hirotani (2005), n, k_e, and B are in the plasma proper frame, while all the rest of parameters (ν, θ, etc.) are in the observer's frame. The standard assumption of equipartition between magnetic field and emitting plasma energy density (Blandford & Königl 1979; Lobanov 1998; Hirotani 2005) is written as:

$$k_e = \frac{B^2}{8\pi mc^2\Lambda}, \tag{A.2}$$

where $\Lambda = \ln\frac{\gamma_{\rm max}}{\gamma_{\rm min}}$ for $\alpha = -1/2$, and $\Lambda = \left(\gamma_{\rm max}^{1+2\alpha} - \gamma_{\rm min}^{1+2\alpha}\right)/(1+2\alpha)$ for $\alpha \neq -1/2$. The geometrical depth along the line of sight in the conical geometry is equal to $2\mathsf{z}\phi/\sin\theta$ in the nucleus frame while for a quasi-parabolic jet is $2r/\sin\theta$, where $r = a\mathsf{z}^{\psi}$ is the jet radius in the core at any given frequency.

First, we suppose that the jet has a constant Lorentz factor. We use the following dependencies for the particle number density and magnetic field in the plasma proper frame $n \propto r^{-2} \propto \mathsf{z}^{-2\psi}$ and $B \propto r^{-1} \propto \mathsf{z}^{-\psi}$. The first expression indicates the continuity of a flow with a constant speed, while the second one corresponds to a magnetic field created by an electric current flowing along the jet axis. The Doppler factor δ is a constant and only changes in derivation of the expressions for $\Omega_{r\nu}$, while B is connected with the different geometry. Setting the constant $C = 2c(\alpha)r_0^2\nu(e/2\pi mc)^{1.5-\alpha}$ we obtain

$$\nu^{2.5-\alpha} = C\left(\frac{\delta}{1+z}\right)^{1.5-\alpha}\frac{r_{\mathsf{z}}}{\sin\theta}k_{e,\mathsf{z}}B_{\mathsf{z}}^{1.5-\alpha}\left(\frac{\mathsf{z}}{Z}\right)^{(2.5-\alpha)\psi}, \tag{A.3}$$

where $k_{e,\mathsf{z}}$ and B_{z} are taken at a distance z, and Z is a position of the core observed at the frequency ν. We see that $\nu \propto Z^{-\psi}$ and from Eq. A.3 we obtain the same equation for $\Omega_{r\nu}$ as Eq. 10 but with $k_r = \psi$. Substituting Eq. A.2 into the relation between $\Omega_{r\nu}$ and the flow physical properties, we have:

$$C\left(\frac{\delta}{1+z}\right)^{1.5-\alpha}\frac{r_{\mathsf{z}}}{\sin\theta}k_{e,\mathsf{z}}B_{\mathsf{z}}^{1.5-\alpha} = \left(\frac{\Omega_{r\nu}}{\mathsf{z}\sin\theta}\right)^{(2.5-\alpha)\psi}, \tag{A.4}$$

and we obtain Eq. 12 for a magnetic field for $\alpha = -1/2$.

For the accelerating flow, we assume linear acceleration with a jet radius $\Gamma = r/R_L$. This means that the dependencies for a particle number density and a magnetic field are different. Indeed, the flow continuity leads in the plasma proper frame to $n \propto r^{-2}\Gamma^{-1} \propto \mathsf{z}^{-3\psi}$, while the toroidal magnetic field created by an electric current in the plasma proper frame can be written as $B \propto r^{-1}\Gamma^{-1} \propto \mathsf{z}^{-2\psi}$. In this case, if there is equipartition at some distance z_0, it does not hold everywhere throughout a jet. The emitting particle energy starts slowly dominating downstream until the acceleration becomes very slow. However, for a mildly relativistic flow the departure from equipartition, which is on the order of $u_{\rm part}/u_{\rm B} \approx \Gamma/\Gamma_0$, with Γ_0 being the bulk motion Lorentz factor at z_0, is not dramatic. The second difference comes from the Doppler factor changing along the accelerating flow. For a given observational angle θ, the Doppler factor has a maximum at approximately $\cos\theta = \beta$, which for a small angle $\theta \ll 1$ transforms into $\Gamma \approx \theta^{-1}$. For NGC 315 ($\theta = 38°$) the Doppler factor has a maximum at $\Gamma \approx 1.6$ and can be treated approximately as a constant. For the smaller Lorentz factors: $\delta \sim 2\Gamma$, while for the larger ones: $\delta \sim 1/\Gamma(1-\cos\theta)$. Thus, we consider three cases for an accelerating flow depending on the value of a Lorentz factor at the cores.

In case A, the Doppler factor is close to its peak and the emission from the fastest parts of a flow reaches the observer as $\theta \sim \Gamma^{-1}$. Substituting the dependencies for n, B, and r on Z into Eq. A.1, we obtain:

$$\nu^{2.5-\alpha} = C\left(\frac{\delta}{1+z}\right)^{1.5-\alpha}\frac{r_{\mathsf{z}}}{\sin\theta}k_{e,\mathsf{z}}B_{\mathsf{z}}^{1.5-\alpha}\left(\frac{\mathsf{z}}{Z}\right)^{(5-2\alpha)\psi}. \tag{A.5}$$

From this, Eq. 10 for $\Omega_{r\nu}$ with $k_r = 2\psi$ follows. Now, the relation of the core shift with jet physical parameters is:

$$C\left(\frac{\delta}{1+z}\right)^{1.5-\alpha}\frac{r_{\mathsf{z}}}{\sin\theta}k_{e,\mathsf{z}}B_{\mathsf{z}}^{1.5-\alpha} = \left(\frac{\Omega_{r\nu}}{\mathsf{z}\sin\theta}\right)^{(5-2\alpha)\psi}, \tag{A.6}$$

and assuming a close-to-equipartition state we obtain Eq. 13 for the magnetic field.

In case B, the fastest components are observed well within the emission cone as $\theta < \Gamma^{-1}$. We consider the case of $\delta = 2\Gamma$ and substitute:

$$\delta = 2\frac{r_{\mathsf{z}}}{R_{\rm L}}\left(\frac{Z}{\mathsf{z}}\right)^{\psi} \tag{A.7}$$

into Eq. A.1. The dependence of the observational frequency on a distance Z can be rewritten as

$$\nu^{2.5-\alpha} = C\left(\frac{2}{1+z}\frac{r_{\mathsf{z}}}{R_{\rm L}}\right)^{1.5-\alpha}\frac{r_{\mathsf{z}}}{\sin\theta}k_{e,\mathsf{z}}B_{\mathsf{z}}^{1.5-\alpha}\left(\frac{\mathsf{z}}{Z}\right)^{(3.5-\alpha)\psi}. \tag{A.8}$$

From this, the relation $k_r = \psi(3.5-\alpha)/(2.5-\alpha) = 4\psi/3$ for $\alpha = -1/2$ and Eq. 14 follow.

In case C, the emission from the fastest components are deboosted due to the relation $\theta > \Gamma^{-1}$, so it is of academic interest only. We substitute, using $\beta \approx 1$,

$$\delta = \frac{R_{\rm L}}{r_{\mathsf{z}}}\left(\frac{\mathsf{z}}{Z}\right)^{\psi}\frac{1}{1-\cos\theta} \tag{A.9}$$

into Eq. A.1 and obtain:

$$\begin{aligned}\nu^{2.5-\alpha} \;&=\; C\left(\frac{2}{1+z}\frac{R_{\rm L}}{r_{\mathsf{z}}}\right)^{1.5-\alpha}\frac{r_{\mathsf{z}}}{\sin\theta(1-\cos\theta)}\times \\ &\times\; k_{e,\mathsf{z}}B_{\mathsf{z}}^{1.5-\alpha}\left(\frac{\mathsf{z}}{Z}\right)^{(6.5-3\alpha)\psi}.\end{aligned} \tag{A.10}$$

The corresponding index is $k_r = \psi(6.5-3\alpha)/(2.5-\alpha) = 8\psi/3$ for $\alpha = -1/2$.

Appendix B: Toroidal and poloidal magnetic field extrapolation in an accelerating jet

The toroidal and poloidal magnetic field components in the core frame (indicated as $'$) are $B_\varphi = B_{\varphi'}/\Gamma$ and $B_p = B'_p$, respectively. In Sect. 4.4, we computed the magnetic field in the plasma proper frame and we called it B_{z} for simplicity. If the toroidal field dominates, $B_{\mathsf{z}} = B_\varphi$, otherwise $B_{\mathsf{z}} = B_p$. In a relativistic flow, the toroidal and poloidal components are related as $B_{\varphi'} = B_{p'}\frac{r}{R_{\mathrm{L}}}$. We assume the magnetic flux is conserved along the jet, with a pure poloidal field following $B'_p r^2 = \mathrm{const}$, and we note that if the poloidal component depends on r the relation still holds with some numerical coefficient. If the toroidal component dominates in the core region, the magnetic field is $B_g = B'_p(r/r_g)^2 = B_\varphi \Gamma R_{\mathrm{L}}/r(r/r_g)^2$. In the accelerating region $\Gamma R_{\mathrm{L}}/r \sim 1$, thus with $r \propto \mathsf{z}^\psi$:

$$B_g = B_{\mathsf{z}} \left(\frac{\mathsf{z}}{\mathsf{z}_g}\right)^{2\psi} . \tag{B.1}$$

Instead, if the poloidal components dominates in the core region, $B_g = B'_p(r/r_g)^2 = B_{\mathsf{z}}(r/r_g)^2$, from which

$$B_g = B_{\mathsf{z}} \left(\frac{\mathsf{z}}{\mathsf{z}_g}\right)^{2\psi} . \tag{B.2}$$

Appendix C: NGC 315 images

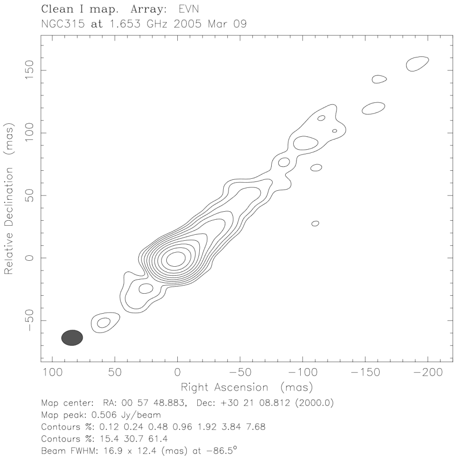

Fig. C.1. VLBI image of NGC 315 at 1 GHz.

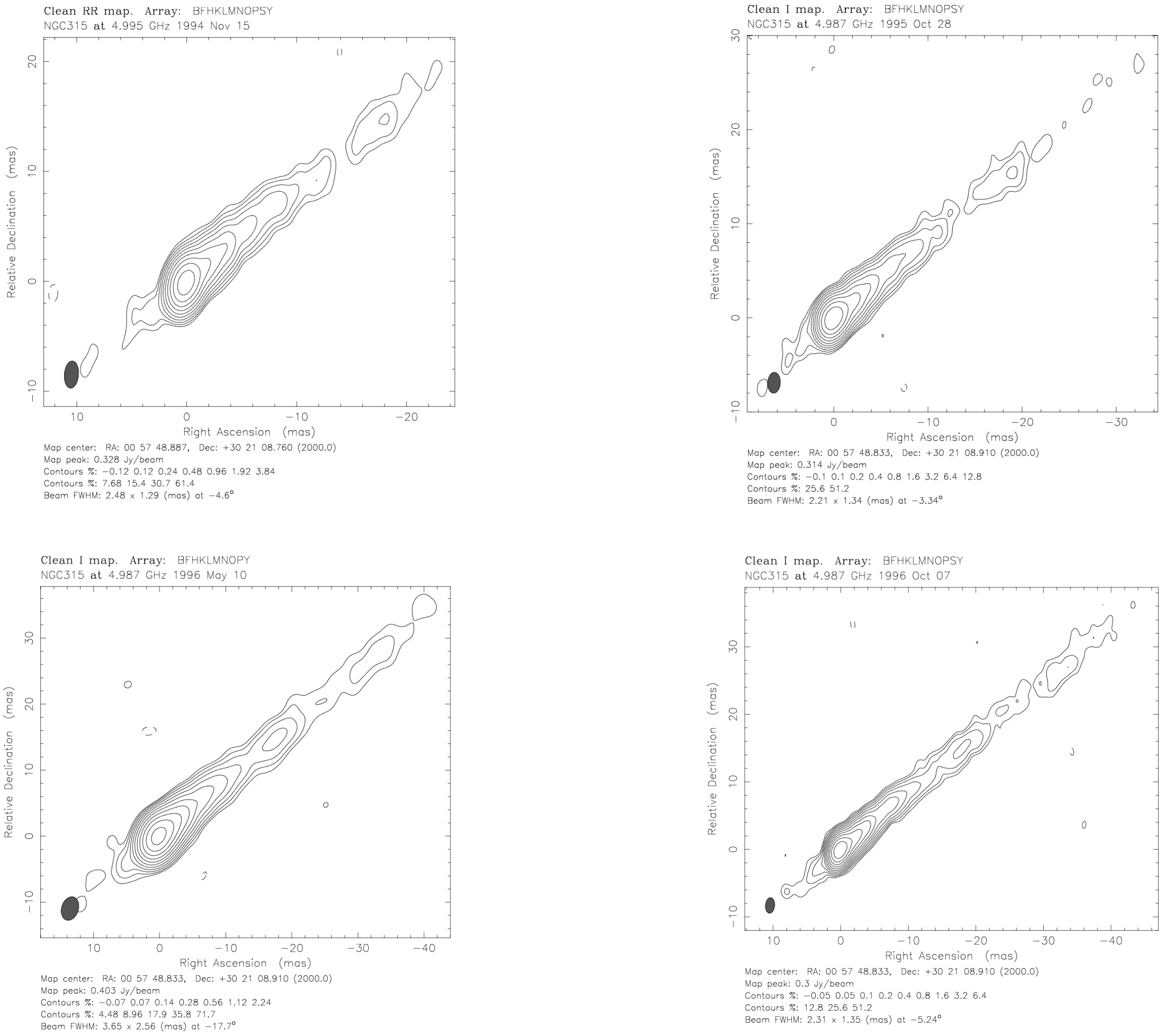

Fig. C.2. VLBI images of NGC 315 at 5 GHz.

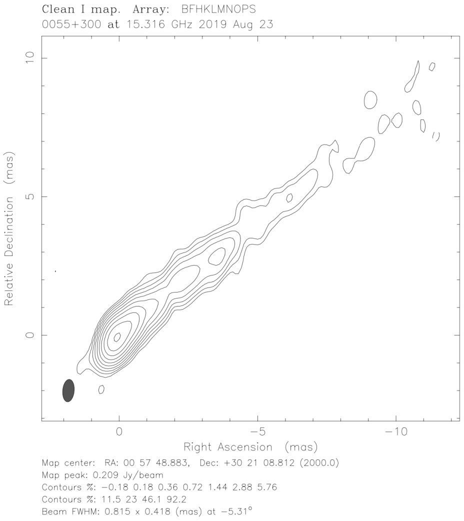

Fig. C.3. VLBI image of NGC 315 at 15 GHz.

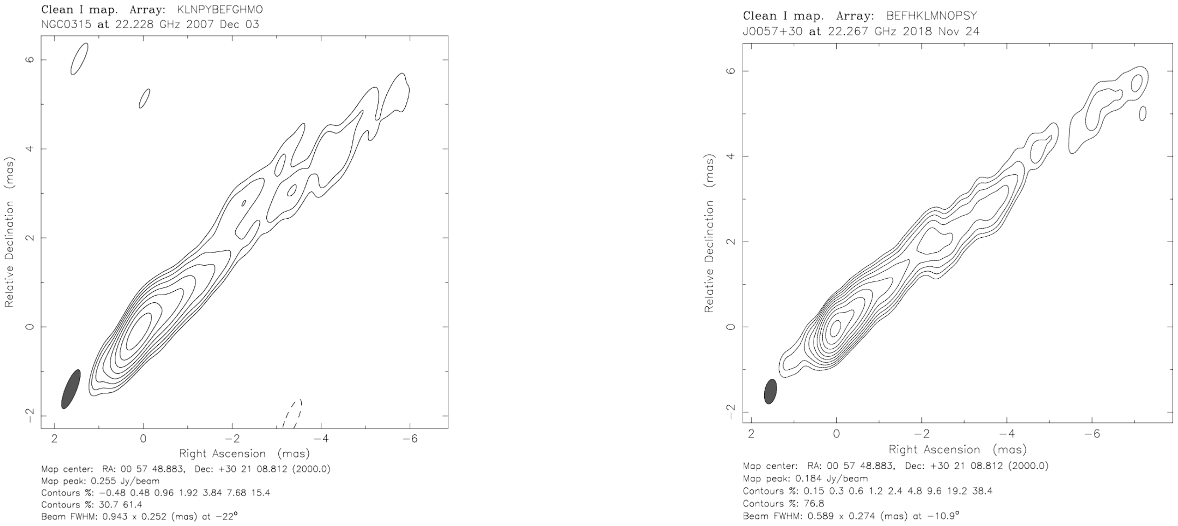

Fig. C.4. VLBI images of NGC 315 at 22 GHz.

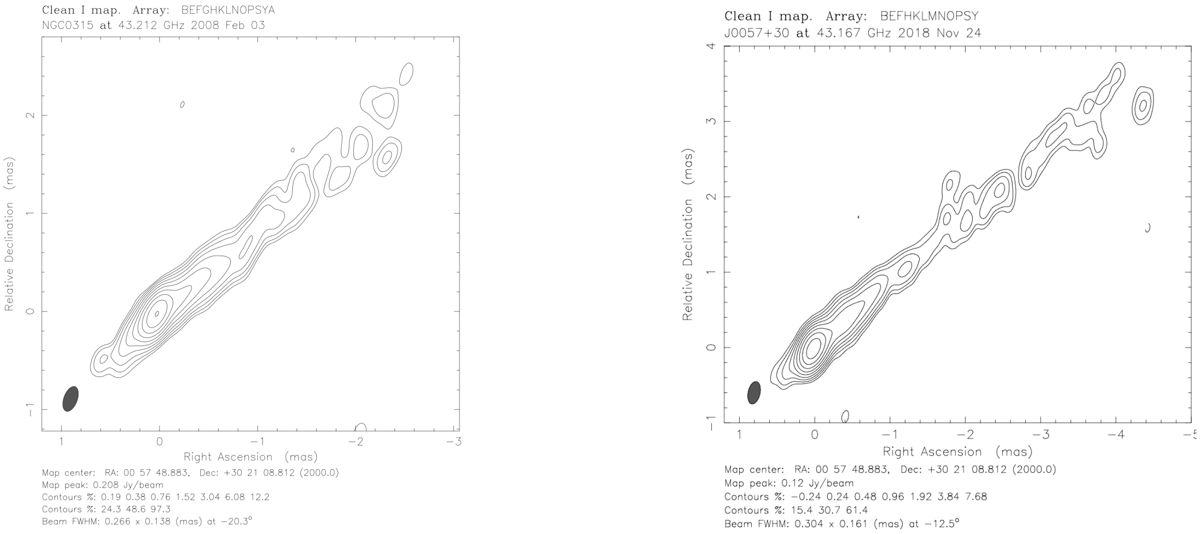

Fig. C.5. VLBI images of NGC 315 at 43 GHz.

5 Jet acceleration in radio galaxies: An application to NGC 315

This chapter presents the second tile of the series of works on NGC 315. In this project, the primary goal is to explore the nature of the jet acceleration mechanism. In detail, we aim at investigating the question that arose in Sect. 2.2.2 on whether thermal acceleration can still be relevant in jets on the sub-parsec and parsec scales. To achieve that, we employ the 2D relativistic magnetohydrodynamic code developed by Martí (2015). We simulate a comprehensive number of models, including thermally, magnetically, and kinetically dominated jets and, as a template for their initial conditions, we adopt the numerous observational constraints on NGC 315 shown in Chapter 4 and published by Boccardi et al. (2021).

Our results suggest that, when the internal energy of jets is not neglected, the conversion of thermal energy into kinetic energy is a viable way to efficiently accelerate them. Specifically, in the case of internal energy-dominated outflows, thermal acceleration becomes the main mechanism. While exploring this scenario, our set of simulated models provides hints on further characteristics of the jet propagation phenomenon. Namely, our simulations suggest that the presence of a shear layer, which can be identified with the accretion disk-launched winds (see Sect. 2.2.1), is a relevant element to favor the jet propagation. Indeed, its presence can delay the growth of instabilities and shield the internal spine from the action of the external medium. Finally, a number of our models can reproduce the opening angle and acceleration profiles of NGC 315. While this is an indicator of the quality of the observational results and models assumed, this comparison provides further insights into the nature of the jets. Indeed, small variations in the jet physical conditions at injection, which may happen on time scales of a few months, may lead to the differences observed in the Lorentz factor and opening angle profiles extracted across different epochs.

M. Perucho supported me while modifying the 2D RMHD code, originally written by J. M. Martí, to adapt it to pursue the goals of this project. The consequent analysis of the results of the simulations was entirely performed by me and, to do that, I used self-written Python codes. The paper has been written in collaboration with M. Perucho, which substantially helped in improving the overall presentation and the discussion of the results. J. López-Miralles and J. M. Martí provided suggestions during the adaptation of the code and later provided comments while writing the text of the manuscript. B. Boccardi provided comments on the final draft and contributed to enriching the comparison of the simulated data with NGC 315 and other AGN jets (Sects. 4.4 and 4.5 in the manuscript). The following manuscript has been accepted for publication and will be published in A&A. NOTE: in this chapter, the Lorentz factor of the bulk flow will be identified as γ, since in theoretical papers Γ is commonly employed for the adiabatic index.

Astronomy & Astrophysics manuscript no. main
December 12, 2023

Magnetic and thermal acceleration in extragalactic jets

An application to NGC 315

L. Ricci[1,2], M. Perucho[3,4], J. López-Miralles[3,5], J. M. Martí[3,4], B. Boccardi[1]

[1] Max-Planck-Institut fuür Radioastronomie, Auf dem Hügel 69, D-53121 Bonn, Germany
[2] Julius-Maximilians-Universität Würzburg, Fakultät für Physik und Astronomie, Institut für Theoretische Physik und Astrophysik, Lehrstuhl für Astronomie, Emil-Fischer-Str. 31, D-97074 Würzburg, Germany
[3] Departament d'Astronomia i Astrofísica, Universitat de València, C/ Dr. Moliner, 50, 46100, Burjassot, València, Spain
[4] Observatori Astronòmic, Universitat de València, C/ Catedràtic José Beltrán 2, 46980, Paterna, València, Spain
[5] Aurora Technology for the European Space Agency, ESAC/ESA, Camino Bajo del Castillo s/n, Urb. Villafranca del Castillo, 28691 Villanueva de la Cañada, Madrid, Spain

Received 11 May 2023 / Accepted 08 December 2023

ABSTRACT

Aims. Relativistic jets launched from active galactic nuclei accelerate up to highly relativistic velocities within a few parsecs to tens of parsecs. The precise way in which this process takes place is still under study. While magnetic acceleration is known to be able to accelerate relativistic outflows, little attention has been paid to the role of thermal acceleration. The latter has been assumed to act only on compact regions, very close to the central engine, and to become negligible on parsec scales. However, this holds under the assumption of small internal energies as compared to the magnetic ones, and whether this is true or what happens when we drop this assumption is currently uncertain.
Methods. We use a 2D relativistic magnetohydrodynamical code to explore jet acceleration from sub-parsec to parsec scales. As initial conditions for our models, we use observational constraints on jet properties derived by means of very long baseline interferometry observations for a Fanaroff Riley I radio galaxy, NGC 315. We investigate the parameter space established for this source and perform a number of simulations of magnetically, thermally or kinetically dominated jets at injection, and compare our results with the observed ones. Furthermore, we employ different models to characterize our jets, involving different magnetic field configurations, i.e., force-free vs. non-force-free configurations, as well as varying shear layer thicknesses.
Results. Our simulated jets show that when thermal energy is comparable to or exceeds magnetic energy, thermal acceleration becomes significant at parsec scales. This result has important consequences, potentially extending the acceleration region far beyond the collimation scales, as thermal acceleration can effectively operate within a conically expanding jet. In all the models, we observe acceleration to be driven by expansion, as expected. A number of our models allow us to reproduce the acceleration and opening angles observed in NGC 315. Finally, our results indicate that disk-launched winds might play an important role in the jet propagation. Namely, when the jet has an initial force-free magnetic field configuration, thicker shear layers are needed to shield the internal spine from the action of the external medium, delaying the growth of instabilities.

Key words. magnetohydrodynamics (MHD) – relativistic processes – methods: numerical – galaxies: jets – galaxies: active

1. Introduction

Active galactic nuclei (AGN) power relativistic outflows that propagate up to hundreds and even thousands of kiloparsecs (Begelman et al. 1984; Blandford et al. 2019). A fundamental ingredient for their capacity to extend through nine orders of magnitude in distance is their inertia (e.g., Perucho 2019, and references therein), achieved by means of the investment of energy into the acceleration of the flow to relativistic velocities. The mechanisms behind the establishment of such outflows have been largely studied in the past years, and substantial progress has been made (e.g., Vlahakis & Königl 2004; Komissarov et al. 2007). However, such studies have focused on the assumption that acceleration is, in essence, magnetically driven, ignoring thermal acceleration.

The crucial region in which this process can be explored in the jet is the so-called acceleration and collimation region. There, jets collimate evolving from a parabolic geometry (i.e., $r \propto z^{\sim 0.5}$, where z is the radial distance from the core and r is the jet radius), to a conical one ($r \propto z^{\sim 1}$), and accelerate up to high relativistic velocities along the same distance (see e.g., Boccardi et al. 2017, and references therein). Therefore, in cold jets, the nature of the collimation and acceleration phenomena seems to be strictly correlated. The current common view of this process suggests that equipartition between magnetic field and particle energy is reached (Nokhrina et al. 2019, 2020) by the end of the acceleration region, and that external conditions, such as the crossing of the Bondi radius (Kovalev et al. 2020), may play a relevant role in shaping the jet expansion profile. It is often considered that equipartition refers to an equilibrium between magnetic and kinetic energy densities in the jet but, from synchrotron radiative output, only the equipartition between magnetic and internal energies can be inferred. It is therefore plausible that even though magnetic and internal energy are in or close to equipartition at the end of the acceleration region, it is the kinetic energy that dominates jet dynamics from that point on.

Jets in Fanaroff-Riley I (FR I; Fanaroff & Riley 1974) radio galaxies, which are used as example of this study, are expected to reach maximum Lorentz factors of $\gamma_{\max} \sim 10$, as seen from statistical studies of BL Lac objects, their blazar counterpart (Hovatta et al. 2009). As mentioned above, acceleration can be related to two main possible sources of energy (see, e.g., Komissarov 2012): i) thermal energy via the Bernoulli mechanism, or ii) magnetic energy via differential collimation mechanism. The former allows the jet to reach a maximum Lorentz factor $\gamma_{\max} = \gamma[1 + 4\varepsilon/(3c^2)]$, where ε is the jet specific internal energy at injection and γ is the initial Lorentz factor, whereas for the latter $\gamma_{\max} = \gamma[1 + B^2/(4\pi\rho c^2)]$ where B and ρ are, respectively, the jet magnetic field and rest-mass density.

The current paradigm of magnetic jet acceleration relies on the theoretical work of Vlahakis & Königl (2003a,b, 2004). The authors suggest that thermal acceleration would be relevant only at very compact scales, and magnetic acceleration would take over and prolong the accelerating process up to parsec scales. Magnetic acceleration was further studied by Komissarov et al. (2007), who showed how the conversion of magnetic energy is a viable way to accelerate the bulk flow by means of numerical simulations. A relevant aspect revealed by these works is that magnetic acceleration does not occur when the outflow is following a conical expansion, but it becomes effective when the jet expands following a parabolic law. In this process, the toroidal field acts not only as a collimating agent, but also as the main driver of jet bulk acceleration. The basic theory behind this process is summarized in Komissarov (2012).

However, this view is founded on a more fundamental assumption that the jet internal energy is rather small as compared to the total jet energy flux. Vlahakis & Königl (2004) used classical expressions to derive this conclusion, which implicitly means that the rest-mass energy of the particles is significantly larger than their internal energy. It is nevertheless unclear that jet thermodynamics can be dealt without considering their relativistic nature (see, e.g., Perucho et al. 2017). On the one hand, jets can be thermodynamically relativistic (i.e., $\varepsilon \geq c^2$). On the other hand, strong jet expansion is prevented by either the ambient pressure or the magnetic tension provided by a toroidal field, which can keep the jet plasma at relativistic internal energies, avoiding its cooling to $\varepsilon \ll c^2$. This is, at least, observed in numerical simulations (e.g., Martí et al. 2016; Moya-Torregrosa et al. 2021; Anglés-Castillo et al. 2021). As a consequence, internal energy could still be relevant for the overall process of jet acceleration up to parsec scales. Thermal acceleration (together with magnetic acceleration) in jets is suggested in López-Miralles et al. (2022) for the case of outflows from high-mass X-ray binaries. In this paper, we relax the assumption of cold jets and explore the different roles that both accelerating mechanisms can play.

As initial template for the physical conditions, we use the radio galaxy NGC 315 as prototype. NGC 315 is a nearby ($z = 0.0165$, Trager et al. 2000), giant FR I (e.g., Laing et al. 2006) radio galaxy whose acceleration and collimation properties have been extensively studied by employing very long baseline interferometry (VLBI) observations. Such observations showed the jet in NGC 315 to accelerate up to $v \sim (0.8 - 0.9)\,c$, and to collimate on similar scales, with the highest Lorentz factor $\gamma \sim 4$ reached at ~ 2 pc (Boccardi et al. 2021; Park et al. 2021; Ricci et al. 2022). Other physical properties such as the magnetic field strength, the jet power and the jet width have been estimated (Boccardi et al. 2021; Ricci et al. 2022) and are also used as initial conditions in our models. The complete characterization of the jet at injection would require initial values for density and pressure. However, they are unknown and we use them as free parameters that allow us to vary the jet configuration and dominant energy channel at the boundary condition of our numerical simulations at the initial state.

The goal of this paper is twofold: while exploring the acceleration in different types of jets, i.e., hot and cold, and the interplay between the separate energy channels along the propagation, we aim at reproducing the final part of the acceleration in NGC 315 and at testing whether the inferred physical properties on sub-parsec scales allow for the jet to remain stable on parsec scales and accelerate up to $\gamma \sim 4$. To achieve the goal of our work, we investigate a large number of setups using the 2D relativistic magnetohydrodinamical (RHMD) code presented in Martí (2015b); Martí et al. (2016).

The paper is structured as follows. In Sect. 2 we describe the numerical setup; in Sect. 3 we present our results; in Sect. 4 we discuss them and in Sect. 5 we draw our conclusions.

2. Numerical simulations

2.1. Numerical methods

The simulations presented in this paper are performed using the conservative, 2D axisymmetric RMHD code presented in Martí (2015b). While for an in-depth study on the jet propagation, a 3D approach could allow us to study the phenomenon with fewer assumptions (allowing for example to explore the effects of the development of helical modes, see, e.g., López-Miralles et al. 2022), we consider the 2D axisymmetric approach well suited for our goals. Indeed, jet acceleration is connected with jet expansion, which is an axisymmetric process. Furthermore, a 2D grid allows to test a large number of models due to the lower computational resources required.

Regarding the effects of our assumption on jet stability, the instability modes that we observe are mostly associated with small-scale structures (see Sect. 3). In the long term, the oscillation of the jet outer radius could trigger the development of pinching modes, which are, in general, not disruptive for relativistic flows (e.g., Perucho et al. 2005). Moreover, the dynamics of the simulated jets at injection is completely dominated by expansion and, in such a situation, the growth of instability modes is negligible (Hardee 1986).

In our code, we employ a second-order Godunov-type scheme with the HLL Riemann solver (Harten et al. 1983) and the piecewise linear method (PLM) for cell reconstruction, where the VanLeer slope limiter preserves monotonicity (van Leer 1974; Mignone & Bodo 2006). The limiter is degraded to MinMod(Roe 1986) when strong shocks are detected in order to avoid numerical oscillations. Time integration follows the third-order TVD-preserving Runge-Kutta scheme of Shu & Osher (1989) with CFL = 0.2. The relativistic correction algorithm CA2 of Martí (2015a) is used to correct the conserved variables after each time iteration. The magnetic field divergence-free constraint is preserved with the constrained transport (CT) method (Balsara & Spicer 1999).

2.2. Model assumptions and transversal equilibrium

We study the acceleration problem by means of the ideal RMHD equations, to which we impose axisymmetry. We describe the system using cylindrical coordinates (r,ϕ,z) where r, ϕ and z are the radial, azimuthal and axial coordinates. Axisymmetry allows us to drop the dependence on the azimuthal cylindrical coordinate in the RMHD equations. We assume both the jet and ambient plasma to be perfect gas with a constant adiabatic index of $\Gamma = 4/3$. Taking into account that the ambient medium is used as a passive element in the simulations and that the jet plasma is hot, we consider this approach sufficient for our purposes.

The code evolves the rest-mass, momentum and total energy densities, and the magnetic field in a conservative way. Besides this, and in order to minimize the perturbation of the flow, the jet is injected in conditions of transversal equilibrium. As a consequence, the radial components of the magnetic field and the flow velocity, $B^r(r)$, $v^r(r)$, at injection are set to zero, and the equilibrium solutions are characterized by six functions, namely the density and pressure, $\rho(r)$, $p(r)$, and the two remaining components of the flow velocity, $v^\phi(r)$, $v^{\rm z}(r)$, and of the magnetic field, $B^\phi(r)$, $B^{\rm z}(r)$.

In what follows, all the quantities will be expressed in code units, in which the initial jet radius, r_j, the ambient density at the jet base, ρ_a, and the speed of light, c, are equal to 1 (and a factor $1/\sqrt{4\pi}$ is absorbed in the definition of the magnetic field).

The transversal equilibrium condition is given by a single ordinary differential equation (see e.g., Martí 2015b):

$$\frac{dp^*}{dr} = \frac{\rho h^* \gamma^2 (v^\phi)^2 - (b^\phi)^2}{r}, \tag{1}$$

in which, $\gamma = 1/\sqrt{1 - v^i v_i}$ ($i = r, \phi, {\rm z}$, and summation over repeated indices is assumed) is the Lorentz factor, p^* and h^* are the total (gas and magnetic) pressure and total specific enthalpy of the jet, namely $p^* = p + b^2/2$ and $h^* = 1 + \varepsilon + p/\rho + b^2/\rho$. In the previous expressions, $b^2 = b^\mu b_\mu$ ($\mu = t, r, \phi, {\rm z}$), where b^μ is the magnetic field four-vector in the fluid rest frame. Its components are defined as $b^0 = \gamma B^i v_i$ and $b^i = B^i/\gamma + b^0 v^i$ which leads to

$$b^2 = \frac{B^2}{\gamma^2} + (B^i v_i)^2\,. \tag{2}$$

Moreover, we assume constant initial density and axial velocity across the jet, and a non-rotating jet model

$$\rho(r) = \begin{cases} \rho_j, & 0 \le r \le 1 \\ 1, & r > 1, \end{cases} \tag{3}$$

$$v^{\rm z}(r) = \begin{cases} v^{\rm z}_j, & 0 \le r \le 1 \\ 0, & r > 1, \end{cases} \tag{4}$$

and $v^\phi(r) = 0$. With these definitions and the corresponding profiles for the azimuthal and axial components of the magnetic field, $B^\phi(r)$, $B^{\rm z}(r)$, Eq. 1 gives the equilibrium pressure profile of the jet at injection.

2.3. Physical model

In code units, the total jet power is given by

$$L_j = \pi\left[\rho_j h_j \gamma_j^2 + (B^\phi_j)^2\right] v^{\rm z}_j\,. \tag{5}$$

The specific enthalpy is defined as:

$$h_j = 1 + \varepsilon_j + p_j/\rho_j \tag{6}$$

with pressure, density and specific internal energy related through an ideal gas equation of state, $\varepsilon_j = p_j/[\rho_j(\Gamma - 1)]$, where Γ is the corresponding adiabatic index.

The different energy flux channels that account for the total jet power (Eq. 5) are computed as follows:

- Magnetic: $F_{\rm M} = (B^\phi_j)^2 v^{\rm z}_j$;
- Internal: $F_{\rm I} = \rho_j \gamma_j^2 v^{\rm z}_j (h_j - 1)$;
- Kinetic: $F_{\rm K} = \rho_j \gamma_j^2 v^{\rm z}_j$.

In addition, we compute the total rest mass energy as $F_{\rm R} = \rho_j \gamma_j v^{\rm z}_j$. As far as the magnetic field configuration is concerned, we use two different approaches: the non-force-free configuration, as defined in Martí (2015b), and the force-free configuration as defined in Moya-Torregrosa et al. (2021). The two models are described in Sect. 2.3.1 and in Sect. 2.3.2, respectively.

We note that the transition of the initial magnetic field and pressure profiles at the jet/ambient medium interface is smoothed out by convolving the original profiles with a continuous function mimicking a shear layer. In this way, we avoid discontinuities and abrupt changes in our initial conditions, making them more stable. As shear layer, we consider the function $f(r) = 1/\cosh(r^m)$ (Bodo et al. 1994; Perucho et al. 2004), in which $m = 2, 4,$ and 8 with $m = 8$ being the value used the most in our models.

Since our simulations are axisymmetric, we assume reflecting boundary conditions (b.c.) on the axis ($r = 0$), while we assume zero gradient b.c. at large values of the radial coordinate. Along the z direction, we use inflow/outflow b.c. at the inner boundary, for the jet and the ambient medium, respectively, and outflow b.c. through the outer one.

In this study, we do not take into account the effects associated with resistivity and, consequently, magnetic reconnection. Although the length scales at which reconnection occurs are expected to be significantly smaller than those addressed in this work, its impact might still be relevant. In particular, the conversion of magnetic energy into thermal energy may elevate the pressure within the jet, increasing its internal energy budget. This effect could potentially manifest on larger scales when an important fraction of magnetic energy across the jet is involved, potentially altering the physical characteristics of the bulk flow and enhancing the role of thermal acceleration, due to the increased internal energy. Although investigating the role of resistivity and magnetic reconnection would be of great interest (see e.g. Medina-Torrejón et al. 2021; Mattia et al. 2023), it is beyond the scope of this work.

2.3.1. Non-force-free configuration

In the non-force free configuration, the azimuthal magnetic field component is expressed as (Martí 2015b):

in which $B^\phi_{\rm j,m}$ is the maximum toroidal field strength reached at the distance $R_{\rm m} = 0.37$. In this configuration, the azimuthal magnetic field grows linearly in the region $r \ll R_{\rm m}$, reaches its maximum at $r = R_{\rm m}$, and then decreases as $\propto r^{-2}$ when $r \gg R_{\rm m}$ as shown in the upper left panel of Fig. 1. The axial component is assumed to be constant across the jet radius,

$$B^{\rm z}(r) = \begin{cases} B^{\rm z}_j, & 0 \le r \le 1 \\ 0, & r > 1. \end{cases} \tag{7}$$

Therefore, the mean[1] azimuthal magnetic field component within the jet is:

$$\bar{B}^\phi_j = 4 B^\phi_{\rm j,m} R_{\rm m}\left[1 - R_{\rm m}\,{\rm atan}\left(\frac{1}{R_m}\right)\right] \tag{8}$$

while the axial one is simply $\bar{B}^{\rm z}_j = B^{\rm z}_j$.

---

[1] The mean quantities are computed as $\bar{q}_j = \int_0^1 q(r) r\,{\rm d}r \Big/ \int_0^1 r\,{\rm d}r$.

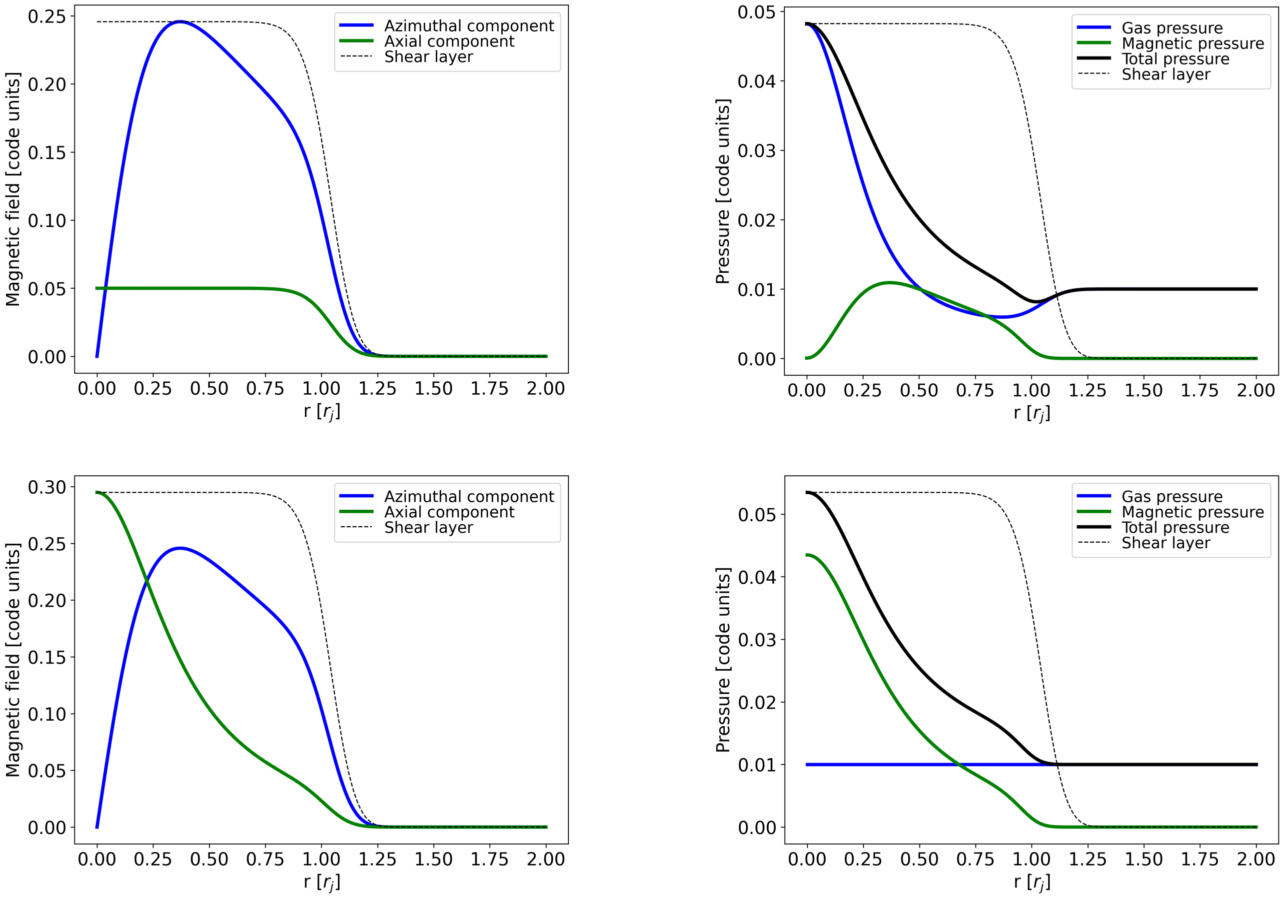

Fig. 1. Initial profiles along the radial distance in the different magnetic field configurations. We use the representative values of $B^{\phi} = 0.24$, $R_m = 0.37$, $v_j = 0.8$, $p_a = 0.01$, and $B^z = 0.05$ (for the non-force free configuration) in code units. Upper panels: non-force-free configuration. Lower panel: force-free configurations. Left panels: Magnetic field distribution of the azimuthal (blue line) and axial (green line) components. Right panels: profile distribution of the gas pressure (blue line), magnetic pressure (green line), and total pressure (black line). The dotted black line indicates the shear layer with $m = 8$ normalized at the higher value in the plot for an easier representation.

By solving Eq. 1 with these magnetic field components, we obtain a gas pressure profile expressed as

$$p(r) = \begin{cases} 2\left[\dfrac{B^{\phi}_{\mathrm{j,m}}}{\gamma_j(1+(r/R_{\mathrm{m}})^2)}\right]^2 + C, & 0 \le r \le 1 \\ p_a, & r > 1. \end{cases} \tag{9}$$

in which the integration constant can be computed using the boundary condition at the jet/ambient medium interface $p^*(r = 1) = p_a$, leading to

$$C = p_a - \frac{(B^z_j)^2}{2} - \frac{(B^{\phi}_1)^2}{2\gamma_j^2}[1 + (R_m)^2] \tag{10}$$

(in this expression, $B^{\phi}_1 = B^{\phi}(r = 1)$). The mean gas pressure is $\bar{p}_j = p_a - (B^z_j)^2/2$ and the magnetic pressure $\bar{p_m} = \bar{b}^2_j/2$. Fiducial magnetic and thermal pressure profiles are shown in the lower left panel of Fig. 1.

The magnetic tension ($\tau_{\mathrm{m}} = -(b^{\phi})^2/r$, see, e.g., Martí et al. 2016; Moya-Torregrosa et al. 2021) is:

$$\tau_{\mathrm{m}}(r) = -\frac{4(B^{\phi}_{\mathrm{j,m}})^2}{\gamma^2 R^2_{\mathrm{m}}} \frac{r}{(1 + (r/R_{\mathrm{m}})^2)^2}. \tag{11}$$

2.3.2. Force-free configuration

In the force-free configuration, the azimuthal magnetic field component has the same profile as in the non-force-free configuration, while the axial component becomes:

$$B^z(r) = \begin{cases} \dfrac{2B^{\phi}_{\mathrm{j,m}}/\gamma_j}{1 + (r/R_{\mathrm{m}})^2}, & 0 \le r \le 1 \\ 0, & r > 1. \end{cases} \tag{12}$$

The axial magnetic field has its maximum at the jet center and decreases towards the outer radius as $\propto r^{-2}$. Its mean value is:

$$\bar{B}^z_j = \frac{2B^{\phi}_{j,m}R^2_m}{\gamma_j}\left[\ln(R^2_m + 1) - \ln(R^2_m)\right]. \tag{13}$$

In this configuration, the gas pressure is constant in the jet, with $p(r) = \bar{p}_j = p_a$, $0 \le r \le 1$, and the pressure equilibrium is achieved by compensating the magnetic tension produced by the toroidal component of the field (see Eq. 11) with the magnetic pressure produced by the axial one.

The advantage of this magnetic configuration is that the gas pressure becomes independent from the jet magnetization, allowing the field to increase without generating non-physical, negative thermal pressures at the jet/ambient boundary (Moya-Torregrosa et al. 2021). This configuration is thus necessary to

Table 1. Initial conditions of the simulated models.

Model code	p_j $[p_a]$	ρ_j $[\rho_a]$	B [G]	ϕ_B [deg]	v_z [c]	$\mathcal{M}_\mathrm{ms}$	F_j $[10^{43}\mathrm{erg/s}]$
FMH1	1.0	0.01	0.42	70.7	0.87	1.12	4.8
FMH1_m4	1.0	0.01	0.42	70.7	0.87	1.12	4.8
FIH2	2.0	0.01	0.46	68.9	0.84	1.05	5.6
FIH3	3.0	0.01	0.49	67.3	0.81	1.01	6.1
FIH4	4.0	0.01	0.52	66.4	0.79	1.00	6.7
FMH1b	1.0	0.01	0.59	74.4	0.92	1.00	12.7
FMH1.3	1.3	0.05	0.55	67.8	0.82	1.00	6.3
FKS1	1.0	0.1	0.39	61.3	0.64	1.00	2.54
FML1	1.0	0.001	0.56	75.3	0.93	1.01	12.5
FMH1c	1.0	0.01	0.68	75.3	0.93	1.00	17.8
FIH3b	3.0	0.01	0.13	60.6	0.61	1.04	1.6
FMH0.3	0.3	0.05	0.66	72.7	0.90	1.03	12.4
NIH4	4.0	0.01	0.29	89.9	0.70	1.06	3.6
NIH1	1.0	0.01	0.22	88.2	0.75	1.09	1.6

Notes. Column 1: model names; Column 2: initial jet thermal overpressure factor; Column 3: initial jet density with respect to the ambient one; Column 4: initial magnetic field strength in G; Column 5: initial magnetic pitch angle; Column 6: initial axial velocity; Column 7: average initial Magnetosonic number; Column 8: total jet flux in units of 10^{43}erg/s.
The model names obey the following logic. i) The first letter is for the magnetic field configuration: F for force-free and N for non-force-free. ii) The second letter is for the dominant energy channel: M for magnetic, I for internal, and K for kinetic. iii) The third letter is for the jet density: S for $\rho_j \geq 0.1\,\rho_a$, H for $0.01\,\rho_a \leq \rho_j < 0.1\,\rho_a$, and L for $\rho_j < 0.01\,\rho_a$. iv) The last number is the same as the jet thermal overpressure factor at injection. In the case of two models with the same nomenclature, we add a letter in progressively alphabetical order at the end of the name. Models with _m4 have the shear layer exponent set to $m = 4$ while for all the other models the exponent is $m = 8$.

Table 2. Modeled, simulated, and final jet flux ratios for the different energy channels. The differences between them are due to the convolution of the initial profiles with the shear layer. The final values are the different ratios in the row of the last cells.

Model code	F^i_K/F_j [%]	F^i_R/F^i_K [%]	F^i_M/F_j [%]	F^i_I/F_j [%]	F^s_K/F_j [%]	F^s_R/F^s_K [%]	F^s_M/F_j [%]	F^s_I/F_j [%]	F^f_K/F_j [%]	F^f_R/F^f_K [%]	F^f_M/F_j [%]	F^f_I/F_j [%]
FMH1	9.03	49.31	54.86	36.11	24.33	65.47	47.92	27.75	35.19	44.95	36.92	27.89
FMH1_m4	9.03	49.31	54.86	36.11	33.10	67.27	43.40	23.50	47.53	52.56	34.56	17.91
FIH2	6.11	54.26	44.99	48.90	18.97	68.99	41.01	40.02	34.98	38.41	36.71	28.31
FIH3	4.63	58.64	39.81	55.56	15.83	72.04	36.94	47.23	31.66	36.48	35.75	32.59
FIH4	3.79	61.31	35.60	60.61	13.72	73.81	33.55	52.73	30.84	33.17	29.88	39.28
FMH1b	5.73	39.19	71.33	22.94	13.53	56.65	68.31	18.16	25.92	30.17	60.96	13.12
FMH1.3	23.99	57.24	51.06	24.95	31.50	65.62	47.49	21.01	51.58	42.62	35.29	13.13
FKS1	51.78	76.84	27.51	20.71	57.98	81.25	24.58	17.44	76.48	68.39	15.10	8.42
FML1	0.66	36.76	72.74	26.60	10.20	60.76	69.15	20.65	19.88	30.58	62.64	17.48
FMH1c	4.68	36.76	76.58	18.74	10.69	54.31	74.38	14.93	22.62	24.82	66.81	10.57
FIH3b	7.34	79.24	4.61	88.05	27.92	87.02	3.82	68.26	47.86	55.33	3.96	48.18
FMH0.3	23.16	43.59	71.28	5.56	26.82	53.22	68.38	4.80	46.36	32.43	47.73	5.91
NIH4	4.63	71.41	21.26	74.11	17.41	81.48	18.96	63.63	29.79	46.76	14.55	55.66
NIH1	13.11	66.14	34.44	52.45	36.57	78.81	24.74	38.69	46.75	60.08	16.86	36.39

Notes. Column 1: model names; Column 2: modeled kinetic flux ratio; Column 3: modeled rest mass flux over modeled kinetic flux ratio; Column 4: modeled magnetic flux ratio; Column 5: modeled thermal flux ratio; Column 6: simulated kinetic flux ratio; Column 7: simulated rest mass flux over simulated kinetic flux; Column 8: simulated magnetic flux ratio; Column 9: simulated thermal flux ratio. Column 10: final kinetic flux ratio; Column 11: final rest mass flux over final kinetic flux; Column 12: final magnetic flux ratio; Column 13: final thermal flux ratio.

simulate models of highly magnetized jets in pressure equilibrium. The resulting initial radial magnetic field and pressure profiles are shown in the bottom panels of Fig. 1.

2.4. Jet and ambient parameters

With the aim to study jet acceleration from sub-relativistic to relativistic outflow velocities, we inject the jets with the lowest possible axial velocity. The injection of low velocity, highly magnetized flows makes them submagnetosonic, which allows waves to propagate upstream and generate inconsistencies between the

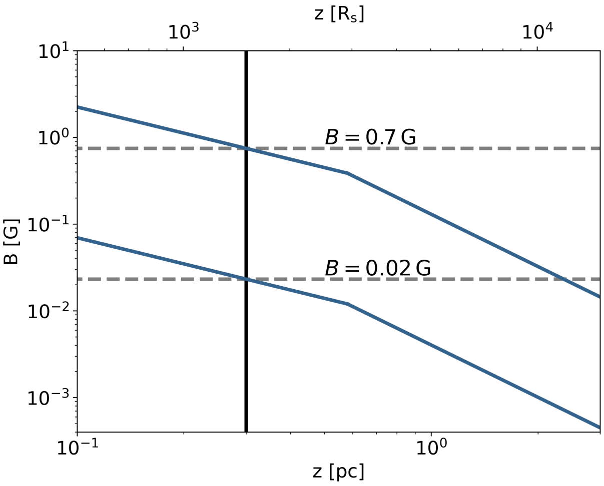

Fig. 2. Expected magnetic field distribution between 0.1 pc and 3 pc. The upper and lower magnetic field limits are extrapolated from the core shift measurement under the different assumption (for the details see Ricci et al. 2022). The black vertical line highlights the starting point of $z_i = 0.3$ pc of our simulations, while the horizontal dashed lines are the expected range of magnetic field at z_i.

jet in the grid and its injection boundary condition. In particular, the axial magnetic field is changed and a jump appears between the boundary and the first cell in the grid, which represents an unphysical situation.

To overcome this problem, the initial jet velocity v^z was adjusted in the different models to result in magnetosonic Mach numbers of at least 1. While this approach prevents us from exploring the acceleration starting from sub-relativistic velocities, it still allows us to achieve our main goal, which is understanding the role played by internal and magnetic energy fluxes in accelerating jets. Specifically, FR I jets can reach velocities up to $\gamma \sim 10$ (e.g., Hovatta et al. 2009) at parsec scales, and from our injection velocities, which imply $\gamma \sim 1-2$, we can explore the increase from mildly relativistic to relativistic speeds for different types of jets, i.e., magnetically, internally or kinetically dominated, and the velocity structures that they generate.

Using our information on NGC 315 as starting point, we design our grids to simulate outflows along the z-coordinate at $z_i = 0.3$ pc, since this corresponds to a distance at which the jet has already velocities in the range $v^z_j \sim 0.3\,c$ to $v^z_j \sim 0.8\,c$, depending on the frequencies and epochs considered (see Fig. 3, Ricci et al. 2022). The grid extends up to $z_o = 3.3$ pc, covering a distance that is large enough to let us explore the acceleration phenomenon from sub-parsec to parsec scales. In the radial direction, the grid extends from $r_i = 0$ up to $r_o = 0.9$ pc, with an initial jet radius of $r_j = 0.03$ pc (see Fig. 3, Boccardi et al. 2021). Taking into account that jets are built with large overpressure factors (see below), this radial size of the grid is large enough to allow for jet expansion. With our choice of the initial jet radius, our numerical domain consists of a grid of $30\,r_j \times 100\,r_j$ with $n_r \times n_z = 600 \times 2000$ cells.

To determine the initial magnetic field we refer to Fig. 2, which highlights the possible magnetic field values, in our region of interest, extracted from the results published in Ricci et al. (2022). According to the different models and different magnetic field evolution, the initial total strength is allowed to span between $B = 0.02$ G and $B = 0.7$ G. The magnetic field structure considered in this paper ranges from helical in the force-free configurations (with the mean pitch angle defined as $\bar{\phi}_{\mathrm{B}_j} = \tan^{-1}(\bar{B}^{\phi}_j/\bar{B}^z_j)$), to a dominating toroidal field in the non-force-free configurations.

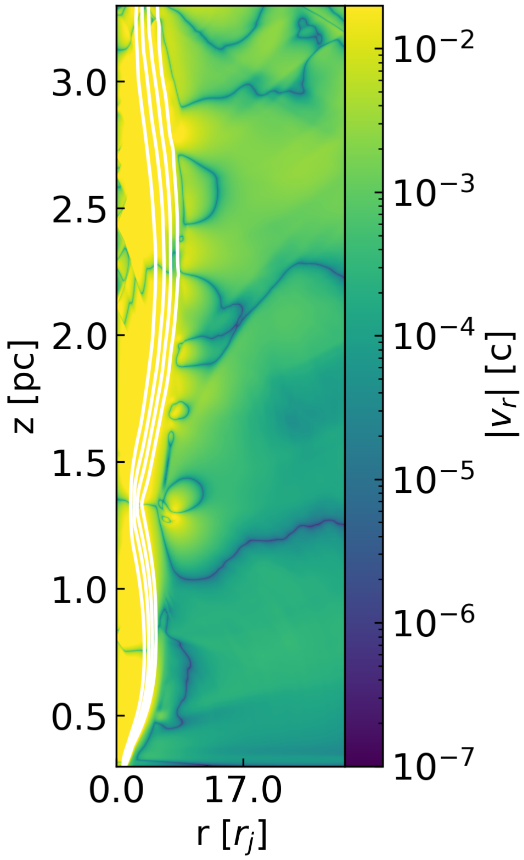

Fig. 3. Absolute value of radial velocity for the model FMH1_m4. The white contours highlight the tracer values at levels of 0.2, 0.4, 0.6, and 0.8 (the tracer levels are in decreasing order, i.e., from 0.8 to 0.2, from left to right). Outside of the jet structure delineated by the shear layer (white contours), the velocity is smaller than 0.01 everywhere in the grid, meaning that this can be considered a steady solution.

The numerical grid is initially filled with a jet with the injected properties (see Table 1) in the region $(r, z) \in [0, 1\,r_j] \times [0, 100\,r_j]$ and an ambient medium that occupies the rest of it. The initial jet overpressure forces its expansion into this ambient medium, which we let evolve until an equilibrium, steady solution is reached. The description of the criteria by which we decide when equilibrium has been reached are described in Sect. 3.1.

By establishing a jet across the whole grid, we avoid jet injection and the generation of a bow shock that would arise from the interaction of the newly ejected jet with the external medium, while focusing on jet physics alone.

We assume jets with kinetic power in the range $L_j \sim 10^{43} - 10^{44}\,\mathrm{erg\,s^{-1}}$, in accordance with the estimate given by Morganti et al. (2009); Ricci et al. (2022) for NGC 315. To build the required jet powers, we distribute the energy among the different channels (see Section 2.3). Regarding the external medium, we refer to the X-ray Chandra observations for the environment surrounding NGC 315. The measurements for the galactic core region, i.e., the inner 0.3 kpc, give pressure and density of $p_0 = 4.5 \times 10^{-10}\,\mathrm{dyn\,cm^{-2}}$ and $\rho_0 = 0.46 \times 10^{-24}\,\mathrm{g\,cm^{-3}}$, respectively (Worrall et al. 2007). However, jet configuration for the aforementioned powers requires pressures that can be six to eight orders of magnitude over these values.

While this raises questions about jet equilibrium and collimation at these scales, it is well possible that the jet is indeed strongly overpressured with respect to its environment, but that this extreme overpressure has been slowly achieved with time. It is relevant to recall that when formed and injected for the first time, jets are surrounded by their own shocked plasma, which is probably overpressured with respect to the jet itself. As it expands, the pressure around the jet falls gradually (see, e.g. Perucho et al. 2014; Perucho 2019; Perucho et al. 2022) and the jet keeps its collimation due to its own velocity, which limits opening angles to $\sim 1/\gamma$. In conclusion, in the case of evolved jets (like those in radio galaxies) one could expect free expansion with large opening angles while the jet accelerates, asymptotically reaching $\sim 1/\gamma$. This is in agreement with the transition from parabolic to conical jet expansion, precisely in the acceleration region.

Unfortunately, in our case, we cannot let the jet to adapt to such extreme conditions in a gradual way, and we establish the overpressure since the beginning of our runs. Furthermore, such large overpressure causes the code to crash as the jet violently expands into the ambient medium. However, since we only need the jet to freely expand, it is enough to give the ambient medium a pressure that allows this, even if the simulated ambient pressure is much higher than that estimated by Chandra. Therefore, we assume arbitrarily initial high pressure and density, with values of $p_a = 1.0 \times 10^{-3}\,\mathrm{dyn\,cm^{-2}}$ and $\rho_a = 1.67 \times 10^{-22}\,\mathrm{g\,cm^{-3}}$, respectively. This medium is set as isothermal, and the pressure (and density) are given a gradient in the z direction to fall with distance as $\propto z^{-1}$. In this way, at injection the jet overpressure factor spans from 1 (i.e., jet in thermal pressure equilibrium with the environment) to 4 and reaches values up to 10^2 at the end of the grid. The initial jet density spans between $\rho_j = 1.67 \times 10^{-25} - 1.67 \times 10^{-23}\,\mathrm{g\,cm^{-3}}$.

Jet pressure and density, together with the magnetic field strength, are modified from model to model in order to explore a variety of initial jet conditions, from highly magnetized, cold jets (with a magnetic energy flux F_M, representing $\sim 75\%$ of the total) to hot jets (with an internal energy flux, F_I, representing $\sim 88\%$ of the total). The parameters that determine each of the simulated models are given in Table 1. The model names are given using the following code: the first letter represents the magnetic field configuration, with F for force-free and N for non-force free, the second letter stands for the type of jet, i.e. magnetic (M), internal (I) or kinetic (K) energy dominated, the third letter gives the code for the jet density, with S for $\rho_j \geq 0.1\,\rho_a$, H for $0.01\,\rho_a \leq \rho_j < 0.1\,\rho_a$, and L for $\rho_j < 0.01\,\rho_a$, while the last numbers refer to the jet thermal overpressure factor at injection. When two different models are expected to have the same nomenclature, we add at the end of the name a letter in progressively alphabetical order (e.g. FMH1b, FMH1c). Models with _m4 have the shear layer exponent set to $m = 4$, i.e., a wider (thicker) shear layer, while for all the other models the exponent is set to $m = 8$.

Table 2 displays the ratio of the different flux channels over the total one (index i) as derived from the jet parameters, together with the simulated ones, which are convolved to the shear layer (index s), and final ones computed at the final row of cells at 3.3 pc (index f). In Appendix A, we discuss the reason and implications in the initial radial profile of the fluxes within the jet, considering their convolution with the shear layer.

3. Results

3.1. From initial conditions to equilibrium

The simulation setup consists of a jet that extends the injection conditions along the numerical grid with constant radius $r = r_j$, with a parameter smoothing function out towards the ambient medium, i.e., a shear layer, as described in Sect. 2.4. The jet structure is computed considering pressure equilibrium with its environment.

Jets immediately start their expansion into the underpressured ambient, transferring energy via radial propagating waves. These waves accelerate the ambient medium in the radial direction. As a consequence, some material is pushed out of the grid, slightly changing the conditions in the ambient. We have run tests with an extended grid to check the influence that this loss may have and found that the jet is unaffected, probably due to the large jet overpressure, which does not change significantly. For proofs in support of this and for a proper description of the pressure wave and its evolution, see Appendix B.

We run the simulations for the necessary amount of time for the jets to reach equilibrium after the expansion is completed. To determine when the steady solution is reached we use the radial velocity as the indicator. Specifically, we consider equilibrium to have been reached in a certain model when $|v^r| < 0.01$ all over the grid, with the exception of jet expansion/recollimation associated with the achieved equilibrium configuration. An example of this is shown in Fig. 3 for model FMH1_m4. In the figure, the white contours highlight the levels of the tracer, i.e., the jet mass fraction. In this case, outside of the jet, the grid shows radial velocities lower than 0.01 everywhere.

Figure 4 shows an example of radial equilibrium profiles at different locations along the jet and for different resolutions, for model FMH1. We show the radial distribution of different physical quantities at $t = 0$ and at the final step, at three different distances, injection (cell 1), half grid (cell $n_z/2$), and $z = z_{\max}$ (cell n_z). The figure shows three sets of panels for the results at three different numerical resolutions: the upper set shows the results for a simulation with 10 cells/r_j, the middle set shows the case with 20 cells/r_j, while the bottom set shows the case with 40 cells/r_j. For the latter case we show only the initial and final cell profiles, since we used a smaller grid of $[30\,r_j \times 30\,r_j]$ for computational time reasons. The bottom right plot of the 10 cells/r_j case shows a change of the axial field at injection, which implies a discontinuity with respect to the boundary condition. This problem, caused by numerical diffusion, disappears at 20 and also at 40 cells/r_j. Having found convergence between our results at 20 cells/r_j, we adopt this resolution for all our simulations. In Appendix C we show further proofs in support of this choice.

The plots show how the initial condition is preserved at injection, but the jet expands significantly, becoming much wider along the grid. These plots also show an increase in axial velocity, which appears to be displaced from the axis. We will discuss this result in the next Section.

3.2. Jet acceleration and expansion profiles

Figures 5 and 6 show the results obtained for all the different models. A clear relation between jet velocity profile and its intrinsic properties is inferred: jets developing strong internal shocks -Mach disks- present stronger acceleration in their outer, expanding layers, whereas those developing milder, conical shocks present a fast spine. Pressure maps (Fig. 6) show

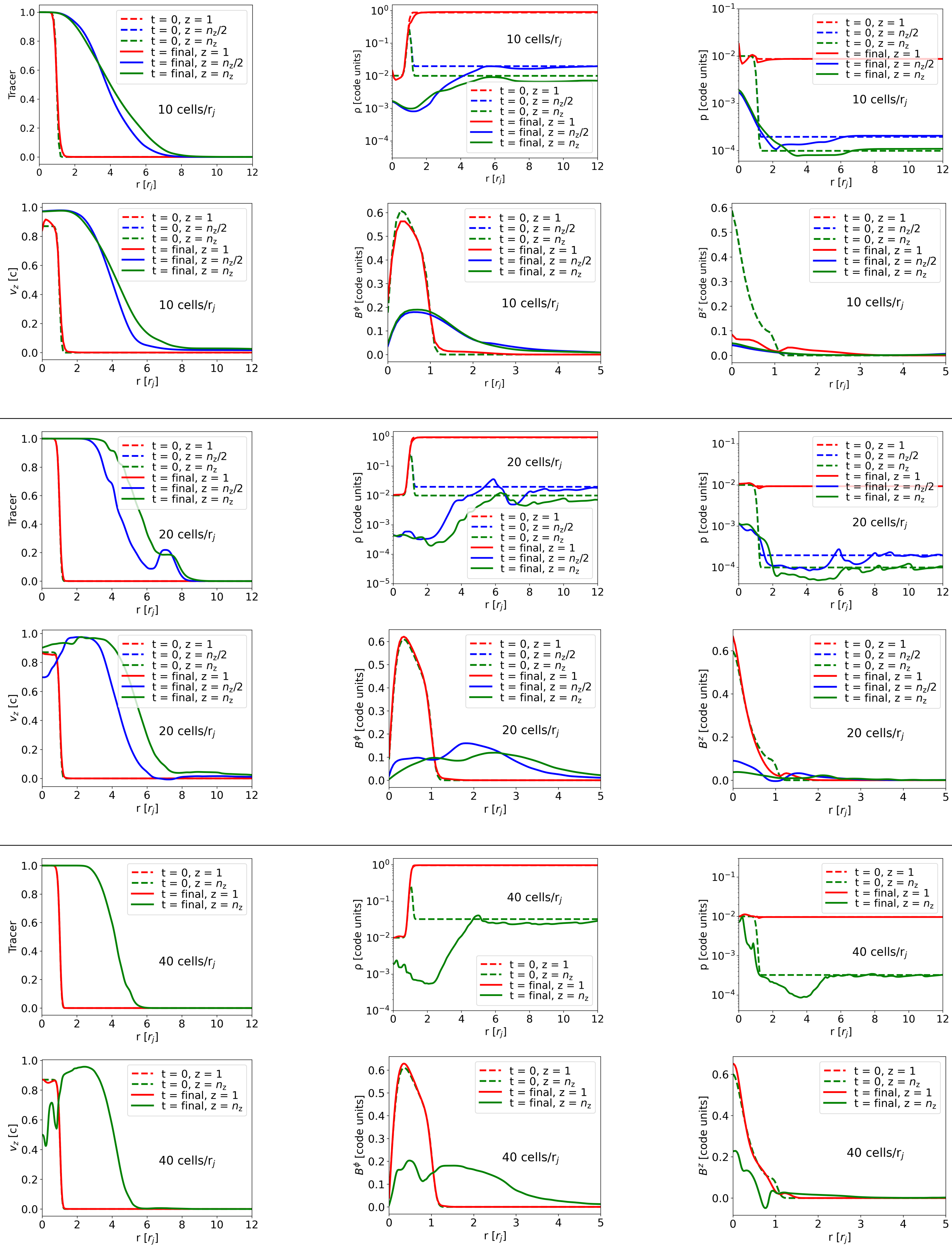

Fig. 4. Radial profiles of the different physical properties for model FMH1 at different distances from the injection (cell 1 in red, half grid in blue, and final cell in green) and at different times (initial in dotted lines and final in continuous lines). In the top panels, we show the radial profiles with a resolution of 10 points, in the middle the ones at a resolution of 20 points, and in the bottom ones the profiles with 40 points (here, the half grid is not shown due to the smaller simulated grid). The convergence in the profiles between 20 and 40 points led us to use resolutions of 20 points for our simulations.

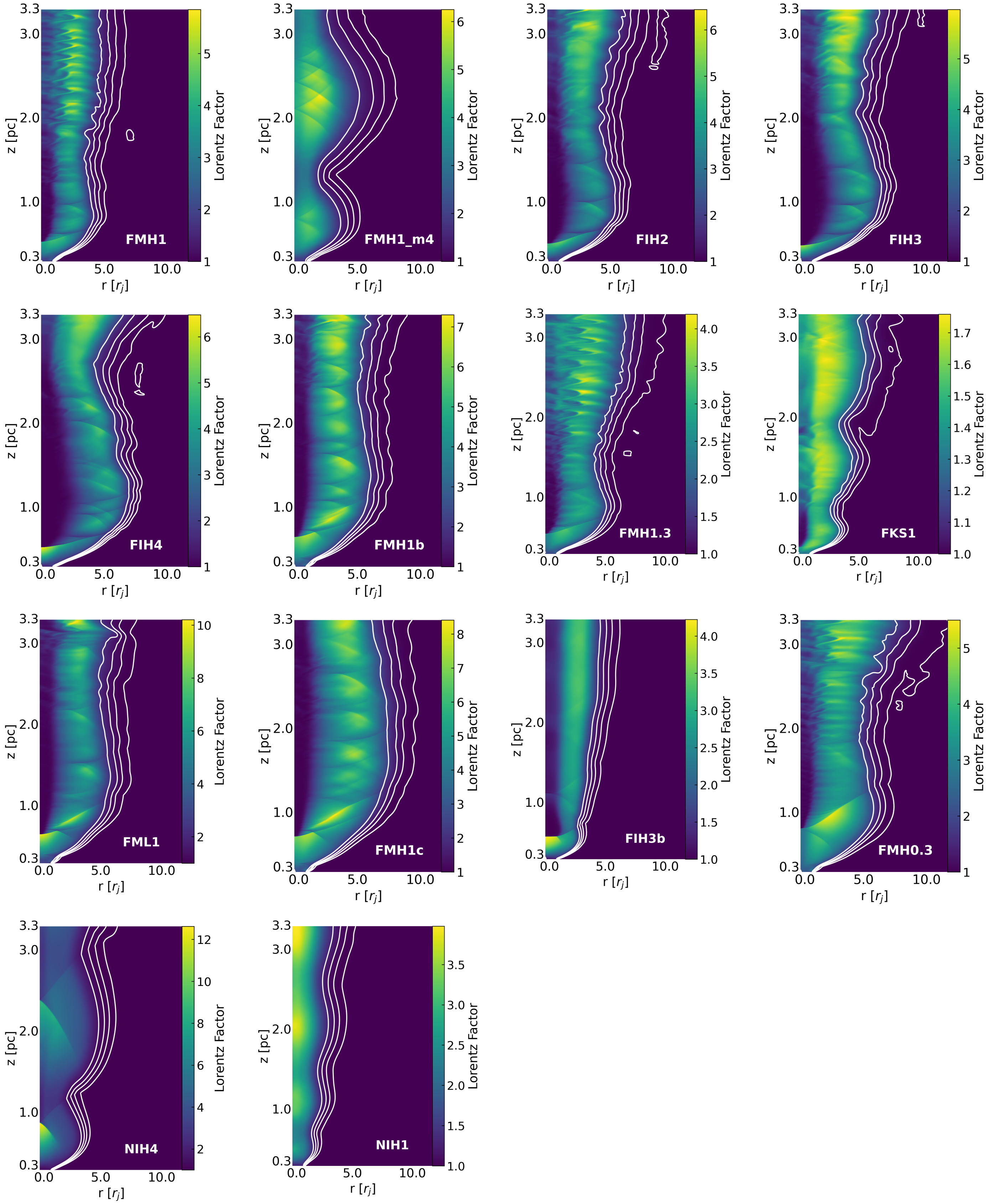

Fig. 5. Lorentz factor maps for the simulated models. The white contours are representative of the tracer at levels of 0.2, 0.4, 0.6, 0.8. The results show the clear correlation between the the jet speed profiles and the intrinsic properties, with the main differences shown between force-free and non-force-free along with magnetically dominated or internally dominated models. For details, see the text.

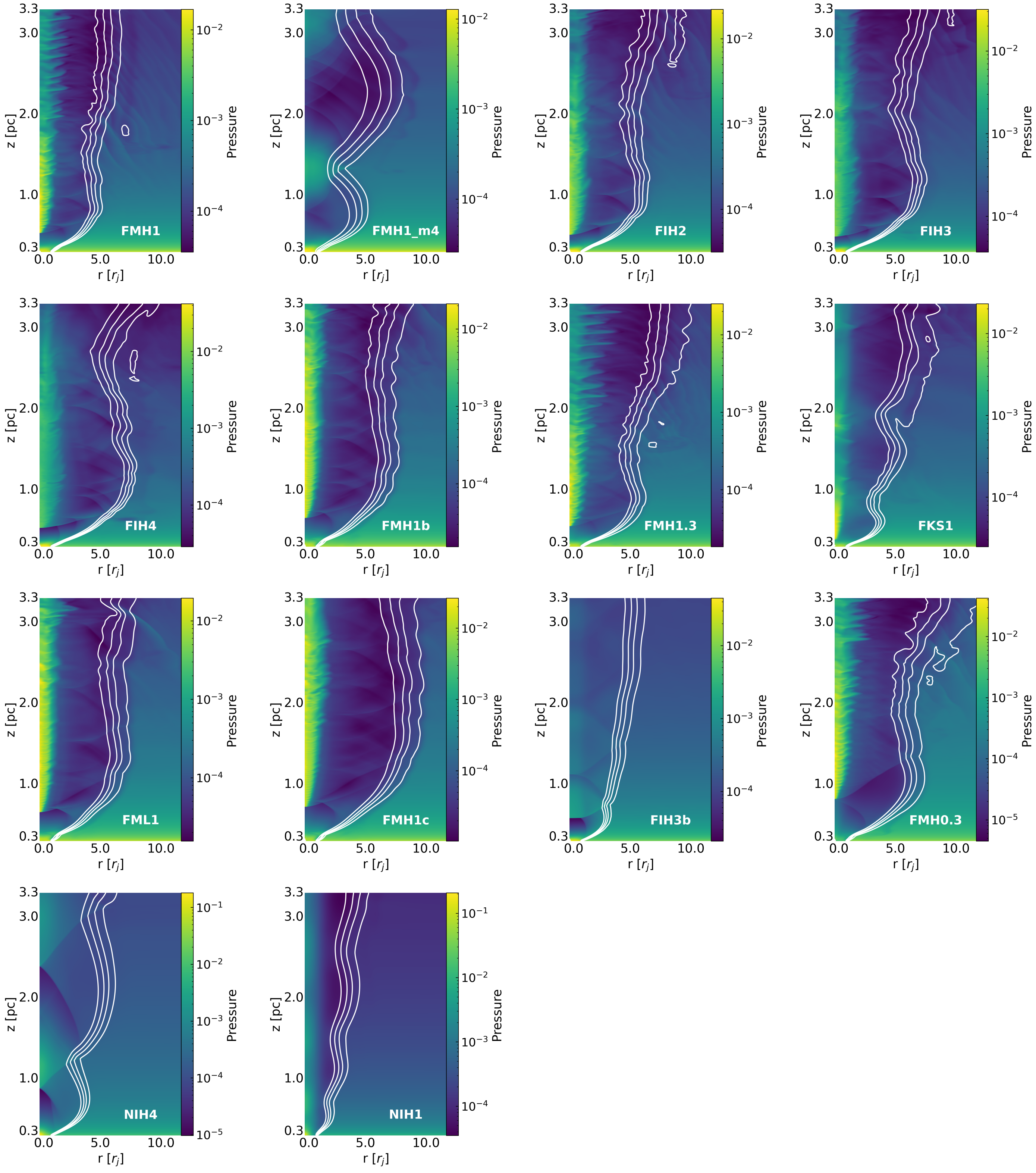

Fig. 6. Pressure maps for the simulated models. The white contours are representative of the tracer at levels of 0.2, 0.4, 0.6, 0.8. As in Fig. 5 the different jet nature leads to the different pressure profiles in the spine and in the shear layer regions.

that the strong discontinuities observed in several models such as FMH1, FIH4, and FIH3b, are caused by the generation of a Mach disk in the jet. The Mach disk formation is driven by the strong expansion, due to the large angles formed by the shock waves with the jet axis (see, e.g., Martí et al. 2018, and references therein). In general, the main difference between the jets showing acceleration at the outer layers and those showing spine acceleration is their force-free versus non-force-free nature, or magnetically versus internal energy dominated.

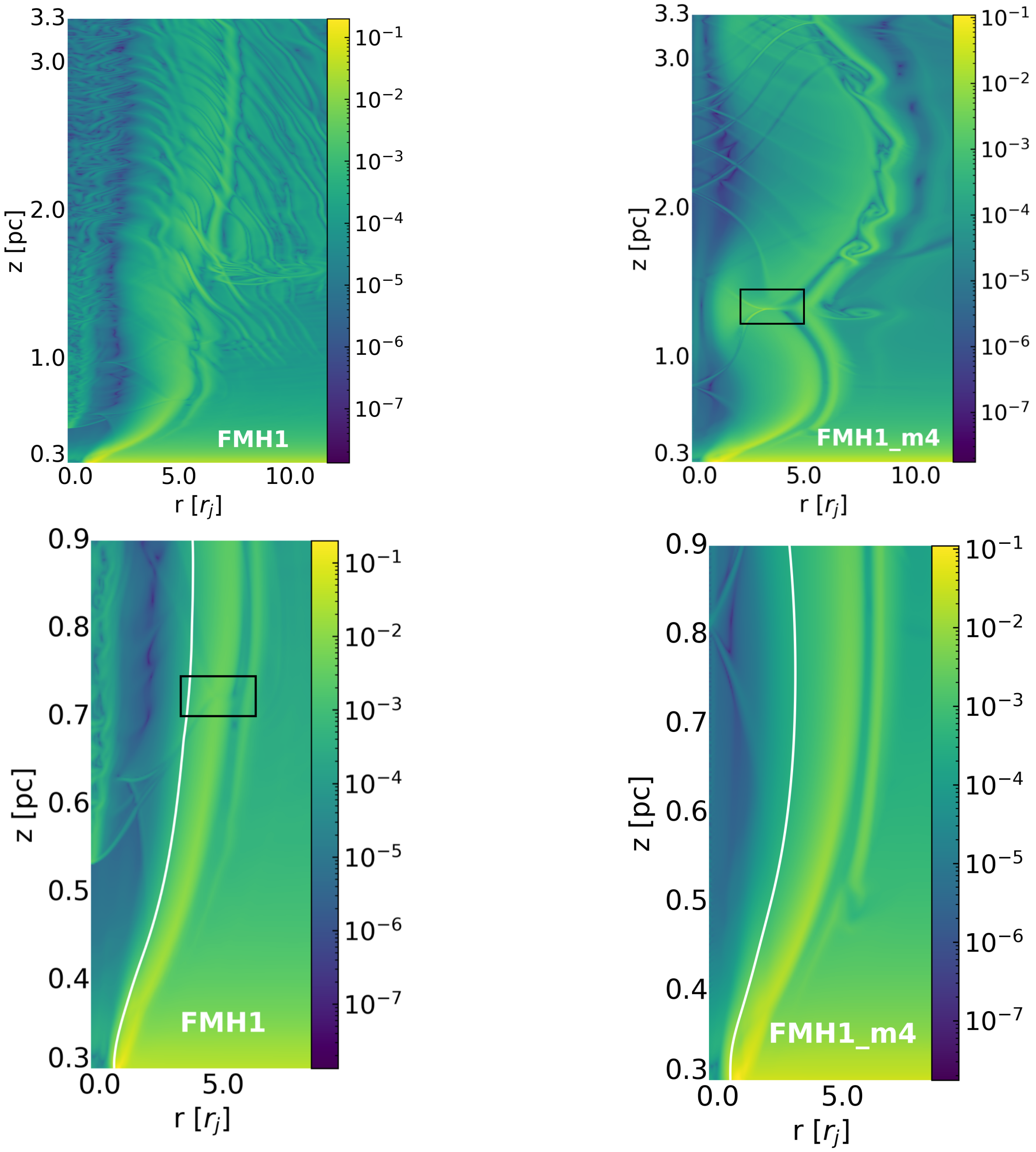

Fig. 7. Modulus of the gradient of the rest-mass density (in logarithmic scale) for models FMH1 (left panels) and FMH1_m4 (right panels). The upper panels show the entire grid, while in the bottom ones we show a zoom-in in the 0.3-0.9 pc region. The modulus of the gradient of the rest-mass density highlights the location of steep sound waves and shock waves. The black squares highlight the triple point associated with the incident/reflected/Mach shocks in the jet-ambient transition surface (for details, see Sect. 4.3). In the bottom panels, the contours represent the tracer at the level $f = 0.9$, showing the transition between the inner jet and the shear layer.

However, we observe that an increase in the width of the shear layer (FMH1_m4 vs. FMH1 models) can completely change the jet acceleration pattern obtained. In the case of FMH1 (top, left panel), the jet expands until the point at which the extension of the planar shock wave at the center of the jet reaches its surface. Beyond this point, we observe a mild expansion/recollimation process. Downstream, in the region that is unaffected by the Mach disk, the jet develops instability patterns and locally dissipates some of the gained kinetic energy, which explains why the internal energy flux at the end of the grid is larger than at ~ 0.5 pc (see Sect. 4.3 for the discussion on this effect). In FMH1_m4 (top, second panel from the left), on the contrary, a Mach disk is not formed and the acceleration of the flow is concentrated towards its axis, unlike all the other force-free models. The corresponding pressure maps show that the main difference between both models is the delay in the wave propagation that the thicker shear layer causes in FMH1_m4 with respect to FMH1: the outgoing waves have to cross a thicker portion of the jet before bouncing back, which delays the bounce and moves it downstream. This delay relaxes the angle formed

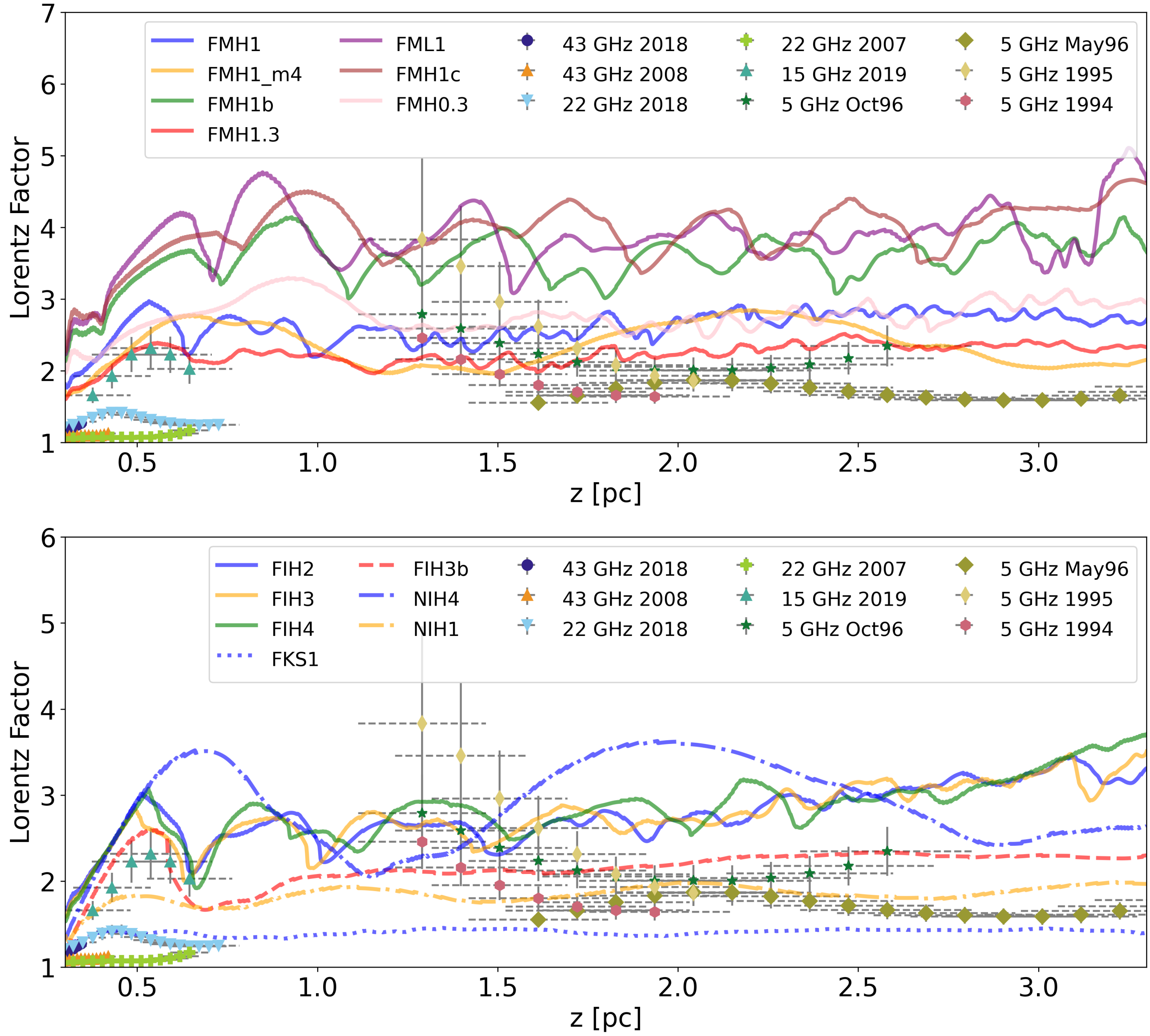

Fig. 8. Radially-averaged Lorentz factor as a function of distance for all the simulated models (top panel: magnetically dominated jet models; bottom panel: thermally and kinetically dominated jet models). The different data points are the Lorentz factor for different epochs and frequencies of NGC 315 inferred by Ricci et al. (2022). The continuous lines represent the force-free magnetically dominated models, the dashed lines the force-free thermally dominated ones, the dotted lines are for the kinetically dominated model, and the dashed-dotted lines for the non-force-free configurations.

by the incident wave and the axis, changing the acceleration pattern and jet structure. Figure 7 shows the modulus of the gradient of the rest-mass density in the (r, z) plane[2], $|\nabla\rho|$, of both FMH1 and FMH1_m4 (top panels), and a zoom of the relevant region where the first recollimation shock forms (bottom panels). The modulus of the gradient of the rest-mass density highlights the location of steep sound waves and shock waves. The images in Fig. 7 show how the different widths of the shear layer changes the wave structure of the models. In model FMH1, the jet dynamics is dominated by instabilities both in the spine and at the jet/ambient medium transition on parsec scales, where we see the formation of vortexes typical of the growth of Kelvin-Helmholtz instabilities. On the contrary, in model FMH1_m4 the jet pinches, but substantially fewer instabilities arise and the jet/ambient medium transition is smoother. In the bottom panels, we can see that the opening angle of the transition between the inner jet and the shear layer is larger in FMH1. The bottom panels display contours for tracer $f = 0.9$ to show the transition between the inner jet and the shear layer, which, at injection, occurs at $0.91 r_j$ in model FMH1, while it is at $0.82 r_j$ in model FMH1_m4. We propose that this difference determines the two possible evolution patterns observed (see Sect. 4.3 for details). We have run other models with wider shear layers (with the same initial conditions as FIH2, FIH4, FMH1c, FIH3b) and we have observed the same behavior: thicker shear layers may result in a dramatic change in the acceleration pattern of force-free jets,

---

[2] computed using centered finite differences.

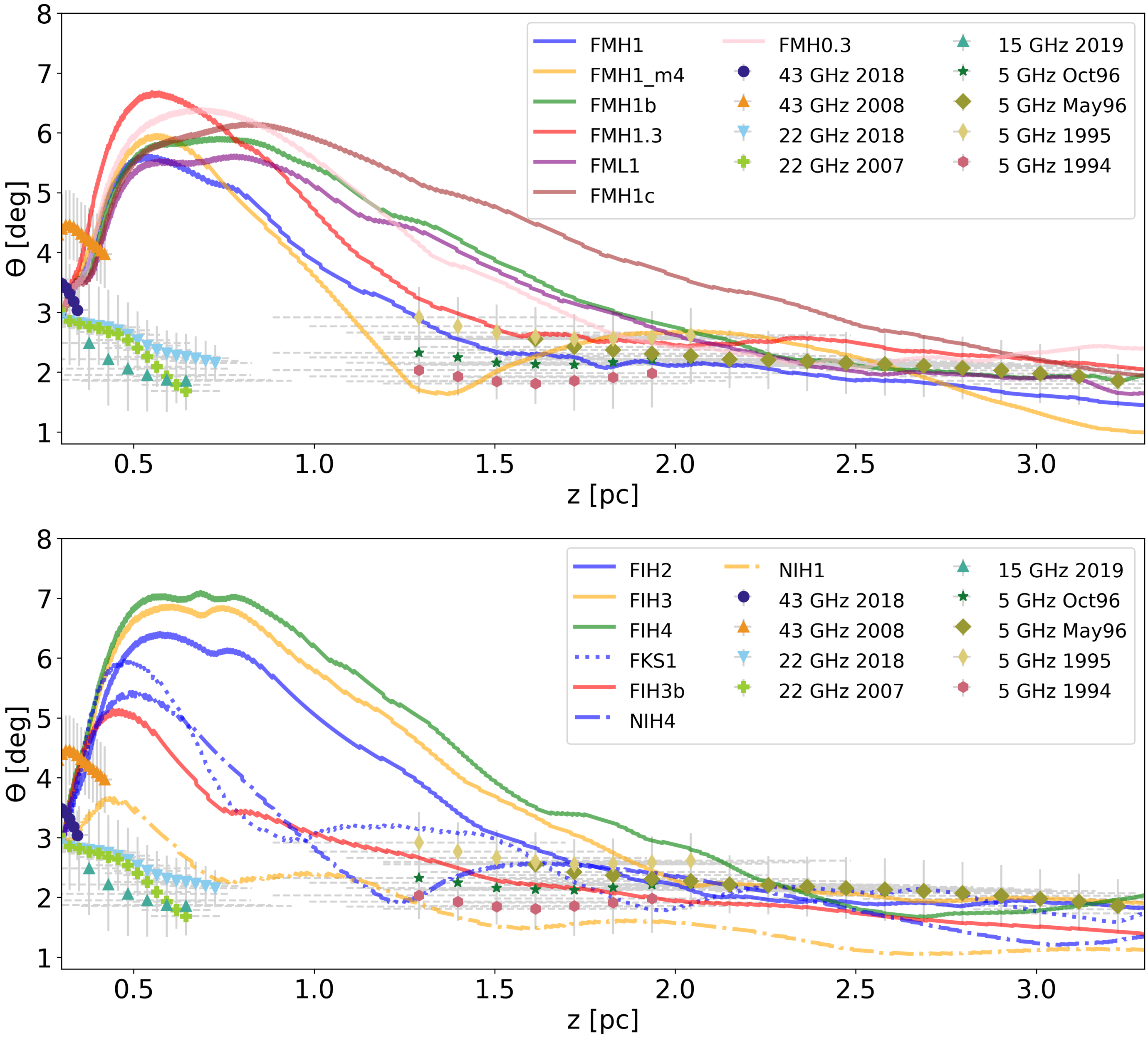

Fig. 9. Half-opening angle as a function of distance for all the simulated models (top panel: magnetically dominated jet models; bottom panel: thermally and kinetically dominated jet models). The force-free magnetically dominated setups are shown in continuous lines, the force-free thermally dominated in dashed lines, the kinetically dominated in dotted lines, and the non-force-free in dashed-dotted lines. The data points represent the intrinsic half-opening angle profiles of NGC 315 obtained by Ricci et al. (2022) for multi-frequency and multi-epoch VLBI observations.

avoiding the formation of Mach disks and favoring spine acceleration, as opposed to thin-layered models (see Appendix D).

In all the force-free models (except FMH1_m4), we observe the formation of the Mach disk with the resulting transversal velocity structure consisting of a slow spine surrounded by a fast sheath. In all cases, although this is better observed in model FMH1, the accelerated region slowly expands towards the jet axis, even if at the end of the grid none of them shows a completely accelerated jet cross-section. Instability modes develop at the interface between the spine and the outer accelerated layer. This triggers dissipation and we thus expect it to contribute to increasing the internal energy of the region. The fast development of instabilities is expected in the case of hot, slow flows (see, e.g., Perucho et al. 2004, 2005).

Non-force-free models show, in contrast, an acceleration pattern concentrated around the jet axis, i.e., they produce a fast spine. The main difference with respect to force-free models is the absence of a Mach disk. This acceleration pattern corresponds to that expected from the Bernoulli process. Highly overpressured jets, such as NIH4, show strong acceleration on the axis before the flow reaches a strong recollimation shock, where the flow is decelerated. The next expansion process produces a second acceleration region, but the Lorentz factor reached is 20% smaller than the one prior to the first recollimation shock. In the case of NIH1, in thermal pressure equilibrium with the environment at injection, acceleration is milder, modulated by recollimation waves/shocks, with a progressively growing velocity from one acceleration region to the next.

Figure 8 shows the radially-averaged Lorentz factor for all the simulated models. For clarity, we divided the profiles into two separate plots: in the top panel we show the magnetically dominated models, while in the bottom panel the thermally dominated ones together with the kinetically dominated FKS1 are displayed. The average Lorentz factor value is computed by weighting the value at each cell with its volume (given by a ring). As a discriminant to determine the jet width we use the tracer parameter with a value of 0.5 as a threshold, i.e., cells with tracer > 0.5 are considered to be part of the jet while cells with tracer $<$ 0.5 are considered ambient medium. Along with the speed profiles, Fig. 8 shows the data points for NGC 315 in the frequency range 5-43 GHz and at different epochs inferred in Ricci et al. (2022). These results were obtained based on the observed jet-to-counterjet intensity ratio, which provides an average velocity in a likely stratified jet structure (hints of an edge-brightening and possible stratified velocity are given in Park et al. 2021). The comparison of the simulation profiles with the observational data is presented and discussed in Sect. 4.4. The plot shows that the simulations with different setups result in average jet acceleration from $\gamma \sim 1-2$ up to $\gamma \sim 2-5$ within a spatial propagation of only 3 pc. The weakest acceleration is observed for model FKS1, as expected for kinetically dominated models, whereas the strongest acceleration is obtained in models with the highest relative magnetic and/or internal fluxes at injection, such as FMH1c, FIH4 or FML1. It is also interesting to mention that force-free models accelerate larger volumes of jet plasma, as the outer regions of the jet represent larger rings in cylindrical coordinates. All models show modulations in the average Lorentz factor produced, as stated above, by expansion and recollimation episodes, in which internal energy flux is invested into acceleration and the jet flow is then decelerated by shocks, where kinetic energy is converted into internal energy. As expected, this is more evident in significantly overpressured models, like FIH4, where the initial acceleration of the jet is followed by a drop in the average Lorentz factor. In the thin shear-layer, force-free jets, the difference in velocity between the plasma flowing along the spine, decelerated by the planar (Mach) shock, and that accelerated at outer radii triggers the development of instabilities. In models FMH1, FMH1.3, and FMH0.3 these instabilities develop to non-linear amplitude within the grid and, on the one hand, allow the gained axial momentum at the accelerated region to be shared with the inner jet spine and, on the other hand, dissipate part of the gained kinetic energy. Altogether, this results in a drop of the maximum average Lorentz factor achieved by the jet during its initial expansion, and a slow recovery with distance. Nevertheless, these models stabilize their Lorentz factors at values between 2 and 3.

Figure 9 shows the half-opening angle of the different models versus distance together with the observational points for NGC 315. We divided the plot as before, the upper panel for the magnetically dominated models, and the bottom panel for the thermally dominated (plus FKS1) ones. In all models, we observe an initial increase of the opening angle due to the expansion of the jet towards the less-pressured ambient medium, followed by a decrease that starts at different distances, but always before ~ 1 pc. The fall in the opening angle profiles is associated with jet collimation, i.e., $r \propto z^{\alpha}$, with $\alpha < 1$. None of the models shows completed collimation on the simulated scales, i.e., $\alpha \approx 1$. All models tend to final half-opening angles of $1-3°$. This plot is very clarifying regarding the causes for jet expansion in the different models: force-free models expand faster than non-force-free models, as can be seen by comparing cases FIH4 (green dashed line) and NIH4 (blue dashed line). This difference also allows us to group the models into two main behavior patterns: 1) the models with the largest initial opening angles develop the Mach disk, while 2) those with smaller initial opening angles develop conical shocks.

The opening angle at injection is also clearly correlated with initial jet overpressure, so force-free models with no thermal contribution to overpressure at injection ($p_j = p_a$) show smaller opening angles, albeit longer expansion regions (FMH1b, FMH1c and FML1). These models also show the largest average Lorentz factors (see Fig. 5), mainly driven by magnetic energy (as can be seen in Table 2 and Fig. 10). Another relevant aspect to consider is that these models in (thermal) pressure equilibrium at injection also have larger initial velocities (see Table 1), which causes smaller opening angles and therefore longer expansion lengths. Figure 9 also shows the half-opening angles derived from the same observational results (Ricci et al. 2022). For the discussion of such comparison, we refer to Sect. 4.4.

Figure 10 shows the evolution of the different energy flux channels, together with the total one, along the z direction. These plots clearly show the correlation between the increase in kinetic energy flux and the drops in either magnetic or internal energy fluxes, or both. From the plots, it becomes evident that, at injection ($z < 0.6$ pc), a clear anti-correlation between internal energy and kinetic energy fluxes is only seen in internal energy dominated (FI and NI models). In the case of magnetically dominated models, it is the magnetic energy flux that shows anti-correlation with the kinetic energy flux, and we can observe regions in which the kinetic and internal energy fluxes are correlated (e.g., FMH1b). We can thus deduce that the dominant acceleration mechanism is controlled by the dominating energy flux, but that, in specific conditions, e.g., in expansions for the case of internal energy, the secondary energy flux can also contribute to acceleration. FKS1 represents an interesting case (Fig 10, third row, central panel), in which the initial expansion results in a small increase of the kinetic energy flux favored by a drop in both internal and magnetic energy fluxes (although this jet reaches the smallest terminal values of the Lorentz factor; see Fig. 5).

Finally, a slight global increase in magnetic flux is observed in the FMH1_m4 model, beyond a distance of $z = 2.5$ pc. The latter is in correspondence with the jet recollimating after an expansion phase (see Fig. 5). During the recollimation, the magnetic field is compressed and its value increases, but an increase in magnetic flux is typically not expected unless there is a boost in velocity due to internal energy, i.e., Bernoulli processes. However, this is not the case in the indicated region, so we propose such a small increase to be due to i) a physical process that transfers kinetic energy to magnetic energy as the reverse of magnetic acceleration, likely a consequence of local differential recollimation effects (a similar behavior is observed in Komissarov et al. 2015, Fig. 10, right panel); ii) small inaccuracies arising during the summing of the different integrated quantities, or iii) numerical diffusion at the jet boundary, i.e., the magnetic field smearing out towards the outer cells. The exploration of such an effect is out of the scope of this paper and will be tackled by future works. Nevertheless, we remark that the fraction of such an increase is negligible with respect to the total jet and does not affect our results.

4. Discussion

Our results show that jet acceleration is driven by the dominant energy flux at injection, either magnetic or internal, but both are

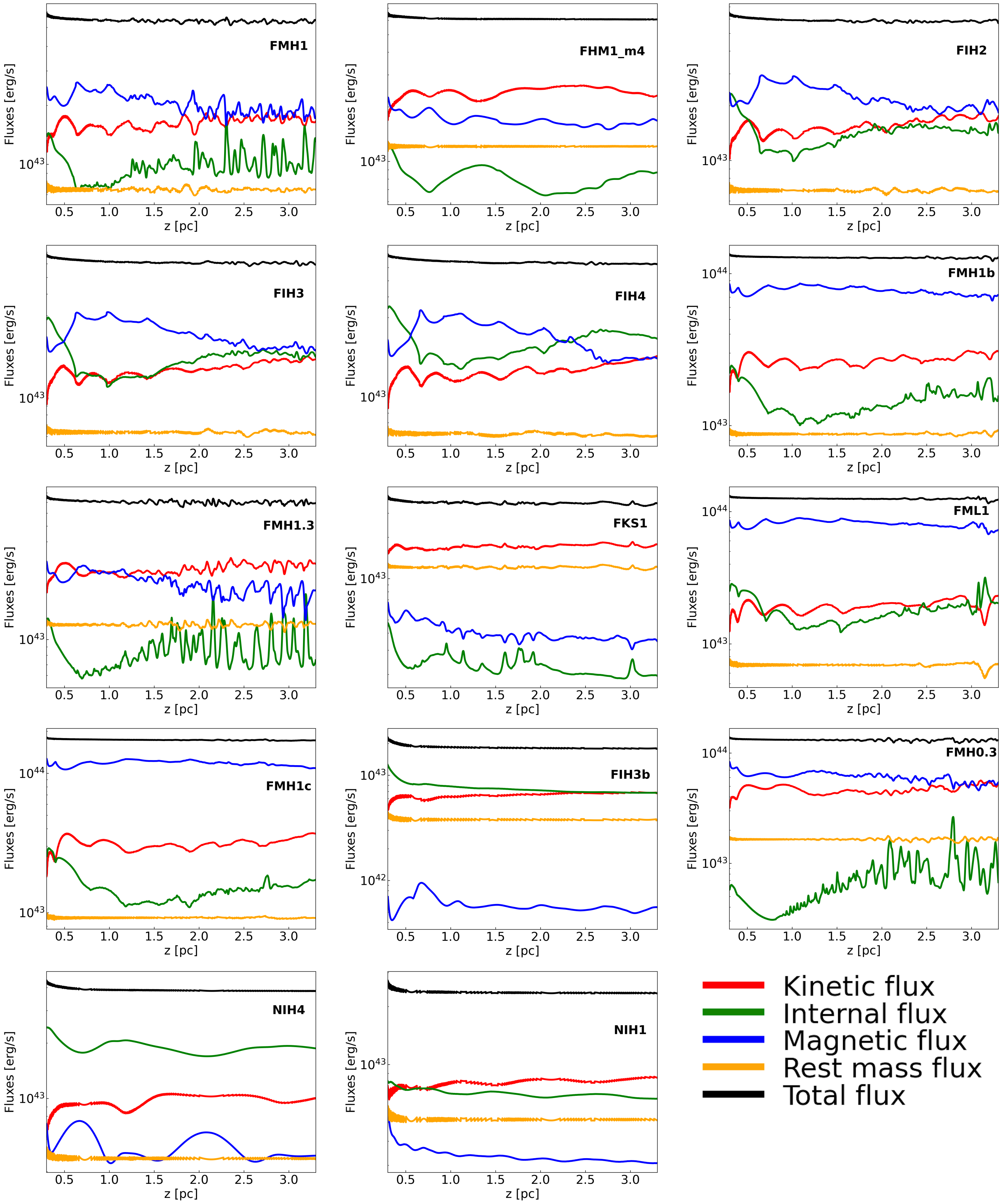

Fig. 10. Evolution of the integrated energy fluxes along the axial direction for all the models reported in Table 1. Black, red, green, blue and orange lines represent, respectively, the total, kinetic, internal, magnetic and rest-mass energy fluxes. Depending on the dominating energy channel, its dissipation in favor of the jet kinetic flux is visible in all the models. An exception is the kinetically dominated model FKS1, in which both the thermal and magnetical channels are dissipated to accelerate the jet, even if not dominant.

successful in increasing the jet Lorentz factor at expanding regions. However, there are significant differences in the acceleration patterns in both cases as shown in Sect. 3.2.

In Sect. 4.1 we discuss the role of thermal acceleration in relativistic jets. The difference in the velocity structures due to the force-free versus non-force-free and thin versus thick shear layers are discussed in Sect. 4.2 and Sect. 4.3, respectively. In Sects. 4.4 and 4.5 we focus on the comparison with the observational data and derive conclusions on how our results can provide insights for jet evolution. Finally, in Sect. 4.6, we comment on the limitations of our study.

4.1. The role of the thermal acceleration

Jets produced by the Blandford-Znajek mechanism (Blandford & Znajek 1977) are probably dilute, hot, and significantly magnetized at sub-parsec scales, where entrainment has still not affected jet composition. Building upon the principle of Bernoulli, thermal acceleration is effective when the enthalpy h is high enough (specifically, $h \gg c^2$). For a steady, relativistic flow, the principle is expressed by the law $h\gamma = \text{const}$, establishing that the flow accelerates when h decreases (as the flow expands). The process of thermal acceleration has been regularly seen in numerical simulations (e.g., Perucho & Martí 2007; Anglés-Castillo et al. 2021). By assuming that jets are hot at injection, we also found evidence for thermal acceleration at these scales: as highlighted in Sect. 3.2 and shown in Fig. 10, we obtain the expected anti-correlation between thermal and kinetic energy fluxes during the evolution of our models. For instance, in the case of FIH3b model, in which the magnetic flux is an order of magnitude lower than the internal one and irrelevant to the acceleration of the jet, the jet is clearly accelerated by the Bernoulli process alone. Interestingly, such model, and so thermal acceleration alone, is able to reach Lorentz factors higher than 2 on scales of $\sim 2-3$ pc, matching thus the observed speed profile of NGC 315 (see Fig. 8).

Thermal acceleration can be relevant in relativistic jets at larger scales than those assigned to magnetic acceleration: if jets keep or gain internal energy on parsec scales, as it can be the case at recollimation shocks, it can act at the following conical expansions. In other words, even when jets are magnetically dominated at injection, once they are collimated and the magnetic acceleration stops, internal energy could still nourish the bulk acceleration. The detection of jet flow acceleration on large scales, e.g., $\sim$ 100 pc in blazar jets (Homan et al. 2015), could be thus interpreted as an observational signature of thermal acceleration.

4.2. Force-free versus non-force-free models

One of the main triggers of the different acceleration patterns in our models is the force-free versus non-force-free nature of the flows. The reason lies in the cancellation of the field force in force-free models, eliminating the contribution of magnetic tension to jet collimation. Indeed, in the force-free configurations, the magnetic tension does not act as a collimating factor, and expansion is therefore enhanced, with half-opening angles reaching 7°. On the contrary, in the non-force-free case, magnetic tension plays an active role in controlling expansion, which can only be temporarily overcome by considerable overpressure (as in, e.g., model NIH4). It is noticeable that the recollimation pattern in the non-force-free model NIH4 is, as a result, very different from that in FIH4, the force-free case: the angle formed by the shock wave and the jet axis is clearly smaller than in FIH4, and therefore NIH4 does not develop a Mach disk.

Because acceleration in the outer layers only takes place in force-free jets, which are, in general, magnetically dominated, we could derive the conclusion that this type of velocity pattern (slow spine and fast sheath) is a signature of magnetic acceleration in the case of thin shear layers, although FI models show that this does not strictly exclude internal energy as an accelerating mechanism. Fast spines would correspond, in contrast, either to internal energy-dominated flows or strongly sheared (possibly wind-shielded, two-flow) jets.

4.3. The role of shear layers

Our simulations show that the different thicknesses of the shear layer can lead to a fundamental change in the acceleration pattern of force-free jets. Fig. 7 shows that this may be caused by the difference in the opening angles of the region separating the inner jet and the shear layers (indicated by a white contour that stands for tracer $f = 0.9$). Initially, thicker layers produce smaller opening angles and limit recollimation to conical shocks, allowing acceleration along the spine, even if modulated by the succession of expansions and recollimations. We propose that the direct consequence of the thicker shear layer is the delaying of the wave propagation. As a result, the triple point, associated with the incident/reflected/Mach shocks in the jet-ambient interaction surface, which is visible in Fig. 7 (highlighted by the black squares) is found in model FMH1 at $\sim$ 0.7 pc while in model FMH1_m4 around 1.3 pc. The role of the width of the shear layer has been confirmed by further simulations (see Appendix D).

Comparing the maximum Lorentz factors reached by the different models (Fig. 5), we observe that FMH1_m4 reaches a slightly larger Lorentz factor than its thin-layered counterpart, FMH1. The most plausible explanation of this result is that the growth of the instabilities observed in model FMH1 dissipates some fraction of the kinetic energy of the flow, whereas the jet of model FMH1_m4 is shielded from its environment by a thick shear layer, which, together with further expansion can contribute to preserving its collimation (see, e.g., Perucho 2019).

Altogether, we can conclude that the role of shear layers at the collimation/acceleration region can be of great importance for jet evolution, with thick-layered jets producing collimated, stable, fast flows with velocity profiles consisting of a fast spine and a slower, shielding layer. On the contrary, thin-layered jets initially develop a slow, hot spine, surrounded by a sheath along which the flow is accelerated. The boundary between these two regions, spine and sheath, is prone to the development of instabilities and can eventually dissipate part of the gained kinetic energy.

We highlight, however, that this is a small-scale effect (see Sect. 3.2, e.g., model FMH1) and is expected to not be largely significant (see the small velocity differences between FMH1 and FMH1_m4, as aforementioned) within the simulated grid because the instabilities have not reached the non-linear regime and have not developed mixing between the hot and slow spines and the faster and cold sheath.

4.4. Comparison with NGC 315

A one-to-one comparison between observations and simulations is, in general, not possible due to limitations of both. Radio maps can be affected by uncertainties in the calibration and imaging processes, as well as by time-variable and local effects that do not necessarily allow us to infer the physical conditions of the underlying plasma flow. In simulations, as discussed, some simplifications are unavoidable. Nonetheless, some general trends can be identified and discussed qualitatively, and we do this in the following by considering NGC 315.

Concerning the jet opening angles, Fig. 9 shows that most of our simulated models succeed in reproducing the terminal values at the end of the collimation region, as inferred from the 5 GHz observations at different epochs ($\theta \sim 1-3°$). These opening angles also agree with the average values observed in radio galaxies (e.g. Pushkarev et al. 2017). In contrast, we observe that the opening angle in the innermost jet, described at the highest radio frequencies (15, 22, and 43 GHz), does not match our synthetic profiles. The limitations suffered by numerical models forced us to inject super magnetosonic flows, as previously explained (Sect. 2.4). This also makes any comparison challenging at the compact scales: while the simulated jets open abruptly from the injection point at ~ 0.3 pc due to initial overpressure, the high-frequency data from the jets in NGC 315 indicate that such an opening happens on smaller scales and that the jet at 0.3 pc is going through the final part of its collimation before transiting to the conical shape (Boccardi et al. 2021). Nonetheless, as mentioned, the observational and simulated data reconcile on parsec scales.

Except for the innermost jet region, an agreement between observations and simulations can be found in the fact that they both show a co-spatiality of the acceleration and collimation processes. The simulations show acceleration episodes between $(0.5-1.0)$ pc and $(1.5-2.0)$ pc (Fig. 8), i.e., along the region where the opening angle is also decreasing (Fig. 9). This is probably the last part of the accelerating region, which in NGC 315 extends within the inner $\sim 1-2$ pc. The co-spatiality agrees with the expectation, for FM models, of a magnetic acceleration being relevant when the jet is evolving with a parabolic or quasi-parabolic shape (Komissarov et al. 2007). Nonetheless, as mentioned in Sect. 4.1, thermal acceleration alone could in principle reproduce the observed velocities on parsec scales.

A comparison between the simulated and observed Lorentz factors may indicate a better agreement for models with jet power $\sim 10^{43}$ erg/s, consistent with the jet power estimated from observational constraints (see, e.g., Morganti et al. 2009; Ricci et al. 2022). Indeed, the average Lorentz factor of ~ 2 on scales of $\sim 2-3$ pc can be reproduced by models with such jet powers. On the contrary, models with higher jet power ($\sim 10^{44}$ erg/s) seems to fail to align with the observational data: while they manage to reach the Lorentz factor peak of $\gamma \sim 4$ at the distance of ~ 1.5 pc (observed in only one epoch), they exhibit terminal Lorentz factors exceeding the maximum observed values by more than a factor of two. Remarkable examples are the highly-magnetized models, such as FML1, FMH1c, and FMH0.3. As in the case of the opening angle, a meaningful comparison on sub-parsec scales is not possible: data at 22 GHz and 43 GHz show acceleration from very small velocities, out of the reach of our setups (see Sect. 2.4).

Another interesting aspect might be noticed from Fig. 8: the Lorentz factor evolution along the jet changes between epochs, even at the same frequency, e.g., the 1996 5 GHz epochs, which are separated by five months. While taking into account that such variations can be a consequence of various local and observational effects, it is also possible that they are the result of intrinsic changes in the injection conditions. Indeed, the jet velocities and variability in Lorentz factors recovered from the family of models with jet powers $\sim 10^{43}$erg/s could potentially match the observed time-dependent changes in the Lorentz factor. The simulations we have presented here differ from each other by only a few parameters, within a range of plausible values derived from observational results (see, e.g., Fig. 2). Thus, we could suggest that the different jet profiles inferred from the same frequencies but different epochs may arise from variations in the jet properties at the formation site, within timescales of a few months. This might show how jets are far from being subject to regular injection and that conditions and, consequently, acceleration patterns, can behave in an extremely dynamic way. Further evidence for time-variability of the physical properties at the jet base is provided by the observed time-dependence of the core shift effect (Plavin et al. 2019), as well as by the well-known flux density variability that characterizes the nuclear regions on timescales from hours to months.

4.5. Comparison with other AGN jets

As discussed, most of the force-free jets we have simulated are characterized by sheath acceleration and by a slow spine. This result appears at odds with observational constraints, which rather indicate the existence of a fast spine and a slow sheath. Such a velocity structure was suggested, for instance, to reconcile the observed spectral properties of FRI radio galaxies with their beamed parent population, the BL Lacs (Chiaberge et al. 2000), and appears required to explain the general anti-correlation between the observed Lorentz factor and the jet viewing angle (see, e.g., Homan et al. 2021, Fig. 12). Misaligned jets, which are seen from the side, are usually characterized by mildly relativistic speeds, as opposed to blazar jets, which are observed closer to the jet axis with Lorentz factors of the orders of tens (e.g., Lister et al. 2019). This is in agreement with the frequent observation of limb-brightening in misaligned jets (see, among others, the recent cases of Centaurus A and NGC 315 by Janssen et al. 2021; Park et al. 2021, respectively), which can be interpreted as due to the Doppler de-boosting of the fast spine. Note that this applies not only to the low-power FRI jets, but also to the powerful FRIIs (see the case of Cygnus A, presented by Boccardi et al. 2016).

Consequently, in this scenario, a match between our simulations and observations implies that jets would need to propagate with shear layers protecting the spine or with non-force-free magnetic field configurations, since jets with fast spine are produced in both families of models. On the opposite side, while faster shear layers with hot spines are likely not suggested from VLBI observations, such a radial velocity structure is not ruled out. In this situation, the initial force-free, thin shear layer models are favored.

As recently shown by Boccardi et al. (2021), the properties of the outer jet sheath may vary depending on the accretion mode in the AGN. Specifically, an extended and possibly disk-launched jet sheath was observed in High Excitation Radio Galaxies (HERG), which are mostly characterized by FRII morphologies. On the other hand, Low Excitation Radio Galaxies (LERG), associated to both FRI and FRII morphologies, showed in comparison a narrow jet anchored in the very inner regions of the accretion flow. In future works, we aim to explore possible connections between HERG/LERG and the different acceleration patterns we observed in this paper.

Furthermore, in a future work, we plan to extrapolate synthetic spectral index maps from our models using the post-processing code published in Fromm et al. (2018). In this way, we will be able to compare the simulated spectral properties with the observations and explore whether the different acceleration patterns we recover, and especially the outer layer acceleration, may result in characteristic signatures that can be related to the underlying magnetic field properties (e.g., Kramer & MacDonald 2021).

4.6. A warning note on our setups: Jet evolution

When jets are initially launched in AGN, they trigger a bow shock that propagates through the ambient medium. Because the jet flow advances faster within the formed jet channel than this forward bow shock, the jets get surrounded by overpressured, shocked jet plasma (known as backflow or cocoon). Therefore, collimation must be, in this initial phase, controlled by both the pressure of this shocked environment and the jet toroidal field. As the jet expands and the bow and reverse shocks propagate to large distances, the pressure in the cavity formed by the jet falls continuously with time (see, e.g., Perucho et al. 2014; Perucho 2019). Then, the gravitational potential of the galaxy, which acts in a dynamical time $\sim 1/\sqrt{G\rho_{DM}}$ (where G is the gravitational constant and ρ_{DM} is the dark matter density in the galaxy), allows the galactic pressure and density profiles to be recovered (see, e.g., Perucho et al. 2014) and therefore, pressure should fall to the original ISM values, i.e., $\sim 10^{-10}$ dyn/cm^2.

The expected jet energy fluxes and magnetic field intensity in this region ($F_j \sim 10^{43} - 10^{44}$ erg/s and $B \sim 0.1 - 1$ G) result in extremely large overpressure of the jet with respect to the ISM. Once the jet is accelerated to relativistic velocities, the opening angle is proportional to the inverse of the Lorentz factor (see Komissarov 2012). The large initial overpressure poses a strong challenge to jet collimation and to numerical simulations aimed at studying this region. In our simulations, we decided to achieve overpressures as large as possible, which could allow free expansion, by introducing significant pressure gradients in distance. Once free expansion is allowed, the ambient pressure becomes relatively irrelevant, and this has allowed us to run our simulations. Establishing ambient media with realistic initial pressure causes the code to crash and makes such simulations impossible.

An obvious question arises: how is it then possible that the jets manage to settle in such ambient media with a pressure that can be orders of magnitude smaller than the jet pressure? We would hypothesize that it is because the jet has adapted to its environment in a continuous, relatively slow way during the time it takes for its terminal shock to reach kiloparsec scales, as opposed to simulations. In addition, this probably makes a non-force-free magnetic field configuration necessary, for magnetic tension to play a significant role in jet collimation in the region where it is precisely still strong, i.e., the sub and trans-Alfvènic regions, until the jet is collimated by its own velocity. Furthermore, the collimating effect of the toroidal field also avoids the loss of internal energy via Bernoulli acceleration, allowing this energy budget to act at larger scales (see also Anglés-Castillo et al. 2021).

5. Conclusions

In this paper we have performed a numerical study of the jet acceleration in typical FR I radio galaxies using the well-known source NGC 315 as a starting model. We explored the evolution on sub-parsec and parsec scales of different axisymmetric jet models using a two-dimensional RMHD code, and compared our final results with the observational properties inferred on the same scales by means of VLBI observations. Our results are summarized here.

- All the simulated models show acceleration from initial Lorentz factor values of $\gamma \sim (1-2)$ up to maximum $\gamma \sim (2-5)$ within the simulated scales of $(0.3-3.3)$ pc (Fig. 8). The flux budget evolution for the different simulated models reported in Fig. 10 clearly shows how the dominant energy flux at injection mainly drives the acceleration. Both the internal and magnetic energy channels are dissipated in turn to accelerate the jet, and so increase the kinetic energy of the beam. Moreover, we notice how in very specific cases, such as during the expansion phase, the internal energy can be dissipated to increase the jet speed, even in magnetically dominated jets. Our results on the acceleration mechanisms are mainly relevant in two different ways. i) They confirm the current magnetic acceleration paradigm (Komissarov et al. 2007; Komissarov 2012). Indeed, in the case of cold, magnetically dominated jets the magnetic energy is converted into kinetic energy, thus accelerating the bulk flow. ii) They expand the current view on thermal acceleration in internally dominated jets. In contrast to what is proposed in (Vlahakis & Königl 2003a,b, 2004), where the thermal acceleration is claimed to play a role only on compact scales before being overtaken by the magnetic acceleration, our findings indicated that when jets are thermodynamically relativistic (Perucho et al. 2017), thermal acceleration remains relevant even at parsec scales. Furthermore, thermal acceleration enables to reach higher Lorentz factors than previously thought, aligning with those observed in AGN jets (in this specific case, in NGC 315). Remarkably, given that thermal acceleration can operate even when the jet undergoes conical expansion, our results suggest that jets can continue to accelerate on large scales, beyond the collimation region.
- We infer an explicit relation between the jet speed profiles and the intrinsic jet properties. The different velocity structures show a dependence on the magnetic field configurations, i.e., force-free vs. non-force-free, and/or the dominating energy flux. When a Mach disk, a strong internal planar shock, is formed due to the fast expansion, the acceleration deviates towards the outer and expanding layers. A mild acceleration on the spine is visible only towards the end of the grid of our simulation domain. On the contrary, when jets develop milder, conical shocks, the acceleration is concentrated in the central spine and smoothly decreases toward the external medium. The Mach disk is prominently visible in the force-free and magnetically dominated scenario. However, a thicker shear layer may delay the propagation and bouncing of the waves long enough to avoid the formation of the Mach disk and altering the downstream evolution of the jet, leading to a spine-accelerated structure. This result implies that the initial thickness of the shear layer, possibly associated with accretion disk-launched winds, is a relevant element in understanding the evolution and propagation of relativistic jets. While the acceleration focused on the outer layers can be a signature of magnetically dominated jets with thin sheaths, this does not necessarily exclude hot jets. In the non-force-free configuration, the Mach disks are completely absent, and a classical expansion/recollimation pattern with spine acceleration is observed.
- The opening angle profiles shown in Fig. 9 highlight how the force-free models expand faster than the non-force-free counterpart. This is attributed to the disengagement of the magnetic field force in the former scenario, which eliminates the contribution of the magnetic tension to the jet collimation. From the comparison of the opening angle (Fig. 9) and Lorentz factor (Fig. 8) profiles, we can distinguish two clear

evolution cases: i) the models that develop strong shocks and have the acceleration focused in the outer layers are the ones showing the fastest growth and higher maxima in the opening angle and ii) those developing conical shocks with a downstream fast-spine structure are the ones with smaller slope and lower maxima.

– As seen in Figs. 8 and 9, a number of models can reproduce both the Lorentz factor and opening angle profiles inferred for NGC 315 employing cm- and mm-VLBI observations. From the comparison with the observed jet speed in NGC 315, we suggest certain models are favored over others when it comes to modeling such a source. On the one hand, jets with power larger than 10^{44} erg/s show Lorentz factors at 3 pc which are remarkably larger than the observed one, giving an indication of a possible upper limit on the jet power of NGC 315. On the other hand, we highlight how different models with jet powers $\sim 10^{43}$ erg/s match the different acceleration profiles obtained across the multi-epoch observations at 5 GHz. This may suggest how the small changes in the jet properties at the injection may lead to consistent variations in the observed terminal Lorentz factor. Such variations can occur over time scales of a few months, indicating how the variations in the injection properties may drive the different observed speed profiles.

Acknowledgements. We would like to thank the referee for the comments, which highly improved the quality of the paper. We thank Eduardo Ros for his comments which improved the readability of the manuscript. Moreover, we thank Giancarlo Mattia for the useful discussion on the possible effects of magnetic reconnection. All the simulations were performed on the Cobra cluster of the Max Planck Society. LR and BB acknowledge the financial support of a Otto Hahn research group from the Max Planck Society. LR is funded by the Deutsche Forschungsgemeinschaft (DFG, German Research Foundation) – project number 443220636. MP and JMM acknowledge support by the Spanish Ministry of Science through Grants PID2019-105510GB-C31/AEI/10.13039/501100011033, PID2019-107427GB-C33, and from the Generalitat Valenciana through grants PROMETEU/2019/071 and ASFAE/2022/005. JLM acknowledges support from the Generalitat Valenciana through grant ASFAE/2022/005.

References

Anglés-Castillo, A., Perucho, M., Martí, J. M., & Laing, R. A. 2021, MNRAS, 500, 1512
Balsara, D. S. & Spicer, D. S. 1999, Journal of Computational Physics, 149, 270
Begelman, M. C., Blandford, R. D., & Rees, M. J. 1984, Reviews of Modern Physics, 56, 255
Blandford, R., Meier, D., & Readhead, A. 2019, ARA&A, 57, 467
Blandford, R. D. & Znajek, R. L. 1977, MNRAS, 179, 433
Boccardi, B., Krichbaum, T. P., Bach, U., et al. 2016, A&A, 585, A33
Boccardi, B., Krichbaum, T. P., Ros, E., & Zensus, J. A. 2017, A&A Rev., 25, 4
Boccardi, B., Perucho, M., Casadio, C., et al. 2021, A&A, 647, A67
Bodo, G., Massaglia, S., Ferrari, A., & Trussoni, E. 1994, A&A, 283, 655
Chiaberge, M., Celotti, A., Capetti, A., & Ghisellini, G. 2000, A&A, 358, 104
Fanaroff, B. L. & Riley, J. M. 1974, MNRAS, 167, 31P
Fromm, C. M., Perucho, M., Porth, O., et al. 2018, A&A, 609, A80
Hardee, P. E. 1986, ApJ, 303, 111
Harten, A., Lax, P., & van Leer, B. 1983, SIAM Rev, 25, 35
Homan, D. C., Cohen, M. H., Hovatta, T., et al. 2021, ApJ, 923, 67
Homan, D. C., Lister, M. L., Kovalev, Y. Y., et al. 2015, ApJ, 798, 134
Hovatta, T., Valtaoja, E., Tornikoski, M., & Lähteenmäki, A. 2009, A&A, 494, 527
Janssen, M., Falcke, H., Kadler, M., et al. 2021, Nature Astronomy, 5, 1017
Komissarov, S. S. 2012, MNRAS, 422, 326
Komissarov, S. S., Barkov, M. V., Vlahakis, N., & Königl, A. 2007, MNRAS, 380, 51
Komissarov, S. S., Porth, O., & Lyutikov, M. 2015, Computational Astrophysics and Cosmology, 2, 9
Kovalev, Y. Y., Pushkarev, A. B., Nokhrina, E. E., et al. 2020, MNRAS, 495, 3576
Kramer, J. A. & MacDonald, N. R. 2021, A&A, 656, A143
Laing, R. A., Canvin, J. R., Cotton, W. D., & Bridle, A. H. 2006, MNRAS, 368, 48
Lister, M. L., Homan, D. C., Hovatta, T., et al. 2019, ApJ, 874, 43
López-Miralles, J., Perucho, M., Martí, J. M., Migliari, S., & Bosch-Ramon, V. 2022, A&A, 661, A117
Martí, J.-M. 2015a, Computer Physics Communications, 191, 100
Martí, J.-M. 2015b, MNRAS, 452, 3106
Martí, J. M., Perucho, M., & Gómez, J. L. 2016, ApJ, 831, 163
Martí, J. M., Perucho, M., Gómez, J. L., & Fuentes, A. 2018, International Journal of Modern Physics D, 27, 1844011
Mattia, G., Del Zanna, L., Bugli, M., et al. 2023, arXiv e-prints, arXiv:2308.09477
Medina-Torrejón, T. E., de Gouveia Dal Pino, E. M., Kadowaki, L. H. S., et al. 2021, ApJ, 908, 193
Mignone, A. & Bodo, G. 2006, Monthly Notices of the Royal Astronomical Society, 368, 1040
Morganti, R., Peck, A. B., Oosterloo, T. A., et al. 2009, A&A, 505, 559
Moya-Torregrosa, I., Fuentes, A., Martí, J. M., Gómez, J. L., & Perucho, M. 2021, A&A, 650, A60
Nokhrina, E. E., Gurvits, L. I., Beskin, V. S., et al. 2019, MNRAS, 489, 1197
Nokhrina, E. E., Kovalev, Y. Y., & Pushkarev, A. B. 2020, MNRAS, 498, 2532
Park, J., Hada, K., Nakamura, M., et al. 2021, ApJ, 909, 76
Perucho, M. 2019, Galaxies, 7, 70
Perucho, M., Hanasz, M., Martí, J. M., & Sol, H. 2004, A&A, 427, 415
Perucho, M. & Martí, J. M. 2007, MNRAS, 382, 526
Perucho, M., Martí, J. M., & Hanasz, M. 2005, A&A, 443, 863
Perucho, M., Martí, J.-M., & Quilis, V. 2022, MNRAS, 510, 2084
Perucho, M., Martí, J.-M., Quilis, V., & Borja-Lloret, M. 2017, MNRAS, 471, L120
Perucho, M., Martí, J.-M., Quilis, V., & Ricciardelli, E. 2014, MNRAS, 445, 1462
Plavin, A. V., Kovalev, Y. Y., Pushkarev, A. B., & Lobanov, A. P. 2019, MNRAS, 485, 1822
Pushkarev, A. B., Kovalev, Y. Y., Lister, M. L., & Savolainen, T. 2017, MNRAS, 468, 4992
Ricci, L., Boccardi, B., Nokhrina, E., et al. 2022, A&A, 664, A166
Roe, P. L. 1986, Annual Review of Fluid Mechanics, 18, 337
Shu, C.-W. & Osher, S. 1989, Journal of Computational Physics, 83, 32
Trager, S. C., Faber, S. M., Worthey, G., & González, J. J. 2000, AJ, 119, 1645
van Leer, B. 1974, Journal of Computational Physics, 14, 361
Vlahakis, N. & Königl, A. 2003a, ApJ, 596, 1080
Vlahakis, N. & Königl, A. 2003b, ApJ, 596, 1104
Vlahakis, N. & Königl, A. 2004, ApJ, 605, 656
Worrall, D. M., Birkinshaw, M., Laing, R. A., Cotton, W. D., & Bridle, A. H. 2007, MNRAS, 380, 2

Appendix A: Radial initial fluxes distribution

The convolution of the jet with the shear layer alters the initial analytical distribution of the fluxes, leading to the differences between the modeled and simulated values reported in Table 2.

In Fig. A.1, we show examples of the two main possibilities presented in this paper using models FMH1 and FMH1c. On the one hand, in the lower power models (left panel), the shear layer carries a relevant fraction of the total jet power, in the form of kinetic energy (in Fig. A.1, the kinetic energy absorbs the contribution of the rest mass). This is the consequence of the density in the jet increasing in the shear layer to match the external one. On the other hand, in the high-power, highly magnetized, models (right panel), the shear layer is magnetically dominated for the majority of its cross-section. As shown in Sects. 3 and 4, these differences do not lead to differences in the steady solutions (models FMH1 and FMH1c both develop the Mach disk and evolve with a similar global structure).

Appendix B: From initial conditions to equilibrium: pressure wave

In Fig. B.1 we highlight the evolution of the pressure wave at the three different time steps of t= 20 r_j/c, t= 40 r_j/c, and t= 70 r_j/c for model FMH1_m4. As explained in Sect. 3.1, since the initial jet is overpressured with respect to the external medium, once the simulation starts the jet abruptly expands towards it, giving the material radial velocities and pushing a fraction of it outside of the right boundary. As seen in Fig. B.2, which shows the axial pressure evolution of the ambient for different time steps, the passage of the pressure wave alters the pressure profile which oscillates around the original one. However, after a sufficient number of time steps, the lower and upper boundary conditions allow us to recover the initial, intended pressure ambient profile. Moreover, to test whether this would lead to differences in our final, steady solutions we run model FMH1_m4 with a larger grid of $[n_x, n_z]$ = [100, 30], in order to avoid the ambient material to leave the grid. Fig. B.3 shows the Lorentz factor for model FMH1_m4 (same as Fig. 5 but cut at 1.2 pc) and the counterpart with the larger grid on the x-axis. No major differences in the final profiles are seen, proving how the lost material dragged out by the pressure wave does not affect our results and thus our conclusions.

Appendix C: Resolution study

For our simulations, we chose a resolution of 20 cells/r_j. A first argument in support of this choice is given in Sect. 3.1 and in particular from the radial profiles shown in Fig. 4, which show how the radial evolution of the different physical quantities do not differ between 20 and 40 points. Further evidence in support of our chosen resolution is given in Fig. C.1 which shows the evolution of both the Lorentz factor (left panel) and opening angles (right panel) for two different models (FMH1 and NIH4) at the two discussed resolutions of 20 and 40 points. In order to save computational time, the simulations with 40 cells/r_j have a smaller grid of $[n_x, n_z]$ = [30, 30], implying a physical distance of 0.3-1.2 pc. In the simulated distances, the two different resolutions lead to the same profiles in both tested models, confirming the validity of our choice of using the resolution of 20 cells/r_j.

Appendix D: Further thicker shear layer models from Table 1

In this Appendix, we report in Table D.1 the other simulated models that we did not include in the main text for the sake of the readability of the paper. In detail, we report here the models for which we have tested the thicker shear layers with m = 2 and 4. As shown in Fig. D.1, in all the cases here reported the increased width of the shear layer with m = 4 is not sufficient to avoid the formation of the Mach disks (see Sect. 3). However, we highlight models FMH1c_m4 and FMH1c_m2. In the former, the shear layer with m = 4 is not enough to lead to the morphology change we discussed in the main text. Instead, the shear layer with m = 2 is thick enough to trigger the change in the acceleration pattern, from the outer layer to the internal spine. This model supports what we proposed in Sect. 4.3 concerning the role of the shear layer.

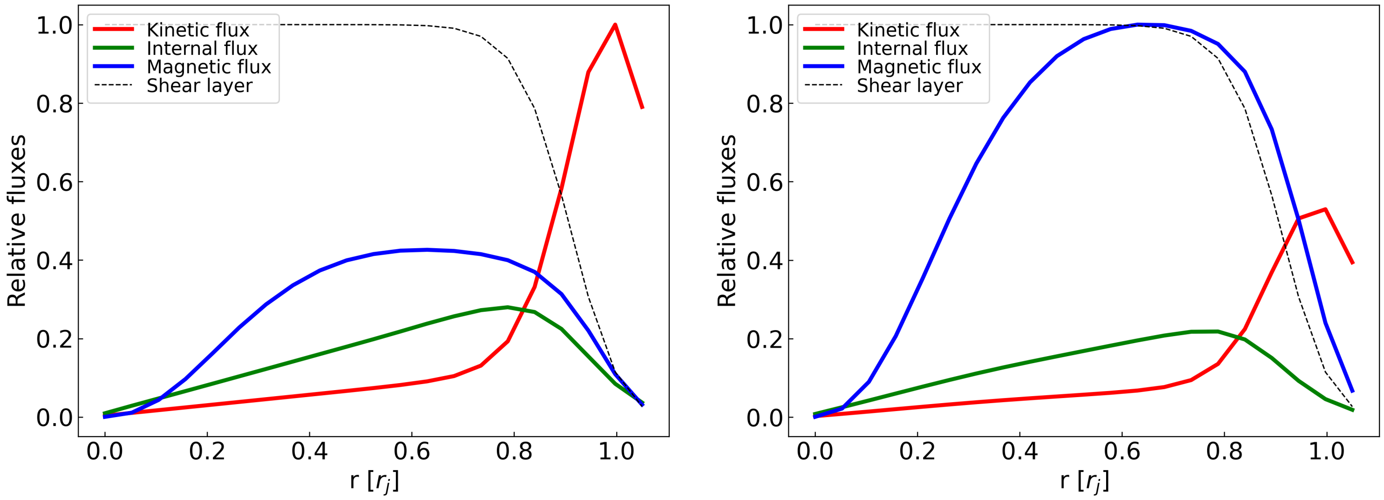

Fig. A.1. Relative initial radial distribution of the different energy channels for models FMH1 (left panel) and FMH1c (right panel). We highlight how the rest-mass contribution is absorbed into the kinetic energy. All the values are normalized to the maximum flux in each respective plot.

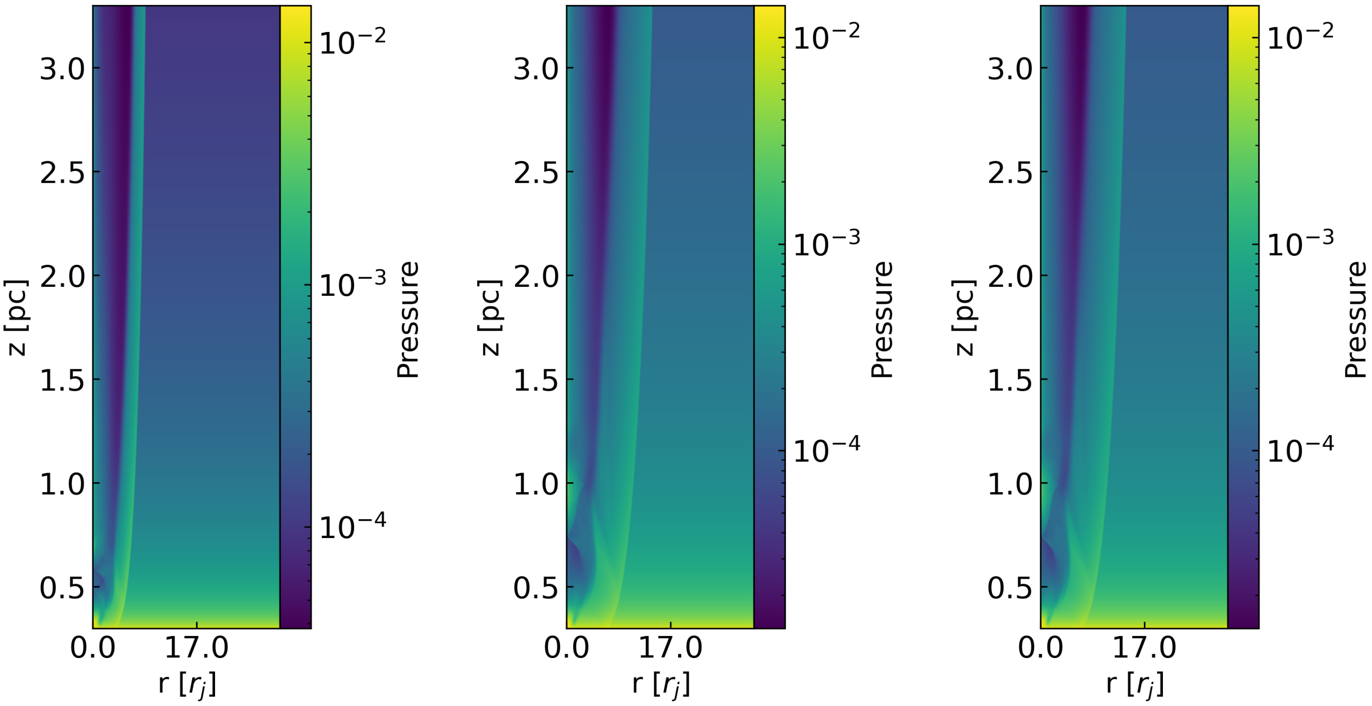

Fig. B.1. Pressure maps at different times for the model FMH1_m4. Starting from left to right the time steps are t= $20\,r_j/c$, t= $40\,r_j/c$, and t= $70\,r_j/c$. The pressure wave moving from the left to the right boundary is clearly visible.

Table D.1. Initial conditions of the other simulated models.

Model code	p_a [code]	p_j [p_a]	ρ_j [ρ_a]	B [G]	$\phi_{\rm B}$ [deg]	v_z [c]	$\mathcal{M}_{\rm ms}$	F_j [10^{43}erg/s]
FIH2_m4	0.01	2.0	0.01	0.46	68.9	0.84	1.05	5.6
FIH4_m4	0.01	4.0	0.01	0.52	66.4	0.79	1.00	6.7
FIH4_m2	0.01	4.0	0.01	0.52	66.4	0.79	1.00	6.7
FMH1c_m4	0.01	1.0	0.01	0.68	75.3	0.93	1.00	17.8
FMH1c_m2	0.01	1.0	0.01	0.68	75.3	0.93	1.00	17.8
FIH3b_m4	0.01	3.0	0.01	0.13	60.6	0.61	1.04	1.6
FIH3b_m2	0.01	3.0	0.01	0.13	60.6	0.61	1.04	1.6

Notes. Column 1: model names; Column 2: initial ambient pressure in code units; Column 3: initial jet overpressure factor; Column 4: ratio between the initial jet density and the ambient one; Column 5: initial magnetic field strength in G; Column 6: initial magnetic pitch angle; Column 7: initial axial velocity; Column 8: average initial Magnetosonic number; Column 9: total jet flux in units of 10^{43}erg/s.

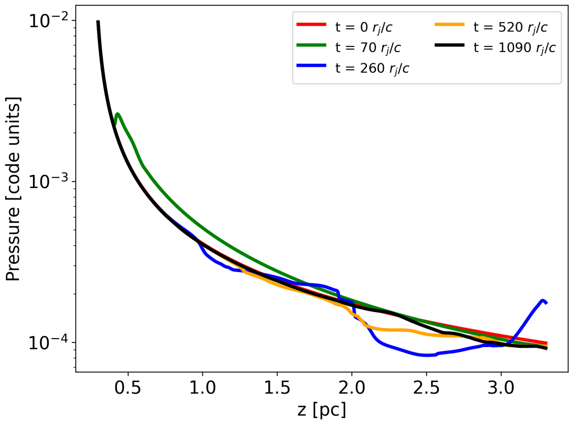

Fig. B.2. Left panel: ambient pressure evolution along the axial direction for the different time steps of t= $0\,r_j/c$ (red line), t= $70\,r_j/c$ (green line), t= $280\,r_j/c$ (blue line), t= $520\,r_j/c$ (orange line), and t= $1090\,r_j/c$ (black line). In the intermediate time steps, the oscillations in the pressure values are due to the passage of the wave. After enough time, such oscillations are absorbed by the boundary conditions and the original profile is recovered.

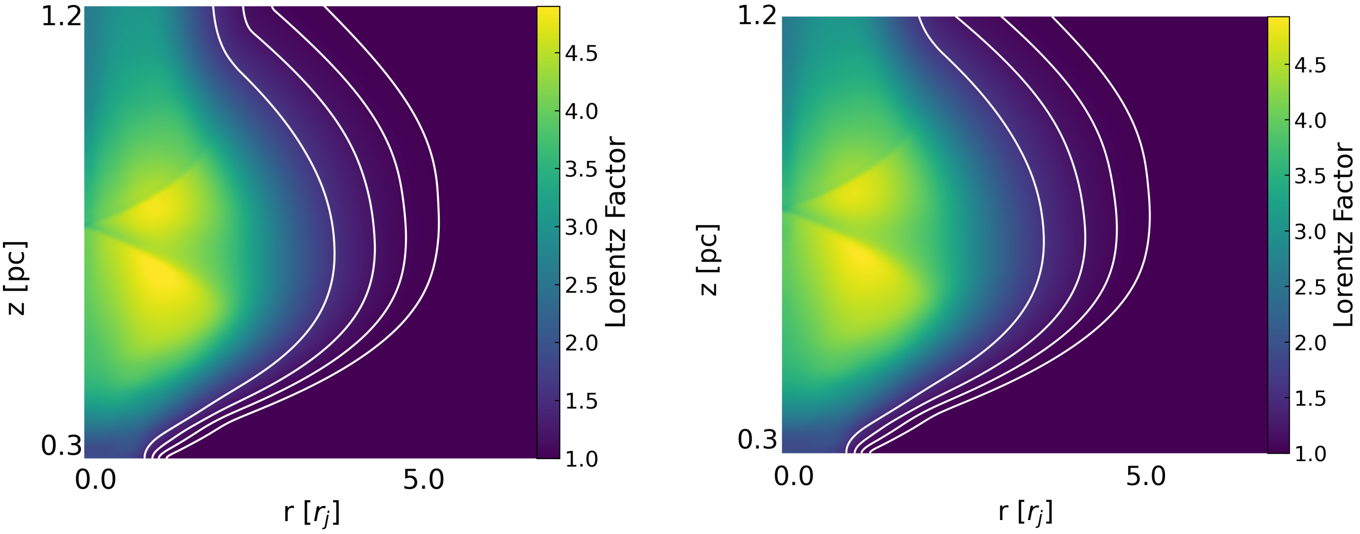

Fig. B.3. Lorentz factor maps for FMH1_m4 with the original grid (left plot) and the alternative grid of $[n_x, n_z] = [100, 30]$. This comparison shows how the material lost in the right boundary does not affect the steady solutions.

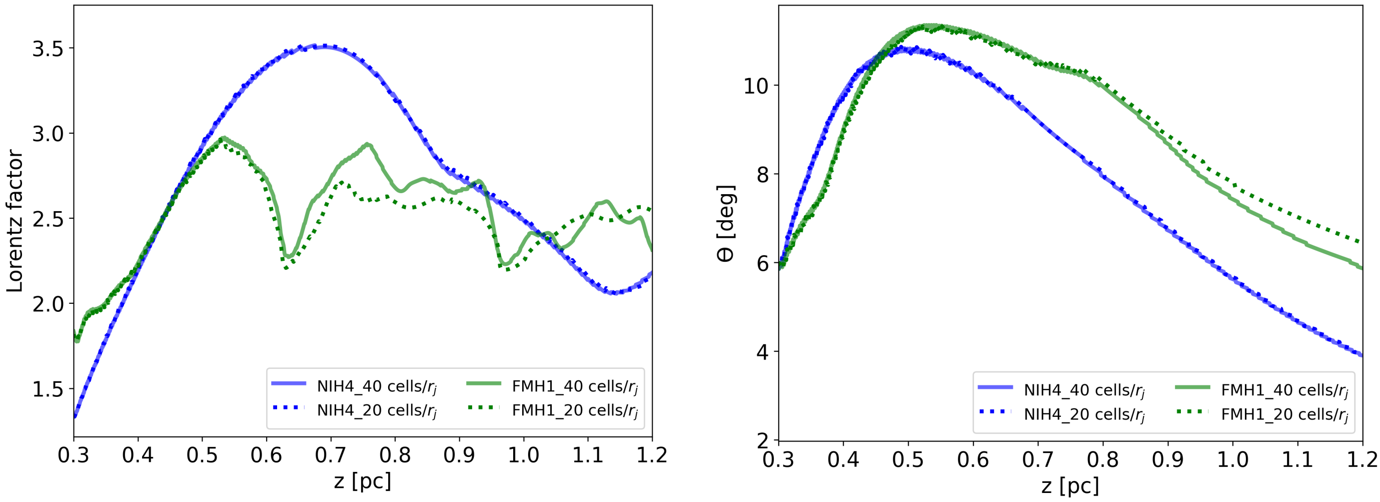

Fig. C.1. Left panel: Lorentz factor evolution up to 1.2 pc for models FMH1 and NIH4 at the resolutions of 20 and 40 cells/r_j. Right panel: half-opening angle obtained in the same models. Blue lines are for model NIH4 (continuous - 40 cells/r_j; dotted - 20 cells/r_j) while green lines are for model FMH1 (same line-style scheme). The comparison shows how the resolution of 20 cells/r_j is enough to reach the saturation point, allowing us to use this resolution value for our simulations.

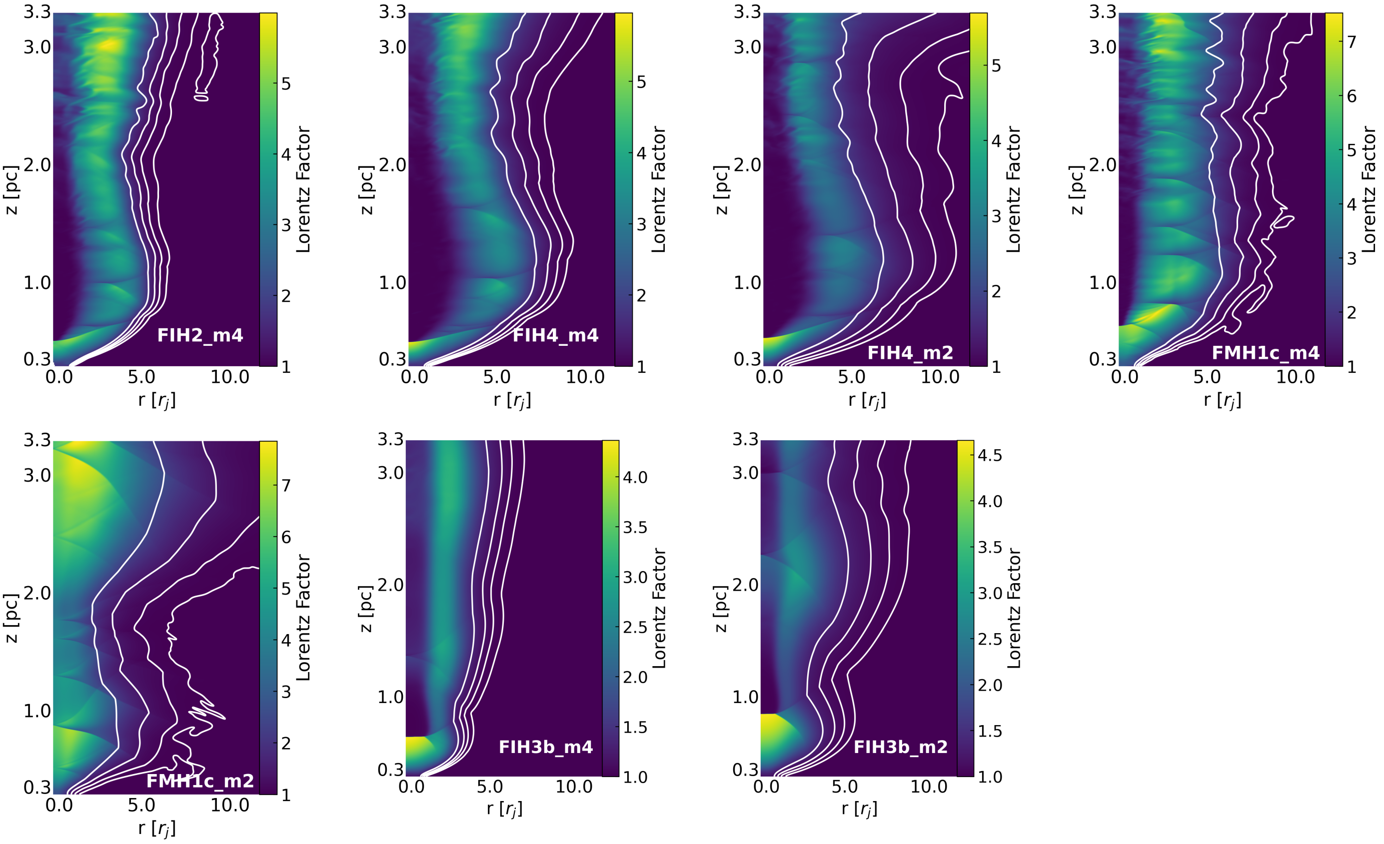

Fig. D.1. Lorentz factor maps for the other simulated models. The white contours represent the tracer at levels 0.2, 0.4, 0.6, 0.8.

6 Spectral properties of the acceleration and collimation region in NGC 315

In the final project of the series of works focused on NGC 315, we further explore the physical jet properties, with an emphasis on the spectral index and magnetic field in the inner parsecs. To accomplish this, we employ: i) new multi-epoch 43 GHz VLBA observations; ii) an archival multi-frequency (1-43 GHz) and simultaneous VLBA data set. The 43 GHz observations were performed in the context of a three-epoch GMVA experiment. The first two epochs (April 2021 and October 2021) at 86 GHz have been analyzed; however, they suffer from major problems preventing us from obtaining images. Namely, in April 2021 the VLBA suffered from bad performances of the 3 mm receiver at different sites, while in October 2021 the observations were afflicted by bad weather in numerous observatories across the globe. The April 2022 epoch has been recently partially re-correlated and the data reduction is currently in progress.

We use the new set of observations to expand the study on the jet collimation, first presented by Boccardi et al. (2021). The new data points are in agreement with the ones previously found, strengthening the scenario of a jet that transits from parabolic to conical shape at $\sim 0.6\,\mathrm{pc}$ downstream the core. Furthermore, by stacking four different observations at 43 GHz, we pinpoint the position of the black hole. The jet width profile suggests that the jet injection occurs $44 \pm 44\,\mathrm{R_S}$ upstream the core at 43 GHz, in agreement with literature results for jets in radio galaxies (Baczko et al. 2022; Hada et al. 2011).

The multi-frequency spectral index study reveals an interesting phenomenon on the sub-parsec, accelerating jet. The high-frequency spectral index maps (22-43 GHz) display a very steep spectrum, reaching values down to ~ -2. This finding aligns with the 22-43 GHz spectral index map presented in Chapter 4 and with the behavior observed for M 87 on the same scales (Ro et al. 2023). This comparison suggests that steep spectra may be a common characteristic in the acceleration and collimation region of AGN jets. Physical explanations are proposed to justify the steep spectrum, including synchrotron losses and different particle acceleration mechanisms, i.e., magnetic reconnection and diffusive shock acceleration. Nonetheless, the physical processes at play are still unclear and subjects for future analyses. Finally, from the combination of our results on the brightness temperature and turnover frequency evolution, by employing theoretical models, we have indications that the magnetic field strength evolves linearly on sub-parsec and parsec scales. This scenario is in agreement with the analysis of the jet and accretion disk magnetization proposed in Chapter 4, strengthening the results presented.

I performed the analysis, from the raw data calibration to the final data products. The exception is the polarization analysis performed by J. Röder. I wrote the text supported by the co-authors, which helped improve the exposition and enrich the discussion. The manuscript will be published in A&A.

Astronomy & Astrophysics manuscript no. output
August 12, 2023

Magnetic and spectral properties of the inner parsec scales jet in NGC 315

L. Ricci[1, 2], B. Boccardi[1], J. Röder[1], M. Perucho[2, 3, 4], G. Mattia[5], M. Kadler[2], P. Benke[1], V. Bartolini[1]

[1] Max-Planck-Institut für Radioastronomie, Auf dem Hügel 69, D-53121 Bonn, Germany
[2] Julius-Maximilians-Universität Würzburg, Fakultät für Physik und Astronomie, Institut für Theoretische Physik und Astrophysik, Lehrstuhl für Astronomie, Emil-Fischer-Str. 31, D-97074 Würzburg, Germany
[3] Departament d'Astronomia i Astrofísica, Universitat de València, C/ Dr. Moliner, 50, 46100, Burjassot, València, Spain
[4] Observatori Astronòmic, Universitat de València, C/ Catedràtic José Beltrán 2, 46980, Paterna, València, Spain
[5] INFN - Sezione di Firenze, Via G. Sansone 1, I-50019 Sesto Fiorentino (FI), Italy

Received / Accepted

ABSTRACT

Aims. The dynamics of relativistic jets in the inner parsec regions is deeply affected by the nature of the magnetic fields. The level of magnetization of the plasma as well as the geometry of these fields on compact scales have not yet been fully constrained.

Methods. In this paper we employ multi-frequency and multi-epoch Very Long Baseline Interferometry observations of the nearby radio galaxy NGC 315. We aim at deriving constraints on the magnetic field properties on sub-parsec and parsec scales by examining observational signatures such as the spectral index, synchrotron turnover frequency, and brightness temperature profiles. This analysis is performed by considering the jet acceleration and collimation region, which can be probed thanks to the source vicinity, as well as in the initial part of the jet conical region.

Results. Our new data confirm previous findings suggesting that the collimation of the jet is completed on sub-parsec scales. From the analysis of a 43 GHz stacked image, we suggest that the black hole is located 41 ± 41 Schwarzschild radii (R_S) upstream of the 43 GHz core, in agreement with findings for other radio galaxy jets. We observe remarkably steep values for the spectral index on sub-parsec scales (down to $\alpha \sim -2$, $S_\nu \propto \nu^\alpha$) which flatten around $\alpha \sim -0.8$ on parsec scales. We propose that such steep values can be a consequence of cooling due to synchrotron losses or the signature of different particle-acceleration mechanisms at play in the two regions. The brightness temperature of the 43 GHz cores indicates a dominance of the magnetic energy at the jet base, while the cores at progressively lower frequencies reveal a gradual transition towards equipartition. Based on the spectral index and brightness temperature along the incoming jet, and by employing theoretical models, we derive that the magnetic field strength has a close-to-linear dependence with distance going from parsec scales up to the jet apex. This is confirmed by the analysis of the synchrotron turnover frequency. The latter is found to lay $15\,\mathrm{GHz} < \alpha_{\mathrm{br}} < 43\,\mathrm{GHz}$ at the location of the 43 GHz core and to decrease down to $\sim 6\,\mathrm{GHz}$ within the innermost $\sim 0.7\,\mathrm{pc}$. Overall, our findings are consistent with a toroidal-dominated magnetic field on all the analyzed scales, although in the collimation region a poloidal-dominated field cannot be ruled out.

Key words. galaxies – individual – jets

1. Introduction

Relativistic jets are plasma outflows launched from the central region of Active Galactic Nuclei (AGN). The most powerful jets have the unique ability to develop structures that propagate up to thousands of parsecs, reaching high relativistic velocities and opening angles of a few degrees (Blandford et al. 2019). Their launching is a consequence of the interplay between the supermassive black hole and the magnetic fields present in the surrounding accretion disk, and is fueled by the extraction of rotational energy from the central object (Blandford & Znajek 1977). The current paradigm asserts that jets initially propagate as Poynting flux-dominated outflows, meaning that their dynamics is dominated by the magnetic fields conveyed from the central region. As the jet propagates, the magnetic fields are expected to play a crucial role, especially in the so-called acceleration and collimation region. This region extends up to $10^3 - 10^7 R_s$[1] from the jet injection point (Boccardi et al. 2021; Kovalev et al. 2020) and, within it, the jets reach small opening angles and high Lorentz factors. The jet acceleration is mainly driven by the conversion of the initial magnetic energy into kinetic energy of the bulk flows (Vlahakis & Königl 2003a,b, 2004). In detail, the hoop stress generated by the toroidal field favors the collimation of the jet and its acceleration. Since this process was shown to become inefficient in a conical jet (Komissarov et al. 2007; Komissarov 2012), the acceleration and collimation mechanisms are expected to be co-spatial. The end of these processes is therefore signaled by a transition in the observed jet shape from (quasi-)parabolic (i.e., $r \propto z^{\sim 0.5}$, where z is the radial distance from the core and r is the jet radius) geometrical shape to conical ($r \propto z^{\sim 1}$).

To test this scenario, observational constraints on the magnetic field properties on sufficiently small scales are necessary. These can be obtained in selected nearby targets thanks to the employment of the Very Long Baseline Interferometry (VLBI) observations performed at centimeter and millimeter wavelengths.

---

[1] R_S is the Schwarzschild radius defined as $R_S = 2GM_{\mathrm{BH}}/c^2$ where M_{BH} is the mass of the black hole

In such studies, magnetic fields of hundreds of mG have been inferred on parsec scales (e.g., O'Sullivan & Gabuzda 2009; Baczko et al. 2016), implying strengths of $10^2 - 10^4$ G assuming the magnetic field strength to vary with distance as z^{-1}. Whether this is a valid assumption, it is currently unknown, and indices flatter than z^{-1} have been recently proposed (e.g., for M 87 Ro et al. 2023).

In this paper, we expand the magnetic field studies in the nearby ($z = 0.0165$, Trager et al. 2000), giant radio galaxy NGC 315. NGC 315 is a Fanaroff–Riley (Fanaroff & Riley 1974) I morphology radio galaxy (e.g., Laing et al. 2006) that extends up to ~ 1 Mpc. This target was chosen due to the richness of available VLBI observations and because its acceleration and collimation region is largely studied and its properties constrained Boccardi et al. (2021); Park et al. (2021b); Ricci et al. (2022). We aim at deriving constraints on the magnetic field properties on sub-parsec and parsec scales by examining the following observational signatures: i) the spectral index, ii) the brightness temperature, iii) the synchrotron turnover frequency.

The paper is structured as follows. In Sect. 2 we describe the data set used; in Sect. 3 we present our results; in Sect. 4 we discuss them and in Sect. 5 we highlight our conclusions.

In this manuscript, we assume a ΛCDM cosmology $H_0 = 71$ h km s^{-1} Mpc^{-1}, $\Omega_M = 0.27$, $\Omega_\Lambda = 0.73$ (Komatsu et al. 2009). The luminosity distance of NGC 315 is $D_L = 70.6$ Mpc, and 1 mas corresponds to 0.331 pc.

2. Data set and maps analysis

2.1. Original data set

In this article we present three new VLBA (Very Long Baseline Array) observations of NGC 315 at 43 GHz, performed in the period April 2021/April 2022 with a time interval of ~ six months. Such experiments were carried out during the GMVA (Global mm-VLBI Array) observing sessions, where the source was also observed at 86 GHz. Data obtained at this higher frequency will be presented in a future article in preparation.

The data reduction was performed in AIPS (Greisen 1990), following the standard procedure for VLBA data sets. The imaging, together with the amplitude and phase self-calibrations, was performed using DIFMAP (Shepherd 1997). The first and second epochs suffered from flux density scaling problems arising, respectively, during the data correlation and due to issues at the focus and rotation at the VLBA stations. [2]. For the April 2021 observations, the problem was solved by applying an antenna-based scaling factor of $\sqrt{2}$, while corrected gain curves provided by the VLBA staff were used for correcting the amplitude calibration of the October 2021 data.

The log of observations and properties of the clean maps produced are reported in Table 1; the clean images are shown in Fig. 1.

2.2. Ancillary data

Along with the new observations, we re-analyze the VLBA multi-frequency, simultaneous data set published by Park et al. (2021b). This comprises observations at seven frequencies in the range 1.7 GHz-43 GHz Table 1. While a spectral index analysis for such observations was already published (Park et al. 2021b), in this work, we aim at expanding it (see Sect. 3.3) by also performing a synchrotron turnover frequency study (see Sect. 3.6). The observations have been analyzed and imaged using the same procedure as in Sect. 2.1. The clean images are mostly comparable to those reported by Park et al. (2021b). Based on our assumption of a flux density uncertainty of 5%, the brightness peaks are all comparable except at 15 GHz. Indeed, at this frequency, we recover a brightness peak ~ 9% higher using the same restoring beam. The image noise level is comparable as well, with the exception of the 2 GHz and 22 GHz images, where our rms noise is 40% and 30% higher, respectively. The higher flux density of our 15 GHz map better matches the value expected based on the results obtained at the other frequencies (see next section).

Unlike it was done by Park et al. (2021b), in our spectral analysis we include the 43 GHz observations. While the quality of the data is poor, and very little of the extended emission can be recovered, we employ such a map to explore the spectral properties in the core region and in the immediate beginning of the optically thin region (see Sect. 3.3). Here, we expect the signal-to-noise ratio to be high enough for our results to be reliable. After imaging in DIFMAP, the polarization calibration, for both the 43 GHz and the VLBA data set, was handled by the ParselTongue-based pipeline GPCAL (Park et al. 2021a).

Finally, to increase the number of data points in the brightness temperature profiles (see Sect. 3.5), we further include the 15 GHz observations from the MOJAVE [3] monitoring program (Lister et al. 2018) and the maps published by Boccardi et al. (2021). From the latter, we also include 22 GHz and 43 GHz observations from 2008 and 2018 which were used in Ricci et al. (2022) to perform a first spectral analysis and are here shown as well to be compared with our new results (Sect. 3.3).

2.3. Flux density

In Fig. 2 we represent the flux density as a function of the frequency for the maps employed in the spectral analysis along with the new 43 GHz observations. We fix the errors on the flux density at 5% of its value. For the 43 GHz map from 2020, we assume a more conservative value of 10%, due to the poor data quality.

To check the consistency of the total fluxes densities obtained for the simultaneous VLBA data set, we fit these data with the synchrotron emission spectrum (Pacholczyk 1970):

$$I_\nu = I_0 \left(\frac{\nu}{\nu_{\rm br}}\right)^{\alpha_t} \left[1 - \exp\left(-\left(\frac{\nu_{\rm br}}{\nu}\right)^{\alpha_t - \alpha}\right)\right] . \quad (1)$$

Here, I_0 is the flux density at the turnover, $\nu_{\rm br}$ is the turnover frequency, α_t is the spectral index of the optically thick region, and α of the optically thin one. All the parameters are left free to vary. As shown by the blue line in Fig. 2, the flux density at each frequency is consistent with the fit and no outlier is present. A comparison with data obtained at different epochs at 22 GHz and 43 GHz shows, however, a significant scatter, indicating that NGC 315 is quite variable at high radio frequencies.

2.4. Core-shift

Due to the opaque nature of the synchrotron emission, the optically thick/optically thin transition surface moves downstream

---

[2] https://science.nrao.edu/facilities/vlba/data-processing/7mm-performance-2021

[3] see https://www.cv.nrao.edu/MOJAVE/sourcepages/0055+300.shtml

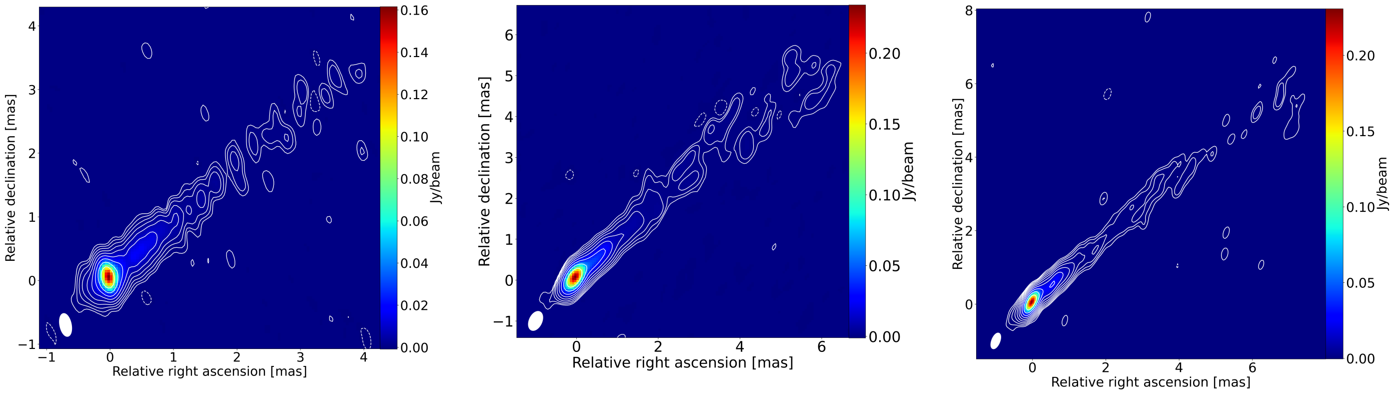

Fig. 1. 43 GHz VLBA observations performed in: left panel - April 2021; middle panel: October 2021; right panel - Apr 2022. The contours are set to (-0.2, 0.2, 0.4, 0.8, 1.6, 3.2, 6.4, 12.8, 25.6, 51.2)% of the respective brightness peaks. The images were produced with uniform weighting and no taper.

Table 1. Summary of the VLBA data. The upper three lines report the properties of the new 43 GHz data while the bottom lines include the simultaneous VLBA data set.

ν [GHz]	Obs date	Beam [mas, mas, deg]	Total flux [Jy]	Brightness peak [Jy/beam]	$\sigma_{\rm rms}$ [mJy/beam]
43.2	24 Apr 2021	0.343×0.16, 11.6	0.340	0.162	0.125
43.2	04 Oct 2021	0.461×0.277, - 25.2	0.404	0.234	0.161
43.2	02 Apr 2022	0.413×0.184, - 22.1	0.413	0.231	0.052
1.5	05 Jan 2020	9.806×6.220, - 2.8	0.387	0.241	0.047
2.3		6.462×4.790, - 0.8	0.454	0.291	0.196
5.0		2.855×1.350, - 5.1	0.594	0.360	0.041
8.4		1.709×1.113, - 10.7	0.657	0.401	0.063
15.3		0.964×0.672, - 9.3	0.626	0.311	0.067
22.2		0.804×0.521, - 9.3	0.524	0.267	0.096
43.1		0.533×0.461, - 9.3	0.325	0.252	0.542

Notes. Column 1: observing frequency in GHz; Column 2: date of the observation; Column 3: beam size and position angle; Column 4: total flux density in Jy; Column 5: brightness peak value in Jy/beam; Column 6: thermal noise in mJy/beam.

of the jet while decreasing the observing frequency. Therefore, the analysis of a multi-frequency data set requires the alignment of the maps to a common reference point, which needs to be determined and which coincides, ideally, with the position of the central black hole. In this work we assume as a reference point the position of the VLBI core at 43 GHz, as previously done by Boccardi et al. (2021); Ricci et al. (2022). Such an approximation can be considered valid when studying jets in radio galaxies, since the mm-core has been observed to lay close to the jet inlet (e.g., Hada et al. 2011; Baczko et al. 2022). Nonetheless, we discuss the validity of this assumption when exploring the real position of the central black hole (Sect. 3.2).

Several methods have been developed to determine the core-shift (see e.g., O'Sullivan & Gabuzda 2009, and references therein). Here, the core shift is computed by performing a 2D-cross correlation analysis by aligning optically thin jet regions identified in consecutive pair of frequencies [4]. In each pair, the maps are created using the same pixel size and restoring beam, and the data are restricted to the same uv-range. Moreover, each map is centered on the brightest pixel. For the beam, we select the equivalent circular beam of the lower-frequency map, while the pixel size is set to 1/10 of the beam. The pixel size is signal-to-noise dependent: in the brightest regions, smaller values, e.g., 1/10 of the beam, can be generally assumed without oversampling the data and generating artifacts. On the contrary, such problems could arise in regions with progressively lower signal-to-noise ratio, such as towards the extended jet emission. Here, pixel sizes of 1/5 of the beam would be more appropriate. In the community, average values of ~ 1/6 - 1/8 of the beam are chosen. In this work, we assume a value of 1/10 for two reasons: i) to obtain a more precise estimate of the core shift, which is crucial to obtain appropriate spectral index and turnover frequency maps; ii) for our goals, we are mostly interested in the innermost jet region, where the emission is brighter. Our results on the core-shift are summarized in Table 2.

In Fig. 3, we show the core shift for two different data sets. The blue data points are those reported in Table 2, while the green ones are taken from Boccardi et al. (2021). As errors, we sum in quadrature the uncertainties on the core and images alignment, both equal to one pixel. The former arises from setting the origin of the maps in the pixel which has the highest flux density. The latter is the minimum displacement that the used method can compute. The blue continuous line represents the power-law fit ($z_{\rm core} \propto \nu^{-1/k_r}$) of the VLBA simultaneous dataset using the best-fit values from Park et al. (2021b). The green continuous line marks the best fit for the 1.5-43.1 GHz data from Boccardi et al. (2021), where the data used were not simultaneous in the

---

[4] The analysis has been performed using the code developed by Tuomas Savolainen.

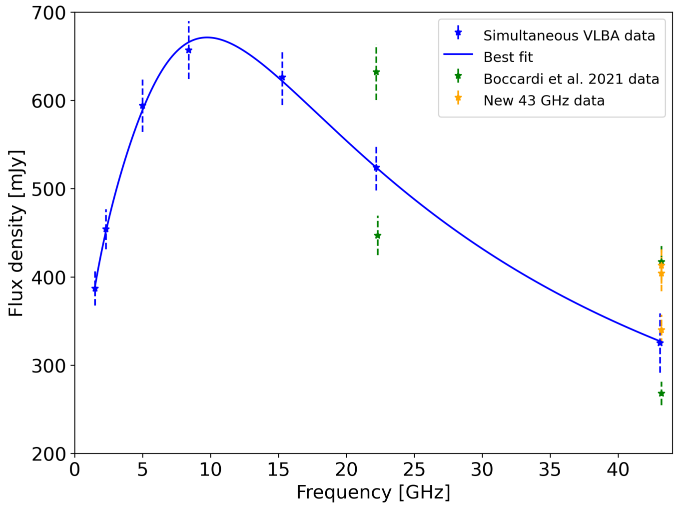

Fig. 2. Flux density as a function of frequency. The blue data points are from the re-analyzed multi-frequency VLBA data set, the green points are from the 22 GHz and 43 GHz observations published in Boccardi et al. (2021), and the yellow points are from the new 43 GHz observations presented in Sect. 2.1.

entire frequency range but only between the pairs of frequencies used for the core-shift determination. Park et al. (2021b) found a best-fitting value of $k_r = 0.72 \pm 0.10$, while Boccardi et al. (2021) found $k_r = 0.84 \pm 0.06$.

Our results obtained from the low-frequency data points (1, 2, and 5 GHz) confirm those of Park et al. (2021b). We do, however, find slightly larger values of core shift at the higher frequencies of 8, 15, and 22 GHz. Indeed, our total displacements are larger since we include the core shift between 22 GHz and 43 GHz, while Park et al. (2021b) computed the core shift relative to the 22 GHz position. As a consequence, our data at high frequencies are more consistent with the estimations by Boccardi et al. (2021) Nonetheless, the best-fitting of the re-analyzed VLBA data, shown in the orange line, leads to $k_r = 0.70 \pm 0.06$, matching the result from Park et al. (2021b).

Time-dependent variations on the core shift are expected due to its dependence on the physical properties of the plasma, such as the strength of the underlying magnetic field and the particle density (Plavin et al. 2020). However, here the differences in displacement are minimal, and could also be related to other factors, such as the uncertainties arising in the imaging process. Throughout the paper, we will use the two different core-shift measurements depending on the observations we are considering: the ones reported in Table 2 for the VLBA simultaneous data set and the ones published in Boccardi et al. (2021) for their data set.

2.5. Gaussian modelfit components

To compute at different locations the jet width and the brightness temperature (see Sect. 3.5) we fit the visibilities with Gaussian circular components. This procedure is performed using the sub-routine *modelfit* in DIFMAP. The main physical parameters (frequency, flux density, position, size) of the components are reported in Appendix A. We perform such analysis for the new 43 GHz VLBA observations, as well as for the VLBA simultaneous data set and the 15 GHz MOJAVE data. For the maps reported in Boccardi et al. (2021), we use the components they report in Appendix A. All the maps are centered in order to have the origin coinciding with the core component associated, and then shifted according to the core-shift estimations (Sect. 2.4).

Table 2. core-shift measurements relative to the 43 GHz core for the simultaneous VLBA data set.

ν [GHz]	Δ_x [mas]	Δ_y [mas]	Δ_z [mas]
1.4	3.90 ± 1.42	-3.33 ± 1.42	5.15 ± 1.42
2.3	2.34 ± 0.90	-1.17 ± 0.90	2.94 ± 0.90
5.0	0.63 ± 0.40	-0.63 ± 0.40	0.89 ± 0.40
8.4	0.40 ± 0.23	-0.40 ± 0.23	0.57 ± 0.23
15.3	0.14 ± 0.14	-0.14 ± 0.14	0.20 ± 0.14
22.2	0.06 ± 0.06	-0.06 ± 0.06	0.09 ± 0.09
43.0	0.0	0.0	0.0

Notes. Column 1: observing frequency in GHz; Column 2: displacement along the right ascension in mas; Column 3: displacement along the declination in mas; Column 4: radial displacement in mas.

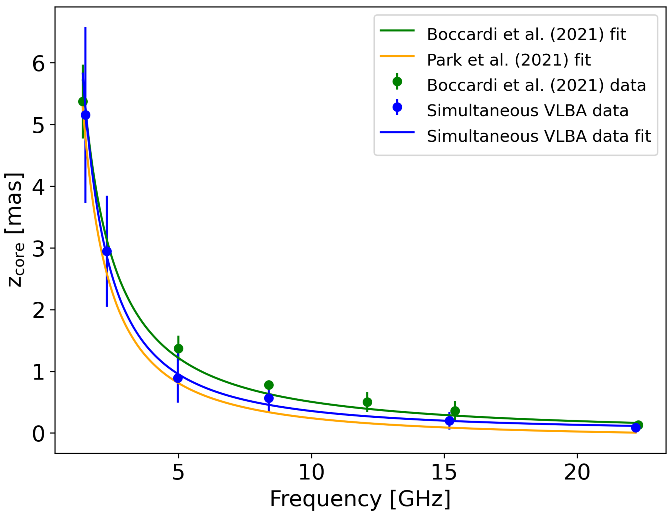

Fig. 3. Core position as a function of frequency for the two different data sets: i) the multi-frequency VLBA data set (blue points); ii) the multi-frequency and multi-epoch data set presented in Boccardi et al. (2021) (green points). The blue line represents the best-fit values presented in Park et al. (2021b), the green line the ones shown in Boccardi et al. (2021), while the yellow line trace the best-fit performed in this paper.

To compute the errors on the modelfit parameters we follow a conservative approach. For the errors on the component fluxes, we assume 10% of their values, for the position we assumed 20% on the radial distance from the core added in quadrature with the uncertainty on the core shift, while for the uncertainty on the size we assume 25% of the FWHM (Boccardi et al. 2021). To remain coherent with their approach, when the Gaussian components are employed to compute the collimation profile (see Sect. 3.1), we filter out the components whose size is 50% smaller than the minor beam axis. To compute the brightness temperature profile we use a less conservative approach, considering all the components having sizes larger than 20% of the minor beam axis. For the core components, being in a region with high signal-to-noise, we use 10% times the minor beam axis as a threshold. While more refined techniques to compute the errors on the modelfit components exist (see e.g., Burd et al. 2022), in our work this analysis is functional to compute the brightness temperature and

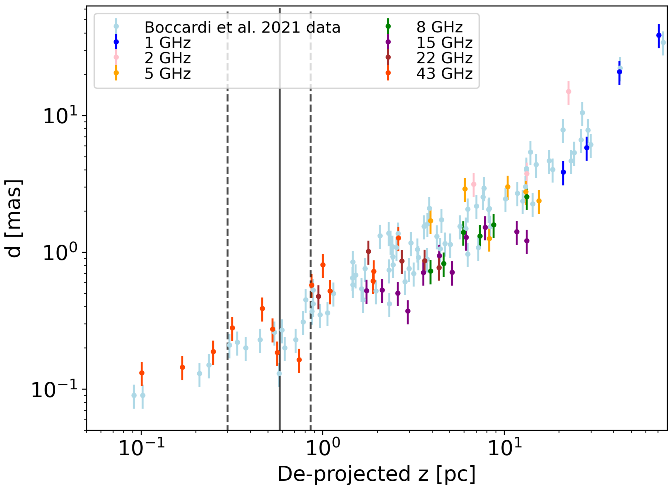

Fig. 4. Expansion profile of NGC 315 using the previously published data points from Boccardi et al. (2021) together with the new measurements from the data set here presented. The black vertical lines highlight the collimation distance proposed in (Boccardi et al. 2021), i.e., z = 0.58 ± 0.28.

perform power-law fits on its evolution at the different frequencies.

3. Results

3.1. Collimation profile

We use the new data at 43 GHz as well as the re-analyzed VLBA data to enrich the description of the jet expansion profile from sub-parsec to parsec scale Fig. 4, previously presented by Boccardi et al. (2021).

The newly added data points show remarkable agreement. Boccardi et al. (2021), by fitting the profile with a broken power-law, inferred the transition from a parabolic to a conical jet shape to happen at a distance of $z_t = 0.58 \pm 0.28$ pc, highlighted by the black vertical lines in Fig. 4. The two innermost data points at 43 GHz are particularly important. Indeed, by showing a slightly wider jet than previously inferred at similar distances, they are strengthening the interpretation of parabolic expansion on sub-parsec scales. Interestingly, in correspondence with the jet break, different data points show a smaller jet width, suggesting the presence of a recollimation region. The expansion profile is further employed in Sect. 3.2 to investigate the real position of the central black hole.

3.2. Black hole position

To gain insights into the real position of the black hole, we use a stacked image obtained by combining 43 GHz observations (Fig. 5, left panel). Specifically, we use four different epochs: the three presented in Sect. 2.1 and the 2018 epoch published in Boccardi et al. (2021). Since our goal requires a stacked image with as high as possible angular resolution in the central region, we use maps obtained with uniform weighting. Consequently, we calculated the average equivalent beam and convolved the images using a beam equal to ~ 65% of its value. Indeed, a super-resolution of the image is possible, at least in the high signal-to-noise regions, assuming a beam down to approximately ~ 65% of its nominal value. This procedure is justified since, while it may result in spurious features in the extended emission, we employ it to explore the bright core region. The obtained stacked image is shown in the left panel of Fig. 5. The jet width profile is obtained on a pixel-base using the code presented in Ricci et al. (2022). For details on the code, we refer to Section 2 of this paper. The jet width profile is shown in Fig. 5, right panel.

Given the observed two-sided expansion, i.e., in the jet side and counter-jet side, we consider the pixel showing the minimum width as the most likely for pinpointing the location of the jet injection point, i.e., of the central black hole. We find the minimum to lay upstream of the brightest pixel, in the direction of the counter-jet, as expected due to the core shift. Specifically, this is located 0.015 ± 0.015 mas = 41 ± 41 R_s upstream the core position at 43 GHz. The suggested position of the black hole is consistent with previous estimations for radio galaxies, i.e., $\lesssim 100\,R_s$ (Hada et al. 2011; Baczko et al. 2022). The width inferred at injection is 35 ± 4 R_s, consistent with the one observed at the jet base in M 87 (about 30 – 40 R_s, Lu et al. 2023).

Using the extrapolated jet width at the suggested jet origin position, we perform a power-law fit along the proposed parabolic region Boccardi et al. (2021) by employing the updated jet width profile (Fig. 4). The obtained function will be needed when extrapolating the magnetic field strength from the turnover frequency values (Sect. 4.1). We assume the most generic power-law function, i.e., $d = d_0 + b(z - z_0)^c$, fixing d_0 and z_0 to the initial position and width observed in Fig. 5. The best-fit parameters are $b = 0.25 \pm 0.04$ and $c = 0.47 \pm 0.12$. The obtained index c defining the jet shape confirms the occurrence of a parabolic expansion on such scales.

3.3. Spectral index

Following the procedure described in Sect. 2.4 to obtain the core-shift values (Table 2) and correctly aligning the images, we compute the spectral index maps between pair of frequencies using the simultaneous observations reported in Table 1. In the total intensity maps, we filter out pixels with brightness below 10 $\sigma_{\rm rms}$. The spectral maps are presented in Fig. 6.

In all maps, we observe a core region characterized by an inverted spectral index, $\alpha > 0$ with $S_\nu \propto \nu^\alpha$, and a jet with steep to very steep spectral index. In two maps, we are able to determine spectral index values in the counter-jet, which are also steep. Interestingly, in the two highest-frequency pairs (15-22 GHz and 22-43 GHz), the optically thick region shows a transverse gradient, with a more inverted index in the south core region. The possibility that this is due to an inexact core-shift determination seems unlikely, since a similar sub-structure has been previously observed by Ricci et al. (2022) at 22-43 GHz using a different data set. Projection or absorption effects might play a role in this. Concerning the latter, the low-frequency data do indicate the occurrence of free-free absorption in the nuclear regions. In particular, an inverted spectrum up to $\alpha = 4.5$ is observed between 1.4 GHz and 2.3 GHz, which may be caused by the passage of synchrotron self-absorbed emission with $\alpha = 2.5$ through optically thick free-free absorbing material with $\alpha = 2$ (see, e.g., Kadler et al. 2004, and references therein).

The counter-jet spectrum is determined for the frequency pairs 2 GHz -5 GHz and 5 GHz -8 GHz. In the former case, the spectral index drops drastically to $\alpha \sim -2$. In the latter case, instead, the spectrum is flatter, i.e., $\alpha \sim -0.5$ showing similar values with respect to the jet. The reason behind this variability is unclear, and a symmetric spectral index gradient in the jet and counter-jet sides is observed only in the second case.

In the jet region, we observe optically thin synchrotron emission at all frequencies. In the four lowest frequency maps, the jet

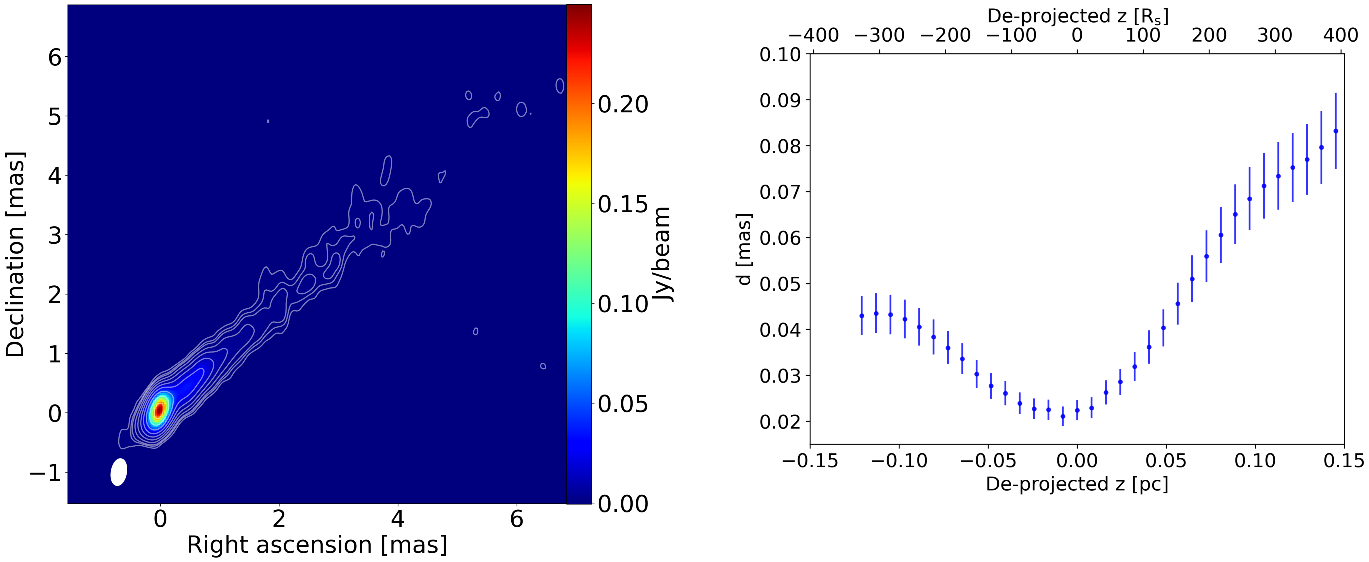

Fig. 5. Left panel: stacked image at 43 GHz created using four different epochs, each restored with a common elliptical beam. Right panel: jet width as a function of the distance from the core, based on the analysis of the super-resolved stacked image. The minimum jet width, observed at 0.015 ± 0.015 mas = 41 ± 41 R_S, may pinpoint the position of the black hole.

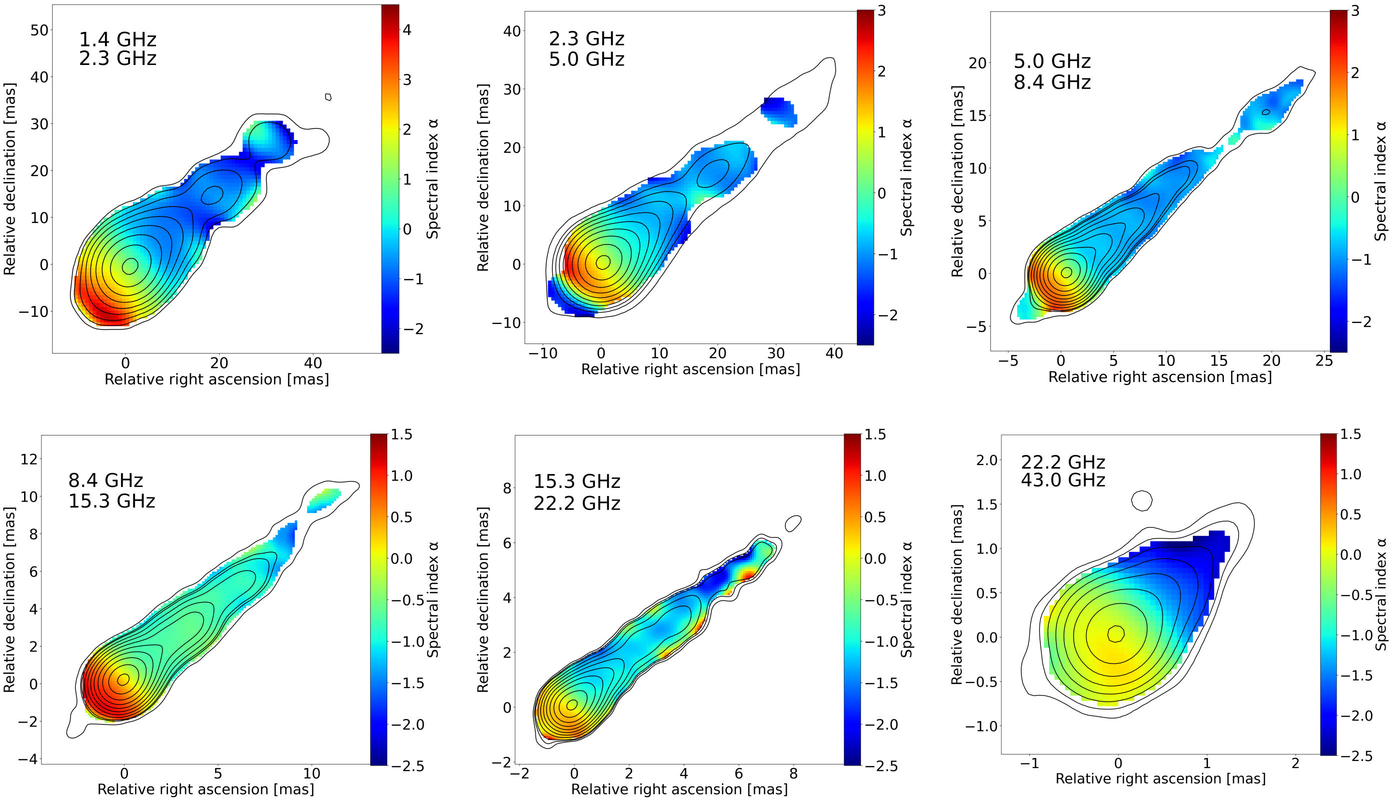

Fig. 6. Spectral index maps between different pairs of frequencies. Top panel starting from the left: (1.4-2.3) GHz, (2.3-5.0) GHz, and (5.0-8.4) GHz. Bottom panel starting from the left: (8.4-15.3) GHz, (15.3-22.2) GHz, and (22.2-43.0) GHz. The contours trace the total intensity emission in the map at the highest frequency. Note the different color scales.

steepens assuming the expected values $-1 \lesssim \alpha \lesssim -0.5$. On the contrary, the two high-frequency maps reach smaller values of the spectral index, between -1 and -1.5 in the 15-22 GHz map and down to ~ -2.2 in the 22-43 GHz map. We notice that the 15-22 GHz spectral index map gives indications of a transverse gradient. Indeed, along the ridgeline at a distance of about 2 pc we observe spectral values $\alpha \sim -1.3$, which rise up to $\alpha \sim -0.5$ towards the edges of the emission. Such structure could be in principle connected with an edge-brightened structure, observed in NGC 315 on similar scales (Park et al. 2021b).

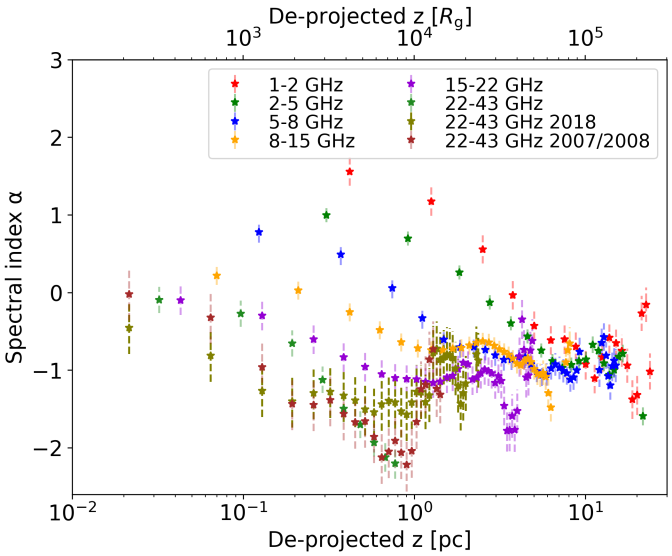

Fig. 7. Average spectral index as a function of distance from the 43 GHz core for different pairs or frequencies. In addition to the VLBA data set here presented, we re-present for comparison the 22-43 GHz spectral index values for the two epochs presented by Ricci et al. (2022). At high frequencies, remarkably steep spectral index values down to $\alpha \sim -2$ are observed within one parsec from the core, corresponding to $\sim 10^4\, R_S$. Downstream, a convergence towards flatter values $\alpha \sim -0.8$ is observed at all frequencies.

In Fig. 7, we display the evolution of the average spectral index values along the jet ridgeline. The positions of the spectral index measurements are shown with respect to the VLBI core at the highest frequency. The errors are computed by summing in quadrature the thermal noise values together with the flux density uncertainties earlier discussed. Our spectral index values are consistent within the errors with the ones inferred by Park et al. (2021b). We highlight that the very steep spectrum region has an extent similar to that of the collimation region (Boccardi et al. 2021). Towards the end of it, i.e., on parsec scales, all the spectral maps converge towards values of ~ -0.8, consistent with the observed radio spectra in the vast majority of AGN jets. We contextualize these results using two spectral maps between 22 and 43 GHz obtained in Ricci et al. (2022). This comparison offers two different insights: while it confirms the steep spectrum on sub-parsec scales, it shows that the 22-43 GHz spectral map fits with the 22-43 GHz 2007/2008 map, although shows slightly lower values than the 22-43 GHz 2018 counterpart. Possible interpretations of such results are discussed in Sect. 4.1. Our results are in agreement with the ones inferred for M 87 by Ro et al. (2023) in two distinct ways. On one hand, the authors recover a steep spectral index down to ~ -2.5 on the same scales, i.e., $\sim 10^3\,\mathrm{R_S}$. On the other hand, the authors are showing that the spectral index value may change across the different epochs, although not dramatically.

3.4. Polarization

Polarization in NGC 315 is generally not observed in a wide range of frequencies from 1 GHz to 43 GHz. This is the case also for the maps analyzed in this paper. Weak polarized features on the mJy-level are occasionally detected, but cannot be cross-identified in neighboring epochs or adjacent frequencies. The lack of jet polarization is a common trait of radio galaxies. The underlying cause of the large-scale depolarization, be it the intrinsic structure of the magnetic field itself, an external Faraday screen, or strong intra-band Faraday rotation, remains unknown (Sokoloff et al. 1998; Bower et al. 2017; Park et al. 2021b).

3.5. Brightness temperature profile

In this section, we discuss the intrinsic brightness temperature profiles for the incoming jet of NGC 315. For a non-thermal source, the apparent brightness temperature is expressed as (e.g. Kadler et al. 2004):

$$T_\mathrm{b} = 1.22 \times 10^{12}(1+z)\left(\frac{S_\nu}{\mathrm{Jy}}\right)\left(\frac{\nu}{\mathrm{GHz}}\right)^{-2}\left(\frac{d}{\mathrm{mas}}\right)^{-2}\ \mathrm{K} \qquad (2)$$

in which S_ν is the flux density, ν is the frequency and d is the diameter of the emitting region. The intrinsic brightness temperature is computed as $T_\mathrm{b}^\mathrm{int} = T_\mathrm{b}/\delta$, where $\delta = [\Gamma(1-\beta\cos\theta)]^{-1}$ is the Doppler factor. To compute the intrinsic brightness temperature, we assume a viewing angle $\theta = 38°$ (see Giovannini et al. 2001; Canvin et al. 2005; Boccardi et al. 2021; Ricci et al. 2022), while the β values are taken from the speed profile obtained by Ricci et al. (2022). We compute T_b^in for all the intensity maps reported in Sect. 2. The errors are computed by propagating the uncertainties on the different parameters defining the Gaussian components described in Sect. 2.5.

In Fig. 8, we report the intrinsic brightness temperature as a function of distance from the jet apex. In the left panel, we show the jet components, while in the right panel the core components. We note that the core components at 43 GHz and 86 GHz should be located on the origin of the x-axis (see Sect. 2.4), but a small shift of 0.01 pc is applied for representing them in logarithmic scale. The data are color-coded by frequency including results from maps at different epochs.

In Fig. 8, the dashed horizontal black lines highlight the median and upper limit values of the equipartition brightness temperature. The latter is achieved when the energy is equally shared between the particles and the magnetic field. From theoretical and statistical studies, it was shown that the equipartition brightness temperature assumes a median value of $T_\mathrm{b} \sim 5\times10^{10}$ K (Readhead 1994; Homan et al. 2021) with the upper limit set to $T_\mathrm{b} \sim 1\times10^{11}$ K (Singal 2009). All jet components fall below the upper limit, while the core components at progressively lower frequencies exceed it. However, the inverse Compton catastrophe limit, set around $(5-10)\times10^{11}$ K (Kellermann & Pauliny-Toth 1969), is never exceeded. On compact scales, the 86 GHz core component lies around 10^{11} K, while the 43 GHz points are slightly below the median equipartition brightness temperature. On the contrary, already on scales of ~ 0.1 pc the T_b values of the core components fall in the range of the equipartition state.

Overall, the trend of the core components suggests that on compact scales and in in its average state, the jet shows brightness temperatures below the equipartition values, pointing towards a magnetized outflow. However, variability in the physical conditions of the core region is suggested by the 86 GHz measurement, which lies in the equipartition range. On sub-parsec scales, a flattening around the equipartition values is observed. This flattening occurs in the proximity of the end of the collimation region, where equipartition conditions are indeed expected.

Brightness temperatures exceeding the equipartition limit, sometime observed in the same region, indicate the occurrence of energy dissipation and particle acceleration processes. Possible particle re-acceleration scenarios are discussed in Sect. 4.1 in the context of the discussion on the observed spectral index values.

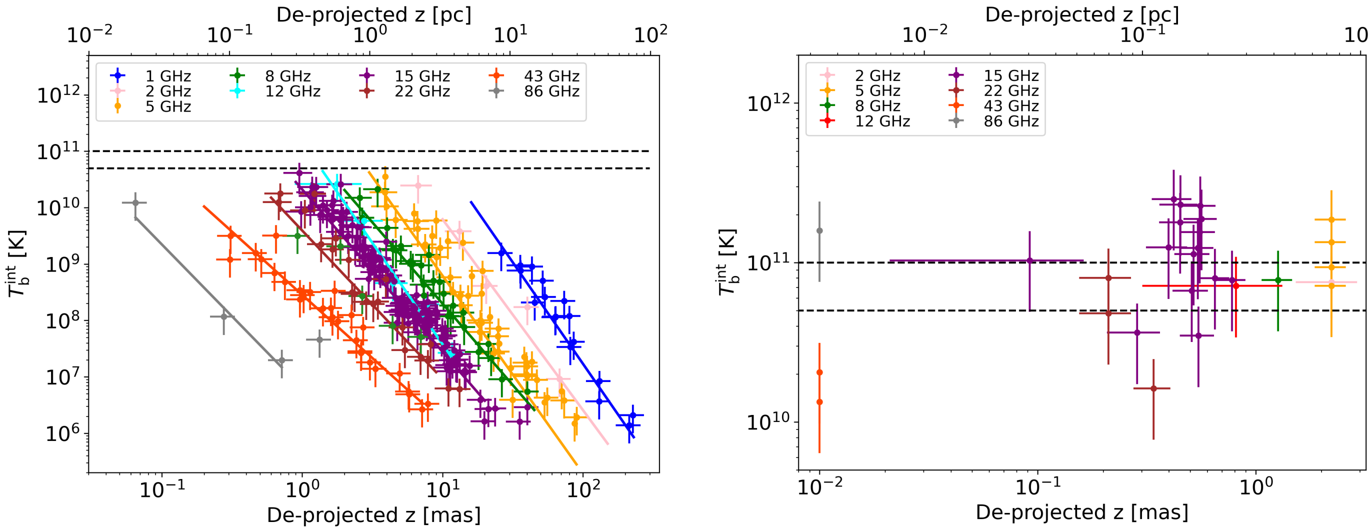

Fig. 8. Intrinsic brightness temperature profiles of the Gaussian component at different frequencies. The horizontal dashed lines represent the median equipartition brightness temperature derived from sample studies, $T_b = 5 \times 10^{10}$ K, and the upper limit $T_b = 10^{11}$ K. Left panel: brightness temperature values for the jet components. The continuous lines are the best-fit power laws at different frequencies. Right panel: brightness temperature values for the core components.

Table 3. Power-law indices of the intrinsic brightness temperature profiles at the different frequencies.

ν [GHz]	ϵ
1.0	-3.59 ± 0.21
2.0	-3.38 ± 0.29
5.0	-3.50 ± 0.17
8.4	-2.88 ± 0.13
12.1	-3.59 ± 0.46
15.4	-2.87 ± 0.06
22.3	-2.63 ± 0.13
43.2	-2.24 ± 0.09
86.2	-2.55 ± 0.41

Notes. Column 1: observing frequency in GHz; Column 2: power-law index with the error.

In the jet, we fit the brightness temperature profiles with a single power-law $T_\text{b} = T_0 r^\epsilon$. For each frequency, the Gaussian components from all the available epochs are fitted jointly. The best-fit values are reported in Table 3. The higher frequencies, i.e., 22, 43, and 86 GHz, show a relatively flat slope with $\epsilon \sim -2.2/-2.6$. On the contrary, at low frequencies, the indices reach values down to -3.59 ± 0.21. Similarly steep profiles are observed in the eastern jet of NGC 1052 on comparable distances (Kadler et al. 2004). We highlight that the flatter values are observed at frequencies that sample the parabolic region, suggesting different physical conditions with respect to the conical expanding region. Implications and consequences on the jet nature from such measurements are discussed in Sect. 4.3.

3.6. Turnover frequency

The turnover frequency is a key parameter in the synchrotron spectrum. Its value is strictly related to the intrinsic properties of the plasma, such as the strength of the magnetic field permeating it (e.g., Lobanov 1998). In this section, we measure the turnover frequency for each pixel in the core and in the sub-parsec jet region using the simultaneous VLBA observations (see Table 1).

To obtain the turnover frequency, we use the five highest-frequency VLBA maps convolved with the same beam, with same pixel size and uv-range. We motivate this choice as follows: i) to properly fit the synchrotron spectrum (Eq. 1), at least four data points are needed; ii) due to the large difference in resolution between the highest and lowest frequency maps, using all the maps would have led to problems in finding a proper common beam and pixel size. By including the 1 GHz and 2 GHz observations, the common circular beam would have been ∼ 5.08 mas and ∼ 3.74 mas, respectively. Convolving the 22 and 43 GHz maps to such large beams would have led to losing the majority of the information contained in them.

Consequently, we compute the turnover frequency by using the maps in the frequency range 5-43 GHz restored with a common circular beam of 1.65 mas, larger than ∼ 65% of the beam at 5 GHz (2.35 mas) and small enough not to lose information in the 22 and 43 GHz maps. The turnover frequency for each pixel is obtained by fitting the data points using Eq. 1. In this case, all the parameters but α_t are left free to vary. α_t is fixed at 2.5, the expected value for a plasma with a homogeneous synchrotron spectrum (see, e.g., Lobanov 1998). The resulting maps are reported in Fig. 9. In the left panel, we show the turnover frequency values, and in the right panel the corresponding flux densities. The pixels set to zero are those in which either the fit failed or the turnover frequency from the fit is outside of the frequency range considered. This is the case for some regions upstream of the jet base, where the spectrum is inverted up to the highest frequency in the considered range.

We highlight that we recover a gradient in the turnover frequency only in the direction of the jet propagation; due to insufficient transverse resolution, we cannot investigate the presence of a transverse gradient in the turnover frequency profile.

In Fig. 10, we show the turnover frequency along the ridgeline as a function of the distance from the 43 GHz core. Because the pixel size in the turnover frequency map is different with re-

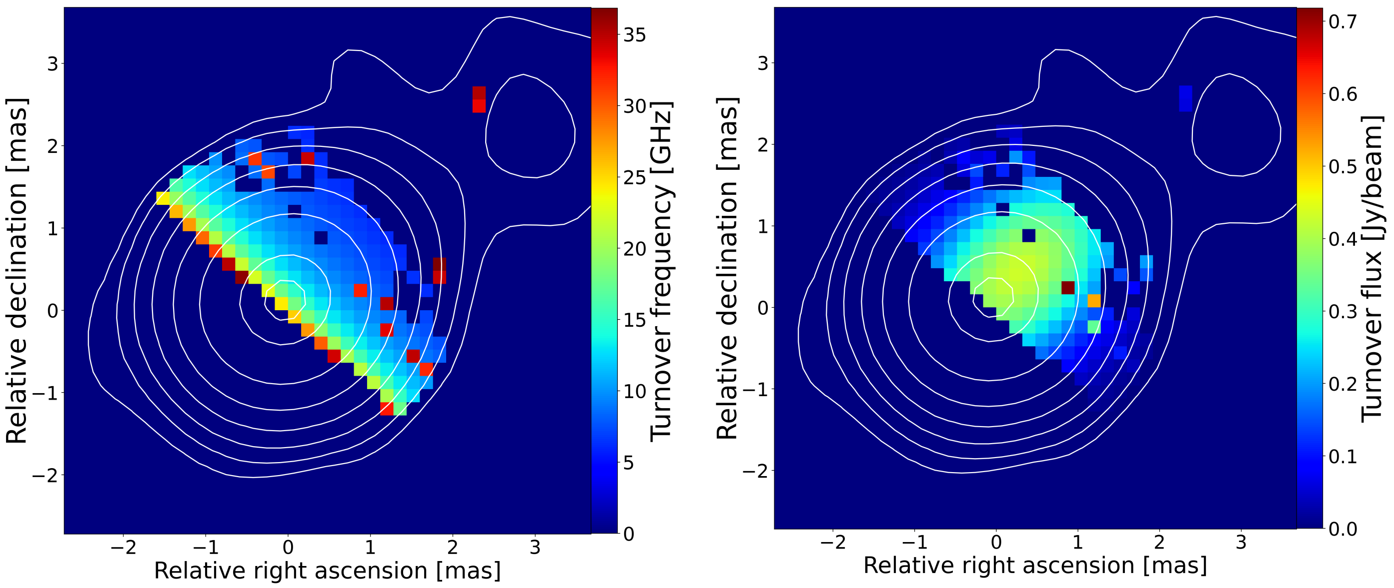

Fig. 9. Left panel: turnover frequency for each pixel obtained by fitting the synchrotron spectrum across five frequencies between 5 and 43 GHz. The constant turnover values in the direction perpendicular to the jet propagation point out that the transversal structure is not resolved. The turnover frequency is clearly seen to decrease as going further from the core. The red pixels are spurious data points arising from a not successful fitting of the data. Right panel: brightness at the respective turnover frequency. In both maps, the contours are from the 43 GHz map.

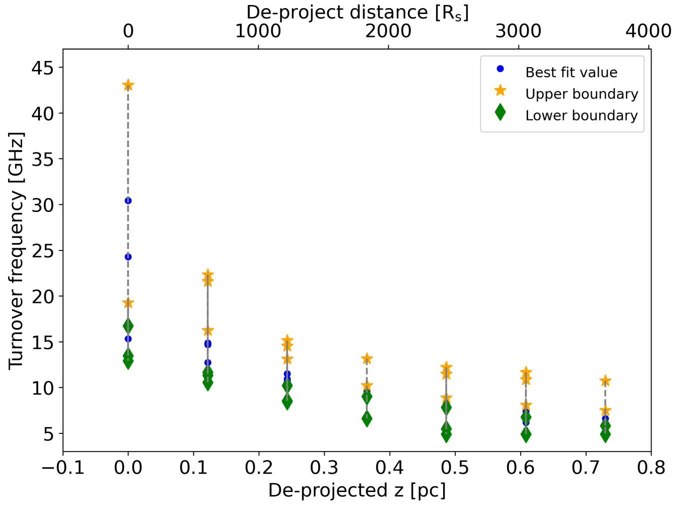

Fig. 10. Turnover frequency along the ridgeline as a function of distance from the 43 GHz core. The multiple data points at the same distance are from the different possible core-shift configurations. The yellow points represent the upper boundary, while the green ones the lower boundary. The turnover frequency decreases from 15 GHz $< \alpha <$ 43 GHz in the 43 GHz core, down to ~ 6 GHz at ~ 0.7 pc.

spect to the one used in the maps employed to infer the core shift, different displacements between each pair of frequencies are consistent with the core-shift values reported in Tab. 2. As a consequence, we extrapolate a number of turnover frequency values at each given distance from the core (Fig. 10) according to all the possible displacements between the maps. We then infer the turnover frequency to be in the range 15 GHz $< \alpha_{\rm br} <$ 43 GHz at the position of the 43 GHz core and to decrease down to ~ 6 GHz around 0.7 pc.

4. Discussion

4.1. Steepness of the spectrum

The variation of the spectral index observed in Fig. 7 indicates a change in the physical conditions along the jet.

Models have been developed to explain the steepening of the spectrum (e.g., Hovatta et al. 2014; Ro et al. 2023). The spectral evolution is regulated by the injection of non-thermal particles as a function of the distance from the core, which can be expressed as $Q \propto z^q$. Here, q defines the energy spectrum of the injection function for the non-thermal electrons. When $q = 0$, particles are injected continuously along the jet, whereas for $q \to -\infty$ particles are only injected once at the launching site. In the former scenario, the spectrum slightly steepens with the distance, reaching values of ~ −0.5. In contrast, in the latter scenario, the spectral index drops abruptly and almost immediately to very low values. In agreement with estimates obtained for M 87 (Ro et al. 2023), intermediate values ($q \sim -10$) may better describe spectral indices down to ~ −2, such as those derived in this study on scales up to 10^3 $\rm R_S$. We note that the steep-spectrum region has roughly the same extent of the collimation (and acceleration Ricci et al. 2022) region. At about 10^4 $\rm R_S$ downstream the core, i.e., in the conical region, the flatter spectrum is better described by $q \simeq 0$, implying a higher rate of injection of non-thermal particles. Such a scenario suggests that cooling of the emitting electrons is important on sub-parsec scales, followed by heating and re-energizing on parsec scales. The cooling can, for instance, be explained by synchrotron losses (Kardashev 1962; Pacholczyk 1970), a phenomenon already proposed to be happening on the same scales in NGC 315 (Ricci et al. 2022) and M 87 (Nikonov et al. 2023). The latter would be driven by the magnetic fields which are expected to dominate the properties of the jet on such scales. The injection of new particles on parsec scales could be a consequence of single or multiple standing shocks. Hints of the presence of a recollimation shock in the proximity of the jet shape transition distance can be noticed in Fig. 4, where the size of the modelfit components at 43 GHz show a local decrease.

4.2. Particle acceleration mechanisms

The differences in spectral index between the sub-parsec and parsec scales raise questions concerning possibly different particle acceleration mechanisms at play. For the sake of simplicity, we focus on the two most common acceleration processes in relativistic objects, i.e. Diffusive Shock Acceleration (hereafter DSA, Blandford & Eichler 1987) and magnetic reconnection (Loureiro & Uzdensky 2016). On sub-parsec scales, the spectral index steepens to ~ -2, implying a particle energy spectrum of $p_{\rm inj} \sim 4$. Although relativistic magnetic reconnection (Sironi & Spitkovsky 2014) is able to provide such a spectrum, it would require a weak magnetization which does not favor the formation of plasmoid instabilities. On the other hand, such a steep energy spectral index shows a potentially better agreement with the DSA mechanism in a moderately magnetized plasma. In particular, in sub-luminal shocks, the index of the particle energy spectrum can steepen up to $p_{\rm inj} \sim 4.5$ due to the DSA mechanism (Sironi & Spitkovsky 2011). We highlight how a moderate magnetization on sub-parsec scales is suggested from the values of the brightness temperature as well (see Sect. 3.5). Zooming out to the parsec scale, the spectral index ($\alpha \sim -1$) is compatible with both DSA acceleration (Sironi & Spitkovsky 2009) and magnetic reconnection (Sironi et al. 2016). However, since magnetic reconnection may be suppressed at the sub-parsec scale, the DSA mechanism may still be dominant due to the decreasing magnetic field strength.

Overall we find that the spectral index does not completely rule out a specific acceleration process, although DSA seems to be a more realistic process at all scales. However, we point out that our investigation of the particle acceleration processes, which is based purely on the relation between the energy spectrum of the particles and the spectral index due to synchrotron emission, allows us only to hint at the most prominent acceleration process in each zone and cannot describe the interaction between the different physical processes. Moreover, the scales at which particles accelerate are too small to be captured by both observations and simulations, particularly in the magnetic reconnection scenario. Although we expect reconnection and shocks on the very small scales to play a significant role in the large-scale spectrum, their interplay (which would span over $\sim 8-10$ order of magnitude in length scales) is still under debate.

High-resolution multi-scale simulations should be able to unveil the true nature of non-thermal particles in astrophysical jets, although, at the current stage, the scale separation between particles acceleration and jet propagation is still a critical issue.

4.3. Magnetic field geometry

The analysis of NGC 315 performed so far indicates that the jet starts off magnetized on compact scales, reaching a moderate magnetization on sub-parsec scales. In the following, we extract further information on the evolution of the magnetic field from the brightness temperature and turnover frequency along the jet.

The slope of the brightness temperature profile is related to the transverse expansion of the components along the jet and to the dominant radiative loss mechanism. Specifically, a newly ejected jet component will undergo stages of Compton, synchrotron, and adiabatic losses. Under the assumption of a shock propagating adiabatically downstream a conical jet with constant Lorentz factor, the evolution of the brightness temperature profile in three different stages is (Lobanov & Zensus 1999; Schinzel et al. 2012):

$$\epsilon_c = -\left[(|p_{\rm inj}| + 5) + |a|\,(|p_{\rm inj}| + 1) \right] / 8 \tag{3}$$

$$\epsilon_s = -\left[4(|p_{\rm inj}| + 2) + 3|a|\,(|p_{\rm inj}| + 1) \right] / 6 \tag{4}$$

$$\epsilon_a = -\left[2(2|p_{\rm inj}| + 1) + 3|a|\,(|p_{\rm inj}| + 1) \right] / 6 \tag{5}$$

Here, the power-law index a describes magnetic field strength profile and $p_{\rm inj} = 1 - 2\alpha$. As mentioned, Eqs. 3 – 5 are valid for the conical jet. By assuming an average value for the spectral index (on parsec scales) of $\alpha = -0.8 \pm 0.3$, in which the error is assumed to consider the observed scatter at that region (see Fig. 7), we predict the power-law slopes for the different types of radiative losses for the two magnetic field geometries, i.e., toroidal ($a = -1$) and poloidal ($a = -2$). We note that these assumptions of the indices for the toroidal and poloidal geometry are valid only when considering a jet expanding with a conical shape. The results are reported in Table 4. By comparing these findings with the values reported in Table 3 we derive that the fit to the data on parsec scales (Fig. 3) is exclusively compatible with a jet dominated by adiabatic losses and threaded by a toroidal field.

Table 4. Expected power-law index for the brightness temperature in the jet using the model by Lobanov & Zensus (1999).

	a = 1	a = 2
ϵ_c	-1.40 ± 0.15	-1.85 ± 0.23
ϵ_s	-4.87 ± 0.70	-6.67 ± 0.07
ϵ_a	-3.87 ± 0.70	-5.67 ± 0.70

Notes. Column 1: expected power-law index considering a toroidal field; Column 2: expected power-law index considering a poloidal field.

To explore the magnetic field in the parabolic region we follow the approach proposed by Kadler et al. (2004). Assuming a power-law for the electron density as $N \propto z^n$ and for the jet diameter as $d \propto z^c$, the power-law index of the brightness temperature is

$$\epsilon = c + n + a(1 - \alpha)\,. \tag{6}$$

This relation, while it allows us to consider a non-conical jet shape, is only valid under the assumption of constant Lorentz factor. This condition is not strictly valid for NGC 315, although the measured Lorentz factor does not vary by a large factor in the parabolic region (Park et al. 2021b; Ricci et al. 2022). Therefore, we adopt this approach to provide an order-of-magnitude estimate of the magnetic field strength from the jet base down to $\sim$ 0.6 pc. We assume: i) an average spectral index for the sub-parsec scales of $\alpha = -1.80 \pm 0.30$, ii) the jet width index as $c = 0.47 \pm 0.12$, iii) the brightness temperature index as $\epsilon = -2.4 \pm 0.2$ from averaging the 43 GHz and 86 GHz profiles. For the particle distribution, we consider two possible index values: $n = -1$, a classical assumption for jet evolution (Kadler et al. 2004), and $n = -2$, which describes a particle population without cooling effects. The inferred index for the magnetic field on the sub-parsec region is $-0.67 \pm 0.10 < a < -0.31 \pm 0.12$.

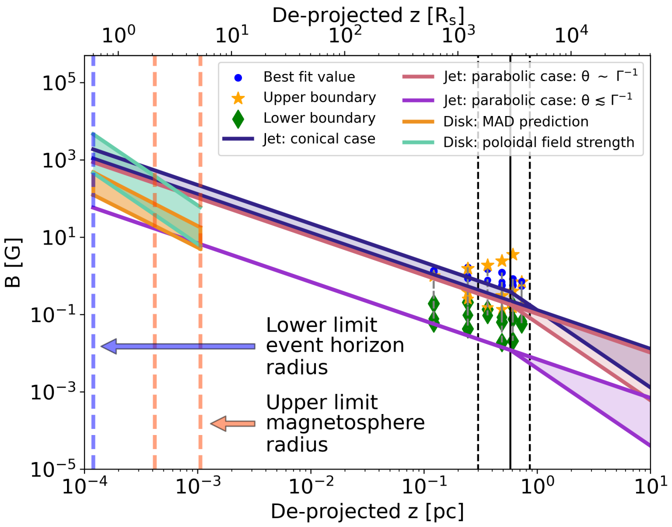

Fig. 11. Magnetic field strength as a function of distance, adapted from Ricci et al. (2022). Here, we add the normalized values extrapolated from the turnover frequency. The different colors for the data points follow the same scheme as in Fig. 10.

While the uncertainties in this method prevent us from obtaining a precise determination of the slope, Eq. 6 indicates that the magnetic field evolves with an index smaller than one within $\sim 10^3\,\mathrm{R_S}$ from the jet injection point. Similar results have been obtained for M 87, since Ro et al. (2023) derived an index of ~ -0.72 on the same scales.

Finally, a further investigation of the magnetic field properties can be based on our previous analysis of the synchrotron turnover frequency. Following (Cawthorne 1991):

$$B(d) = C_0 \nu_{\rm br}^5 d^4 S_{\rm br}^{-2} \tag{7}$$

where C_0 is the normalization factor. The values of $\nu_{\rm br}$ and $S_{\rm br}$ are taken from Fig. 9. We use the fit performed in Sect. 3.2 for the jet width. Fig. 11 shows the plot originally published by Ricci et al. (2022), based on independent constraints, with the addition of the data points derived from Eq. 7. Unfortunately, in Eq. 7 the normalization factor is not known at priori as it depends on the geometrical properties of the source (Lobanov 1998). As a consequence, from this method, we cannot have insights into the magnetic field strengths, and the best-fit values (blue dots, Fig. 11) are normalized, in order to be represented in the plot, to have a magnetic field strength of 1 G for the innermost data point. We perform power-law fits for each set of data points and find indices between -0.5 and -1. Therefore, the turnover frequency analysis supports a (quasi-)linear dependence of the magnetic field strength on the examined scales.

Overall, our analysis indicates that the field is dominated by the toroidal component in the conical region. In the parabolic jet, the combination of the findings from Eq. 6 and Eq. 7 indicates an index $a \lesssim -1$. In the jet collimation region, the toroidal component of the magnetic field has an index equal to the opposite of the jet expansion index, i.e., it is -c=-0.47 in the case of NGC 315. The index of the poloidal component is instead -2c=-0.94. However, a steeper evolution for the toroidal field could be expected in reality due to its dissipation in the acceleration process (see Ricci et al. 2022). Ultimately, from an index of $a \lesssim -1$ in a parabolic-expanding and accelerating jet, while the toroidal magnetic field component is slightly favored, it is not possible to provide a strong constraint on the magnetic field configuration.

5. Conclusions

In this paper, we have presented three new VLBA observations of the nearby radio galaxy NGC 315 at 43 GHz, in addition to other data sets that have been previously reported in the literature. The main goal of this paper was to investigate the properties of the magnetic field in the inner parsec region by exploring the spectral and brightness temperature properties of the jet. Our results can be summarized as follows.

- We used a pixel-based analysis to extrapolate the jet width in the core region using a 43 GHz stacked image. The expansion profile suggests the real injection position of the jet to lay 41 ± 41 R$_s$ upstream of the core at 43 GHz, i.e., toward the counter-jet. We find a minimum width of 35 ± 4 R$_s$, in agreement with jet width measured in M 87 (Lu et al. 2023). Moreover, we enriched the previously published expansion profile (Boccardi et al. 2021) with the new observations. The new data points are in agreement with the previously published results, strengthening the scenario of the jet collimation taking place on sub-parsec scales.
- The spectral index analysis reveals a very steep spectrum on sub-parsec scales, along the acceleration and collimation region. Namely, from the 22-43 GHz spectral index maps we observe values down to ~ -2, as also observed in M 87 (Ro et al. 2023). Downstream the jet, on parsec scales, the spectral index reaches more standard values for optically thin emission of about -0.8. We explored possible physical reasons behind the observed evolution of the spectrum, including cooling due to synchrotron losses to explain the steep values or different acceleration mechanisms between the sub-parsec and parsec region, i.e., DSA and magnetic reconnection. The DSA is slightly favored for explaining the particle re-acceleration occurring in the jet on all scales.
- We examined the brightness temperature as a function of distance from the core. We infer a relatively flat power-law index at 22,43, and 86 GHz ($\epsilon \sim -2.4$), i.e., the frequencies that sample the collimation region, and a steeper trend, i.e., $\epsilon \sim -(2.80 - 3.70)$, at lower frequencies. Moreover, the brightness temperature of the 43 GHz cores indicates a dominance of the magnetic energy at the jet base, while the cores at progressively lower frequencies reveal a gradual transition towards equipartition, which is reached towards the end of the collimation region. A time-variability of the physical conditions is also observed since, particularly at 15 GHz, values exceeding equipartition are often measured. This indicates the occurrence of efficient particle re-acceleration processes on sub-parsec scales.
- We determine a synchrotron turnover frequency in the range $15\,\mathrm{GHz} < \alpha_{\rm br} < 43\,\mathrm{GHz}$ at the location of the 43 GHz core, which decreases down to ~ 6 GHz within ~ 0.7 pc.
- Finally, we employ our observational constraints, together with theoretical models, to explore the geometry of the magnetic field in the inner jet. In the conical region, our results are consistent with a toroidal-dominated magnetic field ($a = -1$). In the parabolic region we derive $a \lesssim -1$, therefore we are not able to provide strong constraints. Overall, however, our findings are more consistent with a toroidal geometry also in this region.

References

Baczko, A. K., Ros, E., Kadler, M., et al. 2022, A&A, 658, A119
Baczko, A. K., Schulz, R., Kadler, M., et al. 2016, A&A, 593, A47
Blandford, R. & Eichler, D. 1987, Phys. Rep., 154, 1

Blandford, R., Meier, D., & Readhead, A. 2019, ARA&A, 57, 467
Blandford, R. D. & Znajek, R. L. 1977, MNRAS, 179, 433
Boccardi, B., Perucho, M., Casadio, C., et al. 2021, A&A, 647, A67
Bower, G. C., Dexter, J., Markoff, S., Rao, R., & Plambeck, R. L. 2017, ApJ, 843, L31
Burd, P. R., Kadler, M., Mannheim, K., et al. 2022, A&A, 660, A1
Canvin, J. R., Laing, R. A., Bridle, A. H., & Cotton, W. D. 2005, MNRAS, 363, 1223
Cawthorne, T. V. 1991, in Beams and Jets in Astrophysics, Vol. 19, 187
Fanaroff, B. L. & Riley, J. M. 1974, MNRAS, 167, 31P
Giovannini, G., Cotton, W. D., Feretti, L., Lara, L., & Venturi, T. 2001, ApJ, 552, 508
Greisen, E. W. 1990, in Acquisition, Processing and Archiving of Astronomical Images, 125–142
Hada, K., Doi, A., Kino, M., et al. 2011, Nature, 477, 185
Homan, D. C., Cohen, M. H., Hovatta, T., et al. 2021, ApJ, 923, 67
Hovatta, T., Aller, M. F., Aller, H. D., et al. 2014, AJ, 147, 143
Kadler, M., Ros, E., Lobanov, A. P., Falcke, H., & Zensus, J. A. 2004, A&A, 426, 481
Kardashev, N. S. 1962, Soviet Ast., 6, 317
Kellermann, K. I. & Pauliny-Toth, I. I. K. 1969, ApJ, 155, L71
Komatsu, E., Dunkley, J., Nolta, M. R., et al. 2009, ApJS, 180, 330
Komissarov, S. S. 2012, MNRAS, 422, 326
Komissarov, S. S., Barkov, M. V., Vlahakis, N., & Königl, A. 2007, MNRAS, 380, 51
Kovalev, Y. Y., Pushkarev, A. B., Nokhrina, E. E., et al. 2020, MNRAS, 495, 3576
Laing, R. A., Canvin, J. R., Cotton, W. D., & Bridle, A. H. 2006, MNRAS, 368, 48
Lister, M. L., Aller, M. F., Aller, H. D., et al. 2018, ApJS, 234, 12
Lobanov, A. P. 1998, A&AS, 132, 261
Lobanov, A. P. & Zensus, J. A. 1999, ApJ, 521, 509
Loureiro, N. F. & Uzdensky, D. A. 2016, Plasma Physics and Controlled Fusion, 58, 014021
Lu, R.-S., Asada, K., Krichbaum, T. P., et al. 2023, Nature, 616, 686
Nikonov, A. S., Kovalev, Y. Y., Kravchenko, E. V., Pashchenko, I. N., & Lobanov, A. P. 2023, arXiv e-prints, arXiv:2307.11660
O'Sullivan, S. P. & Gabuzda, D. C. 2009, MNRAS, 400, 26
Pacholczyk, A. G. 1970, Radio astrophysics. Nonthermal processes in galactic and extragalactic sources
Park, J., Byun, D.-Y., Asada, K., & Yun, Y. 2021a, ApJ, 906, 85
Park, J., Hada, K., Nakamura, M., et al. 2021b, ApJ, 909, 76
Plavin, A., Kovalev, Y. Y., Kovalev, Y. A., & Troitsky, S. 2020, ApJ, 894, 101
Readhead, A. C. S. 1994, ApJ, 426, 51
Ricci, L., Boccardi, B., Nokhrina, E., et al. 2022, A&A, 664, A166
Ro, H., Kino, M., Sohn, B. W., et al. 2023, arXiv e-prints, arXiv:2303.01014
Schinzel, F. K., Lobanov, A. P., Taylor, G. B., et al. 2012, A&A, 537, A70
Shepherd, M. C. 1997, in Astronomical Society of the Pacific Conference Series, Vol. 125, Astronomical Data Analysis Software and Systems VI, ed. G. Hunt & H. Payne, 77
Singal, A. K. 2009, ApJ, 703, L109
Sironi, L., Giannios, D., & Petropoulou, M. 2016, MNRAS, 462, 48
Sironi, L. & Spitkovsky, A. 2009, ApJ, 698, 1523
Sironi, L. & Spitkovsky, A. 2011, ApJ, 726, 75
Sironi, L. & Spitkovsky, A. 2014, ApJ, 783, L21
Sokoloff, D. D., Bykov, A. A., Shukurov, A., et al. 1998, MNRAS, 299, 189
Trager, S. C., Faber, S. M., Worthey, G., & González, J. J. 2000, AJ, 119, 1645
Vlahakis, N. & Königl, A. 2003a, ApJ, 596, 1080
Vlahakis, N. & Königl, A. 2003b, ApJ, 596, 1104
Vlahakis, N. & Königl, A. 2004, ApJ, 605, 656

Appendix A: Gaussian components

Table A.1. Modelfit parameters of the Gaussian components at 1 GHz at the different epochs.

Obs date	S [Jy]	d [mas]	z [mas]	PA [deg]	T_b [10^8K]
Jan 2020	150.84	0.24	4.5	-50.4	14433.74
	75.0	0.72	7.83	-50.37	797.41
	29.08	0.62	11.91	-49.75	416.96
	7.78	1.92	22.15	-50.64	11.63
	4.52	3.85	39.33	-51.04	1.68
	14.27	1.77	16.13	-49.63	25.11
	10.56	2.06	26.64	-50.7	13.72
	4.52	2.81	45.23	-50.82	3.16
	4.95	1.95	31.83	-50.84	7.17
	4.14	20.87	80.23	-49.5	0.05
	3.66	5.82	52.79	-49.48	0.6
	5.32	38.57	131.84	-48.71	0.02

Notes. Column 1: date of the observation; Column 2: flux density in Jy; Column 3: FWHM in mas; Column 4: radial distance after the core-shift correction; Column 5: position angle after the core-shift correction; Column 6: observed brightness temperature in units of 10^8K.

Table A.2. Modelfit parameters of the Gaussian components at 2 GHz at the different epochs.

Obs date	S [Jy]	d [mas]	z [mas]	PA [deg]	T_b [10^8K]
Jan 2020	199.94	0.64	1.37	-72.38	1144.33
	144.74	0.93	4.12	-57.71	392.31
	46.14	1.33	8.13	-51.94	61.15
	15.92	3.77	24.76	-52.27	2.63
	27.66	3.15	12.61	-52.63	6.53
	12.53	14.92	41.98	-52.06	0.13

Notes. See Table A.1

Table A.3. Modelfit parameters of the Gaussian components at 5 GHz at the different epochs.

Obs date	S [Jy]	d [mas]	z [mas]	PA [deg]	T_b [10^8K]
Jan 2020	211.22	0.07	0.26	-48.05	21382.88
	188.45	0.33	1.2	-47.29	858.41
	63.07	0.57	2.85	-49.18	96.29
	29.37	1.7	7.32	-50.0	5.04
	58.75	0.9	4.63	-50.51	35.98
	17.06	2.91	11.31	-49.83	1.0
	3.67	1.26	15.4	-48.34	1.15
	3.6	0.1	5.95	-49.42	178.58
	3.88	0.08	9.11	-50.97	300.73
	2.6	2.77	24.42	-50.49	0.17
	1.09	3.01	19.46	-50.74	0.06
	1.45	2.38	28.87	-51.12	0.13

Notes. See Table A.1

Table A.4. Modelfit parameters of the Gaussian components at 8 GHz at the different epochs.

Obs date	S [Jy]	d [mas]	z [mas]	PA [deg]	T_b [10^8K]
Jan 2020	264.47	0.1	0.41	-43.03	5124.64
	139.98	0.15	1.06	-44.42	1205.51
	47.5	0.22	1.86	-47.63	190.17
	22.91	0.38	2.86	-47.81	30.74
	24.38	0.43	4.91	-50.43	25.55
	8.89	0.73	7.3	-49.23	3.23
	8.54	0.83	8.63	-50.62	2.4
	25.94	0.53	3.79	-48.67	17.89
	10.11	0.48	5.86	-49.61	8.5
	4.92	1.4	11.09	-49.99	0.49
	3.38	1.31	13.67	-48.83	0.38
	3.08	2.55	24.78	-50.87	0.09
	2.07	1.59	16.28	-49.76	0.16
	1.02	0.15	9.7	-50.48	8.78

Notes. See Table A.1

Table A.5. Modelfit parameters of the Gaussian components at 15 GHz at the different epochs.

Obs date	S [Jy]	d [mas]	z [mas]	PA [deg]	T_b [10^8K]
Apr 1995	292.61	0.07	0.34	-56.93	3143.4
	82.15	0.3	1.31	-54.68	48.05
	146.87	0.17	0.75	-55.69	267.51
	74.99	0.45	1.94	-53.67	19.49
	23.05	0.59	3.48	-52.48	3.49
	21.06	0.62	4.52	-48.82	2.88
Dec 1995	270.98	0.13	0.31	-59.7	844.03
	119.63	0.2	0.7	-57.43	157.43
	49.68	0.31	1.65	-54.5	27.21
	65.95	0.17	1.17	-54.98	120.12
	33.39	0.89	3.84	-51.66	2.22
	37.02	0.33	2.22	-54.06	17.89
	16.48	1.19	5.3	-50.52	0.61
May 1996	255.53	0.09	0.32	-60.87	1660.6
	103.15	0.14	0.74	-56.07	277.03
	48.11	0.28	1.67	-54.62	32.3
	55.82	0.09	1.16	-55.56	362.75
	28.57	0.69	4.52	-50.29	3.16
	25.34	0.32	2.3	-54.79	13.03
	19.11	0.55	3.3	-53.2	3.33
Jul 1996	194.48	0.07	0.34	-56.7	2089.23
	90.52	0.12	0.72	-56.92	330.89
	63.95	0.19	1.14	-54.51	93.25
	16.37	0.62	4.63	-49.7	2.24
	41.29	0.29	1.69	-53.75	25.84
	24.6	0.33	2.21	-54.21	11.89
	10.94	0.5	2.93	-53.25	2.3
	9.71	0.67	6.14	-50.74	1.14
	12.46	0.48	3.81	-52.27	2.85
Aug 1997	280.4	0.08	0.35	-57.28	2306.24
	136.95	0.24	0.83	-56.34	125.15
	13.62	0.4	4.03	-51.77	4.48
	54.57	0.2	1.4	-56.22	71.81
	16.04	0.75	4.78	-50.98	1.5
	41.8	0.45	2.0	-55.02	10.87
	18.07	0.81	2.93	-55.26	1.45
	10.17	0.79	6.31	-50.63	0.86
	5.21	1.01	7.69	-49.89	0.27
Jul 1999	338.76	0.13	0.4	-54.06	1055.15
	118.02	0.1	1.0	-51.3	621.24
	51.31	0.3	1.7	-52.14	30.01
	19.55	0.85	3.5	-53.12	1.42
	35.06	0.22	2.44	-53.81	38.13
	18.6	2.04	6.58	-52.27	0.24
	9.53	0.44	4.54	-49.63	2.59

Notes. See Table A.1

Table A.6. Modelfit parameters of the Gaussian components at 15 GHz at the different epochs.

Obs date	S [Jy]	d [mas]	z [mas]	PA [deg]	T_b [10^8K]
Dec 2000	182.41	0.15	0.18	-71.88	426.75
	130.9	0.23	0.61	-54.41	130.25
	78.65	0.27	1.15	-53.93	56.79
	44.84	0.33	1.83	-53.39	21.67
	19.79	0.68	4.42	-51.36	2.25
	12.6	0.01	2.53	-53.41	6632.51
	12.2	0.51	3.3	-54.45	2.47
	6.59	0.64	6.33	-44.57	0.85
Oct 2003	310.09	0.19	0.34	-57.12	452.16
	120.89	0.2	0.86	-53.38	159.09
	86.2	0.74	1.83	-51.45	8.29
	28.62	0.03	1.36	-51.4	1673.92
	24.97	0.74	3.18	-53.33	2.4
	9.22	0.06	1.25	-51.69	134.81
	7.49	0.45	4.92	-50.3	1.95
Feb 2006	277.98	0.01	0.39	-53.68	146325.69
	96.63	0.12	0.77	-55.09	353.23
	21.72	0.86	4.54	-51.08	1.55
	60.51	0.16	1.27	-51.5	124.42
	33.13	0.35	1.84	-51.61	14.24
	30.3	0.63	2.85	-51.83	4.02
	14.24	1.19	6.31	-50.48	0.53
Sep 2008	246.26	0.07	0.26	-60.39	2645.48
	144.46	0.09	0.6	-55.96	938.79
	83.56	0.15	1.03	-53.63	195.49
	50.61	0.2	1.53	-53.42	66.6
	32.65	0.31	2.05	-51.05	17.88
	8.29	0.96	7.46	-51.24	0.47
	20.19	0.38	2.78	-51.03	7.36
	13.75	0.66	4.66	-51.8	1.66
	8.92	0.49	3.5	-53.23	1.96
	6.79	0.68	6.06	-50.79	0.77
	2.27	0.79	9.0	-51.91	0.19
Jun 2009	232.51	0.09	0.25	-59.57	1511.0
	171.09	0.06	0.55	-54.42	2501.67
	37.26	0.21	1.51	-52.8	44.47
	73.63	0.19	1.0	-53.14	107.36
	15.43	0.68	4.96	-50.93	1.76
	16.25	0.31	2.51	-51.59	8.9
	26.9	0.27	2.03	-52.26	19.42
	6.76	0.64	6.53	-51.33	0.87
	13.96	0.42	3.17	-50.63	4.17
	5.33	0.93	7.83	-50.0	0.32
	8.33	0.67	4.09	-52.02	0.98

Notes. See Table A.1

Table A.7. Modelfit parameters of the Gaussian components at 15 GHz at the different epochs.

Obs date	S [Jy]	d [mas]	z [mas]	PA [deg]	T_b [10^8K]
Jul 2009	261.34	0.07	0.28	-58.72	2807.48
	21.51	0.89	4.75	-51.26	1.43
	150.49	0.08	0.59	-55.05	1237.76
	66.26	0.19	1.01	-54.04	96.62
	42.3	0.27	1.58	-52.52	30.54
	23.1	0.65	3.02	-51.2	2.88
	25.88	0.26	2.19	-52.4	20.15
	8.36	0.65	6.42	-51.65	1.04
	6.32	1.13	7.81	-50.2	0.26
	8.65	3.25	13.02	-51.67	0.04
Jan 2010	244.89	0.08	0.28	-62.87	2014.18
	174.58	0.12	0.59	-58.31	638.17
	16.77	0.72	4.92	-51.79	1.7
	84.0	0.16	1.01	-54.74	172.72
	34.19	0.16	1.6	-54.11	70.3
	31.83	0.35	2.18	-53.45	13.68
	19.05	0.71	3.22	-51.0	1.99
	11.88	1.77	7.0	-51.39	0.2
	7.77	3.96	12.21	-49.45	0.03
Dec 2012	239.64	0.09	0.33	-60.71	1557.33
	95.23	0.12	0.73	-54.27	348.11
	48.55	0.52	2.63	-51.83	9.45
	79.65	0.2	1.21	-53.91	104.82
	31.95	0.23	1.73	-52.86	31.79
	14.04	1.53	7.26	-50.54	0.32
	11.69	0.68	5.0	-50.5	1.33
	15.68	0.67	3.91	-52.64	1.84
Aug 2019	151.82	0.08	0.48	-55.48	1248.69
	90.44	0.09	0.9	-50.76	587.74
	50.59	0.13	1.33	-49.12	157.57
	22.23	0.26	1.89	-49.9	17.31
	16.04	0.62	4.93	-51.47	2.2
	11.4	0.23	2.45	-50.04	11.34
	15.26	0.55	3.92	-49.88	2.66
	13.2	0.46	3.28	-48.67	3.28
	7.12	1.34	8.83	-51.21	0.21
	4.95	0.36	5.62	-50.84	2.01
	6.05	1.11	6.84	-50.29	0.26
Jan 2020	197.49	0.1	0.06	-45.0	1088.5
	142.5	0.08	0.5	-48.7	1227.21
	15.57	0.5	4.83	-50.92	3.43
	68.54	0.17	0.93	-46.16	130.72
	31.97	0.24	1.47	-47.6	30.59
	15.72	0.52	3.25	-48.74	3.2
	6.51	0.94	8.18	-50.29	0.41
	15.94	0.21	1.98	-49.82	19.92
	5.53	0.71	6.66	-49.35	0.6
	10.51	0.53	3.95	-49.55	2.06
	7.09	0.23	2.5	-48.24	7.39
	5.95	0.37	5.48	-49.96	2.4
	2.32	0.71	9.58	-51.08	0.25
	1.87	1.29	11.48	-49.43	0.06
	1.85	1.52	14.58	-48.26	0.04
	1.18	1.22	24.72	-50.86	0.04
	0.88	1.41	21.77	-53.81	0.02

Notes. See Table A.1

Table A.8. Modelfit parameters of the Gaussian components at 22 GHz at the different epochs.

Obs date	S [Jy]	d [mas]	z [mas]	PA [deg]	T_b [10^8K]
Jan 2020	142.55	0.14	0.21	-47.28	186.35
	91.79	0.13	0.64	-48.34	139.17
	48.57	0.21	1.01	-46.5	28.22
	28.52	0.48	1.76	-48.45	3.17
	19.14	1.01	3.32	-48.42	0.48
	17.55	0.86	5.07	-50.31	0.61
	5.01	0.16	1.4	-46.35	5.01
	3.93	0.11	2.43	-48.17	8.32
	2.79	0.05	4.01	-48.99	28.59
	2.9	0.87	6.77	-49.03	0.1
	2.27	0.77	8.14	-51.42	0.1

Notes. See Table A.1

Table A.9. Modelfit parameters of the Gaussian components at 43 GHz at the different epochs.

Obs date	S [Jy]	d [mas]	z [mas]	PA [deg]	T_b [10^8K]
Jan 2020	231.63	0.01	0.01	-57.4	15391.98
	41.5	0.12	0.29	-48.92	19.15
	35.99	0.1	0.71	-48.29	23.92
	7.14	0.05	1.16	-48.14	18.98
	4.49	0.16	1.68	-47.83	1.17
Apr 2021	185.79	0.1	0.0	-166.84	123.46
	27.96	0.27	0.99	-49.15	2.55
	34.87	0.13	0.19	-61.49	13.71
	42.16	0.28	0.59	-51.82	3.57
	19.82	0.58	1.62	-52.08	0.39
Oct 2021	215.72	0.01	0.02	-38.67	14334.75
	55.79	0.39	0.87	-49.15	2.44
	50.85	0.14	0.31	-45.17	17.24
	26.47	0.81	1.87	-49.2	0.27
	7.01	0.1	0.59	-52.84	4.66
	4.97	0.62	3.53	-49.38	0.09
Apr 2022	189.41	0.03	0.01	-58.87	1398.49
	27.88	0.09	0.76	-50.1	22.87
	60.2	0.06	0.14	-54.65	111.12
	34.09	0.19	0.46	-46.65	6.28
	25.58	0.18	1.05	-48.04	5.25
	12.81	1.27	4.85	-47.94	0.05
	7.53	0.16	1.38	-49.43	1.95
	8.38	0.52	2.05	-49.37	0.21
	6.14	0.73	3.55	-49.59	0.08

Notes. See Table A.1

7 Summary and outlook

This thesis addresses the formation and propagation of relativistic jets through the study of radio galaxies. Thanks to the small projection effects, these sources offer a unique opportunity to investigate the jet properties on the sub-parsec and parsec scales. Although the launching of jets has been intensively studied throughout the past decades thanks to the possibilities offered by interferometric observations, a comprehensive picture is still missing.

The two major subjects discussed in this work are the disk-jet connection and the nature of the jet acceleration (see Sections 2.2.1 and 2.2.2). For the former, theoretical models such as the SANE (Narayan et al. 2012) and MAD (Bisnovatyi-Kogan & Ruzmaikin 1974, 1976; Narayan et al. 2003) have been proposed to explain the launching of relativistic jets from radiatively inefficient hot disks. However, the number of active galaxies for which such models have been tested is still small. One reason for this is the observational challenge posed by the study of the jet collimation region and nature of the magnetic fields on very compact scales. Regarding acceleration, while the contribution of the magnetic fields to the increase in bulk flow speed has been largely explored (see e.g., Komissarov et al. 2007), little is known about thermal acceleration. The latter is generally believed to be relevant only on very compact scales, slightly downstream of the jet injection, and is neglected on parsec scales. Nonetheless, an increasing number of theoretical works have shown how jets can still be thermodynamically relativistic at such distances (Perucho et al. 2017). In this scenario, the role of thermal acceleration had not been explored yet.

The radio galaxy NGC 315 was chosen as a laboratory to address such topics. NGC 315 represents a perfect target, thanks to its unique properties. The combination of its vicinity and its large black hole mass allows, through VLBI observations, to resolve its radio emission down to hundreds of Schwarschild radii, digging into the core of the jet formation. Moreover, the possibility to detect its counter-jet across different frequencies unlocks powerful ways to explore the source, for instance in the investigation of the black hole position and of the jet speed profile through the analysis of the two-sided expansion profile and the jet to counter-jet ratio, respectively.

The approach in this dissertation was twofold: the experimental results inferred from VLBI observations were presented side-by-side with a theoretical work performed via RMHD simulations. This approach, while creating a unique synergy, is still poorly adopted in the community due to its complexity, and has seen a major development only in recent years thanks to improvements in the numerical techniques and capabilities. In this context, two main obstacles need to be faced. On the one hand, it is necessary to translate the observational properties of jets and their surroundings into a model that the code is able to handle consistently in a reasonable amount of time. A one-to-one conversion is, at the moment, impossible due to the highly turbulent and complex system in which jets develop. As a consequence, a number of assumptions and simplifications need to be made. On the other hand, such simplifications must not be too stringent, and they should allow to extract physical information that can be compared with observations. Considerable effort was dedicated to finding an approach that meets the observational and theoretical aspects halfway: while the models proposed in this work and the results obtained from them can be directly compared, with some caveats, with the observational data, they allow the employed code to successfully run in a time span of a few days in a dedicated cluster.

The observational results presented in this thesis provide new insights into the framework of the jet formation and propagation processes. The analysis of the VLBI observations of NGC 315 presented in Chapters 4 and 6 provide strong constraints on the spectral and magnetization properties of the innermost jet. The multiple spectral index maps indicate a remarkable behavior on sub-parsec scales, with the spectral index reaching very steep values down to ~ -2. Standard values for optically-thin emission, i.e. ~ -0.8, are instead observed on parsec scales. While the physical reasons behind the steep spectra are unclear and will be the subject of future debates, possible explanations account for: i) the strong magnetic fields inferred on the sub-parsec scales, which could lead to cooling due to synchrotron losses; ii) the interplay between different particle acceleration mechanisms such as magnetic reconnection and diffusive shock acceleration. A recent study on M 87, a source very similar to NGC 315 when considering the accretion mode and the jet power, suggests a similar behavior (Ro et al. 2023), indicating a possible common characteristic of the magnetized regions in jets. Concerning the magnetic fields, independent analyses involving the brightness temperature and the turnover frequency profiles show remarkable agreement with each other and point towards a quasi-linear dependence of the magnetic field strength with distance up to the jet base, in agreement with literature studies on AGN jets (see, e.g., O'Sullivan & Gabuzda 2009; Ro et al. 2023). In detail, on parsec scales the spatial evolution of the magnetic field strength follows a power law $\propto \mathrm{z}^{-1}$, indicative of a toroidal-dominated magnetic field in the conical-expanding jet. On sub-parsec scales and up to the jet apex, where the jet has a parabolic shape, the magnetic field evolves with the distance with a power-law index $\lesssim -1$. While slightly favoring a toroidal geometry also in this region, the derived range does not allow us to provide strong constraints. Indeed, in a parabolic jet, the poloidal field is expected to propagate as $\propto \mathrm{z}^{-1}$

while the toroidal component as $\propto z^{-0.5}$, however, the latter is expected to have a steeper evolution being dissipated in the acceleration process. Together with the estimate of the magnetic field strength from the core-shift measurements, a complete overview of the magnetic field properties on parsec scales and up to the nuclear region was presented, showing magnetic field strengths of $10^2 - 10^3$ G at the jet base. To compute the strength of the magnetic field, a new model to extract such information from the core shift in an accelerating and collimating jet was developed and presented in Chapter 4.

In addition to the magnetic fields, the acceleration and collimation processes were studied. The bulk velocities inferred with the jet to counter-jet ratio method indicate a remarkable agreement between the extent of the two. Indeed, both are suggested to be completed within one parsec downstream of the core (see Boccardi et al. 2021, for the extent of the collimation region). According to theoretical models (Komissarov 2012; Komissarov et al. 2007), the co-spatiality of acceleration and collimation suggests that these processes are mainly driven by the conversion of magnetic energy into kinetic energy.

The ensemble of the observational results, when interpreted in the context of theoretical models (Nokhrina et al. 2019, 2020), are consistent with the jet in NGC 315 being launched by a maximally spinning black hole surrounded by an accretion disk that has reached the MAD state.

Thanks to the synergy between the observational and theoretical approaches, in this thesis new insights into the jet acceleration mechanism are presented in Chapter 5. By employing the observational properties of the jet in NGC 315 as starting conditions for the simulated models, the acceleration mechanisms, and in particular its thermal counterpart, are explored. The results suggest that thermal acceleration, which has been widely overlooked in the literature, might play an important role in the establishment of extended jets. Indeed, when the internal energy is sufficiently high, the jet acceleration can be nourished by the conversion of internal into kinetic energy of the bulk flow. The main feature of this mechanism is its efficiency also in conical jets, ideally extending the jet acceleration well beyond its collimation region. By comparing our synthetic results with the observational ones from NGC 315 and other AGN jets, further insights on jet propagation are proposed. Specifically, by directly comparing the simulated and observed speed and opening angle profiles in NGC 315, it is suggested that the variations in the Lorentz factor and width evolution, which are observed across different epochs, may be a consequence of variability in the jet injection conditions, which may occur on time scales of a few months. Another jet property investigated through simulations is its transverse structure. Specifically, the limb-brightening observed in numerous AGN jets, NGC 315 included, can be connected with a stratified structure in which the spine is faster than the surrounding layers. Such a scenario is suggested from the simulations in two different cases: either assuming a non-force-free configuration for the magnetic fields (the gas pressure depends on the magnetic pressure) or including a relatively thick shear layer in the magnetic field force-free configuration (the gas pressure is independent of the magnetic pressure). In the second scenario, the simulation results suggest that, if the highly magnetized jets are expanding with a force-free configuration, winds may be necessary to shield the internal spine from the action of the external medium.

In conclusion, the results presented in this thesis highlight the strength of the direct comparison between observational and theoretical data and may serve as starting points for further studies. In detail, the work presented in Chapter 5 will be the basis for future works aimed at: i) deepening our understanding of the role of the shear layer and the winds, in different categories of AGN; ii) producing synthetic spectral index maps by means of a post-processing analysis and compare them with the results shown in Chapters 4 and 6. In addition, the model developed to compute the magnetic field from the core shift in an accelerating jet can be a relevant resource for the scientific community to provide more precise constraints on the jet magnetization up to its base.

Alongside the scientific results, the algorithms and the pixel-based Python scripts developed to analyze radio images will be made public in the near future. These scripts are part of VCAT, a collection of tools that will allow users to easily extract information and physical parameters from radio maps. This package is currently under development and will soon be released to the community.

References

Abbott, B. P., Abbott, R., Abbott, T. D., et al. 2016, Phys. Rev. Lett., 116, 061102

Allen, S. W., Dunn, R. J. H., Fabian, A. C., Taylor, G. B., & Reynolds, C. S. 2006, MNRAS, 372, 21

Antonucci, R. 1993, ARA&A, 31, 473–521

Asada, K. & Nakamura, M. 2012, ApJ, 745, L28

Baczko, A. K., Ros, E., Kadler, M., et al. 2022, A&A, 658, A119

Balbus, S. A. & Hawley, J. F. 1991, ApJ, 376, 214

Ballantyne, D. R. & Fabian, A. C. 2005, ApJ, 622, L97

Balmaverde, B., Capetti, A., & Grandi, P. 2006, A&A, 451, 35

Baum, S. A., Zirbel, E. L., & O'Dea, C. P. 1995, ApJ, 451, 88

Belladitta, S., Moretti, A., Caccianiga, A., et al. 2020, A&A, 635, L7

Beskin, V. S. & Nokhrina, E. E. 2006, MNRAS, 367, 375

Bisnovatyi-Kogan, G. S. & Ruzmaikin, A. A. 1974, Ap&SS, 28, 45

Bisnovatyi-Kogan, G. S. & Ruzmaikin, A. A. 1976, Ap&SS, 42, 401

Blandford, R., Meier, D., & Readhead, A. 2019, ARA&A, 57, 467

Blandford, R. D. & Königl, A. 1979, ApJ, 232, 34

Blandford, R. D. & Payne, D. G. 1982, MNRAS, 199, 883

Blandford, R. D. & Znajek, R. L. 1977, MNRAS, 179, 433

Boccardi, B., Krichbaum, T. P., Bach, U., Bremer, M., & Zensus, J. A. 2016, A&A, 588, L9

Boccardi, B., Krichbaum, T. P., Ros, E., & Zensus, J. A. 2017, A&A Rev., 25, 4

Boccardi, B., Perucho, M., Casadio, C., et al. 2021, A&A, 647, A67

Böttcher, M., Reimer, A., Sweeney, K., & Prakash, A. 2013, ApJ, 768, 54

Burd, P. R., Kadler, M., Mannheim, K., et al. 2022, A&A, 660, A1

Burke, B. F. & Graham-Smith, F. 2014, An Introduction to Radio Astronomy

Burtscher, L., Meisenheimer, K., Tristram, K. R. W., et al. 2013, A&A, 558, A149

Carroll, B. W. & Ostlie, D. A. 2017, An introduction to modern astrophysics, Second Edition

Casse, F. & Keppens, R. 2002, ApJ, 581, 988–1001

Chiaberge, M., Capetti, A., & Celotti, A. 1999, A&A, 349, 77

Chiaberge, M., Capetti, A., & Celotti, A. 2000, A&A, 355, 873

Chiuderi, C. & Velli, M. 2012, Fisica del Plasma

Clesse, S. & García-Bellido, J. 2015, Phys. Rev. D, 92, 023524

Cotton, W. D. 1995, in Astronomical Society of the Pacific Conference Series, Vol. 82, Very Long Baseline Interferometry and the VLBA, ed. J. A. Zensus, P. J. Diamond, & P. J. Napier, 189

Diamond, P. J. 1995, in Astronomical Society of the Pacific Conference Series, Vol. 82, Very Long Baseline Interferometry and the VLBA, ed. J. A. Zensus, P. J. Diamond, & P. J. Napier, 227

Elvis, M., Wilkes, B. J., McDowell, J. C., et al. 1994, ApJS, 95, 1

Esin, A. A., McClintock, J. E., & Narayan, R. 1997, ApJ, 489, 865

Event Horizon Telescope Collaboration, Akiyama, K., Alberdi, A., et al. 2022a, ApJ, 930, L12

Event Horizon Telescope Collaboration, Akiyama, K., Alberdi, A., et al. 2022b, ApJ, 930, L13

Event Horizon Telescope Collaboration, Akiyama, K., Alberdi, A., et al. 2022c, ApJ, 930, L14

Event Horizon Telescope Collaboration, Akiyama, K., Alberdi, A., et al. 2022d, ApJ, 930, L15

Event Horizon Telescope Collaboration, Akiyama, K., Alberdi, A., et al. 2022e, ApJ, 930, L16

Event Horizon Telescope Collaboration, Akiyama, K., Alberdi, A., et al. 2022f, ApJ, 930, L17

Event Horizon Telescope Collaboration, Akiyama, K., Alberdi, A., et al. 2019a, ApJ, 875, L4

Event Horizon Telescope Collaboration, Akiyama, K., Alberdi, A., et al. 2019b, ApJ, 875, L1

Event Horizon Telescope Collaboration, Akiyama, K., Alberdi, A., et al. 2019c, ApJ, 875, L2

Event Horizon Telescope Collaboration, Akiyama, K., Alberdi, A., et al. 2019d, ApJ, 875, L3

Event Horizon Telescope Collaboration, Akiyama, K., Alberdi, A., et al. 2019e, ApJ, 875, L5

Event Horizon Telescope Collaboration, Akiyama, K., Alberdi, A., et al. 2019f, ApJ, 875, L6

Fanaroff, B. L. & Riley, J. M. 1974, MNRAS, 167, 31P–36P

Fendt, C. & Čemeljić, M. 2002, A&A, 395, 1045

Ferrari, A. 2011, Stelle, galassie e universo

Grandi, P., Malaguti, G., & Fiocchi, M. 2006, ApJ, 642, 113

Grandi, P. & Palumbo, G. G. C. 2004, Science, 306, 998

Greisen, E. W. 1990, in Acquisition, Processing and Archiving of Astronomical Images, 125–142

Groves, B. 2007, in Astronomical Society of the Pacific Conference Series, Vol. 373, The Central Engine of Active Galactic Nuclei, ed. L. C. Ho & J. W. Wang, 511

Gubbay, J., Legg, A. J., Robertson, D. S., et al. 1969, Nature, 224, 1094

Hada, K., Doi, A., Kino, M., et al. 2011, Nature, 477, 185

Hardcastle, M. J., Evans, D. A., & Croston, J. H. 2007, MNRAS, 376, 1849

Hardee, P., Mizuno, Y., & Nishikawa, K.-I. 2007, Ap&SS, 311, 281

Heckman, T. M. & Best, P. N. 2014, ARA&A, 52, 589

Högbom, J. A. 1974, A&AS, 15, 417

Hönig, S. F. 2019, ApJ, 884, 171

IceCube Collaboration, Aartsen, M. G., Ackermann, M., et al. 2018, Science, 361, 147–151

Janssen, M., Falcke, H., Kadler, M., et al. 2021, Nature Astronomy, 5, 1017

Kalogera, V. & Baym, G. 1996, ApJ, 470, L61

Keek, L. & Ballantyne, D. R. 2016, MNRAS, 456, 2722

Kellermann, K. I. & Pauliny-Toth, I. I. K. 1969, ApJ, 155, L71

Kellermann, K. I., Sramek, R., Schmidt, M., Shaffer, D. B., & Green, R. 1989, AJ, 98, 1195

Komissarov, S. S. 2012, MNRAS, 422, 326

Komissarov, S. S., Barkov, M. V., Vlahakis, N., & Königl, A. 2007, MNRAS, 380, 51

Kovalev, Y. Y., Lobanov, A. P., Pushkarev, A. B., & Zensus, J. A. 2008, A&A, 483, 759

Kovalev, Y. Y., Pushkarev, A. B., Nokhrina, E. E., et al. 2020, MNRAS, 495, 3576

Kovačević-Dojčinović, J., Marčeta-Mandić, S., & Popović, L. Č. 2017, Frontiers in Astronomy and Space Sciences, 4, 7

Kramer, J. A. & MacDonald, N. R. 2021, A&A, 656, A143

Lister, M. L., Aller, M. F., Aller, H. D., et al. 2016, AJ, 152, 12

Lister, M. L., Cohen, M. H., Homan, D. C., et al. 2009, AJ, 138, 1874

Liu, B. & Bromm, V. 2022, ApJ, 937, L30

Lobanov, A. 2017, Nature Astronomy, 1, 0069

Lobanov, A. P. 1998, A&AS, 132, 261

López-Miralles, J., Perucho, M., Martí, J. M., Migliari, S., & Bosch-Ramon, V. 2022, A&A, 661, A117

Lynden-Bell, D. 1969, Nature, 223, 690

Maraschi, L., Ghisellini, G., & Celotti, A. 1992, ApJ, 397, L5

Martí, J.-M. 2015, MNRAS, 452, 3106

Martí, J. M., Perucho, M., Gómez, J. L., & Fuentes, A. 2018, International Journal of Modern Physics D, 27, 1844011

Matthews, L. D., Crew, G. B., Doeleman, S. S., et al. 2018, PASP, 130, 015002

Mattia, G. & Fendt, C. 2020, ApJ, 900, 60

Mattia, G. & Fendt, C. 2022, ApJ, 935, 22

Mayer, L. 2019, in Formation of the First Black Holes, ed. M. Latif & D. Schleicher, 195–222

Merritt, D. 1999, in Astronomical Society of the Pacific Conference Series, Vol. 182, Galaxy Dynamics - A Rutgers Symposium, ed. D. R. Merritt, M. Valluri, & J. A. Sellwood, 164

Miller-Jones, J. C. A., Bahramian, A., Orosz, J. A., et al. 2021, Science, 371, 1046

Mizuno, Y., Gómez, J. L., Nishikawa, K.-I., et al. 2015, ApJ, 809, 38

Moran, J. M. 1976, Methods of Experimental Physics, 12, 228

Morganti, R. 2017, Frontiers in Astronomy and Space Sciences, 4, 42

Murphy, G. C., Ferreira, J., & Zanni, C. 2010, A&A, 512, A82

Nakahara, S., Doi, A., Murata, Y., et al. 2020, AJ, 159, 14

Nandra, K. & Pounds, K. A. 1994, MNRAS, 268, 405

Narayan, R., Chael, A., Chatterjee, K., Ricarte, A., & Curd, B. 2021, arXiv e-prints, arXiv:2108.12380

Narayan, R., Igumenshchev, I. V., & Abramowicz, M. A. 2003, PASJ, 55, L69

Narayan, R., SÄ dowski, A., Penna, R. F., & Kulkarni, A. K. 2012, MNRAS, 426, 3241

Nokhrina, E. E., Gurvits, L. I., Beskin, V. S., et al. 2019, MNRAS, 489, 1197

Nokhrina, E. E., Kovalev, Y. Y., & Pushkarev, A. B. 2020, MNRAS, 498, 2532

O'Sullivan, S. P. & Gabuzda, D. C. 2009, MNRAS, 400, 26

Pacholczyk, A. G. 1970, Radio astrophysics. Nonthermal processes in galactic and extragalactic sources

Padovani, P. 2016, A&A Rev., 24, 13

Padovani, P., Alexander, D. M., Assef, R. J., et al. 2017, A&A Rev., 25, 2

Park, J., Hada, K., Nakamura, M., et al. 2021, ApJ, 909, 76

Perucho, M., Martí, J.-M., Quilis, V., & Borja-Lloret, M. 2017, MNRAS, 471, L120

Peterson, B. M. 2006, in Physics of Active Galactic Nuclei at all Scales, ed. D. Alloin, Vol. 693, 77

Plavin, A., Kovalev, Y. Y., Kovalev, Y. A., & Troitsky, S. 2020, ApJ, 894, 101

Pushkarev, A. B., Kovalev, Y. Y., Lister, M. L., & Savolainen, T. 2017, MNRAS, 468, 4992

Reber, G. 1944, ApJ, 100, 279

Rees, M. J. 1966, Nature, 211, 468

Ro, H., Kino, M., Sohn, B. W., et al. 2023, arXiv e-prints, arXiv:2303.01014

Ryle, M. & Hewish, A. 1960, MNRAS, 120, 220

Salpeter, E. E. 1964, ApJ, 140, 796

Sambruna, R. M., Eracleous, M., & Mushotzky, R. F. 1999, ApJ, 526, 60

Sbarrato, T., Ghisellini, G., Giovannini, G., & Giroletti, M. 2021, A&A, 655, A95

Scipione, V., Torresi, E., Grandi, P., & Palumbo, G. G. C. 2011, in The X-ray Universe 2011, ed. J.-U. Ness & M. Ehle, 282

Seyfert, C. K. 1943, ApJ, 97, 28

Shakura, N. I. & Sunyaev, R. A. 1973, A&A, 24, 337–355

Shepherd, M. C., Pearson, T. J., & Taylor, G. B. 1994, in Bulletin of the American Astronomical Society, Vol. 26, 987–989

Stokes, G. G. 1851, Transactions of the Cambridge Philosophical Society, 9, 399

Tsang, O. & Kirk, J. G. 2007, A&A, 463, 145

Urry, C. M. & Padovani, P. 1995, PASP, 107, 803

Vlahakis, N. & Königl, A. 2003a, ApJ, 596, 1080

Vlahakis, N. & Königl, A. 2003b, ApJ, 596, 1104

Vlahakis, N. & Königl, A. 2004, ApJ, 605, 656

Wang, F., Wu, X.-B., Fan, X., et al. 2015, ApJ, 807, L9

Whysong, D. & Antonucci, R. 2004, ApJ, 602, 116

Wilkinson, P. N. 1989, in NATO Advanced Study Institute (ASI) Series C, Vol. 283, Techniques and Applications of Very Long Baseline Interferometry, ed. M. Felli & R. E. Spencer, 69–93

Wilson, A. S. & Colbert, E. J. M. 1995, ApJ, 438, 62

Wu, X.-B., Wang, F., Fan, X., et al. 2015, Nature, 518, 512

Yuan, F. & Narayan, R. 2014, ARA&A, 52, 529

Yuan, F., Wang, H., & Yang, H. 2022, ApJ, 924, 124

Yuan, G.-W., Lei, L., Wang, Y.-Z., et al. 2023, arXiv e-prints, arXiv:2303.09391

Zamaninasab, M., Clausen-Brown, E., Savolainen, T., & Tchekhovskoy, A. 2014, Nature, 510, 126

Zel'dovich, Y. B. & Novikov, I. D. 1964, Soviet Physics Doklady, 9, 246

Zel'dovich, Y. B. & Novikov, I. D. 1967, Soviet Ast., 10, 602

The completion of my doctoral dissertation involved many excellent people and collaborators, whom I would like to thank in the following. First of all, I am grateful to Prof. Dr. J. Anton Zensus for the possibility and honor of being a student of the Max Planck Institute for Radio Astronomy and for the interest that he showed throughout my path. I would like to thank Prof. Dr. Andreas Eckart as well, for having followed my progress over the years.

I would like to deeply thank my supervisor, Dr. Bia Boccardi, for the patience and availability shown over the last three years. The skills that I developed as a researcher are mostly thanks to her and I will make treasure of the lessons that she taught me in our numerous meetings. Moreover, it is mandatory for me to thank Dr. Manel Perucho for the precious and fruitful collaboration. I genuinely enjoyed all my moments in Valencia: every single visit was work-wise exhausting but extremely pleasant and interesting. In this context, I would like to thank Dr. J. M. Martí and J. López-Miralles, for their crucial contribution to the success of the theoretical project, and all the other people working at the University of Valencia for always making me feel welcome.

I thank also the IMPRS and the University of Köln for the numerous courses and seminars that I was able to follow and helped me in developing important skills. Specifically, I am grateful to Dr. Rainer Mauersberger, Dr. Gunther Witzel, Simone Pott, and Arne Hoyer for their work and passion in making the life of PhD students easier and more interesting. Moreover, I would like to thank Prof. Dr. Eduardo Ros for his help throughout my years at the Max Planck Institute and for the very interesting and funny conversations.

In addition, I would like to thank and hug all my travel companions, who helped me in making my PhD experience way funnier: Georgios, Jan, Petra, Joana, Vieri, Alexsei, Hui-Hsuan, Jongseo, Hendrik, Eftychia, and Sebastiano. The time we spent together meant a lot to me. In particular, I am extremely grateful to Petra, Vieri, Jan, and Joana for having actively helped me during the production of the results presented in this thesis. A further special thank is mandatory for Petra, Vieri, and Joana, for their amazing friendship and for the help and unconditional support that I received during the most stressful moments of my PhD studies.

Finally, a special thanks to Dr. Giancarlo Mattia. Our long-term friendship means a lot to me and I am grateful for the incredible help that I received since my bachelor studies. I genuinely hope that our scientific collaboration will continue for a lot of years to come.

Here, I would like to show my gratitude to all the people outside of the working environment who were crucial in making my years in Bonn one of the best experiences that I will ever be able to make. The list of people is long and is impossible to cite them all, nonetheless, I want to particularly thank: Nicole, Enrico, Fadi, Johannes, Gwydyon, Andrea (Frau), Fabienne, Kasia, Piotr, and Maria. Your friendship during these years was precious and gave me the strength and courage to proceed with my studies.

Impossible for me not to thank all the people sparse around the world, whose support has been crucial, especially during the long and exhausting lockdown that we all had to experience, and that, unfortunately, affected my first year in Bonn. Therefore, thanks to Alessandra, Agata, my wrestling group (Cesare, Beppe, and Crocco), my historical group (Matteo, Dela, Sonny, Fabio, Federico, Daniel, and Riccardo), Serena, and Valeria. A special thanks to my best friends in the world, simply for everything: Nora, Lauda, and the Arfò (Luca, Alberto, and Andrea). A special thought to Andrea, for our weekly calls and checkups on our mental health: those calls have been very important to me.

A lovely thank you to Katharina, which recently entered my life but since then has become a fundamental tile of it. Your support and understanding across the last months of the PhD and during the writing of the dissertation has been wholesome and I am extremely grateful for that. *"... they pulled me to them once you realize all you can do is admire them, can't resist anyway."*

I conclude my long list of thanks with a thought for my family. I have no words that can properly describe how grateful I am for all the support and for the opportunities that they gave me in my life. Studying is a privilege (even if it should not be) that they gave me with complete trust together with the opportunity to focus on my career without ever having to worry about anything. Emma, Gianni, and Daniel: thank you for everything from the bottom of my heart. In particular, I am moved by the support and love that my mother (Emma) gave me over the years: nobody knows how many times I called her in need of help, and every single time she was there ready to help me. In conclusion, I would like to dedicate a thought to my grandparents Luigina and Nino. They helped me to become the person I am today and the memories of us together will accompany me for the rest of my life.

Luca Ricci

✉ lricci@mpifr-bonn.mpg.de in Luca Ricci
✉ luca.ricci.1195@gmail.com

Current position

Since Sep 2020	**Doctoral researcher,** Max Planck Institute for Radio Astronomy, Bonn Otto Hahn Research Group led by Dr. Biagina Boccardi Since Feb 2023, affiliated also with Julius-Maximilians-Universität Würzburg Thesis title: "Jet formation and propagation in the nearby giant radio galaxy NGC 315" Supervisors: Prof. Dr. J. Anton Zensus & Prof. Dr. Andreas Eckart Advisor: Dr. Biagina Boccardi

Education

Apr 2020	**Master Degree in Astrophysics** University of Turin, Turin, Italy Thesis title: "Spectral and dynamical ages of radio galaxies: observations and modelling of 3C 449" Advisor: Dr. Luisa Ostorero Co-Advisors: Prof. Raffaella Morganti, Prof. Silvano Massaglia Final grade: 110/110 cum laude
Oct 2017	**Bachelor Degree in Physics** University of Turin, Turin, Italy Thesis title: "Free-falling galaxies: dynamical constraints from wide-angle-tailed radio sources" Advisor: Dr. Luisa Ostorero Co-Advisor: Prof. Andrea Mignone Final grade: 106/110
July 2014	**High school diploma** Liceo Scientifico "A. Einstein", Turin, Italy Final Grade: 86/100

Full list of publications and manuscripts

Refereed Articles and Manuscripts

① **L. Ricci**, B. Boccardi, J. Röder, *et al.*, "Magnetic and spectral properties of the inner parsec scales jet in ngc 315," draft manuscript.

② **L. Ricci**, M. Perucho, J. López-Miralles, J. M. Martí, and B. Boccardi, "Magnetic and thermal acceleration in extragalactic jets: An application to ngc 315," submitted to A&A.

③ **L. Ricci**, B. Boccardi, E. Nokhrina, *et al.*, "Exploring the disk-jet connection in ngc 315," *Astronomy and Astrophysics*, vol. 664, A166, 2022. DOI: `10.1051/0004-6361/202243958`.

④ B. Boccardi including **L. Ricci**, "Jet collimation in ngc 315 and other nearby agn," *Astronomy and Astrophysics*, vol. 647, A67, 2021. DOI: `10.1051/0004-6361/202039612`.

Conference Proceedings

① B. Boccardi, E. Madika, and **L. Ricci**, "Accretion mode and jet collimation in active galactic nuclei," vol. 342, 2021, pp. 1071–1076. DOI: `10.1002/asna.20210085`.